Wideband Blocker-Tolerant Receivers for Sub-7 GHz 5G Applications

Montazerolghaem, M.A.

DOI
10.4233/uuid:551f9935-ecdf-452a-8504-cd51a72f70ac

Publication date
2025

Document Version
Final published version

Citation (APA)
Montazerolghaem, M. A. (2025). *Wideband Blocker-Tolerant Receivers for Sub-7 GHz 5G Applications*. [Dissertation (TU Delft), Delft University of Technology]. https://doi.org/10.4233/uuid:551f9935-ecdf-452a-8504-cd51a72f70ac

Important note
To cite this publication, please use the final published version (if applicable).
Please check the document version above.

Wideband Blocker-Tolerant Receivers for Sub-7 GHz 5G Applications

Mohammad Ali Montazerolghaem

Wideband Blocker-Tolerant Receivers for Sub-7 GHz 5G Applications

Mohammad Ali Montazerolghaem

Wideband Blocker-Tolerant Receivers for Sub-7 GHz 5G Applications

Dissertation

for the purpose of obtaining the degree of doctor
at Delft University of Technology,
by the authority of the Rector Magnificus Prof.dr.ir. T.H.J.J. van der Hagen
chair of the Board for Doctorates,
to be defended publicly on

Tuesday, 10 June 2025 at 15:00 o'clock

by

Mohammad Ali MONTAZEROLGHAEM

Master of Science in Electrical Engineering, Amirkabir University of Technology, Tehran, Iran
born in Esfahan, Iran.

This dissertation has been approved by the promotors.

Composition of the doctoral committee:

Rector Magnificus,	chairman
Dr. M. Babaie,	Delft University of Technology, promotor
Prof. dr. ir. L. C. N. de Vreede,	Delft University of Technology, promotor

Independent members:

Prof. dr. P. Wambacq,	Vrije Universiteit Brussel, Belgium
Dr. J. Craninckx,	IMEC, Belgium
Dr. D. Manstretta,	University of Pavia, Italy
Dr. N. Reiskarimian,	Massachusetts Institute of Technology, USA
Prof. dr. K. A. A. Makinwa,	Delft University of Technology
Prof. dr. ir. W. A. Serdijn	Delft University of Technology, reserve member

This thesis was supported by Nederlandse Organisatie voor Wetenschappelijk Onderzoek (NWO)/Ampleon Partnership Program under Project 16336 (DIPLOMAT).

Mohammad Ali Montazerolghaem,
Wideband Blocker-Tolerant Receivers for Sub-7 GHz 5G Applications,
Ph.D. Thesis Delft University of Technology,

Keywords: Blocker-tolerant, current-mode receiver (RX), fifth-generation (5G), user equipment applications, base station applications, N-path filters, out-of-band linearity, in-band linearity, programmable zeros, surface acoustic wave (SAW)-less RX, second-order transimpedance amplifier (TIA), harmonic rejection (HR), high-order bandpass filter, preselect filter, software-defined radio, wideband RX.

ISBN 978-94-6518-062-5

Printed in the Netherlands.

To my dearest Bahar, who has always stood by my side.

"*Once, a king assembled a group of wise men to create a ring to make him happy when he was sad. That ring was inscribed with the phrase: 'This too shall pass.'*"

Attar Neyshaburi, 1145-1221

Contents

Contents **i**

1 Introduction **1**
1.1 Wireless Communication . . . 1
1.2 RX Design for 5G Mobile Communication . . . 3
1.2.1 Enhancing Data Rate . . . 4
1.2.2 Demand for Wideband RXs . . . 6
1.2.3 Blocking Scenarios in 5G Applications . . . 7
1.3 N-path Filters . . . 7
1.3.1 Phase Noise Requirements of N-path Filters . . . 10
1.4 Current Mode RXs . . . 11
1.4.1 Mixer-First RXs . . . 12
1.4.2 LNTA-Based RXs . . . 14
1.5 Thesis Objectives . . . 17
1.6 Thesis Outline . . . 17

2 A Highly Selective Receiver With Programmable Zeros and Second-Order TIA 19
2.1 Introduction . . . 19
2.2 Evolution of the Programmable Zeros . . . 20
2.2.1 Implementation of the Programmable Zeros . . . 23
2.2.2 RX Bandwidth and Input Impedance at Zeros Frequencies . . . 24
2.2.3 Improving Far-Out Out-of-Band Linearity . . . 25
2.2.4 Design Guide for the RX RF Front-End . . . 26
2.2.5 Loop Stability of the RX RF Front-End . . . 29
2.3 Second-Order TIA . . . 31
2.3.1 TIA Performance over PVT Variations . . . 33
2.3.2 Stability Analysis of the TIA's Amplifier . . . 36
2.3.3 Design Guide for the Second-order TIA . . . 38
2.3.4 TIA Selectivity and Area Trade-Off . . . 39

2.4 Circuit Implementation . . . 40
2.5 Noise Analysis . . . 44
2.6 Experimental Results . . . 46
2.7 Conclusion . . . 54

3 A Highly-Linear Receiver Using Parallel Preselect Filter for 5G Microcell Base Station Applications 57
3.1 Introduction . . . 57
3.2 Proposed RX Structure . . . 59
3.2.1 Parallel Preselect Filter . . . 61
3.2.2 Implementation of the Parallel Preselect Filter . . . 62
3.2.3 Design Guide for the Parallel Preselect Filter . . . 64
3.3 Translational Feedback Network . . . 68
3.3.1 Input Matching in Current-Mode RXs . . . 68
3.3.2 Delay of the Transconductance . . . 69
3.3.3 Proposed Translational Feedback Network . . . 71
3.3.4 Effect of RX Delay . . . 73
3.4 Circuit Implementation . . . 75
3.5 Noise Analysis . . . 78
3.6 Measurement Results . . . 80
3.6.1 Wideband Operation . . . 81
3.6.2 Linearity Measurements . . . 86
3.6.3 3GPP Requirements . . . 87
3.6.4 High-order QAM . . . 88
3.6.5 Performance Summary and Comparison . . . 90
3.7 Conclusion . . . 90

4 A Sub-7GHz Linear Receiver for 5G Local Area Base Station Applications 93
4.1 Introduction . . . 93
4.2 In-Band Linearity Requirement . . . 95
4.3 Transimpedance Amplifier . . . 96
4.3.1 Transfer Function . . . 97
4.3.2 Input Impedance . . . 98
4.3.3 Linearity . . . 100
4.3.4 Performance over PVT Variations . . . 105
4.3.5 Noise . . . 106
4.3.6 DC Offset . . . 108
4.3.7 Discussion . . . 108
4.4 Proposed RF Front-End . . . 109
4.4.1 Expanding RX Operating Frequency . . . 109
4.4.2 3-dB Bandwidth Expansion . . . 110

4.4.3 Impact of PVT-induced Variations of Positive Feedback Amplifier 113
4.5 RX In-Band Linearity 114
4.5.1 LNTA 116
4.5.2 TIA 117
4.5.2.1 Feedforward Path 118
4.5.2.2 Feedback Path 119
4.5.2.3 Overall TIA 119
4.5.3 RX Chain 120
4.5.4 Discussion 122
4.6 Circuit Implementation 123
4.7 Measurement Results 127
4.8 Conclusion 135

5 Conclusion **137**
5.1 Thesis Outcomes 137
5.2 Recommendations for Future Developments 139

Bibliography **145**

List of Figures **157**

List of Tables **167**

Summary **169**

Samenvatting **173**

List of Publications **177**

Acknowledgement **179**

Chip Micrograph Gallery **183**

About the Author **185**

Chapter

1

Introduction

1.1 Wireless Communication

In 1895, Guglielmo Marconi transmitted and received the first wireless signal to overcome the limitations of wired communication. Little did he know that his invention made so much change in the future of humanity. Marconi's breakthrough revolutionized human communication by enabling the exchange of messages invisibly through the air, what we now know as wireless communication nowadays. What began as a simple transmission and reception has evolved through the years to become the backbone of technologies that connect everything from smartphones and satellites to the Internet of Things (IoT) and smart homes.

In the late 1980s, wireless communication took a significant leap forward by introducing the Global System for Mobile Communications (GSM). The main difference between GSM and previous technologies was utilizing digital communication to enhance the quality, security, and efficiency of mobile communication. GSM also introduced some brilliant technologies, such as short message service (SMS), which made mobile communication part of our daily lives. GSM paved the way for modern mobile communication, and even today, GSM is still in use across many parts of the world.

As shown in Fig. 1.1, GSM operates using a cellular network structure that

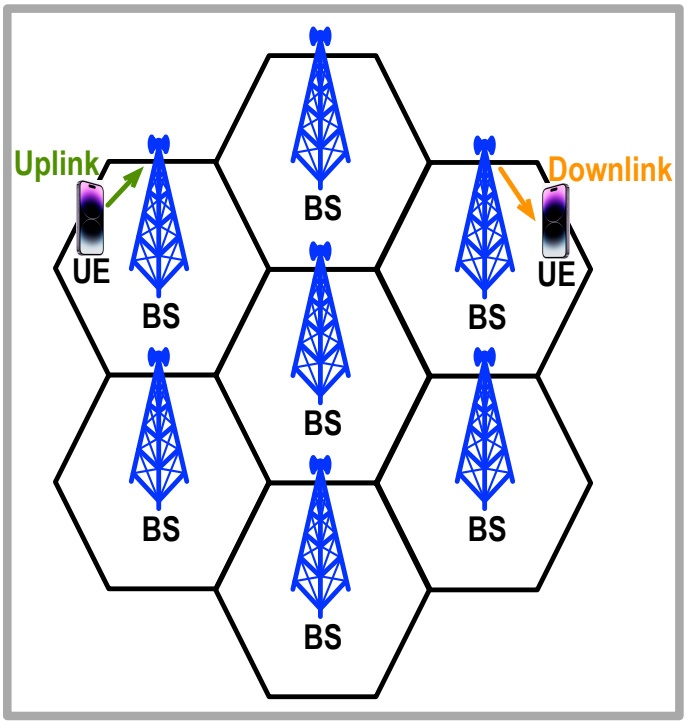

Figure 1.1: A simplified example of cellular network used for GSM.

divides a geographic area into multiple cells. Each cell is served by a base station (BS), which facilitates communication with end users, referred to as user equipment (UE). In this network, UE continuously searches for the nearest cell to establish a communication link with the BS. Communication between the UE and BS occurs over two distinct links: uplink and downlink. A downlink refers to the transmission of signals from the BS to the UE, while an uplink involves the UE transmitting signals to the BS. This bidirectional communication is the cornerstone of GSM functionality, ensuring seamless connectivity within the cellular network.

Transceivers play a critical role in establishing communication links between UE and BS. In modern radio systems, transceivers consist of three main building blocks: the transmitter (TX), receiver (RX), and local oscillator (LO). The RX receives signals transmitted by the BS, while the TX handles signal transmission to the BS. The LO facilitates frequency conversion, upconverting baseband signals to RF for transmission and downconverting RF signals to baseband for processing. As illustrated in Fig. 1.2, transceiver architectures can employ two duplexing schemes: frequency division duplexing (FDD) and time division duplexing (TDD). In FDD, the TX and RX operate simultaneously on different frequencies, with RX working on downlink and TX on uplink frequencies. In

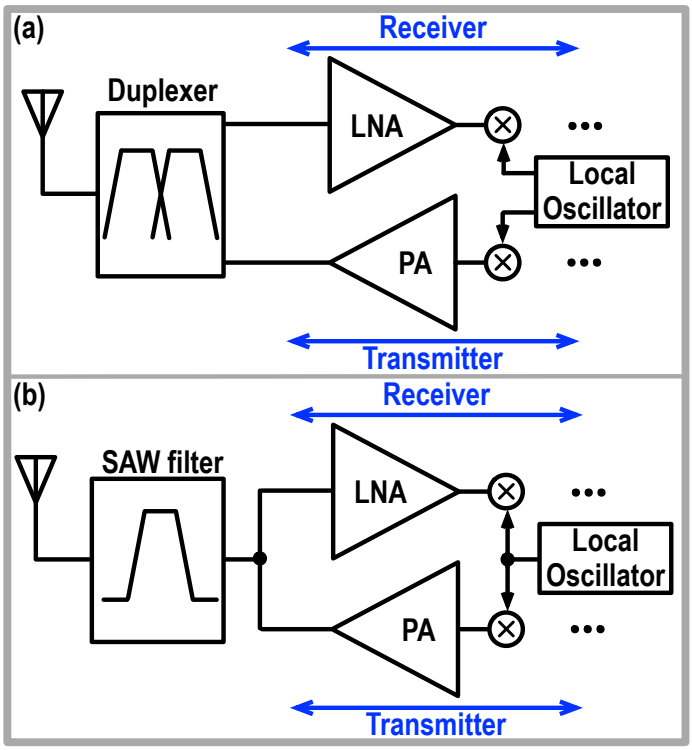

Figure 1.2: Two well-known transceiver architectures used in wireless communications: (a) FDD and (b) TDD.

TDD, TX and RX operate alternately on the same frequency (uplink and downlink have the same operating frequency). This thesis focuses on the design of RXs for UE and BS applications.

1.2 RX Design for 5G Mobile Communication

Building on the foundational principles of GSM, the evolution of mobile communication has now reached its fifth generation (5G). To meet the growing consumer demand for higher data rates, 5G technology has been deployed across low-band, mid-band, and high-band frequencies (see Fig. 1.3). While 5G radios operating in high-frequency bands can achieve extremely high data rates, their significant path loss limits their application to short-range communication. As a result, low-band and mid-band frequencies gained more attention for long-range communication and will be the focus of this thesis. The design of RXs for 5G low-band and mid-band frequencies faces new challenges, which will be discussed in the following subsections.

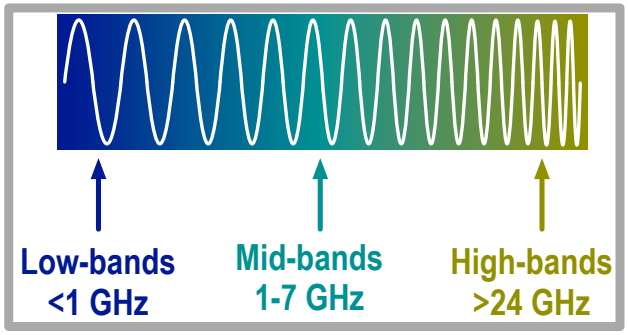

Figure 1.3: 5G spectrum.

1.2.1 Enhancing Data Rate

In 1948, Claude Shannon introduced his theory to determine the channel capacity (C), which represents the maximum achievable data rate over a communication channel. Shannon's formula for channel capacity is expressed as:

$$C = BW \cdot \log_2\left(1 + \frac{S}{N}\right), \tag{1.1}$$

where BW is the channel bandwidth, and S/N represents the signal-to-noise ratio (SNR). As evident from (1.1), one of the simplest ways to increase data rate is by expanding channel bandwidth. For instance, compared to the 200 kHz channel bandwidth of GSM, 5G applications utilize 100 MHz channel bandwidth. However, this improvement comes with its own challenges. In the RX baseband domain, active low-pass filters are typically employed to suppress out-of-band blockers, and their 3-dB bandwidth is directly determined by the channel bandwidth. Consequently, increasing the channel bandwidth complicates the amplifier's design in the active low-pass filters, requiring more advanced techniques to maintain their performance.

In 5G applications, high-order modulation schemes are also employed to enhance data rates. As illustrated in Fig. 1.4, achieving the same bit error rate (BER) with high-order modulation schemes requires a higher SNR. For instance, to achieve a BER of $= 10^{-2}$, 16-QAM (Quadrature Amplitude Modulation) demands approximately 6 dB higher SNR compared to QPSK (Quadrature Phase Shift Keying). Utilizing higher channel bandwidths and more complex modulation schemes directly affects the reference sensitivity (P_{sen}), which is expressed as:

$$P_{sen} = -174 + 10\log_{10} BW + \mathrm{NF} + SNR_{min}, \tag{1.2}$$

where SNR_{min} is the minimum required SNR for a given modulation scheme,

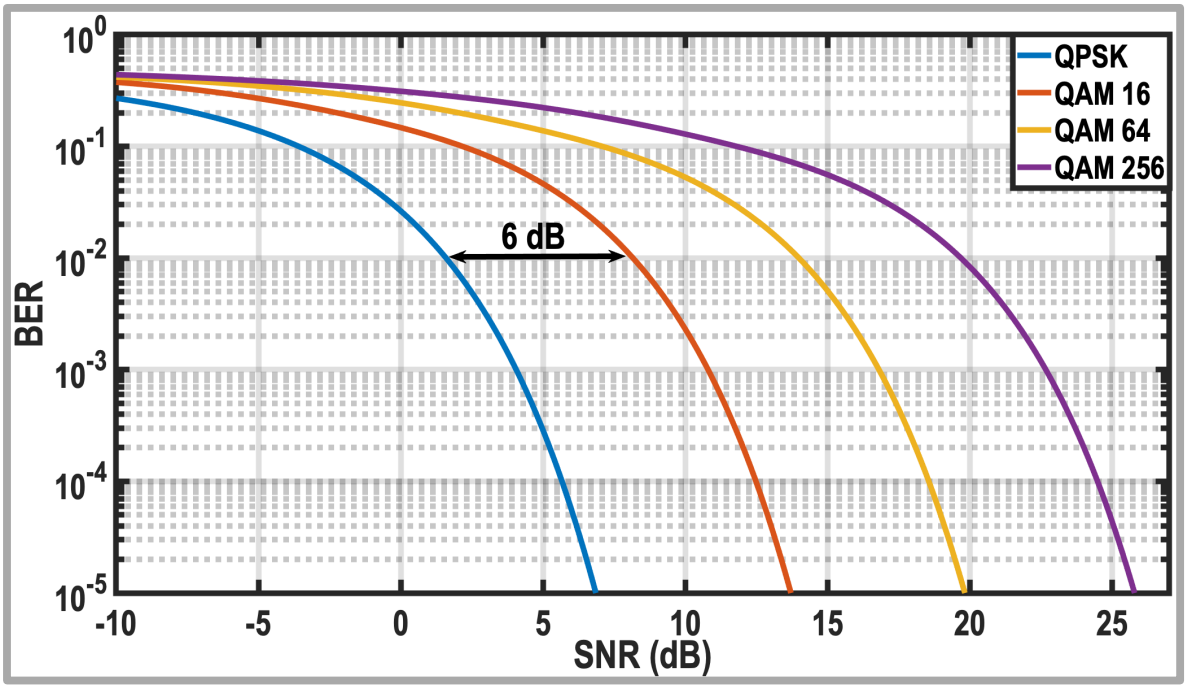

Figure 1.4: BER versus SNR for different modulation schemes.

NR operating band	Uplink operating band	Downlink operating band	Duplex mode
n1	1920 – 1980 MHz	2110 – 2170 MHz	FDD
n2	1850 – 1910 MHz	1930 – 1970 MHz	FDD
n3	1710 – 1785 MHz	1805 – 1880 MHz	FDD
n5	824 – 849 MHz	869 – 894 MHz	FDD
n7	2500 – 2570 MHz	2620 – 2690 MHz	FDD
n34	2010 – 2025 MHz	2010 – 2025 MHz	TDD
n38	2570 – 2620 MHz	2570 – 2620 MHz	TDD
n39	1880 – 1920 MHz	1880 – 1920 MHz	TDD
n50	1432 – 1517 MHz	1432 – 1517 MHz	TDD

Figure 1.5: Some examples of new radio operating bands.

and NF is the RX noise figure. From Equation (1.2), it is evident that increasing channel bandwidth and adopting higher-order modulation schemes will degrade P_{sen}. To overcome this, lowering NF is crucial to improve SNR, enabling the adoption of higher-order modulation schemes to enhance spectral efficiency. Furthermore, as mentioned earlier, low-band and mid-band frequencies are preferable for long-range communication, and achieving sub-3dB NF performance extends the communication range in these bands.

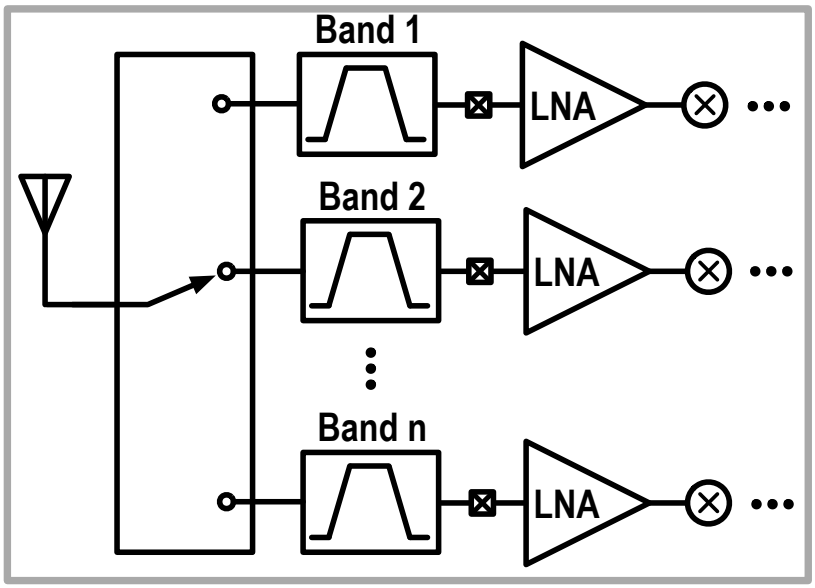

Figure 1.6: Conventional RX architecture with band-select filters to choose different frequency bands.

1.2.2 Demand for Wideband RXs

Several new radio operating bands have been introduced for the low-band and mid-band frequencies of 5G applications. Examples of new radio bands, along with their downlink frequencies, uplink frequencies, and duplexing modes, are provided in Fig. 1.5 [1, 2]. As illustrated in Fig. 1.6, conventional RX architectures rely on multiple band-select filters to isolate the desired receive band and attenuate out-of-band blockers. Surface acoustic wave (SAW) filters are commonly employed for this purpose. However, SAW filters have drawbacks—they are bulky and costly, increasing the overall size and expense of cellular devices [3]. Additionally, SAW filters typically introduce a 2–3 dB loss in the receive chain, degrading NF and, consequently, reducing network coverage. Furthermore, an RF switch is also used to select the desired RX path, further contributing to signal loss. Eliminating the RF switch and SAW filters is highly desirable to enable wideband RX designs that are more cost-effective, compact, and CMOS-compatible. However, removing band-select filters presents its own challenges, as it makes wideband RXs more susceptible to out-of-band blockers. For instance, in GSM applications, the RX must handle out-of-band blockers as strong as 0 dBm, a requirement that can be difficult to achieve in CMOS technology with limited supply voltage. Therefore, a blocker-tolerant RX is crucial for 5G applications.

1.2.3 Blocking Scenarios in 5G Applications

As discussed earlier, a wideband receiver (RX) is essential to cover the sub-7 GHz spectrum required for 5G applications. Additionally, the RX must support high bandwidth to enable enhanced data rates. These two critical requirements impose stringent linearity demands on the RX design.

Although the 5G channel bandwidth has increased compared to previous standards, the offset frequency of close-in blockers has remained constant due to the congested spectrum at low-band and mid-band frequencies. For instance, in 5G user equipment applications, the maximum channel bandwidth has expanded from 20 MHz of 4G applications to 100 MHz. However, the close-in blocker offset frequency remains at 85 MHz. The situation is even more challenging in 5G base station applications, where the channel bandwidth can reach up to 200 MHz or even 400 MHz, while the close-in blocker offset frequency is just 20 MHz. Hence, wideband RXs should provide sufficiently high selectivity to suppress close-in blockers and prevent RX desensitization.

In base station co-location applications, strong blockers from other standards, such as GSM, necessitate high out-of-band linearity in the receiver (RX) design. The blocker power in such scenarios is influenced by the size and type of the base station. For instance, in medium-range base station applications, the RX must handle continuous wave (CW) out-of-band blockers with power levels as high as 8 dBm. In contrast, for local area base stations, the blocker power is typically -4 dBm. Finally, 5G base station RXs must contend with in-band modulated blockers. In local area base station receivers, the in-band blocker power can reach -35dBm, requiring an in-band third-order intercept point (IIP3) of at least -10.5dBm. Achieving such a high IIP3 is particularly challenging for RXs designed for high-bandwidth applications.

1.3 N-path Filters

As mentioned earlier, several new radios are defined for the low-band and mid-band frequencies of 5G applications. Typically, SAW filters are utilized to select the desired frequency band and suppress close-in and far-out blockers in 5G systems. However, this approach comes with trade-offs, including NF degradation, increased cost, and a larger form factor. To address these challenges, achieving on-chip selectivity has become a priority. In recent years, N-path filters have gained more attention as a solution for providing on-chip selectivity for 5G applications.

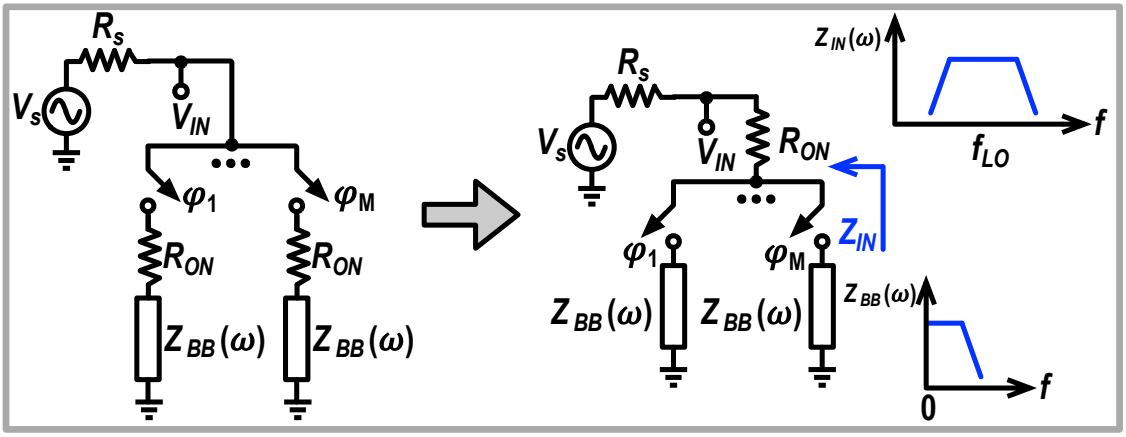

Figure 1.7: A typical implementation of N-path filter.

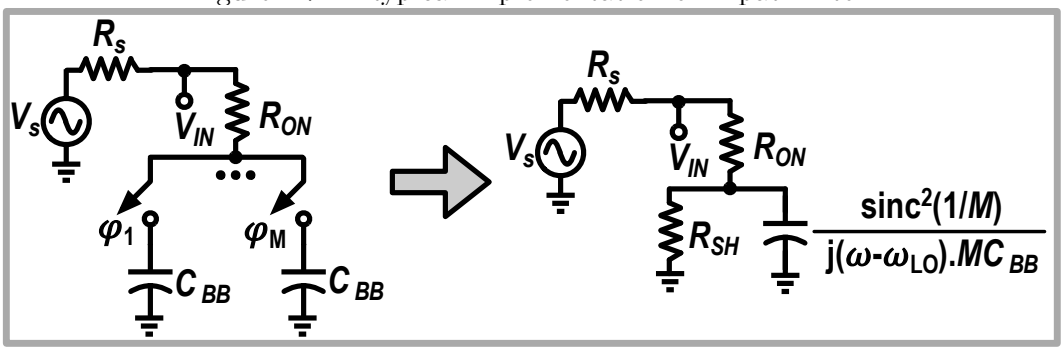

Figure 1.8: Replacing Z_{BB} with baseband capacitors and its equivalent model.

Although the introduction of N-path filters dates back to the 1940s and 1950s [4–7], they have recently attracted interest due to improvements in CMOS technology, which enable the realization of better switches [8–18]. Fig. 1.7 shows a typical N-path filter, comprising M switches and M baseband impedance ($Z_{BB}(\omega)$), connected to the antenna with an equivalent impedance of R_S. The switches have on-resistance equal to R_{ON}. Instead of M resistors, the on-resistance of the switches can be modeled by a single resistor in the RF domain, as shown in Fig. 1.7. Due to the transparency of the passive mixers, the baseband impedance upconverts to the RF domain, and the input impedance of the N-path filter can be approximated by [13]

$$Z_{IN}(\omega) = \frac{1}{M}\text{sinc}^2\left(\frac{1}{M}\right) Z_{BB}\left(\omega - \omega_{LO}\right), \tag{1.3}$$

where ω_{LO} is the LO frequency. In other words, the low pass filter in the baseband domain is upconverted to the RF domain and appears as a bandpass filter in the RF domain. The center frequency of this bandpass filter is tunable with the LO frequency.

The easiest way to implement Z_{BB} is by using M capacitors (C_{BB}), as shown

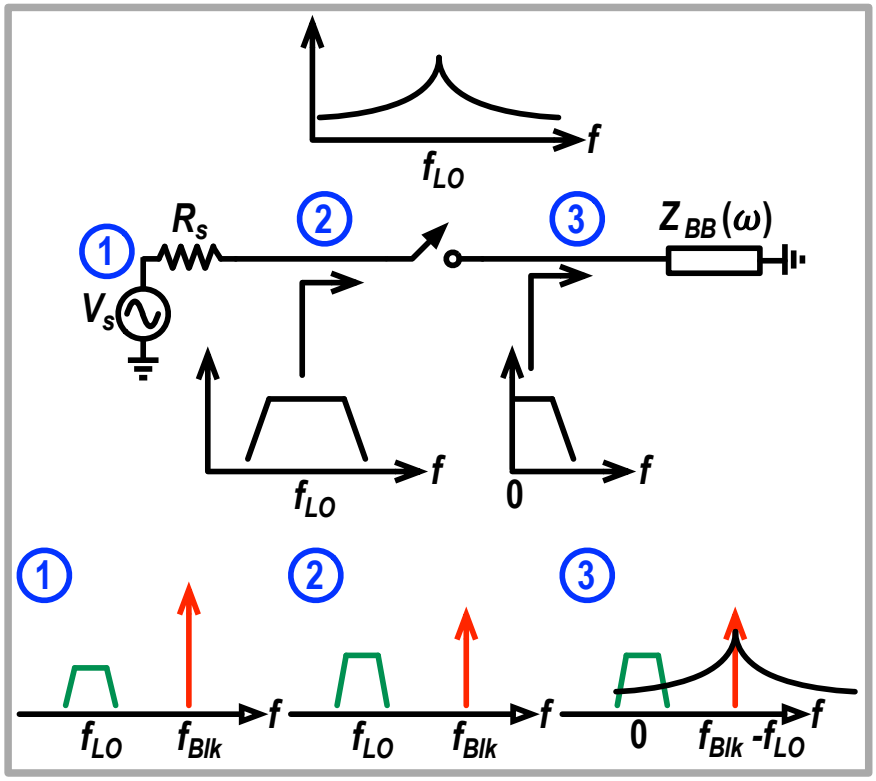

Figure 1.9: NF degradation due to the mixing between the LO phase noise and out-of-band blocker.

in Fig. 1.8. Ideally, the input impedance of the N-path filter becomes open around the operating frequency, and the input voltage of the N-path filter (V_{IN}) equals the source voltage (V_S). However, in practice, V_{IN} is a staircase approximation of V_S, introducing loss to the system. As depicted in Fig. 1.8, this loss can be modeled with a shunt resistor (R_{SH}) [19] in parallel with the ideal impedance of N-path filters. R_{SH} can be approximated by

$$R_{SH} = \frac{\text{sinc}^2\left(\frac{1}{M}\right)}{1-\text{sinc}^2\left(\frac{1}{M}\right)}\left(R_{ON}+R_S\right). \tag{1.4}$$

Increasing M reduces $\left(1-\text{sinc}^2\left(1/M\right)\right)$ to 0 and results in higher R_{SH}. In other words, increasing M makes a better approximation of the input signal and reduces the loss of the system.

Although N-path filters offer high-Q and tunable band-pass filtering in the RF domain, several challenges remain to be solved before they can effectively replace SAW filters. First, the filtering order of conventional N-path filters is limited to first-order, making them vulnerable to close-in blockers, especially in high-bandwidth applications. Additionally, the out-of-band rejection of N-path

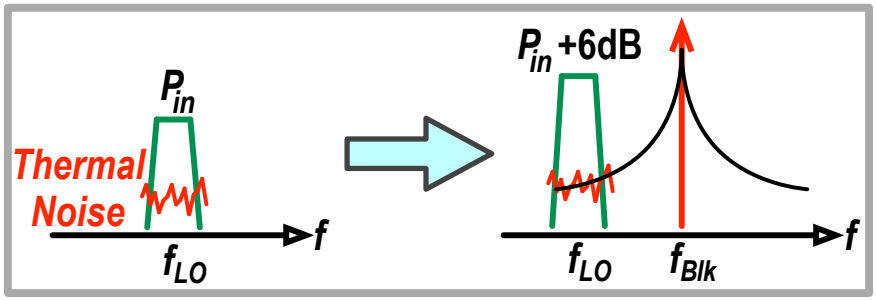

Figure 1.10: SNR degradation due to the reciprocal mixing of LO phase noise and out-of-band blockers.

filters is constrained by the on-resistance of the switches. Hence, large switches are needed to achieve decent out-of-band rejection in the RF domain, demanding high power consumption of the LO circuitry to drive them. Another issue is the parasitic capacitors of the switches, which shift the center frequency of the N-path filters toward the lower side of the LO frequency. These parasitic effects, along with charge injection from the switches, also result in asymmetric performance around the LO frequency. Finally, the phase noise of LO mixes with the out-of-band blockers and appears in the baseband domain. Due to the transparency of passive mixers, the down-converted phase noise of LO upconverts to the RF domain and appears at the input voltage of N-path filters. Hence, reciprocal mixing degrades the RX noise performance in the presence of out-of-band blockers, which will be discussed in the next Subsection.

1.3.1 Phase Noise Requirements of N-path Filters

As illustrated in Fig. 1.9, out-of-band blockers mix with LO phase noise, resulting in in-band noise that degrades the sensitivity of the RX. As mentioned earlier, in traditional RX designs, SAW filters are used to suppress out-of-band blockers, thereby mitigating the LO phase noise requirements. However, modern RXs aim to replace SAW filters with N-path filters. Consequently, it is crucial to analyze the LO phase noise requirements under different blocking scenarios of 5G applications.

In 5G blocking scenarios, the power of the desired signal is at least 6 dB higher than the reference sensitivity (the base station applications have the minimum increase). This means, to some extent, SNR degradation is acceptable. Hence, as shown in Fig. 1.10, the power of reciprocal mixing can be in the level of thermal noise, leading to an additional 3 dB noise figure penalty. In user equipment applications and base station applications, the maximum blocker power is -15 dBm. Assuming that the RX NF is 3 dB, the required LO phase

noise can be calculated as follows:

$$PN@f_{LO} = -174\,\text{dBm/Hz} + NF - P_{Blk} = -156\,\text{dBc/Hz}. \tag{1.5}$$

In typical modern RXs, a divide-by-two block is used to generate the nonoverlapping LO phases. The divide-by-two block improves the LO phase noise by 6 dB. Hence, the oscillator phase noise at $2f_{LO}$ should be -150 dBc/Hz, a value achievable with state-of-the-art oscillators [20]. It is important to note that the required phase noise corresponds to a high offset frequency from $2f_{LO}$. The LO buffers driving the passive mixers and the divider itself should have reasonably lower phase noise, a typical implementation is proposed in [21].

In 5G co-location base station applications, the power of out-of-band blockers is -4 dBm for local-area applications and +8 dBm for medium-range applications. Consequently, the required oscillator phase noise at $2f_{LO}$ is -161 dBc/Hz and -173 dBc/Hz for local-area and medium-range applications, respectively. While -161 dBc/Hz is considered achievable in CMOS technology [20], achieving -173 dBc/Hz for medium-range base stations is highly challenging.

1.4 Current Mode RXs

Several attempts have been made to implement tunable band-select filters using N-path filters and enhance their selectivity [22–27]. For instance, to achieve sharp filtering and high out-of-band linearity, the authors in [22] proposed a band-select filter based on implementing transmission zeros in a passive network. While the transmission zeros can be tuned, the operating frequency is limited to only 0.8-1.1 GHz. Alternatively, the approach in [23] introduced an active N-path filter to realize a wideband third-order band-select filter. However, the operating frequency is still limited to 0.1-1.1 GHz. All of these designs degrade the RX line-up NF by at least 2.8 dB. Hence, a wideband RX without a band-select filter is desirable for 5G applications to avoid NF degradation.

Typically, modern RXs adopt a current-mode architecture to achieve wideband operation and blocker tolerance. In these RXs, as illustrated in Fig. 1.11, the RF input voltage is first converted to an RF current by either a low-noise transconductance amplifier (LNTA) or an implicit or explicit 50 Ω matching in mixer-first RXs. Passive mixers then down-convert the RF current, and finally, a transimpedance amplifier (TIA) converts the down-converted current to a baseband voltage. In this way, the virtual ground of the TIA reduces the voltage gain in the RF domain, and the voltage gain is carried out in the baseband domain to achieve decent linearity performance. Moreover, the TIA provides

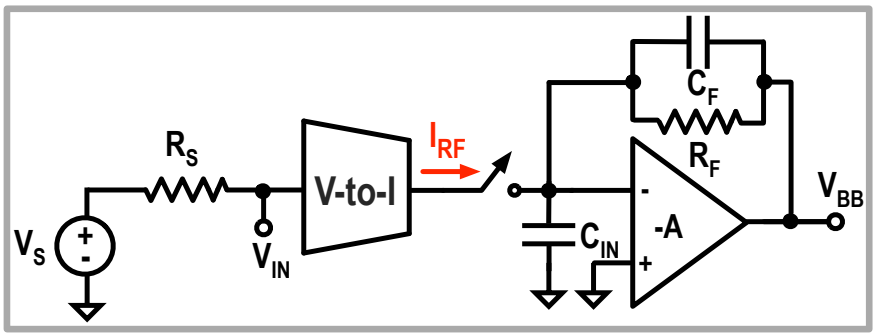

Figure 1.11: Conventional current-mode RX architecture.

baseband domain filtering, suppressing the close-in and far-out blockers. Hence, current-mode RXs are appealing candidates for the 5G user equipment and base station applications. Despite their advantages, current-mode RXs (both LNTA-based and mixer-first architectures) still face challenges in meeting the stringent requirements of 5G applications. The following subsections will discuss the shortcomings of mixer-first and LNTA-based RXs for 5G user equipment and base station applications.

1.4.1 Mixer-First RXs

Fig. 1.12 (a) shows the conventional mixer-first RX architecture, in which the input matching is achieved by the transparency of passive mixers [19, 28, 29]. Since the LNTA is removed in mixer-first RXs, they usually achieve decent out-of-band linearity, making them a suitable candidate for 5G user equipment applications. However, removing LNTA requires large switches to achieve decent NF and out-of-band linearity performance. Consequently, they suffer from high LO leakage to the antenna, and their operating frequency is also limited to below 5 GHz [19, 28, 30–49].

Moreover, since TIA provides input-matching, its input impedance is always higher than 0. Hence, a voltage swing will appear at the TIA input, degrading the in-band linearity of mixer-first RXs. To solve this issue, as shown in Fig. 1.12 (b), an input-matching resistor can be added in series with the passive mixers and TIAs to minimize the voltage swing at the TIA input [50]. However, adding the series resistor drastically degrades the NF performance. To cancel the noise of the matching resistor, a noise-canceling path can be added in parallel with the mixer-first RX [21] (see Fig. 1.12 (c)). To relax the LNTA linearity requirement, the noise canceling structure can also be implemented in the baseband domain as depicted in Fig. 1.12 (d) [51, 52]. However, this comes at the cost of higher power consumption since the number of TIAs is doubled, which can be a severe issue in high bandwidth applications.

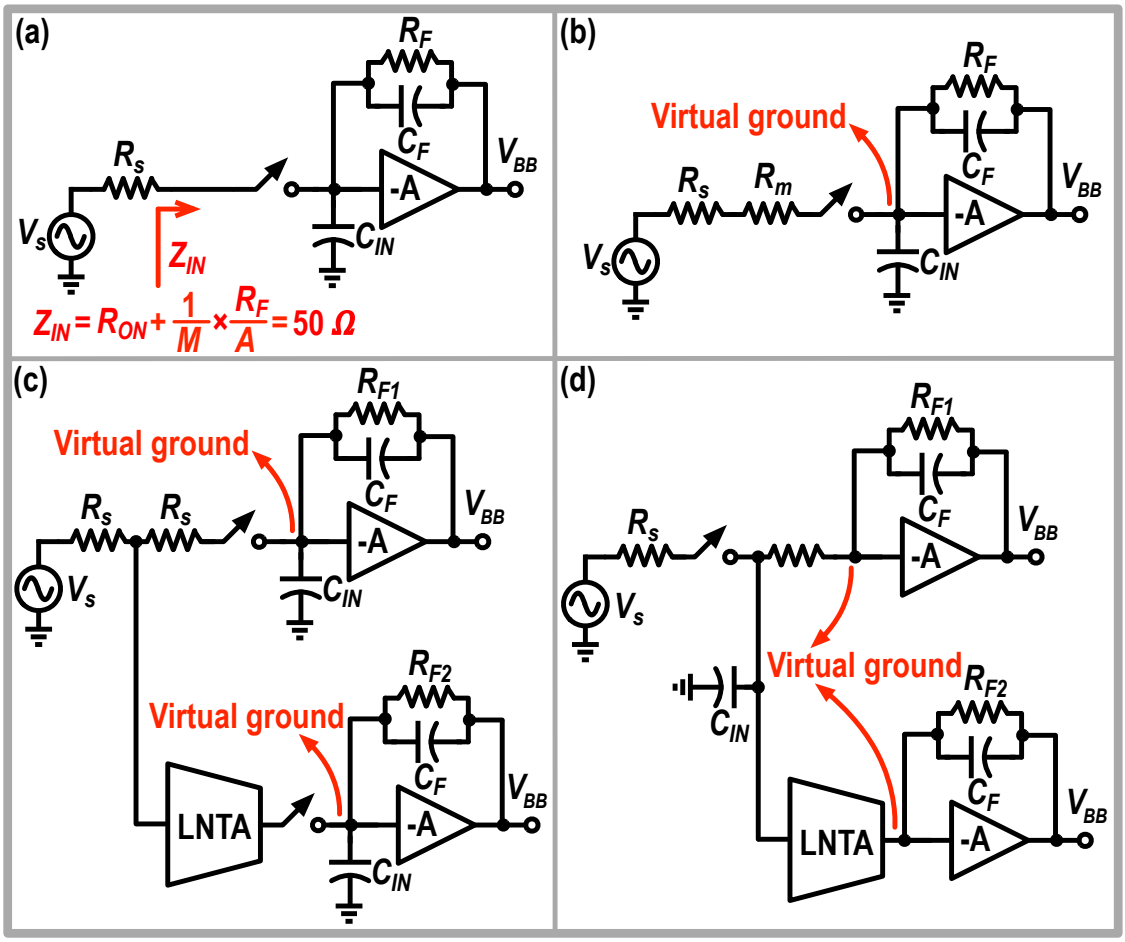

Figure 1.12: (a) Conventional mixer-first RXs block diagram; (b) Adding a matching resistor to improve the in-band linearity performance of mixer-first RXs; Canceling the noise of matching resistor in (c) RF and (d) baseband domain.

As mentioned earlier, the RX should provide sharp filtering to suppress close-in blockers of 5G applications. However, most prior art mixer-first RXs [19, 28, 30–35, 37, 51–53] only offer first-order filtering, making them prone to close-in blockers. Several attempts have been made to improve the selectivity of the mixer-first RXs [54–63]. For example, [54] and [59] introduced a positive feedback technique to achieve a second-order filtering response, and [58, 60, 61] proposed a third-order TIA to improve further the selectivity of the mixer-first RXs. Although [54] achieves decent NF and linearity, its gain is low, requiring an analog-to-digital converter (ADC) with high dynamic range. To relax the ADC requirements, its gain needs to be increased, but in this case, its reported selectivity may not be enough to suppress the close-in blockers of the 5G applications. Moreover, [56, 58–61] could not simultaneously achieve sharp filtering and sub-3dB NF.

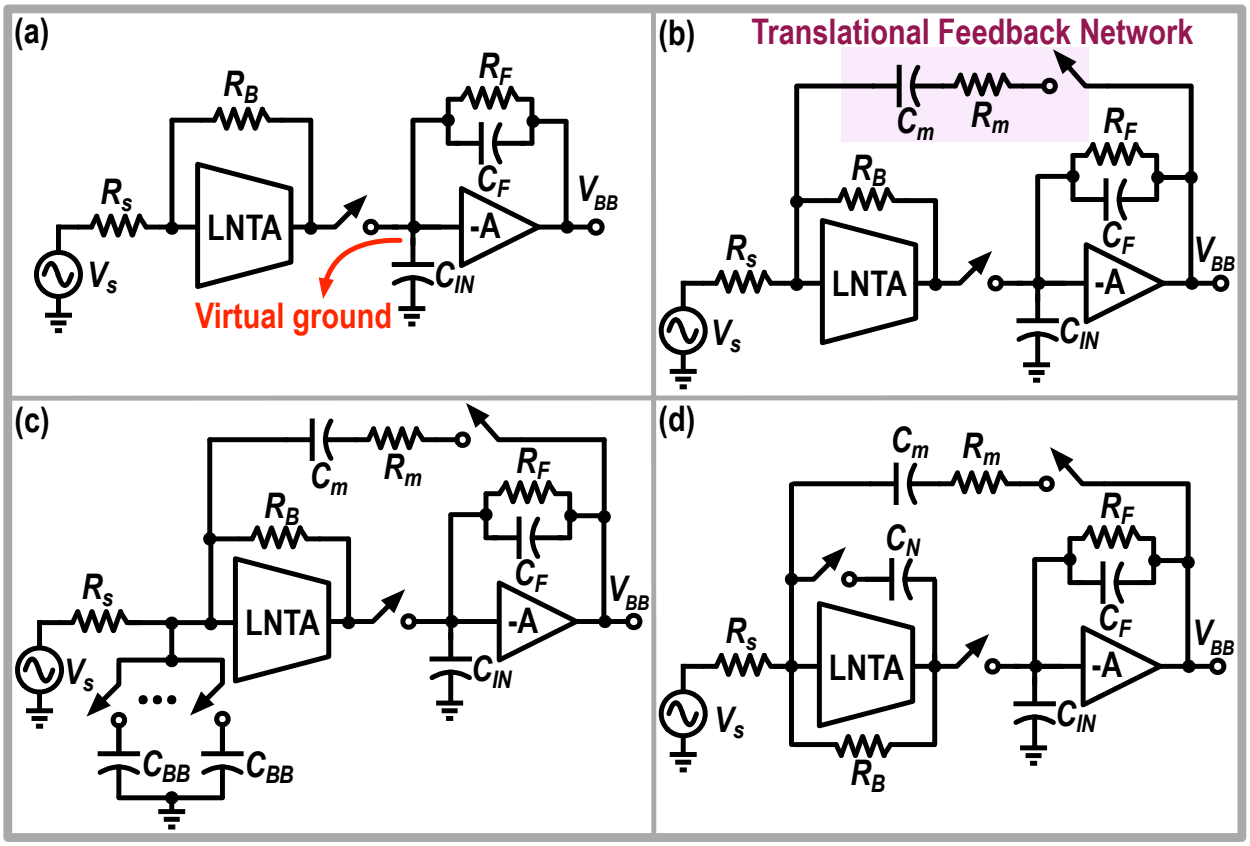

Figure 1.13: (a) Conventional LNTA-based RX architecture; (b) Adding a translational feedback network to achieve input-matching in LNTA-based architectures; (c) An N-path filter is placed at the RX input to achieve RF filtering; (d) Utilizing N-path notch filter in the feedback of LNTA to achieve RF filtering.

1.4.2 LNTA-Based RXs

Alternatively, as shown in Fig. 1.13 (a), a low-noise transconductance amplifier (LNTA) can be placed before the passive mixers to achieve a lower NF in wideband RXs. In conventional LNTA-based RXs, the feedback resistor of LNTA, R_B, provides input matching [64]. To achieve decent in-band linearity, the TIA must have virtual ground, reducing the LNTA voltage gain. Hence, the value of R_B should be reduced to achieve input matching, which degrades NF. To solve this issue, as illustrated in Fig. 1.13 (b), [65–67], a translational feedback network is utilized for input matching purposes. The output voltage of TIA is upconverted to RF using passive mixers and applied to the RX input via a matching resistor and capacitor (R_m and C_m). Since the voltage gain of RX is high, a large value can be chosen for R_m, which has a negligible effect on NF performance. Since the band-pass filter is removed from the receiver line-up, the out-of-band blockers appear at the LNTA input without any attenuation,

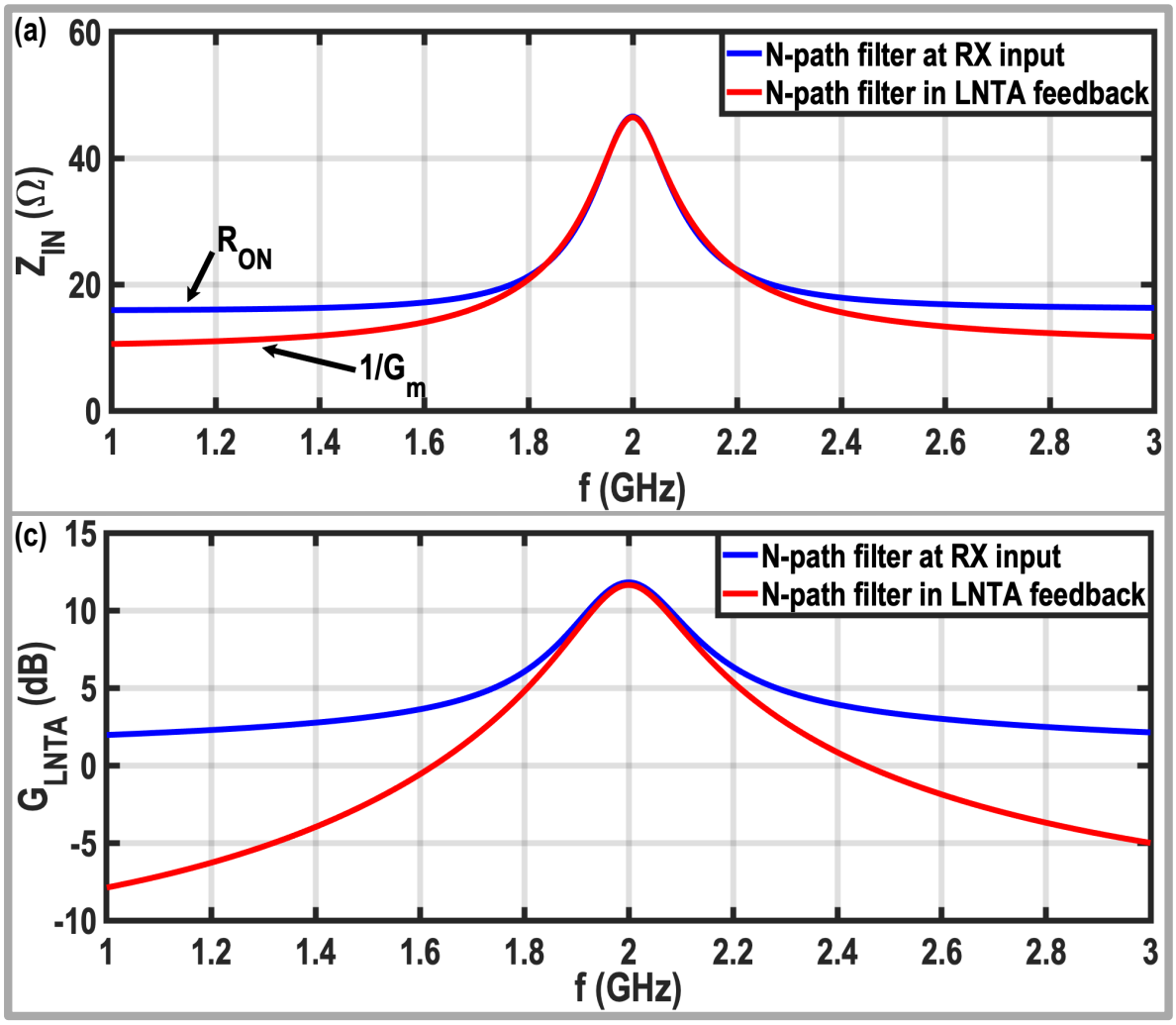

Figure 1.14: The simulated input impedance (a) and LNTA gain (b) of the conventional LNTA-based RXs.

thus significantly degrading the RX linearity. Moreover, the RX selectivity reduces its gain at out-of-band frequency, leading to a smaller Miller effect of R_M. Hence, the RX input impedance increases at out-of-band frequencies. The out-of-band blockers create higher voltage swings at the RX input, exacerbating the out-of-band linearity issue in the LNTA-based RXs. The RF filtering at the RX input is appealing for LNTA-based RXs to improve their out-of-band linearity performance.

Different flavors of N-path filters can be used to enhance the selectivity and linearity of the LNTA-based RXs. As depicted in Fig. 1.13 (c), in [68] and [69], an N-path filter is placed at the LNTA input to filter out the out-of-band blockers before entering the RX. However, as shown in Fig. 1.14 (a), since

the RX input impedance at out-of-band offset frequencies is limited to the switches' on-resistance (R_{ON}), large switches must be used to provide enough filtering for the large blockers, thus increasing the LO buffers' dynamic power consumption and the LO leakage to the RX input port. Moreover, the large parasitic capacitance of the N-path filter switches at the RX input reduces the RX maximum operating frequency and bandwidth.

In order to alleviate those issues, as shown in Fig. 1.13 (d), [70–84] placed an N-path notch filter in the LNTA's feedback to reduce the switches' sizes by benefiting from the Miller effect. Around the operating frequency, the N-path notch filter exploits high impedance, and the LNTA converts the input voltage to an RF current. Then, as the offset frequency deviates from the passband edges toward the out-of-band frequencies, the N-path notch filter impedance drops with a -20 dB/dec slope to reach its final value, i.e., R_{ON}. Hence, at far-out offset frequencies, a feed-forward current flows from the input of the LNTA to its output through the N-path notch filter; and as shown in Fig. 1.14 (b), if $G_m R_{ON} = 1$ (G_m is the LNTA's transconductance), a null appears in the transfer function of the LNTA voltage gain (G_{LNTA}) [81, 85]. Moreover, the Miller effect of the N-path notch filter is seen at the RX input, and thus, RF filtering is also achieved at the RX input transfer function (G_{IN}), improving the RX out-of-band linearity performance. Interestingly, the RX input impedance is inversely proportional to G_m at out-of-band offset frequencies, and increasing G_m improves the out-of-band linearity and NF simultaneously (see Fig. 1.14 (a)). However, as can be inferred from Fig. 1.14, due to the first-order filtering of the N-path notch filter, G_{IN} and G_{LNTA} reach their minimum values at very large offset frequencies. The amount of attenuation at low offset frequencies is limited at both LNTA input and output, making the RX prone to the close-in blockers of 5G applications. A straightforward solution for this issue is significantly increasing the order of the N-path notch filter to achieve the required filtering. However, this comes at the cost of much higher power consumption and circuit complexity [60]. Another way to improve the linearity performance of the LNTA-based RX is by adopting a quantized RF front-end [86, 87]. However, this technique requires performing complex calibration to improve the out-of-band linearity, and the operating frequency is limited due to the parasitic capacitors of the multiple low-noise amplifiers (LNAs) at the RX input. Hence, despite all the mentioned benefits of prior art structures, additional techniques are required to *efficiently* handle the close-in blockers and avoid RX desensitization.

1.5 Thesis Objectives

This thesis proposes LNTA-based RXs suitable for low-band and mid-band frequencies of 5G user equipment and base station applications.

The proposed RXs support RF bandwidth exceeding 100 MHz to enhance the data rates. Hence, this thesis investigates techniques to enhance the bandwidth of the TIA and N-path notch filter without compromising their performance. These techniques introduce complex conjugate poles, enabling the LNTA-based RXs to maintain a flat in-band gain response. Since the proposed RXs have high bandwidth, they are susceptible to close-in blockers of 5G applications. To address this, this thesis proposes RXs with high selectivity in the RF and baseband domains to suppress close-in blockers and prevent voltage clipping in the baseband domain.

In base station applications, the blocking scenarios are tougher than those in the user equipment applications. Firstly, in co-location applications, strong CW out-of-band blockers exist, which should be handled by the RX. Hence, this thesis investigates N-path filters with high out-of-band rejection for the 5G co-location applications. Additionally, base station applications also face large in-band blockers, demanding a robust TIA with high loop gain. This thesis determines a TIA with a higher loop gain to handle in-band blockers of base station applications.

The proposed RXs should cover the sub-7 GHz bands of 5G applications. Hence, this thesis explores a technique to minimize the parasitic capacitors at the LNTA input and output without sacrificing NF and linearity performance. Achieving a sub-3dB NF is critical to maximizing the link budget. Hence, linearity enhancement techniques that are proposed for co-location applications should not compromise NF.

Since the proposed RXs are designed for 5G user equipment and base station applications, their design is guided by the stringent requirements for 5G reference sensitivity and blocking scenarios. This thesis evaluates the proposed RXs against the reference sensitivity and blocking requirement of the 5G standard.

1.6 Thesis Outline

This dissertation is organized as follows:

In Chapter 2, a wideband blocker-tolerant RX is presented for 5G user equipment applications. Two programmable zeros close to the channel passband are introduced to sufficiently suppress close-in blockers of 5G-user equipment

applications. As the effect of these zeros diminishes at higher out-of-band offset frequencies, an auxiliary current sinking path is added to reduce the RX input impedance at those frequencies. Additionally, a simple second-order TIA is employed to enhance RX selectivity. The proposed TIA synthesizes two complex conjugate poles to achieve a flat gain response and a -40 dB/dec roll-off. Finally, extensive measurement results are provided in this chapter to validate the performance of the proposed RX. These measurements demonstrate the RX's ability to meet the stringent requirements of 5G user equipment applications, in terms of sensitivity, selectivity, and blocking performance.

Chapter 3 presents a wideband highly linear RX capable of handling blocking scenarios in 5G-microcell base station applications by introducing three different techniques. First, a parallel preselect filter is introduced to satisfy the base station co-location blocking requirements. Next, a combination of third-order RF and baseband filters is adopted to attenuate close-in blockers by a -120 dB/dec roll-off. Finally, a translational feedback network is proposed to reduce the in-band gain ripple to below 0.5 dB and provide better than -19 dB input matching. The chapter concludes with detailed measurement results, which highlight the RX's out-of-band linearity and selectivity, proofing the RX's ability to handle the demanding requirements of 5G microcell base stations.

In Chapter 4, a sub-7 GHz RX for 5G-local-area base station applications is introduced. A Rauch TIA is used to enhance RX selectivity and provide higher loop gain around the bandwidth edge, thus improving in-band linearity for high-bandwidth applications. A third-order impedance in the TIA's feedback further improves RX selectivity. Additionally, an N-path notch filter with a shared switch architecture is incorporated to enhance out-of-band linearity without limiting the RX's operating frequency. A positive feedback technique is also employed to extend the RF bandwidth without degrading out-of-band rejection. The chapter ends with a discussion of the RX's performance, highlighting RX's ability to achieve both high in-band and out-of-band linearity, crucial features for 5G local area base station applications.

Chapter 5 concludes this dissertation by summarizing the outcomes of this research and also provides suggestions for future works.

Chapter

2

A Highly Selective Receiver With Programmable Zeros and Second-Order TIA

2.1 Introduction

As mentioned earlier, the introduction of 5G applications has imposed several challenges on the RX design for user equipment applications. The RX's maximum RF bandwidth (BW_{RF}) is expanded from 20 MHz to 100 MHz, increasing the design complexity of the baseband amplifiers. Moreover, despite increasing the BW_{RF}, the offset frequency (f_{OS}) of the close-in out-of-band blocker from the passband edge remains the same (i.e., at 85 MHz) due to the congested sub-6 GHz spectrum. Such a small f_{OS}/BW_{RF} (i.e., 0.85) requires sharp filtering to handle the -15 dBm continuous wave (CW) out-of-band blocker of the 5G user equipment application.

Although mixer-first RXs are popular for their simplicity and out-of-band linearity performance, they often suffer from achieving decent NF and high selectivity at the same time. Hence, an LNTA structure can be adopted with an N-path notch filter in its feedback to achieve a decent NF and out-of-band

This chapter is written based on ISSCC 2021 [88] and JSSC2024 [89] papers.

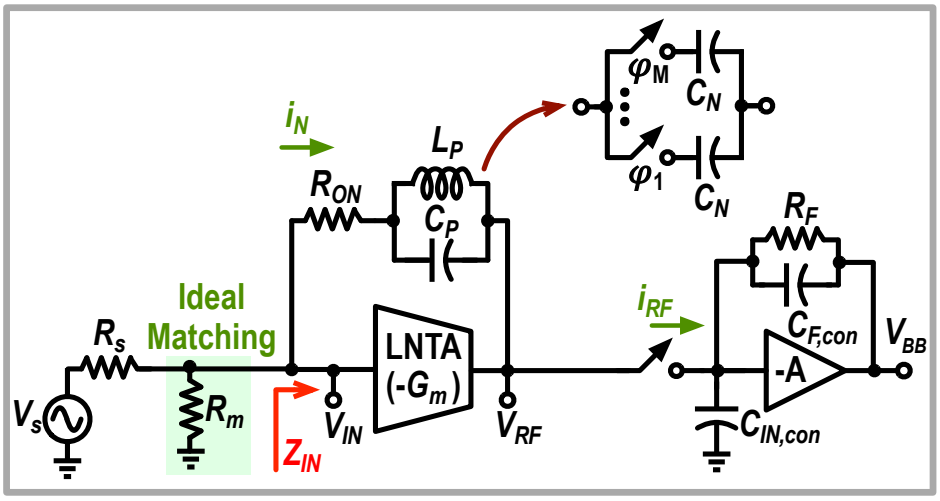

Figure 2.1: Conventional LNTA-based RX architecture with the equivalent model of the N-path notch filter in its feedback. Note that for simplicity, in these conceptual diagrams, an explicit shunt resistor, R_m, is used for the input matching.

linearity performance, as shown in Fig. 2.1. The N-path notch filter can be modeled with a parallel tank (L_P and C_P). This has a high impedance around the operating frequency, which reduces with -20 dB/dec slope till it reaches R_{ON}. Due to the feedforward current (see i_N in Fig. 2.1), a null appears in the LNTA transfer function at far-out offset frequencies, as illustrated in Fig. 2.2 (a). Since this null is located at far-out offset frequencies, this structure is still sensitive to the close-in blockers of 5G user equipment applications.

To improve those limitations, in this Chapter, two programmable zeros and an auxiliary current-sinking path in the LNTA feedback are introduced to suppress close-in and far-out blockers, respectively. Furthermore, a second-order transimpedance amplifier (TIA) with complex-conjugate poles is also adopted to improve out-of-band linearity further and achieve a flat in-band gain response. This Chapter is organized as follows: Sections 2.2 and 2.3 describe the evolution and implementation of the RX RF front-end and second-order TIA, respectively. Section 2.4 presents the RX circuit implementation. Section 2.5 elaborates on the RX noise analysis. The measurement results are shown in Section 2.6, and Section 2.7 concludes this Chapter.

2.2 Evolution of the Programmable Zeros

Although conventional LNTA-based RXs have nulls in G_{LNTA} at far-out offset frequencies, they do not provide enough attenuation for the close-in blockers. Note that these nulls appear at offset frequencies where the impedance of the

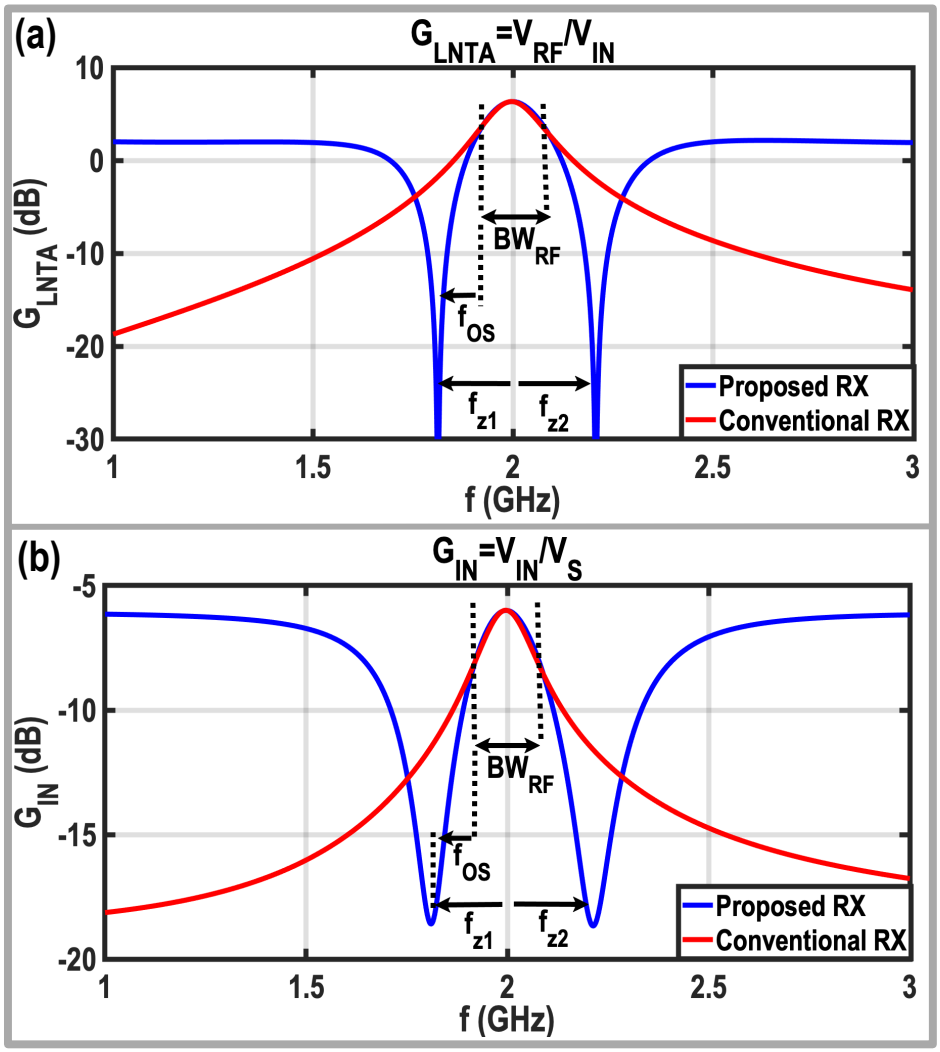

Figure 2.2: Comparison between the simulated (a) G_{LNTA} and (b) G_{IN} of the conventional LNTA-based architecture and the proposed RX. Note that LNTA, mixers, and TIAs are implemented using ideal elements, and the notch filters are realized by RLC components with $R_{ON} = 7.7\,\Omega$.

notch filter approaches zero. Consequently, if one shifts the short impedance of the notch filter toward the frequencies of the close-in blockers, G_{IN} and G_{LNTA} will reach their minimum possible values at those frequencies, thus suppressing the close-in blockers sufficiently before entering the RX and baseband amplifiers. Hence, as depicted in Fig. 2.3, by adding a series tank (L_S and C_S) to the existing parallel tank (L_P and C_P), we introduce two zeros to the LNTA's feedback impedance. Note that the series and parallel tanks have the same resonant frequency, i.e., $f_{LO} = \omega_{LO}/(2\pi)$.

Due to the presence of the parallel tank, the proposed impedance shows high impedance inside the desired band. Consequently, as depicted in Fig. 2.2, the

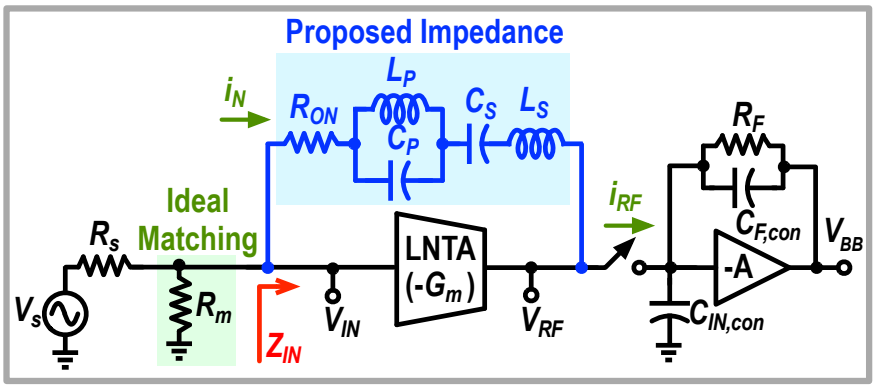

2

Figure 2.3: The proposed impedance in the feedback of the LNTA. For simplicity, the same shunt resistor is used for the input matching.

LNTA acts as a transconductance stage, and no significant difference between the in-band responses of G_{IN} and G_{LNTA} of the conventional and proposed RXs is observed. To calculate the zeros frequencies, the proposed LNTA feedback impedance, Z_F, is derived as follows:

$$Z_F = \frac{s^4 C_S L_S C_P L_P + s^2 \left(C_S L_S + C_P L_P + C_S L_P\right) + 1}{s C_S \left(s^2 C_P L_P + 1\right)}. \tag{2.1}$$

Hence, the zeros frequencies can be derived as:

$$f_{1,2}^2 = f_{LO}^2 \times \left(1 + \frac{1}{2}\omega_{LO}^2 C_S L_P \left(1 \mp \sqrt{1 + \frac{4}{\omega_{LO}^2 C_S L_P}}\right)\right), \tag{2.2}$$

and assuming that $\omega_{LO}^2 C_S L_P \ll 1$, (2.2) can be simplified as follows:

$$f_{1,2} = f_{LO}\sqrt{1 \mp \omega_{LO}\sqrt{C_S L_P}} = f_{LO}\sqrt{1 \mp \sqrt{\frac{C_S}{C_P}}}. \tag{2.3}$$

Finally, considering $C_S/C_P \ll 1$, (2.3) can be recalculated as follows:

$$f_{1,2} = f_{LO} \mp \frac{f_{LO}}{2}\sqrt{\frac{C_S}{C_P}} = f_{LO} \mp f_{z1,2}, \tag{2.4}$$

where the relative zeros frequencies from f_{LO} are given by

$$f_{z1,2} \approx \mp \frac{f_{LO}}{2}\sqrt{\frac{C_S}{C_P}}. \tag{2.5}$$

Intuitively, for frequencies below f_{LO}, the parallel tank becomes inductive,

and the series tank becomes capacitive; thus, their series combination creates a zero at a frequency close to but lower than f_{LO} (f_{z1}). Similarly, for frequencies above f_{LO}, a zero (f_{z2}) is realized since the parallel and series tanks become capacitive and inductive, respectively. As can be gathered from the simulation results in Fig. 2.2 (a), the locations of G_{LNTA} nulls in the proposed RX are moved to the close vicinity of the operating band, thus greatly attenuating close-in blockers at the LNTA's output and avoiding RX desensitization. Moreover, at close-in blocker offset frequencies, the proposed RX offers around 5 dB better rejection at the RX input compared to the conventional RXs, as shown in Fig. 2.2 (b). Beyond the zeros frequencies, the performance of the proposed RF front-end degrades; its solution will be discussed in Section 2.2.3.

2.2.1 Implementation of the Programmable Zeros

To achieve programmable zeros with wideband operation, the resonators must be replaced with tunable filters. To do so, as shown in Fig. 2.4, the series tank is firstly replaced with its counterpart, i.e., a parallel tank in series with a gyrator consisting of a feedforward (g_{ma}) and a feedback (g_{mb}) transconductance [3]. Here, we decided to have the same component values for both resulting parallel tanks to be convenient in the final implementation and achieve a symmetric schematic for the proposed filter. Considering the gyrator's impedance inversion characteristics, we have

$$C_S = g_{ma}g_{mb}L_P = \frac{g_{ma}g_{mb}}{C_P\ \omega_{LO}^2}, \tag{2.6}$$

and

$$L_S = \frac{C_P}{g_{ma}g_{mb}}. \tag{2.7}$$

By substituting the equivalent value of C_S from (2.6) into (2.5), the zeros frequencies in this implantation may be approximated by

$$f_{z1,2} = \mp\frac{1}{4\pi C_P}\sqrt{g_{ma}g_{mb}}. \tag{2.8}$$

Interestingly, the zeros frequencies can be tuned by $g_{ma}g_{mb}$ and C_P. Finally, to obtain a programmable network, each parallel tank is easily replaced with an N-path notch filter, as shown in Fig. 2.4. The unit capacitor of each N-path

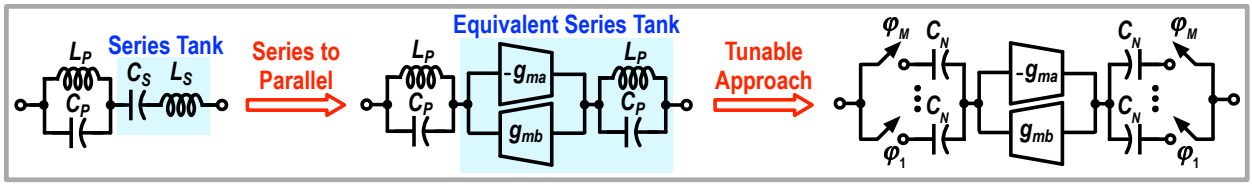

Figure 2.4: Evolution of implementing the proposed impedance using two N-path notch filters and a gyrator.

notch filter, C_N, can be estimated by

$$C_N = \frac{2}{M}\text{sinc}^2\left(\frac{1}{M}\right) \times C_P, \tag{2.9}$$

where M is the number of local oscillator (LO) phases in the N-path notch filter [9].

2.2.2 RX Bandwidth and Input Impedance at Zeros Frequencies

Fig. 2.5 shows the RX preliminary schematic, where the proposed programmable filter is placed in the LNTA's feedback. The RX input impedance can be approximated by

$$Z_{IN}(\omega) \approx \frac{1 + g_{ma}g_{mb}Z_N(Z_N + Z_{RF})}{g_{ma}(Z_N + Z_{RF}) + G_m Z_{RF}} \times \frac{1}{g_{mb}}, \tag{2.10}$$

where Z_{RF} is the load impedance of the LNTA seen from the RF port of passive mixers, and Z_N is the equivalent impedance of the identical N-path notch filters, given by

$$Z_N = R_{ON} + \frac{j\omega L_P}{1 - \omega^2 L_P C_P}. \tag{2.11}$$

In current-mode RXs, Z_{RF} is designed to be low enough in order to sink the RF current of the LNTA. Consequently, by considering $Z_N \gg Z_{RF}$ and assuming $g_{ma}g_{mb}Z_N^2 \gg 1$, Z_{IN} around the zeros frequencies can be approximated by

$$Z_{IN}(\omega \approx \omega_{z1,2}) \approx R_{ON} + \frac{j}{\sqrt{g_{ma}g_{mb}}}. \tag{2.12}$$

As can be gathered from (2.8) and (2.12), enhancing $g_{ma}g_{mb}$ increases the zeros frequencies, and at the same time, reduces the RX input impedance around the implemented zeros.

As the next step, the RX 3-dB bandwidth is estimated using the input

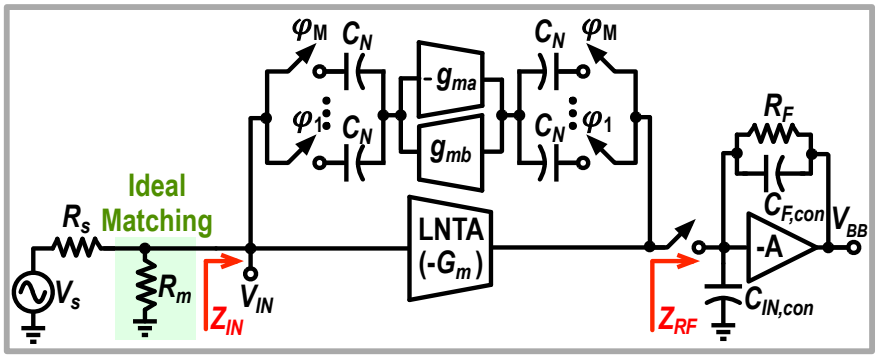

Figure 2.5: Preliminary block diagram of the proposed RX, where the proposed programmable filter is placed in the LNTA's feedback.

transfer function of the RX,

$$G_{IN} = \frac{1}{2} \times \frac{Z_{IN}}{Z_{IN} + \frac{R_S}{2}}. \tag{2.13}$$

Assuming $Z_N \gg Z_{RF}$ around the operating frequency, the 3-dB bandwidth can be calculated by setting $|G_{IN}(f_{LO} \pm f_{3dB})| = |G_{IN}(f_{LO})|/\sqrt{2}$:

$$f_{3dB} = \frac{2}{2\pi C_P R_S \times \left(1 + \sqrt{1 + \frac{16}{g_{ma} g_{mb} R_S^2}}\right)}. \tag{2.14}$$

Here, f_{3dB} is $\mathrm{BW_{RF}}/2$. Interestingly, increasing $g_{ma}g_{mb}$ enhances the 3-dB bandwidth, and a larger C_P is required to keep the desired bandwidth constant.

2.2.3 Improving Far-Out Out-of-Band Linearity

Unfortunately, the proposed impedance becomes an open circuit at the far-out out-of-band frequencies, and the RF filtering at the RX input diminishes at those offset frequencies, as can be gathered from Fig. 2.2. Hence, far-out blockers create a high voltage swing at the RX input, deteriorating the RX linearity performance. To resolve this issue, as shown in Fig. 2.6 (a), an auxiliary N-path notch filter is added from the antenna to the output port of the gyrator. Its bandwidth is intentionally chosen 2× larger than that of the main notch filter such that this extra path acts as an open circuit for the desired band and the close-in blockers, thus keeping the RX response at those frequencies intact. At far-out offset frequencies, all N-path notch filters exhibit low impedance, and the auxiliary N-path notch filter shorts the input of the gyrator to its output. Therefore, the gyrator's impedance inversion operation vanishes, and the effect

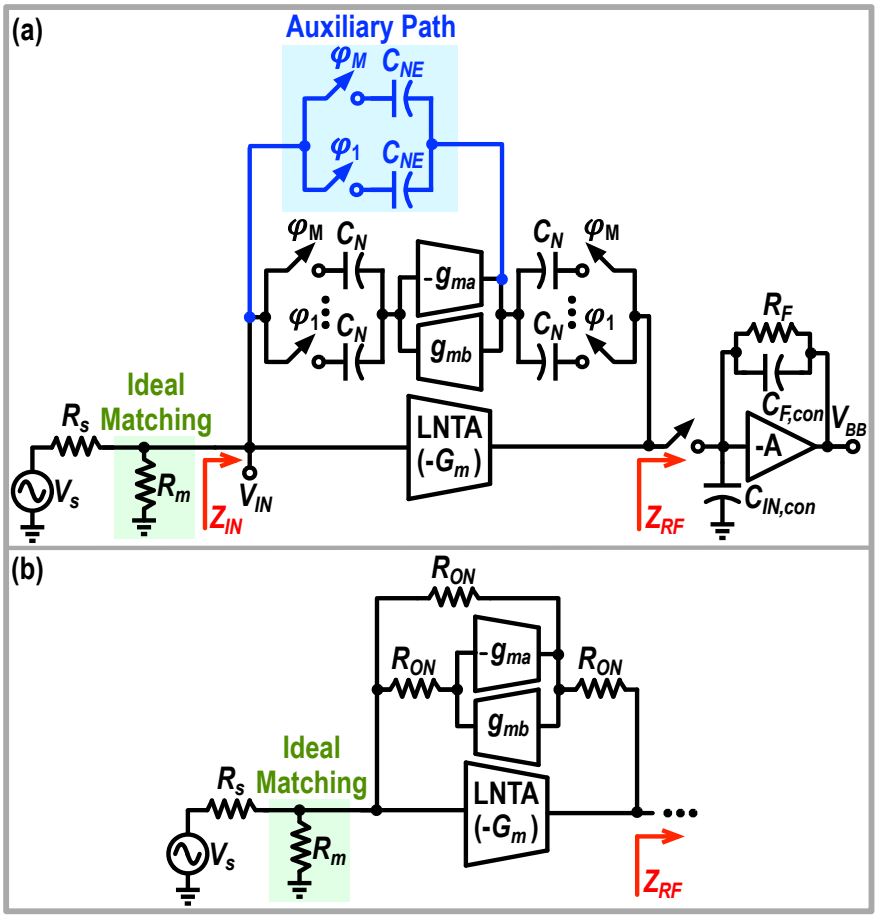

Figure 2.6: (a) Block diagram of the RX front-end. An auxiliary N-path filter is added to reduce the RX input impedance at far-out frequencies; (b) The equivalent model of the proposed RX architecture at far-out offset frequencies.

of zeros in G_{IN} and G_{LNTA} is diminished. At far-out frequencies, as shown in Fig. 2.6 (b), the RX front-end is simplified to three transconductances ($-G_m$, $-g_{ma}$, and g_{mb}) with low-ohmic resistive shunt feedback, thus approximately reducing the RX input resistance to $1/(G_m + g_{ma} - g_{mb})$.

2.2.4 Design Guide for the RX RF Front-End

In this subsection, we develop a design guide for estimating the components of the RX RF front-end (i.e., G_m, g_{ma}, g_{mb}, and C_N) to satisfy the 5G user equipment specifications, i.e., the desired bandwidth and required blocker input 1-dB compression point (B1dB). In this analysis, without loss of generality, the loss of the N-path notch filters is neglected, and the input matching is accomplished by a shunt resistor at the RX input (see Fig. 2.6).

The first step is to estimate the values of g_{ma}, g_{mb} and C_N based on the 3-dB

bandwidth and the location of the zeros set by the 3GPP standard. Here, we define a parameter, χ, for relating the zeros frequencies to the 3-dB bandwidth,

$$\chi = \mp \frac{f_{z1,2}}{f_{3dB}}. \tag{2.15}$$

Equivalently, (2.15) leads to $f_{OS} = (\chi - 1) f_{3dB}$. Note that χ is always larger than one since the frequencies of the zeros must lie outside the RX 3-dB bandwidth. By assuming $f_{LO} \gg \chi f_{3dB}$, and substituting (2.15) into (2.8), the 3-dB bandwidth of the RX can be approximated as

$$f_{3dB} = \frac{\sqrt{g_{ma} g_{mb}}}{4\pi \chi C_P}. \tag{2.16}$$

The RX 3-dB bandwidth can be calculated using (2.16) and (2.14). Therefore, by equating (2.14) and (2.16), we have

$$\sqrt{g_{ma} g_{mb}} = \frac{2\,(\chi^2 - 1)}{\chi R_S}. \tag{2.17}$$

Choosing χ fixes the value of $\sqrt{g_{ma} g_{mb}}$, and accordingly, via (2.12), the RX input impedance at zeros' frequencies. Moreover, increasing the zeros' frequency offset from the passband edges (i.e., larger χ) leads to larger $g_{ma} g_{mb}$, and thus, higher power consumption in the gyrator.

Based on the 3GPP standard, the location of the close-in blocker is 85 MHz from the 3-dB bandwidth edge, and $\mathrm{BW_{RF}}$ is 100 MHz. However, in this work, we target $\mathrm{BW_{RF}} = 200$ MHz, resulting in $\chi = 185/100 = 1.85$. Despite that, we choose $\chi = 1.5$ to place zeros closer to passband edges, thus reducing power consumption. This results in $\sqrt{g_{ma} g_{mb}} = 33.3\,mS$, and $Z_{IN}(\omega_{z1,2}) = 30\,\Omega$. Moreover, to guarantee the gyrator's stability, one should set $g_{ma} \geq 4 \times g_{mb}$, leading to $g_{ma} = 72\,mS$ and $g_{mb} = 16\,mS$.

On the other hand, by substituting $\sqrt{g_{ma} g_{mb}}$ from (2.17) into (2.14), C_P can be estimated by

$$C_P = \frac{2}{2\pi f_{3dB} R_S \times \left(1 + \sqrt{1 + \left(\frac{2\chi}{\chi^2 - 1}\right)^2}\right)}. \tag{2.18}$$

Accordingly, C_N is determined using (2.9) and (2.18). Considering $f_{3dB} = 100$ MHz, C_P and C_N are approximated to be 17.7 pF, and 4.2 pF, respectively. Since the auxiliary N-path notch filter should have more bandwidth than the

main notch filter, the auxiliary path unit capacitor, C_{NE}, is chosen $\approx 2\times$ smaller than C_N.

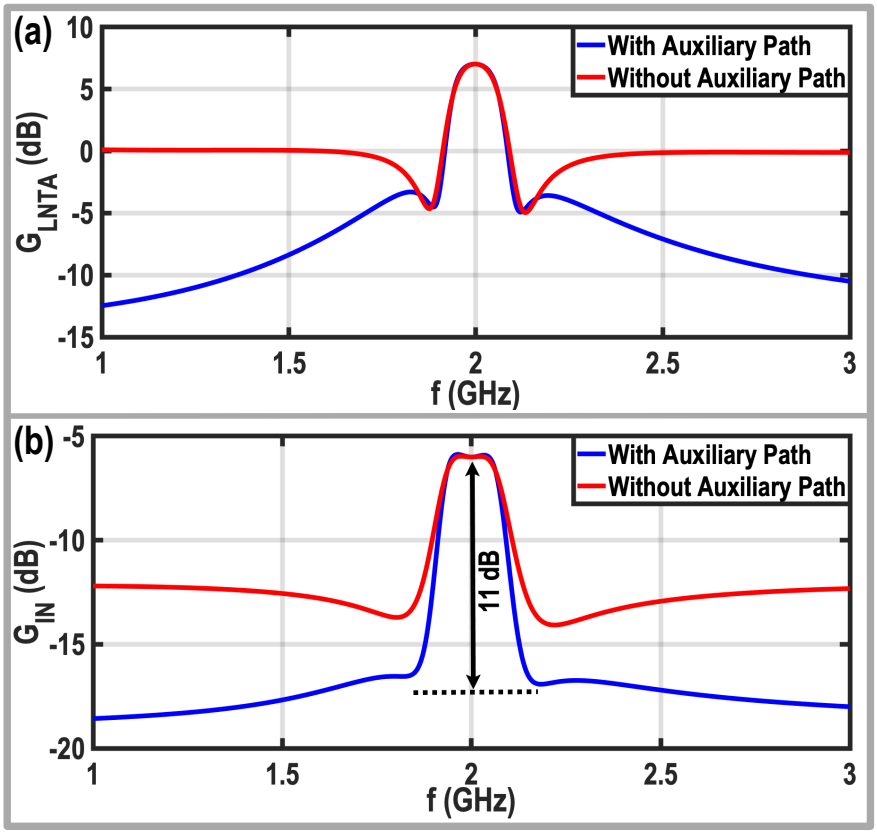

Figure 2.7: The circuit level simulation results of (a) G_{LNTA} and (b) G_{IN} for the proposed structure shown in Fig. 2.6, using the components' values calculated in the design guide.

The design guide finishes with G_m estimation. At far-out frequencies, the LNTA's input voltage can be calculated by

$$V_{IN} = \frac{V_{s,B}}{1 + (G_m + g_{ma} - g_{mb})\, R_s}, \tag{2.19}$$

where $V_{s,B}$ is the maximum blocker voltage, approximated by $\sqrt{8R_s \times 10^{B1dB/10}}$. In order to tolerate the blocker, the RX input voltage must be below the LNTA's input 1-dB compression voltage (V_{Blk}). Consequently,

$$G_m \geq \frac{1}{R_s}\left(\frac{\sqrt{8R_s \times 10^{\frac{B1dB}{10}}}}{V_{Blk}} - 1\right) + g_{mb} - g_{ma}. \tag{2.20}$$

Based on the 3GPP standard, the required B1dB is -15 dBm; however, we target 0 dBm B1dB at far-out offset frequencies. Considering a simulated V_{Blk}

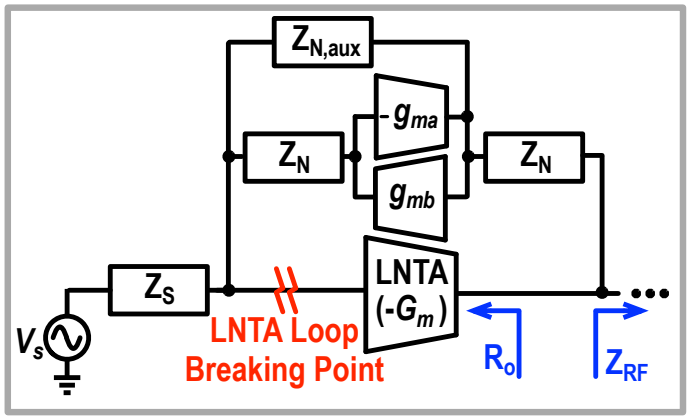

Figure 2.8: The simplified model of the RX front-end for the stability analysis.

of 0.14 V, G_m should be larger than 16 mS to tolerate the aimed blocker power. However, the calculated G_m based on the linearity spec does not satisfy the NF requirement (see (2.42) in Section 2.5), and we choose $G_m = 130$ mS to achieve sub-3dB NF.

Fig. 2.7 illustrates the simulation results of the proposed structure in Cadence. In this simulation, the calculated components' values from the design guide are used. The simulated $\mathrm{BW_{RF}}$ is around 170 MHz, and the location of the zeros is 70 MHz from the passband edges, indicating that the presented design guide provides a sufficiently accurate initial estimation for the circuit parameters of the proposed RX RF front-end. As can be gathered from the simulated results in Fig. 2.2 and Fig. 2.7, although the depth of G_{IN} nulls is almost maintained, the amount of G_{LNTA} rejection at the zero frequencies is reduced in the active realization of the proposed feedback network compared to its passive implementation. Due to the active implementation of the series inductor, the feed-forward current does not flow from the LNTA input to its output, thus lowering the nulls' depth. Consequently, the active implementation of the feedback network brings programmability for the null locations and operating RX frequency but at the cost of a lower G_{LNTA} rejection at zeros' frequencies.

2.2.5 Loop Stability of the RX RF Front-End

To ensure that the proposed feedback impedance does not sacrifice the RX stability, this subsection investigates the loop gain (LG) of the RX front-end at in-band and out-of-band frequencies by using the simplified model in Fig. 2.8, and breaking the loop at the LNTA's input. Since the bandwidth of the auxiliary path is higher than that of the main N-path notch filters, the LG at

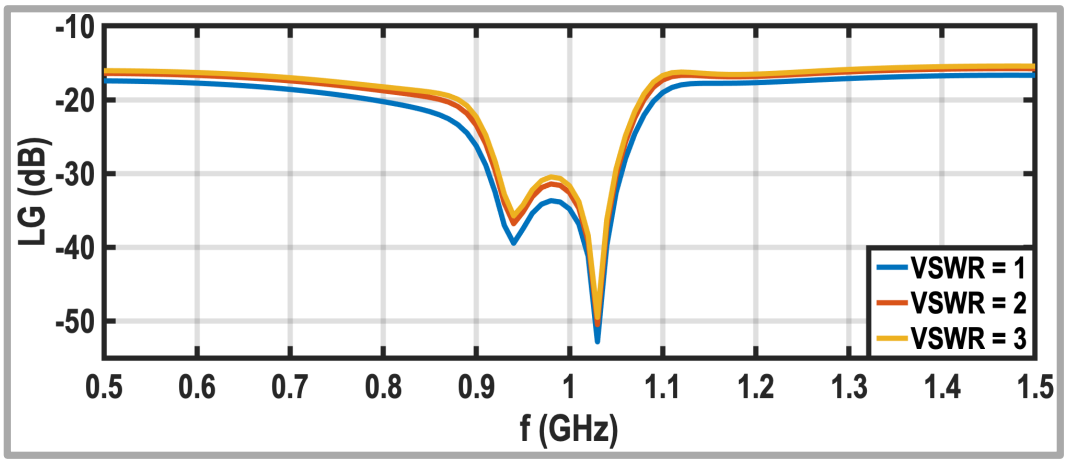

Figure 2.9: Simulated loop gain of the RX front-end for different VSWR values.

in-band and close-in out-of-band frequencies can be approximated by

$$LG_{IB} = G_m \left(Z_{RF} \parallel R_o\right) \times \frac{Z_S}{Z_S + Z_N} \times \frac{g_{mb}\left(Z_N + Z_S\right)}{1 + g_{ma} g_{mb} Z_N \left(Z_N + Z_S\right)}, \tag{2.21}$$

where R_o is the LNTA's output resistance, and Z_S is the antenna impedance with an ideal value of $50\,\Omega$. Since $Z_S \ll Z_N$ and $Z_{RF} \ll R_o$ at in-band and close-in out-of-band frequencies, (2.21) can be simplified to

$$LG_{IB} = \frac{G_m}{g_{ma}} \times \frac{Z_S}{Z_N} \times \frac{Z_{RF}}{Z_N}. \tag{2.22}$$

Since both Z_S and Z_{RF} are much smaller than Z_N, LG_{IB} is much smaller than 1 around the operating frequency, ensuring the stability of the RX front-end. Interestingly, enhancing g_{ma} improves the stability and reduces the RX input impedance around the implemented zeros but pushes zeros frequencies toward higher out-of-band frequencies. However, at out-of-band frequencies, the value of Z_N reduces, increasing LG of the LNTA feedback network.

At far-out offset frequencies, the auxiliary N-path notch filter exhibits low impedance and eradicates the gyrator effect on the receiver operation. Therefore, the LG at far-out out-of-band frequencies can be estimated by

$$LG_{OOB} = G_m Z_{RF} \times \frac{Z_S}{Z_S + Z_{RF} + Z_N + Z_{N,aux}}. \tag{2.23}$$

Since $Z_S > Z_N + Z_{N,aux} + Z_{RF}$ at far-out out-of-band frequencies, (2.23) can be simplified to

$$LG_{OOB} = G_m Z_{RF}. \tag{2.24}$$

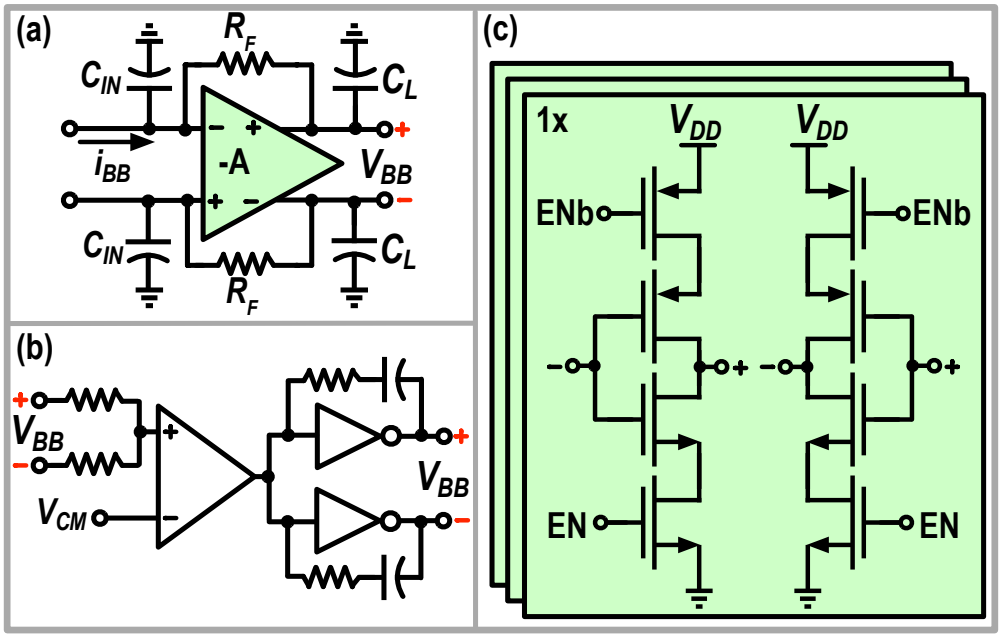

Figure 2.10: Schematics of (a) the second-order TIA, (b) its common-mode feedback circuit, and (c) the utilized TIA amplifier.

Hence, the combination of mixers' on-resistance and TIAs' input impedance must stay low enough at far-out out-of-band frequencies to guarantee the RX front-end stability.

The loop stability of the proposed RF front-end is simulated in Cadence using 'pstb'. Fig. 2.9 illustrates the simulated LG for three different voltage standing wave ratios (VSWRs). To consider the worst case, the loop gain is simulated when the angle of the reflection coefficient is zeros ($\theta = 0$), and hence, the antenna impedance is 100 Ω and 150 Ω for VSWR=2 and 3, respectively. For all the VSWRs, LG is below 0 dB with enough margin, confirming the RX front-end stability.

2.3 Second-Order TIA

The conventional TIA [90], shown in Fig. 2.6, offers a first-order filtering roll-off. However, since the RF front-end merely offers 11 dB rejection at the RX input for close-in blockers, they may still create a large voltage swing at the conventional TIA output, and desensitize the RX line-up, especially when a large TIA feedback resistance (R_F) is required to reduce the noise figure contribution of the subsequent stages. Consequently, a second-order TIA is desired to handle the close-in blockers of 5G applications. Unlike the conventional TIA, the second-order TIA also has complex conjugate poles and features a flat in-band

gain response.

Here, as depicted in Fig. 2.10 (a), we propose to remove C_F from the conventional TIA feedback and replace it with a load capacitor (C_L) at the TIA output to achieve second-order filtering. R_F remains in the feedback of the TIA to convert down-converted current to a baseband voltage. The transfer function of the TIA can be derived as:

$$\frac{V_{BB}}{i_{BB}} \approx \frac{-R_F}{s^2 C_{IN} C_L \frac{R_F}{g_{mt}} + s\left(\frac{C_{IN}}{g_{mt}} + \frac{C_L}{g_{mt}} + \frac{C_{IN}}{g_{mt}}\frac{R_F}{r_{ot}}\right) + 1}, \tag{2.25}$$

where V_{BB} and i_{BB} are the TIA's output voltage and input current, respectively (see Fig. 2.10 (a)). Moreover, g_{mt} and r_{ot} are the transconductance and output resistance of the TIA amplifier. As can be inferred from (2.25), the transfer function of the TIA is a second-order low-pass filter with a damping ratio (ζ) and natural frequency (ω_n) of

$$\zeta = \frac{1}{2}\frac{1}{\sqrt{g_{mt} R_F}} \times \left(\sqrt{\frac{C_{IN}}{C_L}}\left(1 + \frac{R_F}{r_{ot}}\right) + \sqrt{\frac{C_L}{C_{IN}}}\right), \tag{2.26}$$

$$\omega_n = \sqrt{\frac{g_{mt}}{C_{IN} R_F C_L}}. \tag{2.27}$$

Usually, ζ is set to $\sqrt{2}/2$ to achieve a Butterworth low-pass filter and reach the maximum bandwidth. In this way, the 3-dB bandwidth of the TIA is ω_n. As illustrated in Fig. 2.11, adding C_L improves the filtering response of the TIA to a second-order response. Moreover, two complex conjugate poles of the second-order TIA enhance the 3-dB bandwidth, and a flat gain response is also achieved.

It is instructive to investigate the trade-off between TIA's 3-dB bandwidth and power consumption. At first glance, as can be inferred from (2.27), the most power-efficient way to increase the TIA's 3-dB bandwidth by a factor of β is to reduce C_{IN} and C_L by the same factor. However, one of the main roles of the TIA input capacitor is absorbing the out-of-band blocker currents. Since the location of the close-in blocker remains almost constant from the passband edges for different channel bandwidths in 3GPP standard [2], by an aggressive C_{IN} reduction, the TIA amplifier has to absorb a significant portion of the out-of-band blocker currents instead of C_{IN}, thus degrading the RX out-of-band linearity performance. In other words, the linearity performance of the RX is

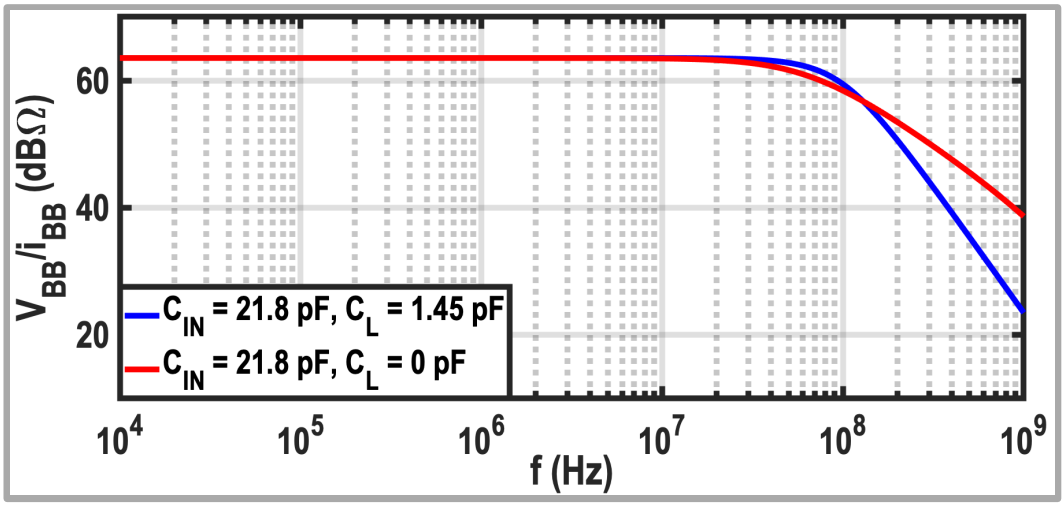

Figure 2.11: Simulated TIA transfer function with/without C_L.

sacrificed for the sake of power consumption. To alleviate this issue, the value of g_{mt} should be increased accordingly to maintain the RX linearity performance. Hence, to increase the 3-dB bandwidth of the TIA by the factor of β, it is wise to reduce C_{IN} and C_L by $\beta^{2/3}$, and simultaneously increase the value of g_{mt}, and therefore, the TIA's power consumption should be increased by $\beta^{2/3}$.

2.3.1 TIA Performance over PVT Variations

Since the damping ratio and natural frequency of the second-order TIA are related to the values of resistors, capacitors, and amplifier's transconductance and output resistance, this section investigates the sensitivity of the TIA frequency response over process, voltage, and temperature (PVT) variations.

The TIA's damping ratio is related to the ratio of C_{IN} to C_L (see (2.26)) and, consequently, remains almost constant with capacitor changes over PVT variations. However, as shown in Fig. 2.12 (a), the TIA's 3-dB bandwidth is inversely proportional to the absolute values of C_{IN} and C_L, and changes by $\approx \mp 20\%$ due to the expected $\pm 20\%$ capacitor deviation over PVT variations. On the other hand, as can be gathered from (2.25) and simulation results in Fig. 2.12 (b), the foreseen $\pm 20\%$ R_F variations change the transimpedance gain and 3-dB bandwidth of the second-order TIA significantly (i.e., $\pm 20\%$ and $\mp 10\%$ respectively), but its impacts on the damping ratio is negligible (i.e., $\approx \pm 1\%$).

Next, g_{mt} and r_{ot} fluctuations can also affect the TIA performance. Interestingly, the intrinsic gain ($g_{mt} \times r_{ot}$) of a single-stage inverter-based amplifier used in this design is almost constant over PVT variations, as can be gathered from Monte Carlo simulations in Fig. 2.13 (maximum 0.5 dB gain variation is

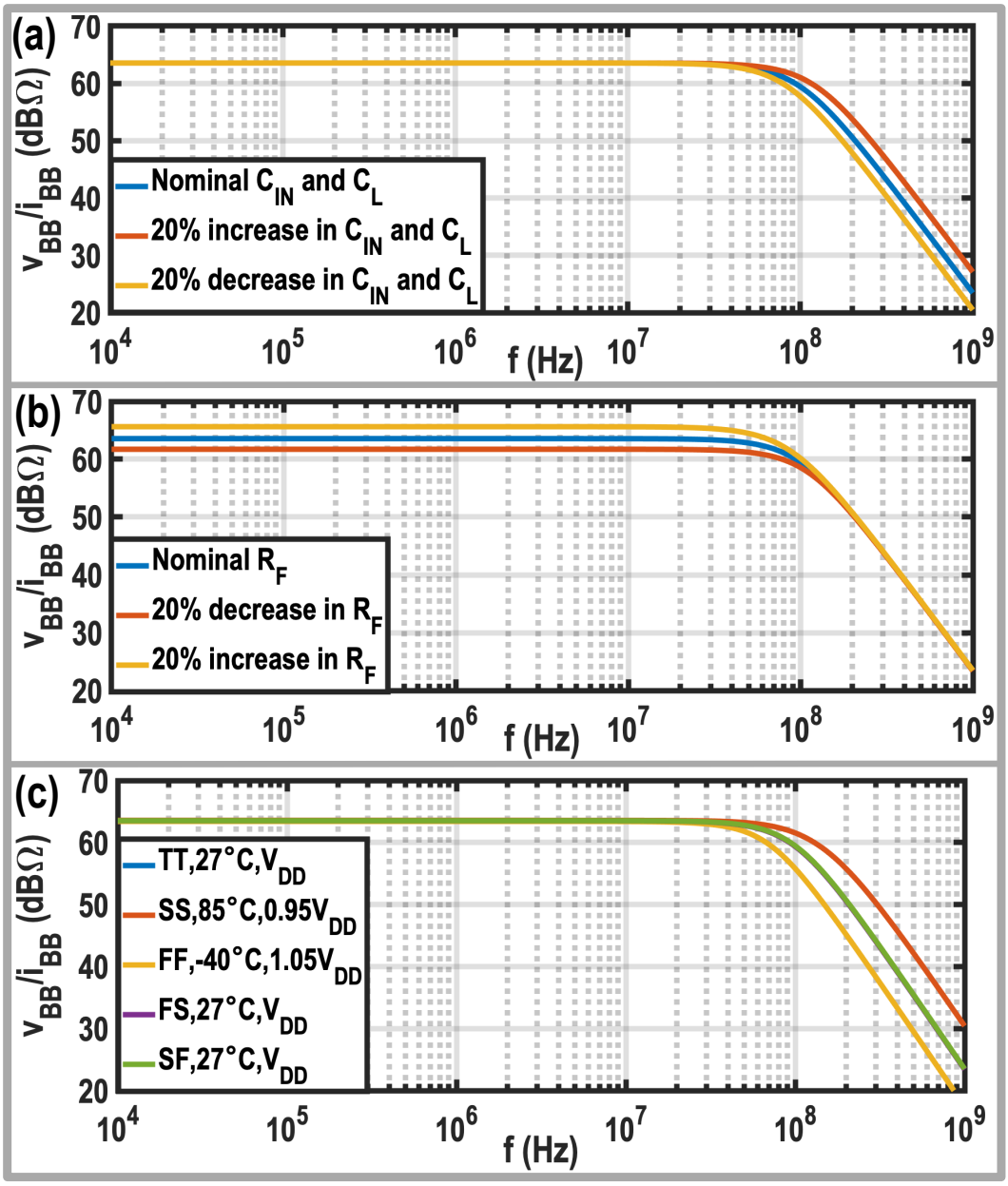

Figure 2.12: The deviations of the frequency response of the second-order TIA against (a) ±20% variations of C_{IN} and C_L, (b) ±20% R_F variations, and (c) only g_{mt} and r_{ot} changes over PVT variations.

observed). Hence, we can model g_{mt} and r_{ot} over PVT variations by

$$g_{mt} = (1+\alpha)\, g_{mtTT}, \tag{2.28}$$

$$r_{ot} = \frac{r_{otTT}}{(1+\alpha)}, \tag{2.29}$$

where α is a process-dependent scaling factor; g_{mtTT} and r_{otTT} are, respectively,

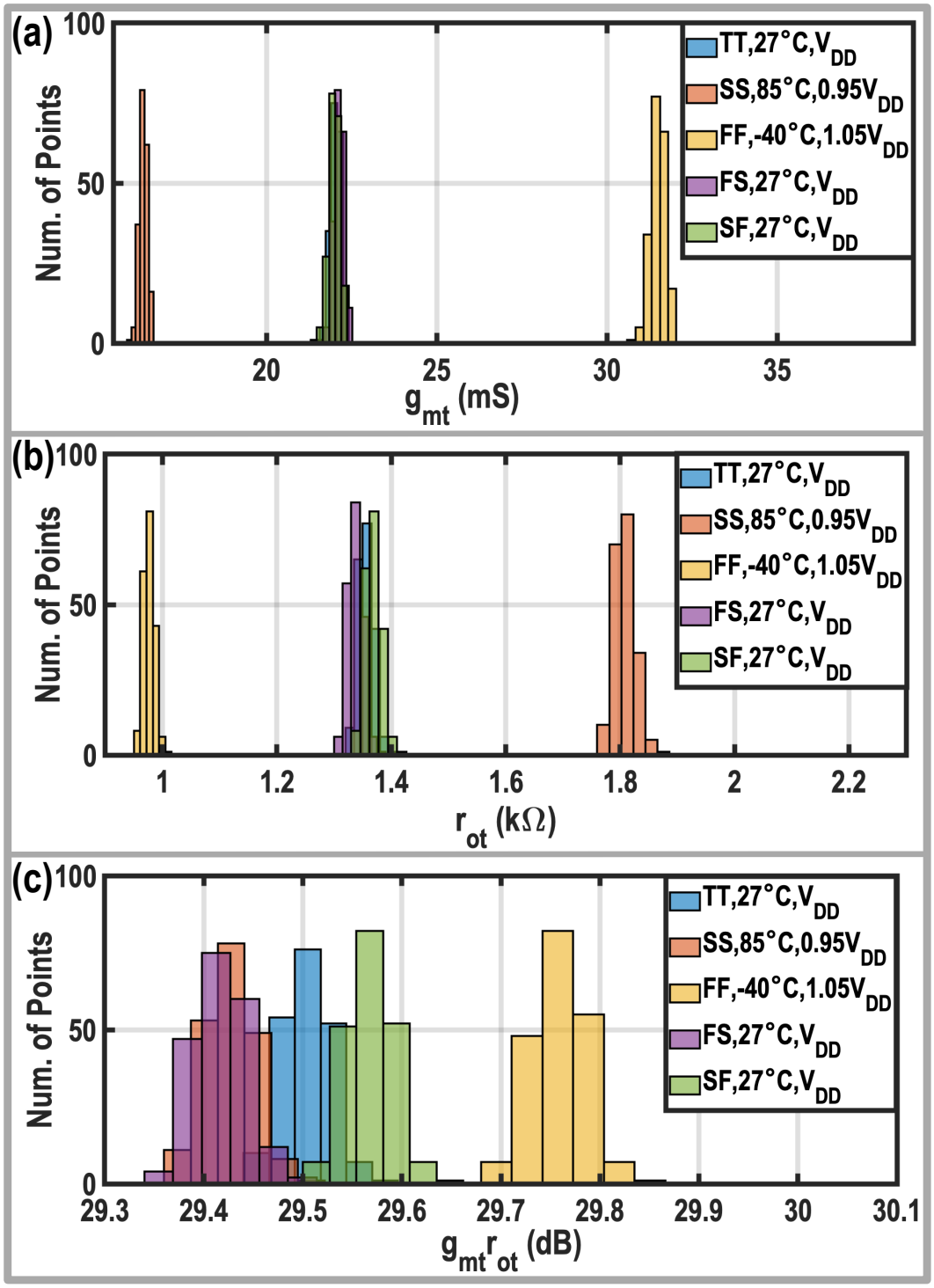

Figure 2.13: The fluctuation of (a) g_{mt}, (b) r_{ot}, and (c) $g_{mt} \times r_{ot}$ over PVT variations using Monte Carlo simulations.

the nominal values of the amplifier's transconductance and output resistance at the typical-typical process corner. By replacing (2.28) and (2.29) into (2.26)

and assuming that $C_{IN} \gg C_L$, the damping ratio of the TIA can be rewritten as

$$\zeta \approx \frac{1}{2}\frac{1}{\sqrt{g_{mtTT}R_F}}\sqrt{\frac{C_{IN}}{C_L}}\left(1+\frac{R_F}{r_{otTT}}+\frac{\alpha}{2}\left(\frac{R_F}{r_{otTT}}-1\right)\right). \tag{2.30}$$

Therefore, by choosing $r_{otTT} \approx R_F$, the sensitivity of the damping ratio to the g_{mt} and r_{ot} variations is vastly reduced. However, as shown in Fig. 2.12 (c), the 3-dB bandwidth of the TIA is still sensitive to g_{mt} variations.

Considering the presented analysis, the damping ratio of the second-order TIA is almost insensitive to PVT variations. However, the 3-dB bandwidth and RX gain are PVT-sensitive and require calibrations. In practice, g_{mt} value is mainly determined based on noise requirement and can be stabilized over PVT variations using constant-g_m techniques. Then, R_F is tuned to adjust the RX gain. Finally, while maintaining C_{IN} to C_L ratio to keep the damping ratio constant, C_{IN} and C_L values are adjusted to get the desired 3-dB bandwidth.

2.3.2 Stability Analysis of the TIA's Amplifier

As mentioned earlier, C_F is removed from the TIA amplifier feedback to implement a second-order TIA. However, in conventional TIAs, C_F creates a zero improving the stability of the TIA amplifier [90]. Hence, it is instructive to analyze the effect of the adopted technique on the TIA amplifier stability. In order to do so, the same method presented in [91] is utilized to calculate the TIA amplifier's LG. Since the feedback type of the TIA amplifier is voltage-to-current, the Y matrix is employed to calculate the loading effect of the feedback impedance, as shown in Fig. 2.14 (a). Consequently, the LG can be calculated by

$$LG = \frac{g_{mt}\left(R_F \parallel r_{ot}\right)}{\left(1+sC_{IN}R_F\right)\left(1+sC_L\left(R_F \parallel r_{ot}\right)\right)}. \tag{2.31}$$

As illustrated in Fig. 2.14 (b) and can be gathered from (2.31), the LG of the TIA amplifier has two poles. The dominant pole of LG is $1/(C_{IN}R_F)$, and the non-dominant pole of LG is $1/(C_L\left(R_F \parallel r_{ot}\right))$. The phase margin of the TIA amplifier should be better than 45° to ensure its stability. Hence, the non-dominant pole of LG should be larger than the unity-gain bandwidth (ω_u) of the TIA amplifier:

$$\omega_{nd} \geq \omega_u \Longrightarrow \frac{C_{IN}}{C_L} \geq \frac{g_{mt}\left(R_F \parallel r_{ot}\right)^2}{R_F}. \tag{2.32}$$

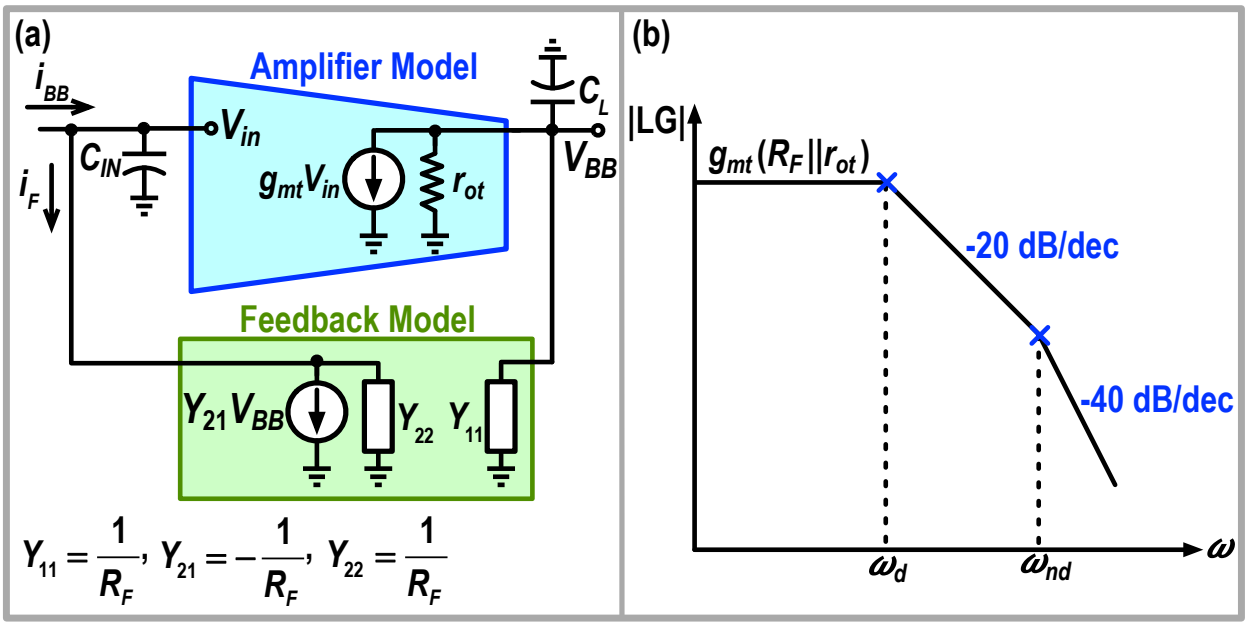

Figure 2.14: (a) Feedback model with Y parameters for the second-order TIA; (b) Bode plot of the TIA amplifier loop gain.

Consequently, to ensure the stability of the TIA's amplifier, C_{IN} must be chosen much larger than C_L.

Figure 2.15 shows the simulated magnitude and phase response of the loop gain of the TIA's amplifier using 'stb' analysis in Cadence. Since the TIA employs a single-stage amplifier, the adopted method does not cause any stability issues, and a phase margin of 69° is obtained. It is worth mentioning that in applications with high in-band linearity requirements, a multi-stage amplifier is required, and any internal pole of the multi-stage amplifier should be considerably higher than ω_u to ensure the amplifier stability.

One may notice that the TIA can be stabilized even by choosing the dominant pole to be $1/(C_L\,(R_F \parallel r_{ot}))$ and wonder if this choice would result in a better performance. However, in this case, the TIA output would be shorted to ground at far-out out-of-band frequencies since C_L must be much larger than C_{IN} to ensure TIA's stability. Consequently, the input impedance of the TIA increases from $1/g_{mt} + R_F/(g_{mt}r_{ot})$ to R_F at those frequencies, degrading the RX out-of-band linearity and sacrificing the stability of the RX front-end, as can be gathered from (2.24) in Section 2.2.5.

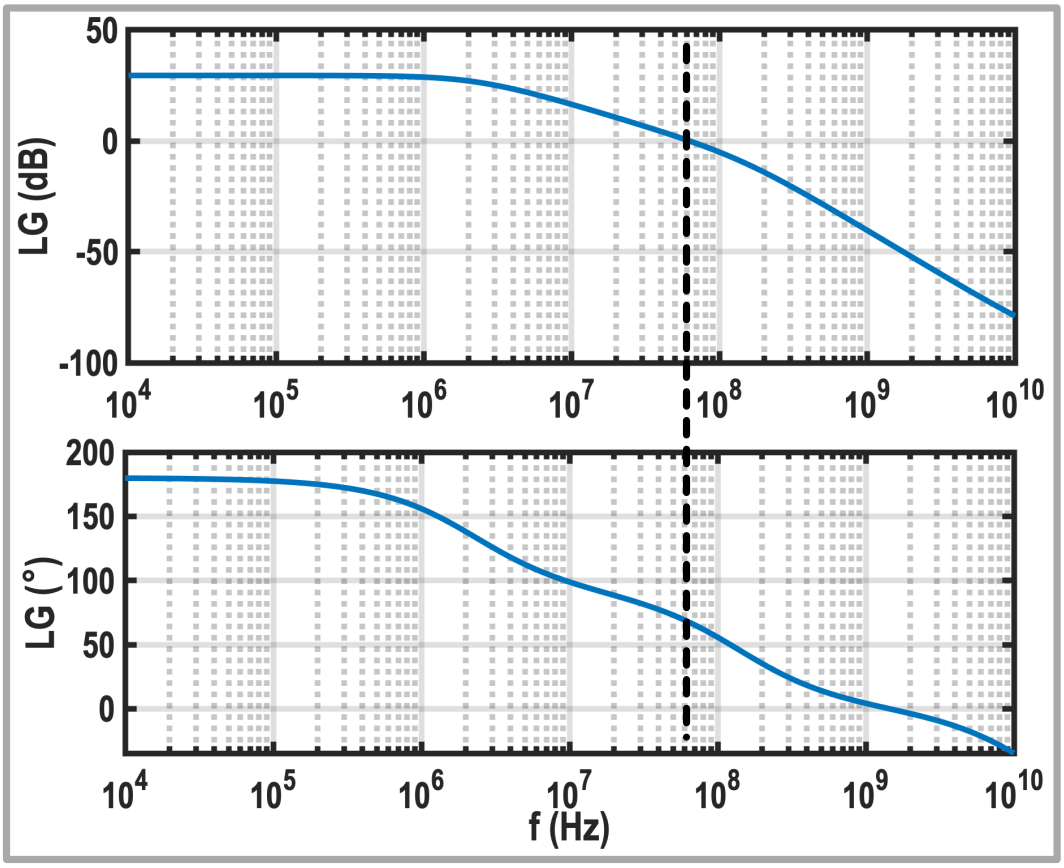

Figure 2.15: Simulated magnitude and phase response of the TIA's loop gain.

2.3.3 Design Guide for the Second-order TIA

In this subsection, we develop a design guide for estimating the components (i.e., R_F, g_{mt}, r_{ot}, C_{IN}, and C_L) of the second-order TIA based on the noise requirement, 3-dB bandwidth, and stability of the TIA amplifier. First, the R_F value is chosen based on the RX required gain. Then, the value of g_{mt} is determined such that the TIAs' noise has a negligible effect on the NF. Based on the simulated NF of the proposed RX versus g_{mt} in Fig. 2.16 (a), a g_{mt} larger than 17.5 mS is needed to limit its NF penalty to $\approx$0.1 dB. Later, in Section 2.5, we will develop a closed-form equation for the RX NF so that the required g_{mt} value can also be estimated analytically.

In the next step, as can be gathered from Fig. 2.16 (b), the channel length (L_t) of the input transistors of the inverter-based amplifier is chosen 240 nm to achieve a flicker noise corner of $\sim$100 kHz, much smaller than the RX 3-dB bandwidth. By knowing g_{mt} and L_t, the output resistance of the inverter-based amplifier can be easily determined. Finally, by considering a simulated r_{ot} of 1.5 kΩ, and assuming $C_{IN} \gg C_L$ due to stability issues, C_{IN} and C_L can be

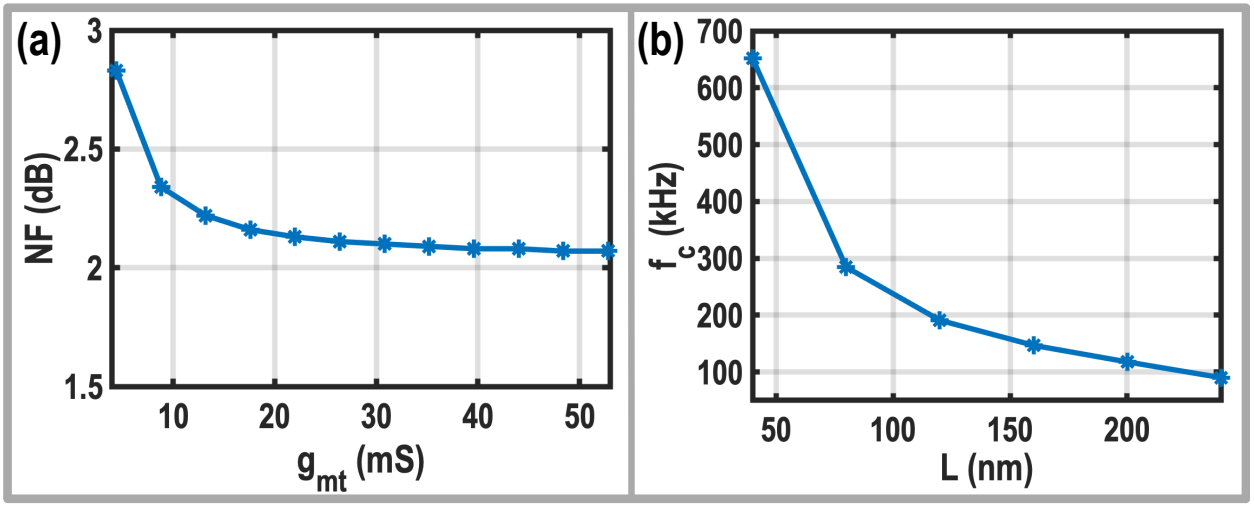

Figure 2.16: (a) Simulated RX NF versus g_{mt}; (b) simulated flicker noise corner of the TIA amplifier versus the channel length of its input transistors.

estimated using damping factor (2.26) and natural frequency (2.27) equations,

$$C_{IN} = \frac{2\zeta g_{mt}}{\omega_n \left(1 + \frac{R_F}{r_{ot}}\right)}, \tag{2.33}$$

$$C_L = \frac{\left(1 + \frac{R_F}{r_{ot}}\right)}{2R_F \zeta \omega_n}. \tag{2.34}$$

Considering $\zeta = \sqrt{2}/2$, $\omega_n = 2\pi \times 100\,\text{MHz}$ and R_F=1.6 kΩ, the calculated values of C_{IN} and C_L are 21.8 pF and 1.45 pF, respectively. All the circuit parameters calculated in the design guide are then used to simulate the filter transfer function. As shown in Fig. 2.11, the simulated 3-dB bandwidth and filtering roll-off of the designed TIA are respectively 88 MHz and -38 dB/dec, confirming the validity of the developed design guide.

2.3.4 TIA Selectivity and Area Trade-Off

Although the adopted second-order TIA has two complex conjugate poles and offers better selectivity than conventional first-order TIA, it is instructive to compare the total value of their required capacitors to realize the same 3-dB bandwidth. The 3-dB bandwidth of the conventional TIA, illustrated in Fig. 2.6 (a), can be calculated by

$$f_{3dB} = \frac{1}{2\pi \left(C_{F,con} R_F + C_{IN,con} \left(\frac{1}{g_{mt}} + \frac{R_F}{1+g_{mt} r_{ot}}\right)\right)}. \tag{2.35}$$

One can choose $C_{IN,conv} = 0$ and set the 3-dB bandwidth by $C_{F,con}R_F$ to minimize the required capacitor. However, in this way, the TIA amplifier should absorb all the out-of-band blocker current, increasing the TIA's power consumption. As a compromise between the power consumption and area, the poles created by $C_{F,conv}$ and $C_{IN,conv}$ should contribute equally to the 3-dB bandwidth. Hence,

$$C_{F,conv} = \frac{1}{4\pi f_{3dB} R_F}, \tag{2.36}$$

$$C_{IN,conv} = \frac{g_{mt} r_{ot}}{4\pi f_{3dB} \left(R_F + r_{ot}\right)} \tag{2.37}$$

Considering the same parameters used in the second-order TIA design, $R_F = 1.6\,k\Omega$, $f_{3dB} = 100\,\text{MHz}$, $g_{mt} = 20\,mS$, and $g_{mt}r_{ot} = 30$, $C_{F,conv}$ and $C_{IN,conv}$ become 0.5 pF and 7.7 pF, respectively. As estimated in Section 2.3.3, the total required capacitor of the adopted second-order TIA is 23.25 pF, thus demanding 2.75× larger capacitance than the conventional TIA. However, since the value of the TIA capacitors for the 5G channels with large bandwidths is relatively small, they do not occupy a large chip area, and it is wise to use second-order TIAs to achieve higher selectivity. For the 5G low channel bandwidth, the location of the close-in blocker from pass band edges remains constant, and even a more area-efficient first-order TIA can provide sufficient blocker attenuation due to the higher ratio of the blocker offset frequency to the channel bandwidth. Consequently, for future implementation of 5G RXs with programmable channel bandwidths, switchable load (C_L) and feedback (C_F) capacitors must be placed to achieve area efficiency and selectivity simultaneously. In low (high) bandwidths, C_F (C_L) and C_L (C_F) banks would respectively be turned on and off to realize first-order (second) filtering.

2.4 Circuit Implementation

Fig. 2.17 shows the entire RX block diagram in which eight-phase passive mixers are used to down-convert the RF current of the LNTA. Then, the second-order TIAs convert the down-converted RF current to baseband voltages. Similar to [21] and as shown in Fig. 2.10 (b), a common-mode feedback (CMFB) circuit sets the DC operating point of the TIAs' outputs around mid-rail voltage. Harmonic rejection (HR) is implemented by combining the weighted TIAs' outputs to generate in-phase (I) and quadrature (Q) baseband signals.

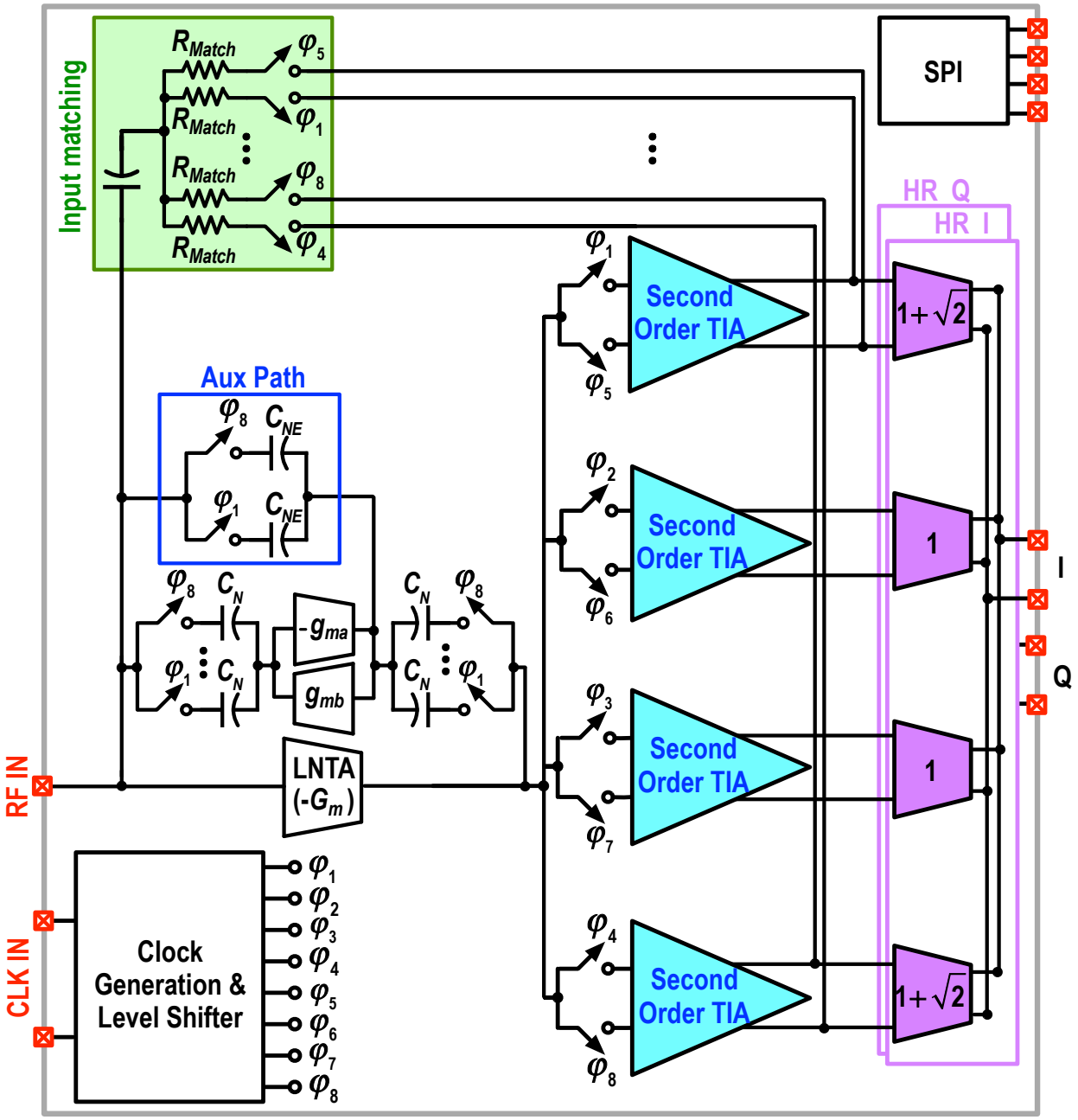

Figure 2.17: The block diagram of the proposed RX.

Therefore, the third and fifth harmonic of the LO will be rejected, improving the NF and linearity of the RX. The 50 Ω matching is implemented by up-converting baseband voltages at TIAs' outputs, combining the up-converted signals through the matching resistors (R_{Match}), and applying the resulting signal back to the RX input [65–67]. In this way, thanks to the RX voltage gain, the matching resistors become significantly large and negligibly contribute to the RX NF. Since the voltage gain from the antenna to the TIA output has a positive sign, a

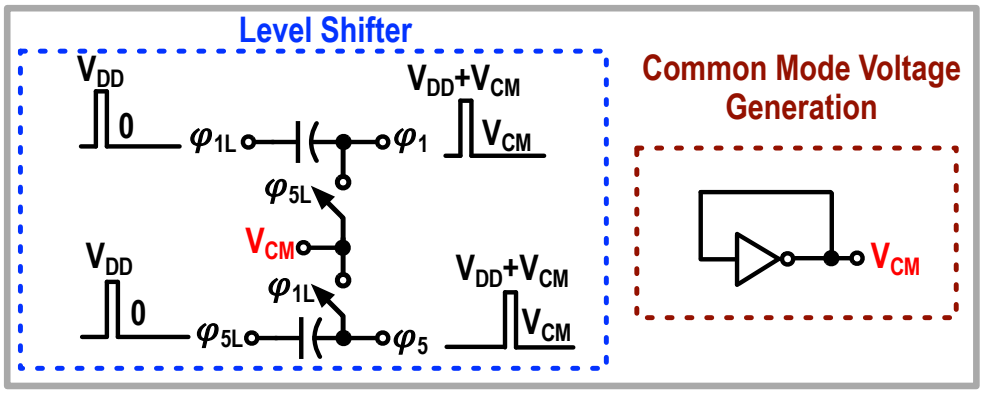

Figure 2.18: Schematics of the implemented level shifter for biasing the LOs.

-1 multiplication is required in the translational network to guarantee negative feedback. The -1 multiplication is easily implemented by applying out-of-phase LO clocks to the associated down-converting and up-converting passive mixers of each TIA.

NMOS transistors are used to implement the passive mixers. The drains of those devices are biased at $V_{CM} \approx V_{DD}/2$, since they are connected to the input and output of the LNTA. Hence, as shown in Fig. 2.18, level shifters are used to shift the LO levels from 0 - V_{DD} to V_{CM} - V_{DD} + V_{CM}. V_{CM} is generated inside the chip using an inverter with shorted input and output. Unlike the RX implemented in our previous work [88], the bulks of NMOS transistors are biased to V_{CM} in the respin prototype to improve the RX linearity performance. As shown in 2.19 (a), the LNTA is implemented using inverter-based amplifiers with shunt-resistive feedback to bias the transistors in saturation. Despite the simplicity of the inverter-based LNTA, G_m, the power consumption, and the input-referred noise voltage of the LNTA are sensitive to the PVT variations. In a future implementation, a constant-g_m biasing technique can be adopted to resolve this issue.

In the gyrator-based implementation of an active inductor, an undesired equivalent series resistance exists, which is inversely related to the voltage gain of the feedforward transconductance (g_{ma}) [4]. Hence, the feedforward transconductance is implemented with a cascode inverter-based amplifier to reduce the undesired series resistance of the gyrator. However, in the first implementation of the proposed RX [88], a common gate amplifier was used to implement the feedback transconductance (g_{mb}). The input impedance of the feedback transconductance can be approximated by $1/g_{mb}$, which loads the feedforward transconductance, reducing its gain. Thus, the series resistance

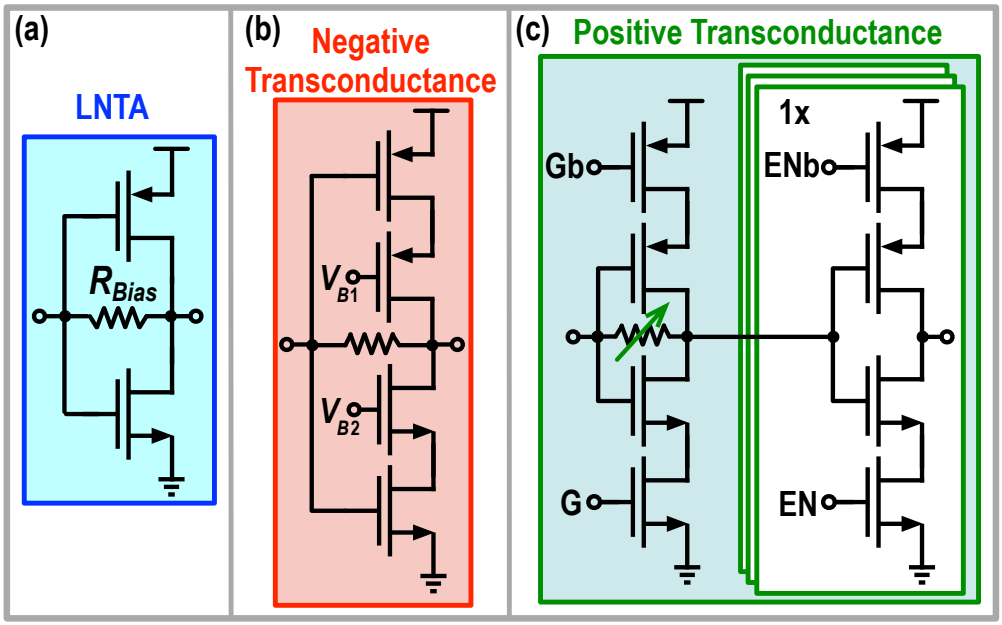

Figure 2.19: Schematics of the implemented (a) LNTA, (b) positive, and (c) negative transconductance of the gyrator.

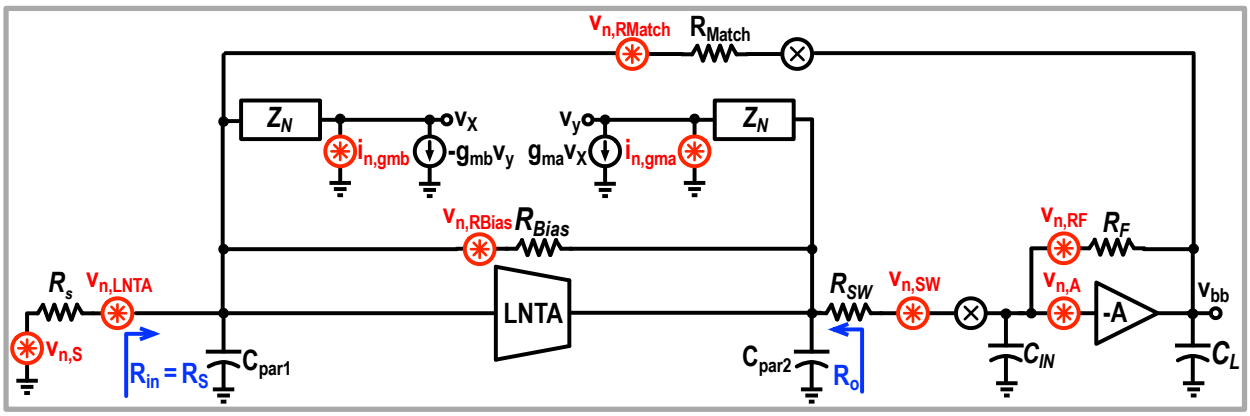

Figure 2.20: Simplified model of the proposed RX for NF calculation.

increases, degrading the selectivity of the proposed RX. To solve this issue, in the respin prototype, two series amplifiers are adopted to implement the feedback transconductance, as illustrated in Fig. 2.19 (c). For measurement purposes, different components of the TIA (the amplifier, C_L, and C_{IN}) and gyrator (g_{ma} and g_{mb}) are tunable and can be programmed through a serial peripheral interface (SPI).

Since this design employs a supply voltage higher than the 40-nm nominal voltage (i.e., 1.3 V rather than 1.1 V), time-dependent dielectric breakdown (TDDB) and hot carrier injection (HCI) [92,93], as two main failure mechanisms in CMOS circuits, are considered here to investigate the RX reliability. The HCI

degradation occurs when the drain current and drain–source voltage (V_{DS}) of a transistor are large simultaneously. The maximum V_{DS} of all transistors in the LNTA and TIAs' amplifiers is $0.5V_{DD} = 0.65\,\text{V}$, which is much less the standard voltage of thin-oxide transistors. Moreover, the transistors in the LO buffers do not conduct any current when their V_{DS} is 1.3 V. Consequently, the proposed RX is not vulnerable to HCI. On the other hand, the thickness of gate-oxide for 40-nm transistors is ∼2.5 nm, and based on analysis in [93] [94] and the reliability rules of the process design kit, they can withstand a maximum gate-drain and gate-source voltage of 1.6 V without facing a gate-oxide breakdown in 10 years.

2.5 Noise Analysis

Fig. 2.20 shows the simplified noise model of the proposed RX, in which the gyrator noise is modeled with two current sources at its input and output, i.e., $i^2_{n,gmb} = 4kT\gamma g_{mb}$ and $i^2_{n,gma} = 4kT\gamma g_{ma}$, where γ is the average thermal noise excess factor of NMOS and PMOS transistors used in gyrators feedforward and feedback transconductors. By taking the same procedure presented in [19,21,95], the noise factor of the proposed RX can be approximated by

$$\begin{aligned} F = &\left(1 + \frac{\gamma}{G_m R_s} + \frac{R_s}{R_{Bias}} + \frac{R_s}{R_{Match}}\right. \\ &+ \left(\frac{R_S}{Z_N}\right)^2 \times \frac{\gamma}{g_{ma} R_S}\left(1 + \frac{1}{g^2_{mb} Z^2_N}\right) \\ &+ \frac{1}{A^2_v} \times \left(\frac{R_o}{Z_N}\right)^2 \times \frac{\gamma}{g_{mb} R_S}\left(1 + \frac{1}{g^2_{ma} Z^2_N}\right) \\ &+ \frac{1}{A^2_v} \times \left(\frac{R_{SW}}{R_S} + \frac{M \times R_S}{R_F}\right)\Bigg) \times \frac{1}{\text{sinc}^2\left(\frac{1}{M}\right)} \\ &+ \frac{1}{A^2_v} \frac{\rho v^2_{n,A}}{4kTR_S} \times \left(\frac{R_o + R_{SW}}{\rho R_F} + \frac{R_o + R_{SW} + Z_{eq}}{Z_{eq}}\right)^2 . \end{aligned} \tag{2.38}$$

Here, R_{SW} is the on-resistance of the down-converting passive mixers, R_{Bias} is the shunt bias resistor of the LNTA, A_v is the voltage gain from the antenna to the LNTA's output ($A_v = G_m R_o/2$), $v_{n,A}$ is the input-referred noise voltage of the TIA amplifier, and $\text{sinc}^2(1/M)$ accounts for the loss of passive mixers. Moreover, ρ and Z_{eq} are given by

$$\rho = \frac{1}{M}\text{sinc}^2\left(\frac{1}{M}\right), \tag{2.39}$$

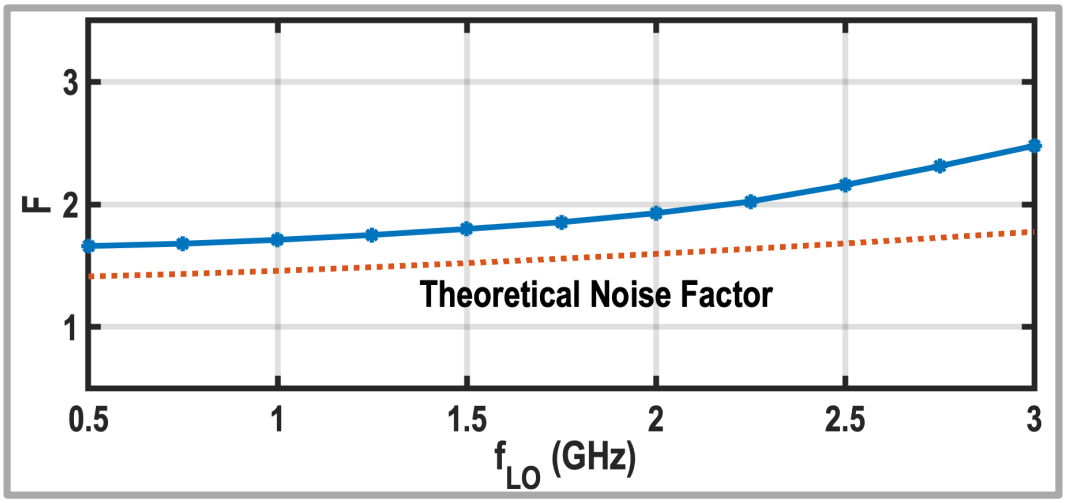

Figure 2.21: The simulated noise factor of the proposed RX realized with real devices versus the LO frequency.

$$Z_{eq} = Z_{sh} \parallel \frac{1}{j\omega_{BB} \times \frac{C_{IN}}{\rho}}, \tag{2.40}$$

$$Z_{sh} = \frac{M\rho}{1 - M\rho} \left(R_o + R_{SW}\right). \tag{2.41}$$

At the low in-band offset frequencies, the N-path notch filter exploits high impedance (i.e., $Z_N \gg R_s, R_o$), and the gyrator noise does not degrade the noise factor. Assuming that R_F and R_{Match} are large enough, (2.38) at low in-band offset frequencies can be simplified to

$$F = \left(1 + \frac{\gamma}{G_m R_s} + \frac{R_s}{R_{Bias}} + \frac{1}{A_v^2} \times \left(\frac{R_{SW}}{R_S} + \frac{M \times R_S}{R_F} + \frac{v_{n,A}^2}{M \times 4kTR_S}\right)\right) \times \frac{1}{\mathrm{sinc}^2\left(\frac{1}{M}\right)}. \tag{2.42}$$

Considering $G_m = 130\,mS$, $\gamma = 1$, $R_o = 60\,\Omega$, $R_{Bias} = 400\,\Omega$, $M = 8$, $R_{SW} = 10\,\Omega$, $R_F = 1.6\,k\Omega$, and $g_{mt} = 20\,mS$, the theoretical noise factor is 1.41. As illustrated in Fig. 2.21, the simulated noise factor of the RX realized with real devices is 1.66 at low LO frequency, which is 0.25 higher than the ideal case, since the noise of gate and bulk resistors is not modeled in our analysis. The parasitic capacitors at the input and output of the LNTA reduce A_v at high LO frequencies, increasing the noise contribution of passive mixers, TIA feedback resistors, and TIA amplifiers, as predicted by (2.38) and confirmed by the noise factor simulation results in Fig. 2.21. Consequently, the noise factor degrades to 2.47 at 3 GHz LO frequency.

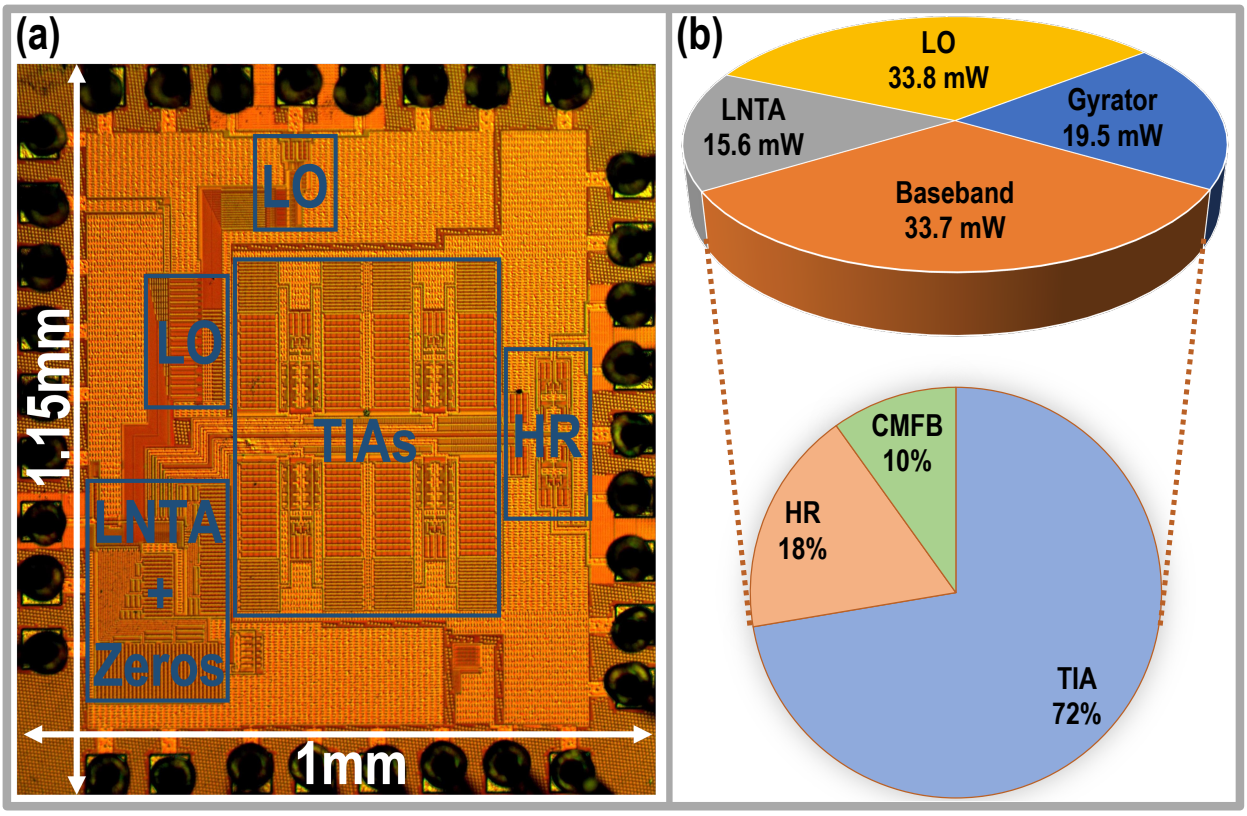

Figure 2.22: (a) Die micrograph of the proposed RX; (b) Power consumption breakdown at 1.5 GHz LO frequency.

2.6 Experimental Results

The proposed RX was fabricated in TSMC 40 nm bulk CMOS technology. As shown in Fig. 2.22 (a), the RX occupies $1 \times 1.15\,\text{mm}^2$ with a core area of $0.5\,\text{mm}^2$. The chip consumes 84-140 mW from a 1.3 V supply voltage over the 0.5-3 GHz operating frequency. The power consumption breakdown at 1.5-GHz LO frequency is also depicted in Fig. 2.22 (b).

Fig. 2.23 (a) and (b) show the RX gain and in-band S_{11} versus the operating frequency when the auxiliary path is enabled. The RX gain is 37.2 dB at 0.5 GHz LO frequency and decreases to 34.6 dB at 3 GHz LO frequency. Due to the higher parasitic capacitance of the N-path notch filters, the measured BW_{RF} is 160 MHz. The input matching of the proposed RX is better than -8 dB over the 3dB bandwidth and for the entire operating frequency. Fig. 2.23 (c) shows the RX input impedance on Smith chart for 1.5-GHz LO frequency when the auxiliary path is active. The input impedance is around 50 Ω across the 3-dB bandwidth (highlighted in red). Then, the input impedance reaches ≈ 10 Ω at far-out out-of-band offset frequencies.

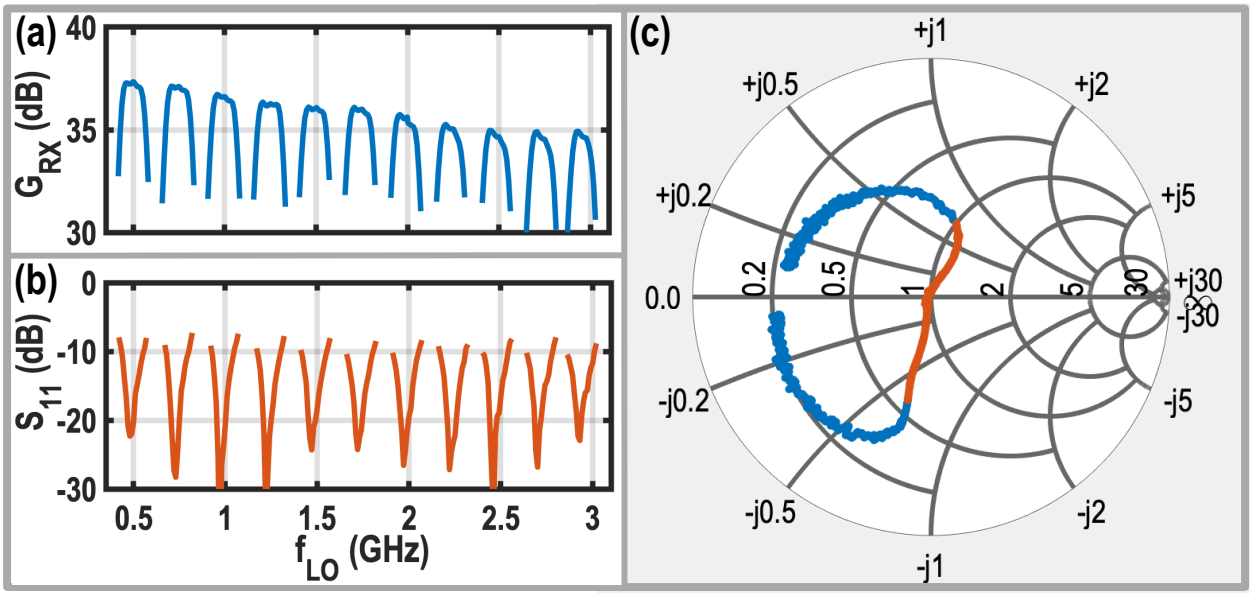

Figure 2.23: Measured (a) G_{RX}, (b) in-band S_{11}, and (c) the Smith chart view of the measured S_{11} at $f_{LO} = 1.5\,\text{GHz}$.

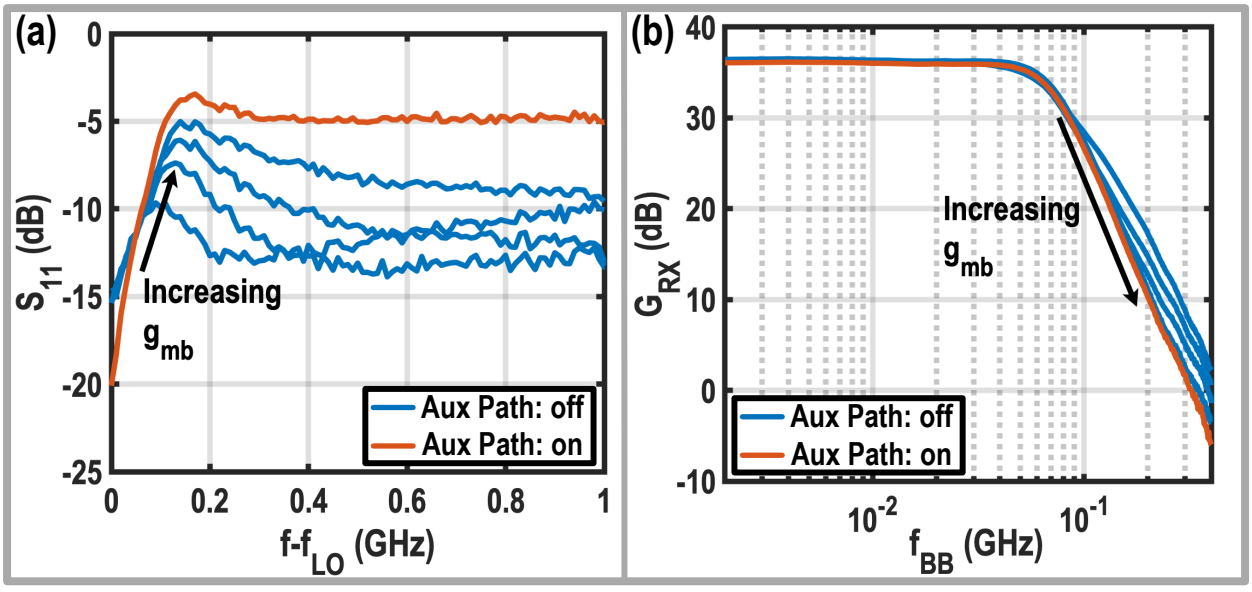

Figure 2.24: Effect of the programmable zeros on (a) S_{11} and (b) G_{RX} at $f_{LO} = 1.5\,\text{GHz}$.

The effect of the zeros' on the RX input impedance is investigated in Fig. 2.24 (a) by turning off the auxiliary path and sweeping the value of g_{mb} at $f_{LO} = 1.5\,\text{GHz}$. As mentioned earlier and predicted by (2.8) and (2.12), enhancing g_{mb} increases the zeros frequencies and reduces the input impedance of the proposed RX at the location of the zeros. Hence, measured S_{11} approaches ≈-5 dB for the highest g_{mb}, and the zero frequency is increased from f_{OS} ≈10 MHz ($\chi = 1.125$)

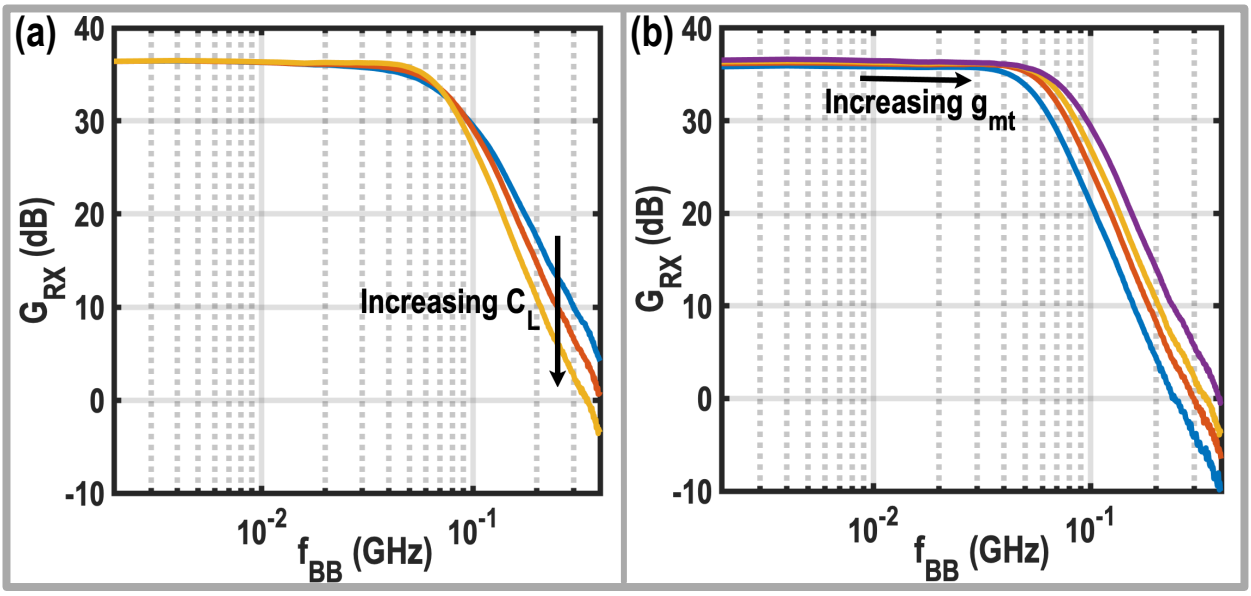

Figure 2.25: (a) Improving the RX selectivity by adjusting the value of C_L at $f_{LO} = 1.5\,\text{GHz}$; (b) enhancing the 3-dB bandwidth of the RX by increasing g_{mt} at $f_{LO} = 1.5\,\text{GHz}$

.

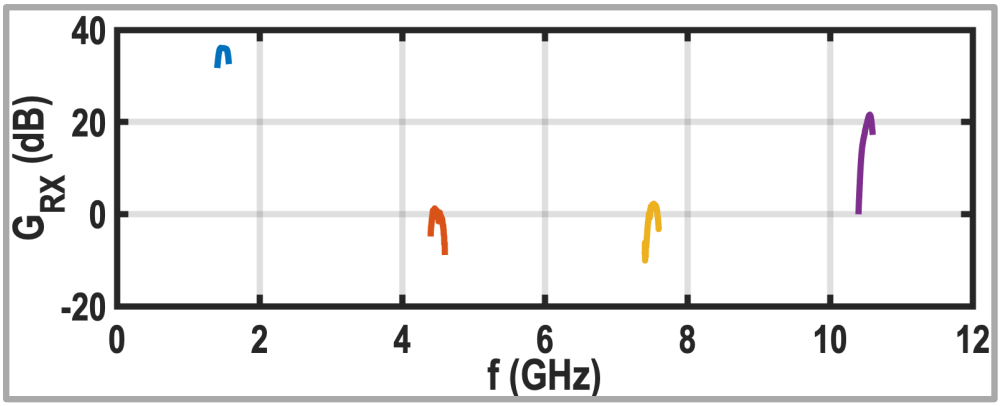

Figure 2.26: Harmonic rejection performance of the proposed RX

to f_{OS} ≈100 MHz ($\chi = 2.25$) by moving from the lowest g_{mb} setting to the highest one. Moreover, enabling the auxiliary path increases S_{11} to above -5 dB beyond the zero frequency, as it reduces the RX input impedance at far-out offset frequencies.

The effect of the programmable zeros on the RX gain is shown in Fig. 2.24 (b). Enhancing g_{mb} increases the zeros frequencies, offering ≈4.6 dB better rejection for the close-in blockers. The auxiliary path also improves the out-of-band rejection of the RX by at least ≈2 dB at far-out offset frequencies. Note that the auxiliary path has a negligible effect on the RX 3-dB bandwidth. For the rest of the measurements, the auxiliary path is enabled, and g_{mb} is set to its

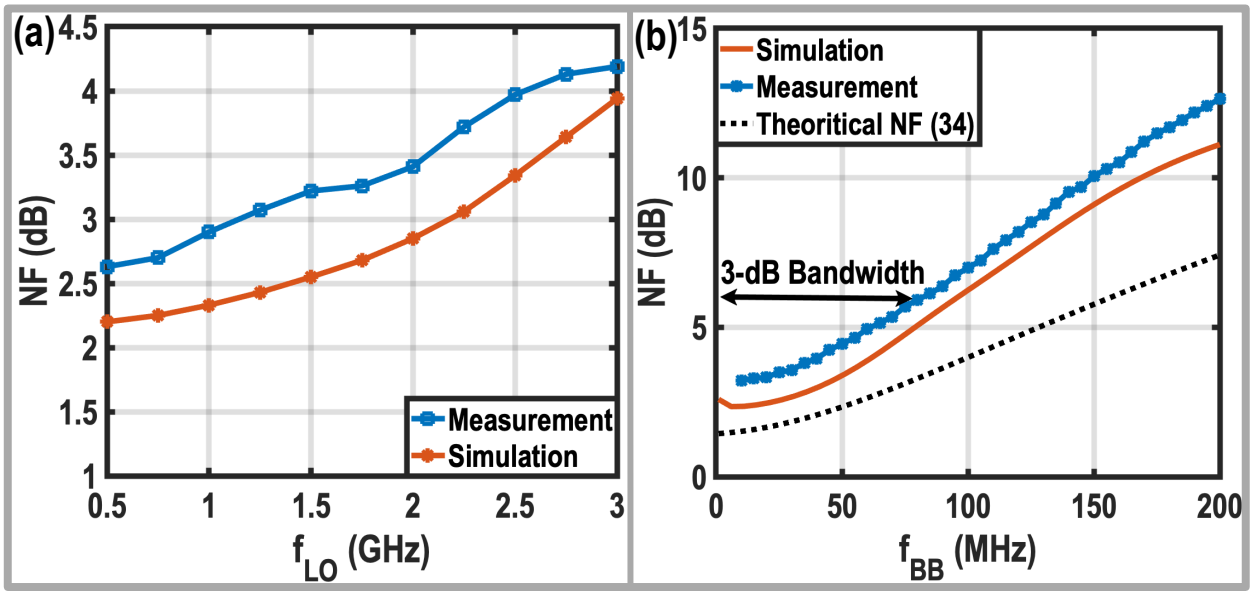

Figure 2.27: (a) Measured NF versus the LO frequency; (b) Measured NF versus the baseband frequency at $f_{LO} = 1.5\,\text{GHz}$.

maximum value.

As can be deduced by (2.26) and Fig. 2.25 (a), enhancing C_L reduces the damping factor and realizes two complex poles and a flat in-band gain in the transfer function of the RX gain. Moreover, as can be inferred from (2.27) and Fig. 2.25 (b), the 3-dB bandwidth of the TIA can be controlled by g_{mt} while keeping the passive components of the TIA constant. The RX BW_{RF} can be tuned from 119 MHz to 168 MHz by increasing g_{mt} while the value of ζ remains almost constant. For the rest of the measurements, g_{mt} is adjusted to its nominal value, and the C_L tuning word is set to achieve a second-order Butterworth response with a 160 MHz bandwidth.The harmonic rejection performance of the proposed RX is shown in Fig. 2.26. The harmonic rejection is better than 34 dB for the third and fifth harmonics. Note that the RX gain is still high for the seventh harmonic, with only a lower value due to the reduced gain of passive mixers at the seventh harmonic.

Fig. 2.27 (a) and (b) depict the measured NF versus the LO frequency and the baseband frequency. NF is 2.6 dB at the minimum LO frequency and increases to 4.2 dB at the maximum operating frequency. At the RX passband edges, the impedance of the N-path notch filters and the TIA input capacitor is reduced. Hence, as can be gathered from (2.38), the noise contribution of the gyrator noise and the TIA amplifier increases at the 3-dB bandwidth edge. Consequently, as shown in Fig. 2.27 (b), the NF degrades by 2.7 dB at the RX

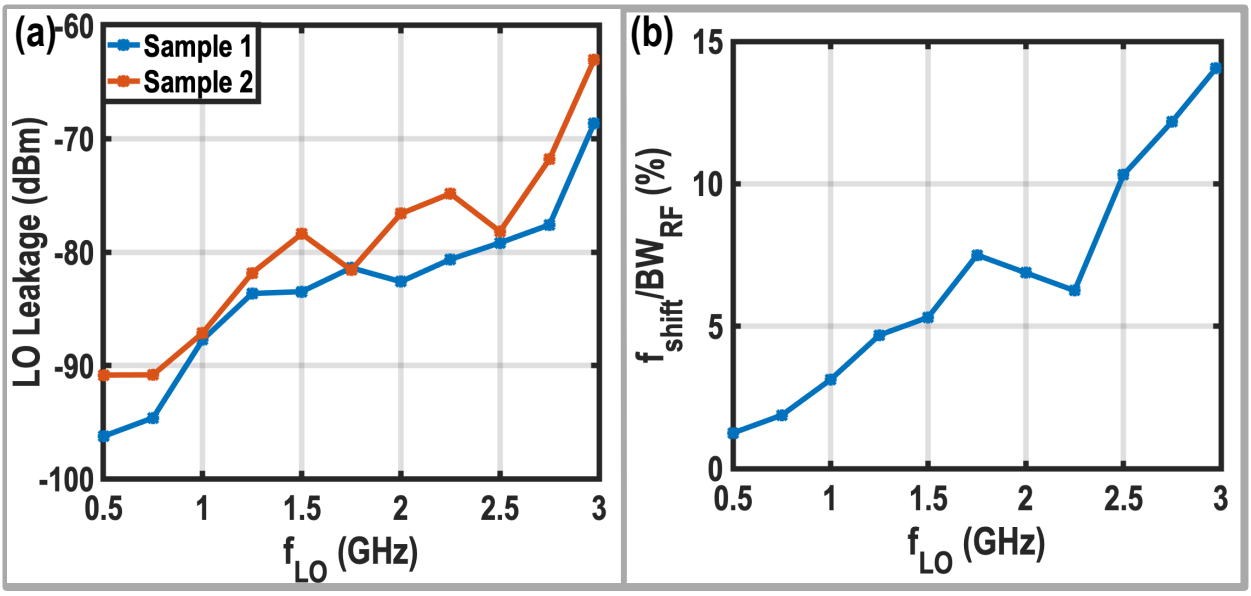

Figure 2.28: Measured (a) LO leakage for two samples and (b) frequency shift of the proposed RX normalized to BW_{RF} versus the LO frequency.

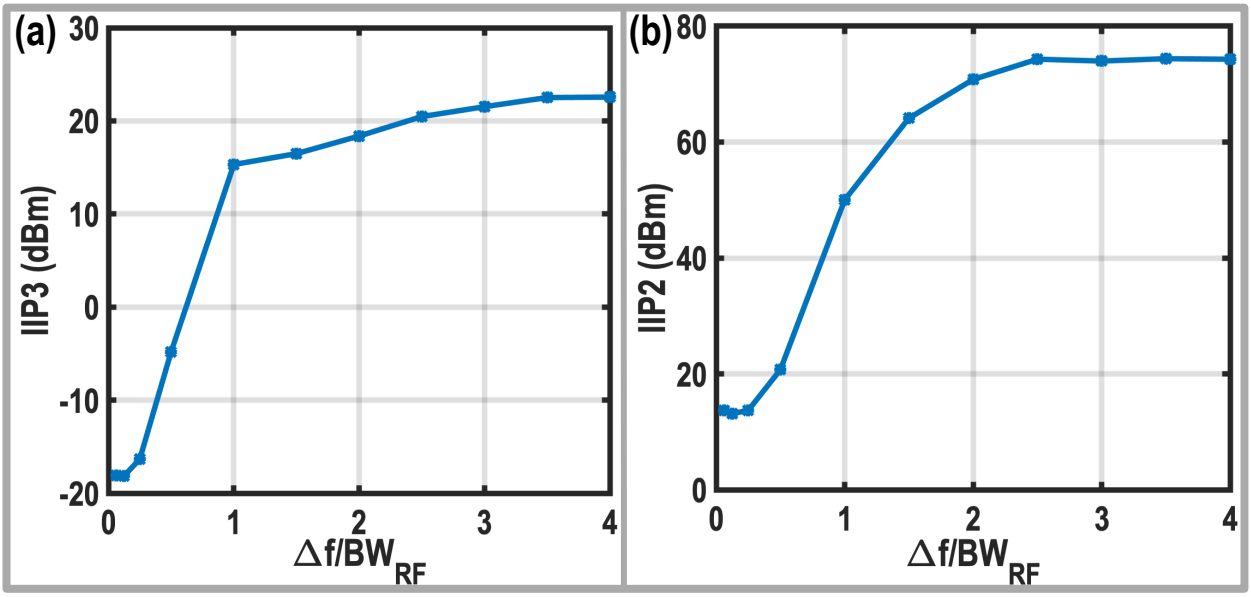

Figure 2.29: Measured (a) IIP3 and (b) IIP2 versus the offset frequency (Δf) normalized to $\mathrm{BW_{RF}}$ at $f_{LO} = 1.5\,\mathrm{GHz}$.

passband edges.

As illustrated in Fig. 2.28 (a), the worst measured LO leakage is -90.9 dBm at the minimum LO frequency and reaches -63 dBm at the maximum LO frequency. As discussed in [70] and [96], the parasitic capacitors of the passive mixers and the LNTA's delay shift the center frequency of the RX gain towards the lower side of the LO frequency. This is a drawback of channel selection at the

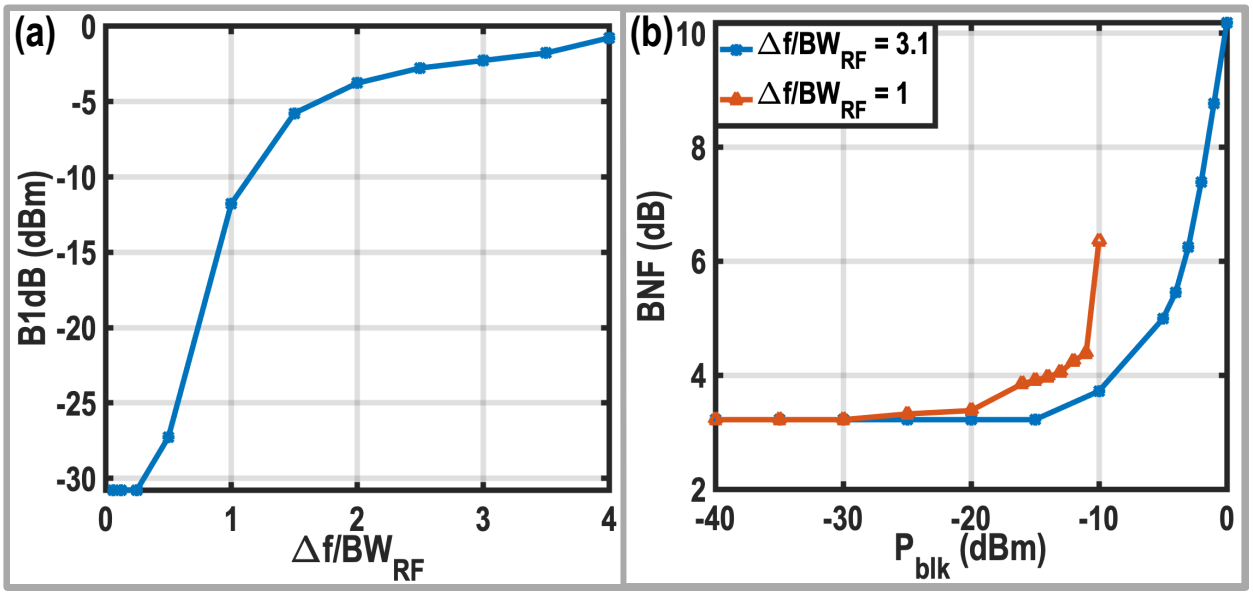

Figure 2.30: Measured (a) B1dB versus the blocker offset frequency, and (b) blocker noise figure versus the blocker power at $f_{LO} = 1.5\,\text{GHz}$.

RF front end. Fig. 2.28 (b) shows the frequency shift of the RX gain (f_{shift}) normalized to BW_{RF}, in which the worst frequency shift is 14% of the BW_{RF}. Consequently, in future implementations, a polyphase N-path notch filter [70] should be adopted in the auxiliary path to alleviate this issue. Simulation results show that this well-known technique can bring back the center frequency of the RX gain to f_{LO}, without affecting the zeros frequencies.

After showing the wideband operation of the proposed RX, the LO frequency is fixed at 1.5 GHz, and the rest of the measurements are carried out. The RX small-signal linearity measurements are depicted in Fig. 2.29. For third-order intercept point (IIP3) measurement, the tones are located at $f_1 = f_{LO} + \Delta f$ and $f_2 = f_{LO} + 2\Delta f$-5 MHz. Moreover, the locations of the two tones are $f_1 = f_{LO} + \Delta f$ and $f_2 = f_{LO} + \Delta f$-5 MHz for the second-order intercept point (IIP2) measurements. The RX in-band IIP3 is -18 dBm, and thanks to the RX sharp filtering, it improves to 15.3 dBm when $\Delta f/BW_{RF}$ is 1. The out-of-band IIP3 of the proposed RX reaches to 22.5 dBm at far-out offset frequencies. The measured in-band IIP2 is 13.4 dBm, and it reaches 74.3 dBm at far-out out-of-band offset frequencies.

A small signal at $f_{sig} = f_{LO}$+5 MHz is accompanied by a large blocker located at $f_{blk} = f_{LO} + \Delta f$ for the B1dB measurements. As shown in Fig. 2.30 (a), the RX in-band B1dB is -30.8 dBm, and improves to -11.8 dBm when $\Delta f/BW_{RF}$ is 1. The out-of-band B1dB of the RX is -0.3 dBm. The RX NF is plotted

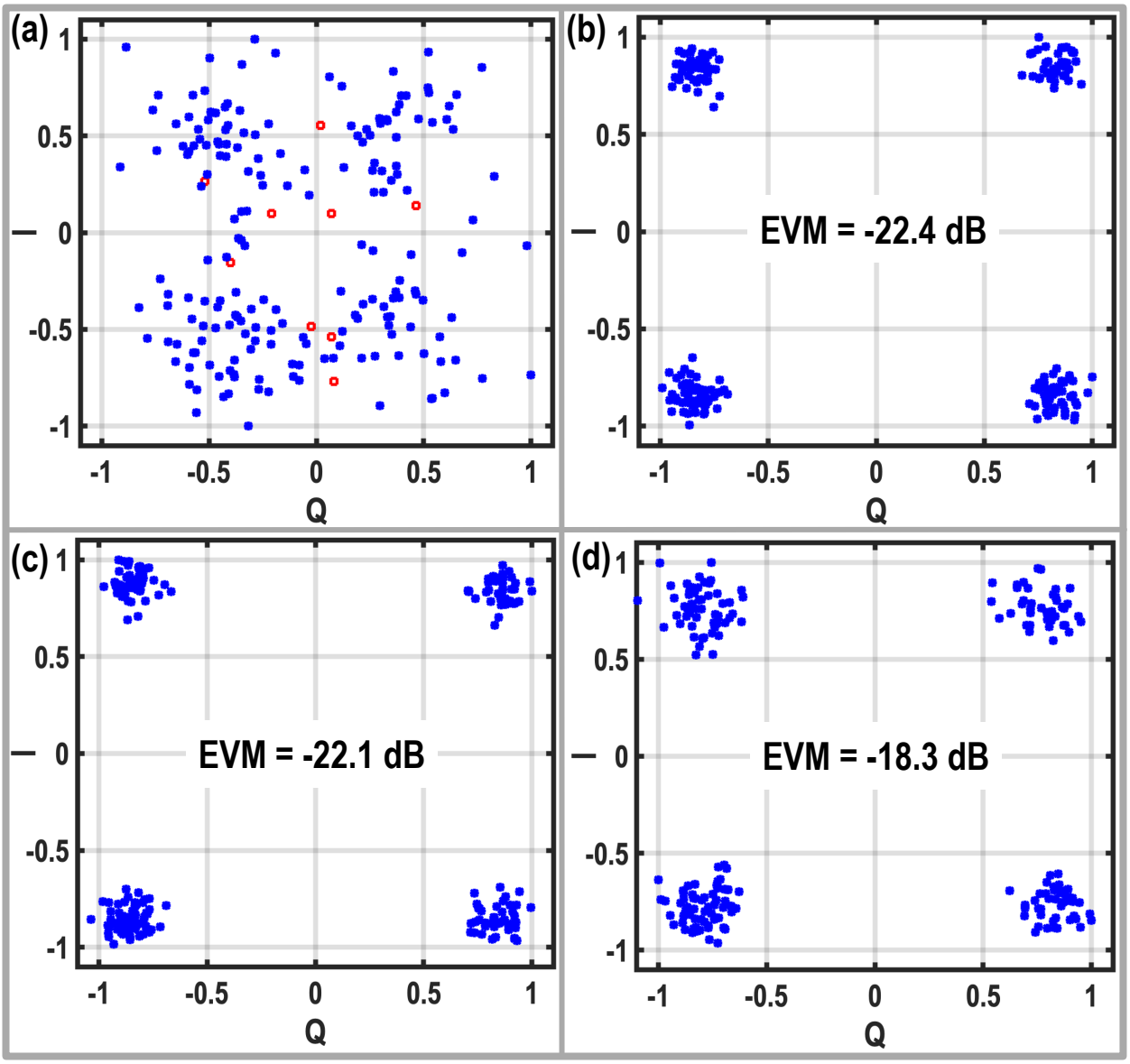

Figure 2.31: (a) Measured constellation at reference sensitivity; Measured constellation in the presence of (b) -44 dBm blocker located at 15 MHz offset, (c) -30 dBm blocker at 60 MHz offset frequency, and (d) -15 dBm blocker at 85 MHz offset frequency while signal power is 16 dB higher than the reference sensitivity level.

versus the blocker power located at $\Delta f/BW_{RF} = 1$ and $\Delta f/BW_{RF} = 3.1$ in Fig. 2.30 (b). A -10 dBm blocker located at $\Delta f/BW_{RF} = 1$ increases the NF to 6.3 dB, and a 0 dBm blocker placed at $\Delta f/BW_{RF} = 3.1$ degrades the NF to 10.2 dB. The NF degradation arises from the reciprocal mixing and nonlinearity of the proposed RX. For blocker power levels below -2 dBm, reciprocal mixing serves as the dominant noise source. However, for blocker power exceeding -2 dBm, the nonlinearity of the LNTA also becomes significant, steepening the slope of NF degradation relative to blocker power.

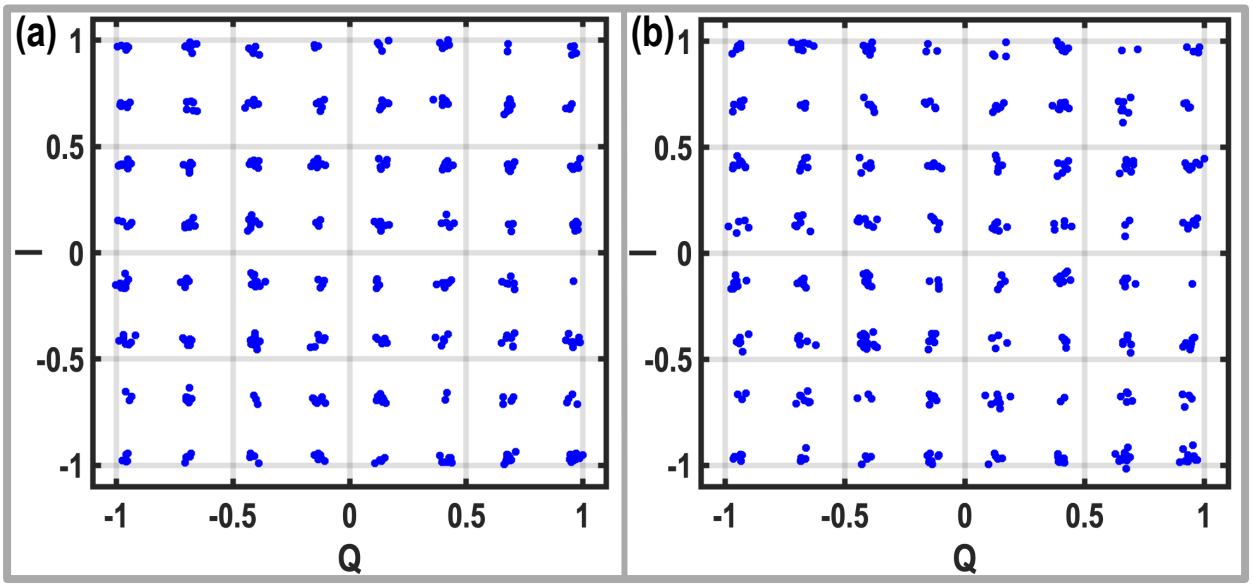

Figure 2.32: The measured constellation of 100 MS/s -60 dBm QAM-64 signal: (a) without blocker and (b) with -5 dBm blocker located at $\Delta f/\omega_{3dB} = 3.1$.

The performance of the RX is also investigated based on the 3GPP requirements for user equipment applications. The first test is reference sensitivity, and to do so, a 100 MS/s QPSK signal with -86.7 dBm power is applied to the proposed RX. In this case, the throughput of the RX should be better than 95%. Fig. 2.31 (a) shows the constellation of the received signal. The throughput of the RX is 95.5%. Note that red squares denote the missing symbols in Fig. 2.31 (a).

The out-of-band blocking test of the user equipment application is divided into three ranges. In the first range, a -44 dBm CW blocker is located between 15 MHz and 60 MHz offset from the 3-dB bandwidth edge. In the second range, the blocker is located between 60 MHz and 85 MHz offset, and its power increases to -30 dBm. The last range is the most difficult blocking scenario in which a -15 dBm CW blocker is present at 85 MHz offset frequency. Based on the 3GPP standard, the power of the desired signal in all the above-mentioned tests should be increased by $9 + 10\log_{10}(\mathrm{BW_{RF}}/20)$ dB compared to the reference sensitivity power level [2]. Since the bandwidth of the desired signal is 100 MS/s, its power is increased by 16 dB. As can be gathered from the constellation diagrams in Fig. 2.31 (b)–(d), all the symbols are received correctly, and the measured error vector magnitude (EVM) is always better than -18.3 dB. Hence, the proposed RX successfully passes all out-of-band blocking tests defined in the 3GPP standard for TDD mode.

High-order modulation schemes are used in 5G applications to increase the

data rate and spectral efficiency. Hence, the performance of the proposed RX is also investigated for QAM-64 signal. A 100 MS/s QAM-64 signal with -60 dBm is applied to the RX. Fig. 2.32 (a) shows the measured constellation in which the EVM is -29 dB. Moreover, to test the large signal performance of the RX, a -5 dBm blocker is combined with the desired signal and applied to the RX input. As shown in Fig. 2.32 (b), the measured EVM only degrades by 1.9 dB and reaches -27.1 dB.

Table 2.1 summarizes the measured performance of the proposed RX and bench-marks it with state-of-the-art LNTA-based RXs. The proposed RX shows a competitive NF compared to state-of-the-art LNTA-based RXs [21, 45, 79, 81, 87, 88, 97, 98]. Moreover, at the cost of higher power consumption, the fabricated prototype outperforms other LNTA-based RXs in terms of linearity except [87]. However, [87] has a relatively narrow operating frequency range, uses several supply voltages, and requires a complex calibration procedure to reach the reported linearity performance. Moreover, this work is the only RX that reports EVM while facing a large CW blocker.

2.7 Conclusion

This chapter demonstrates a wideband RX in 40 nm bulk CMOS technology for 5G TDD user equipment applications. The proposed programmable zeros and the adopted second-order TIA increase the selectivity of the proposed RX and satisfy the 5G stringent linearity requirements for close-in blockers. Moreover, an auxiliary path is introduced to sink the blocker current, improving the far-out linearity performance of the proposed RX. Two design guides are provided to determine the components' values of the proposed RX RF front-end and the second-order TIA. The proposed RX could successfully satisfy the requirements of the 5G TDD user equipment application for reference sensitivity and out-of-band blocking tests.

Table 2.1: Performance Summary And Comparison With State-Of-The-Art RXs.

	This Work	This Work	Murphy	Hedayati	Musayev	Wang	Razavi	Kim	Guo
	Respin Prototype	ISSCC 2021 [88]	JSSC 2012 [21]	JSSC 2015 [97]	JSSC 2019 [98]	JSSC 2021 [79]	JSSC 2022 [81]	OJSSC 2022 [87]	RFIC 2023 [45]
Technology	40nm CMOS	40 nm CMOS	40nm CMOS	40nm CMOS	65nm CMOS	45nm SOI	28nm	65nm CMOS	65nm CMOS
f_{RF} (GHz)	0.5 – 3.0	0.4 – 3.2	0.09 – 2.7	0.1 – 2.8	0.7 – 1.4	0.2 – 2	0.4 – 6	1.6 – 2.2	1 – 3
Gain (dB)	37	36	72	50	36.8	40	54	23.2	40
NF (dB)	2.6 – 4.2	2.7 – 3.6	1.9	1.8	1.9	2.1 - 2.5	2.1†/4.42§	2.5	2.2
BW_{RF} (MHz)	160	160	6	10	30	20	0.2 - 160	80	850
LO Leakage (dBm)	-94 – -66	-86 – -69	-65	-82	NA	-94 – -79	NA	NA	NA
In-band Flatness	Yes	Yes	No	No	No	No	No	No	Yes
Out-of-band IIP3 (dBm)	16.5 $\Delta f/BW_{RF}$ = 1.5	10 $\Delta f/BW_{RF}$ = 1.5	13.5 $\Delta f/BW_{RF}$ = 3.3	5 $\Delta f/BW_{RF}$ = 5	1	14 $\Delta f/BW_{RF}$ = 5	3§ $\Delta f/BW_{RF}$ = 12.5	26.1 $\Delta f/BW_{RF}$ = 1.5	8 $\Delta f/BW_{RF}$ = 2.5
B1dB (dBm)	-2.7 $\Delta f/BW_{RF}$ = 2.5	-5 $\Delta f/BW_{RF}$ = 2.5	-2 $\Delta f/BW_{RF}$ = 13.3	NA	-8.5	NA	NA	0.5	NA
Out-of-band IIP2 (dBm)	64 $\Delta f/BW_{RF}$ = 1.5	50 $\Delta f/BW_{RF}$ = 1.5	55 $\Delta f/BW_{RF}$ = 3.3	50 $\Delta f/BW_{RF}$ = 5	35	60 $\Delta f/BW_{RF}$ = 5	20§ $\Delta f/BW_{RF}$ = 12.5	71 $\Delta f/BW_{RF}$ = 2.5	NA
0 dBm BNF (dB)	10.2 $\Delta f/BW_{RF}$ = 3.1	8.4 $\Delta f/BW_{RF}$ = 3.1	4.1 $\Delta f/BW_{RF}$ = 13.3	14 $\Delta f/BW_{RF}$ = 5	6.6	6.7 $\Delta f/BW_{RF}$ =4	5.2†/7.4§	5.9	3.6 $\Delta f/BW_{RF}$ = 1.5
EVM wo/wi blocker	-29 / -27.1&	-26.4 / -25.5£	NA	NA	NA	NA	-25.3¢ / NA	NA	NA
Supply (V)	1.3	1.3/1.2	1.3	1.1	0.8/1/1.2	1.2	1	0.4/1.2/2.5	1.2
Active Area (mm^2)	0.5	0.6	1.2	0.8	0.25	1.05	1.9	0.33	0.5
Power (mW)	72.8 + 22.5 mW/GHz	58.5 + 17.6 mW/GHz	35.1 – 78	27 – 40	14 + 37.2 mW/GHz	68 – 95	23 – 49	6.5 + 18.5 mW/GHz	44 + 14 mW/GHz

& 100 MS/s -60 dBm QAM-64 with -5 dBm blocker, £ 143 MS/s -60 dBm QAM-64 with -8 dBm blocker, † Low noise mode, § Harmonic Reject, $ Highest bandwidth, ¢ 80 MS/s -57 dBm QAM-64

2

CHAPTER

3

A Highly-Linear Receiver Using Parallel Preselect Filter for 5G Microcell Base Station Applications

3.1 Introduction

The advent of 5G mobile communication has introduced new challenges for base station RXs operating in the sub-6 GHz spectrum. The RX must support up to 200 MHz BW_{RF} while facing a close-in out-of-band blocker with -15 dBm power, located just 20 MHz from the bandwidth edge. Additionally, the RX must handle far-out out-of-band blockers with +8 dBm power in co-location scenarios. These blocking requirements are significantly more stringent than those in 5G user equipment applications. Although introducing zeros into the LNTA's transfer function is a promising technique for user equipment applications, it does not provide sufficient attenuation for the close-in blockers present in 5G base station applications. Furthermore, the base station RXs must have a higher B1dB than that of user equipment to avoid desensitization due to the +8 dBm blockers of co-location applications.

This chapter is written based on CICC 2022 [99] and JSSC 2023 [100] papers.

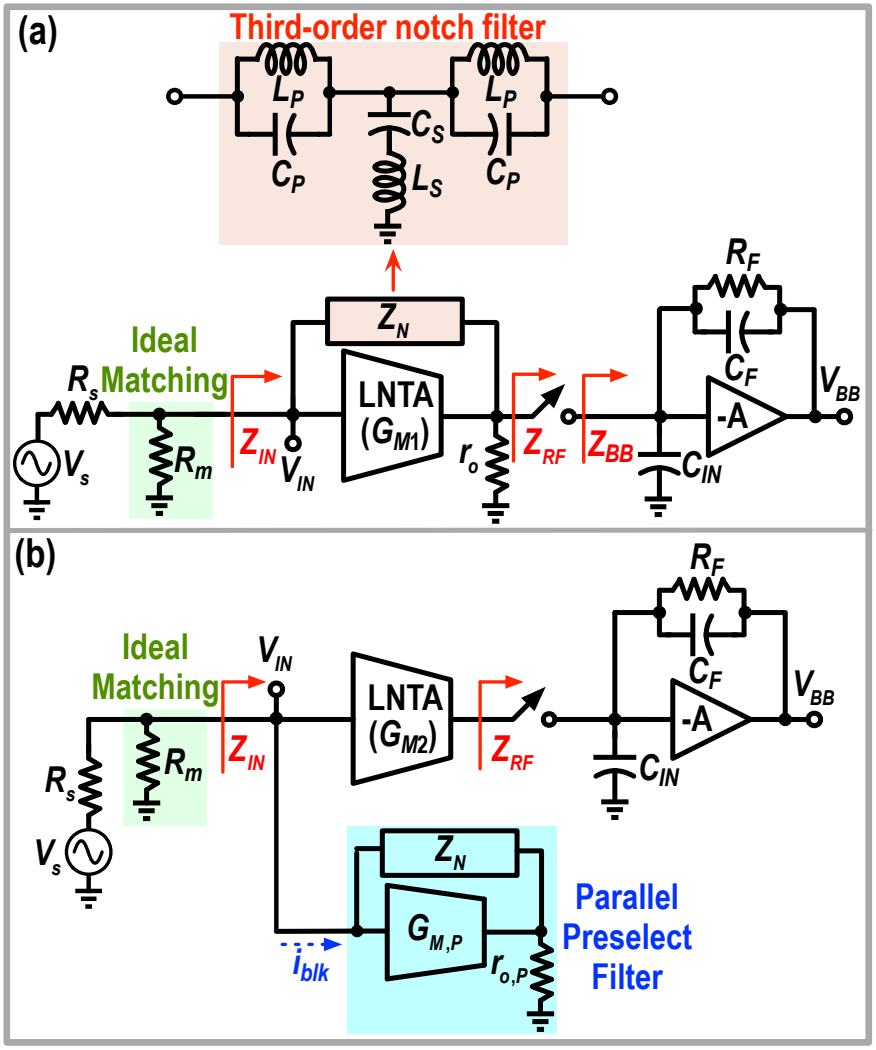

Figure 3.1: (a) Conventional LNTA-based structure to achieve RF selectivity [64,71,73–75,78–80,85]; (b) proposed RX with a parallel preselect filter.

To solve these issues, an LNTA-based RX prototype is proposed in this Chapter that shows similar out-of-band linearity as prior art mixer first RXs without sacrificing NF. Firstly, a parallel preselect filter is placed at the input of the RX to improve the RF selectivity and achieve B1dB better than +5 dBm. Secondly, we propose a third-order RF and baseband filtering to achieve -120 dB/dec selectivity. Finally, a translational feedback network is introduced to reduce the in-band gain fluctuations to below 0.5 dB. The rest of this Chapter is organized as follows: Section 3.2 discusses the proposed RX structure with a parallel preselect filter. Section 3.3 describes the feedback network and the theory behind it. Circuit implementation is elaborated in Section 3.4, followed by noise analysis in Section 3.5. Measurement results are shown in Section 3.6,

and Section 3.7 concludes the Chapter.

3.2 Proposed RX Structure

Fig. 3.1 (a) shows a simplified block diagram of a conventional current-mode RX in which LNTA converts the RF input voltage to an RF current. Passive mixers down-convert the LNTA's RF current, and the transimpedance amplifier (TIA) eventually converts it into a BB voltage. For simplicity, as shown in Fig. 3.1 (a), the input matching is provided by an ideal 50 Ω shunt resistor (R_m) at the RX input. Moreover, a notch filter is placed in the feedback of the LNTA to provide RF selectivity in conventional LNTA-based RXs [64, 71, 73–75, 78–80, 85]. Through the Miller theorem, the RX's input impedance can be calculated by

$$Z_{IN} = \frac{1}{G_{M1}} + \frac{Z_N}{1 + G_{M1} Z_L}, Z_L = r_{o1} \parallel Z_{RF}, \tag{3.1}$$

where Z_N is the equivalent impedance of the notch filter. Furthermore, G_{M1} and r_{o1} denote the transconductance and output resistance of the LNTA, and Z_{RF} is the impedance seen from the input port of the passive mixers (see Fig. 3.1 (a)). Transparency of the passive mixers up-converts the TIA's low-pass input impedance to a band-pass impedance at RF frequencies. Based on the method presented [13], the up-converted BB impedance can be approximated as

$$Z_{RF} \approx R_{ON} + \frac{Z_{BB}(\omega - \omega_{LO})}{M}, \tag{3.2}$$

where Z_{BB} is the input impedance of the TIA, ω_{LO} is the LO frequency, and M is the number of non-overlapping LO phases. In current-mode RXs, Z_{RF} usually has a small value to sink the RF current of the LNTA (i.e., $Z_{RF} \ll r_{o1}$). Hence, the LNTA's voltage gain can be approximated by $G_M Z_{RF}$. In other words, TIA's low input impedance loads LNTA, thus, reducing the voltage swing at the LNTA's output which improves the in-band linearity of the RX.

Note that the second term in (3.1) is frequency-dependent and defines the transition slope from the in-band frequencies to the out-of-band frequencies. Around the operating frequency, the notch filter is open; thus, the LNTA current is absorbed by the TIA. However, the notch filter shorts the LNTA's input and output ports at high offset frequencies, improving the RX's out-of-band linearity. Hence, the filtering order of the notch filter is directly seen at the input impedance of the RX.

As mentioned earlier, sharp filtering is required to attenuate the -15 dBm

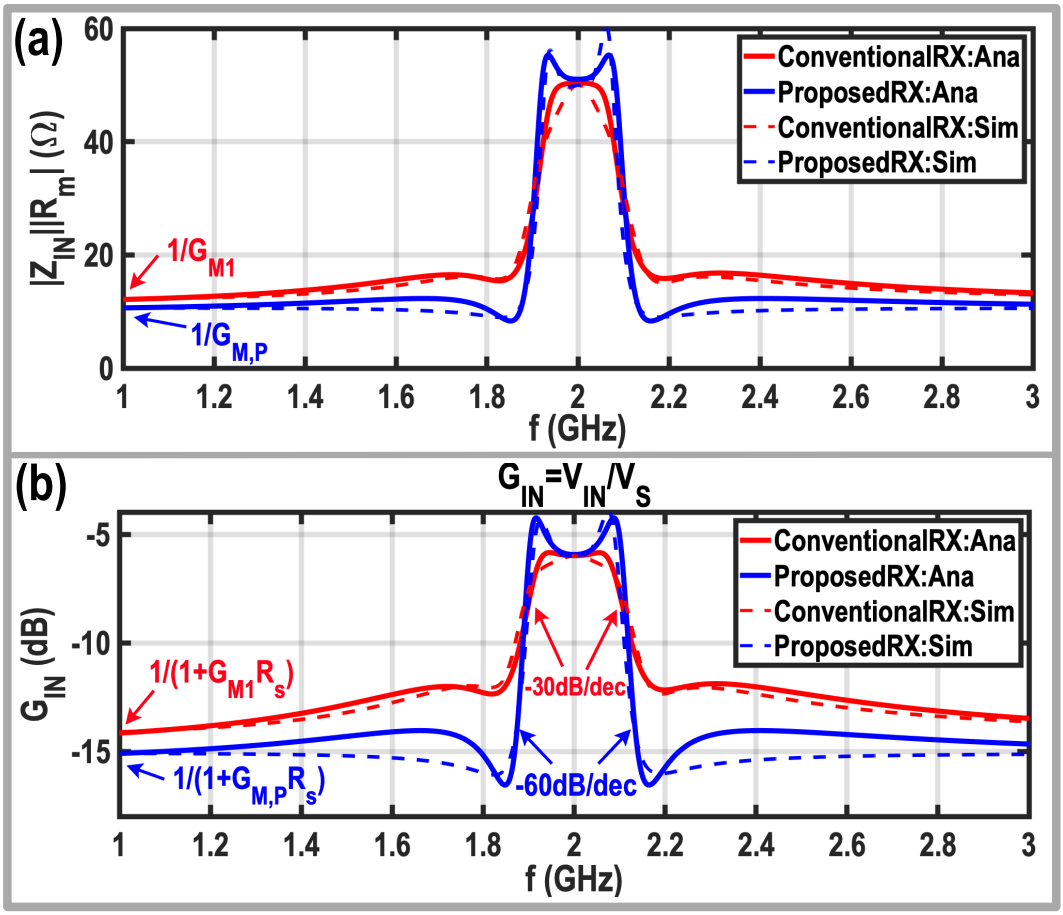

Figure 3.2: Comparison between the analytical and simulation results of (a) $Z_{IN} \parallel R_m$ and (b) G_{IN} of the conventional and proposed RX when Z_N is an LC-based third-order notch filter.

close-in blocker in the base station applications. To improve the RF selectivity, one can increase the notch-filter order. However, when Z_N is replaced with an ideal LC-based third-order notch filter (see Fig. 3.1 (a)), the simulated transfer functions of the input voltage gain G_{IN} and $Z_{IN} \parallel R_m$ are not optimal, as their roll-offs are smaller than the ideal -60 dB/dec, as can be gathered from Fig. 3.2 (a) and (b). The reason behind this degradation can be intuitively explained as follows. The load of the LNTA, Z_{RF}, has a bandpass shape, and the LNTA's voltage gain drops with a -20 dB/dec slope. Hence, the effective filtering shape and slope at the RX's input are corrupted by the notch filter interaction with the LNTA's voltage gain at out-of-band frequencies. In order to solve this issue, we need to exempt the LNTA from RF filtering at the RX input by removing the notch filter from its feedback at the cost of lower far-out blocker rejection at the LNTA's output. Then, RF filtering should be achieved using another technique.

3.2.1 Parallel Preselect Filter

A preselect filter can be adopted to improve the RF selectivity of the LNTA-based RXs. The preselect filter can be placed in series [22, 23], or parallel [68] with the RX input. The series implementation degrades the NF of the entire receive chain. Unlike series preselect filters [22, 23], the parallel preselect filter can be turned off to reduce power consumption and improve the NF in the absence of blockers. An N-path filter can serve as a parallel preselect filter [68]. However, the filtering order of the N-path filter is only first-order [68], and the amount of attenuation for the close-in blockers of the base station application is negligible. High-order mixer-first RXs [59–62] can also be used in parallel with the RX input to provide RF filtering. However, mixer-first RXs require a large input capacitor at the TIAs' inputs to sink the blocker current and improve the out-of-band linearity, thus, substantially increasing chip area. Moreover, at far-out offset frequencies, the input impedance of the RX is related to the R_{ON} of the switches. Hence, large switches are required to provide enough filtering for the large blockers of the co-location applications, demanding high dynamic power consumption.

In order to solve the issues mentioned above, we propose adding a high-order parallel preselect filter at the RX input. As depicted in Fig. 3.1 (b), the parallel preselect filter comprises a transconductance stage and a notch filter. Now, the RX's input impedance can be rewritten as

$$Z_{IN} = \frac{1}{G_{M,P}} + \frac{Z_N}{1 + G_{M,P} r_{o,P}}, \tag{3.3}$$

where $G_{M,P}$ and $r_{o,P}$ are, respectively, the transconductance and the output resistance of the parallel preselect filter. As can be deduced from (3.3), the voltage gain of the parallel preselect filter is constant over frequency, and the frequency-dependent part of the RX's input impedance is only related to Z_N. Hence, if one replaces Z_N with the same LC-based third-order notch filter, the RF selectivity at the RX's input will be third-order (see the simulation results in Fig. 3.2 (a) and (b)). The parallel preselect filter plays two roles in the proposed RX structure. First, it provides sharp filtering at the RX input to attenuate close-in blockers. At far-out frequencies, since the notch filter is short, the input impedance of the RX becomes $1/G_{M,P}$. Hence, its second task is to sink the blocker current at far-out offset frequencies, thus relaxing the LNTA linearity requirements (see Fig. 3.1 (b)). Compared to the case of using high-order mixer-first RXs [59–62] as the parallel preselect filter, the

far-out input impedance of the proposed RX is reduced by raising the dc power consumption of the transconductance stage (i.e., via increasing $G_{M,P}$) instead of consuming more dynamic power in LO buffers to drive enormous low-R_{ON} switches. Moreover, the proposed structure does not need any baseband TIAs. Consequently, depending on the technology node, for the same amount of far-out input impedance and filtering order, the proposed parallel preselect filter would be more power efficient, especially at higher operating frequencies and bandwidths.

It is instructive to compare the performance of the conventional RX in Fig. 3.1 (a) and the proposed RX in Fig. 3.1 (b) when they consume the same power in the front-end components (i.e., $G_{M1} = 2G_M$, $G_{M2} = G_M$, and $G_{M,P} = G_M$) and exhibit the same in-band gain and linearity. The conventional RX would offer a lower noise figure since the front-end noise factor increases from $1/(2G_M R_s)$ to $1/(G_M R_s)$ for the proposed structure, as quantified in Section 3.5. The conventional RX would also show a higher out-of-band linearity for far-out blockers, since its input impedance would be 2× lower at far-out frequencies, as can be gathered from the first terms in (3.1) and (3.3). However, the values of mixers' on-resistance and TIA feedback resistor, R_F, in the conventional RX must be 2× lower to show the same in-band gain and linearity compared to the proposed RX. This demands 2× more power consumption for driving the main mixers, and occupying a 2× larger area for implementing TIA's feedback capacitance, C_F, to keep the RX bandwidth the same. More importantly, as discussed in the previous paragraph and can be gathered from Fig. 3.2 (a) and (b), the proposed RX maintains the filtering shape and slope and offers much better out-of-band linearity for the close-in blockers, making it more suitable for our application.

3.2.2 Implementation of the Parallel Preselect Filter

The next step is to realize Z_N with a tunable third-order notch filter. We propose to employ a third-order high-pass filter and translate its impedance to RF frequency using the transparency of the passive mixers, as shown in Fig. 3.3 (a). The third-order high-pass filter mainly comprises two series capacitors (C_H) and one shunt inductor (L_H).

When the switches of one of the high-pass filter branches are ON, a current proportional to the out-of-band blockers flows through the corresponding inductor. However, when the switches are turned off, the inductor current cannot abruptly go to zero; thus, a parallel capacitance, C_P, is intentionally

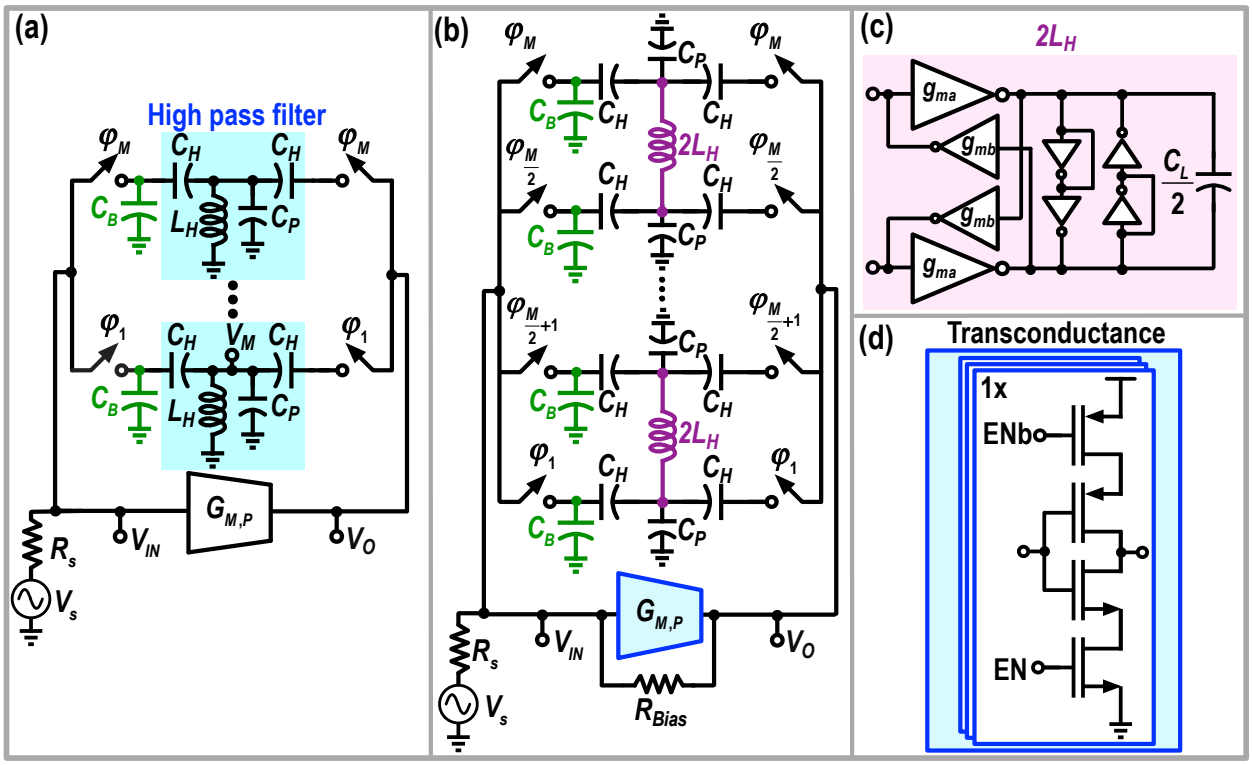

Figure 3.3: (a) Initial schematic and (b) final implementation of the proposed parallel preselect filter using impedance up-conversion of a third-order high-pass filter; (c) implementation of the BB inductor using active gyrator; (d) schematic of the parallel preselect filter's transconductance.

added to provide a return path for the inductor current. To solve this problem while maintaining the filtering shape and order, C_P and L_H must resonate at a frequency higher than the desired BB bandwidth, but lower than the minimum LO frequency. In the presence of large blockers at far-out frequencies, a large voltage appears at the BB port of the switches, disrupting the parallel preselect filter operation due to switch failures. Consequently, as shown in Fig. 3.3 (a), M shunt capacitors (C_B) are added at the source terminal of the switches to further attenuate the far-out blockers at those nodes, thus improving the out-of-band B1dB without affecting the parallel preselect filter bandwidth and roll-off.

Fig. 3.3 (b) shows the final implementation of the parallel preselect filter. To implement the BB inductors, the ground ports of the inductors which driven by 180° out-of-phase clocks (i.e., j_i and $j_{i+M/2}$ where $i = 1...M/2$) are connected, and then they are replaced with one inductor. As shown in Fig. 3.3 (c), the resulting inductor can be easily realized using a gyrator with a load capacitor. This way, C_P is implicitly realized by the gyrator's parasitic capacitance. The same bias circuit as in [101] is also used to keep the common-mode voltage of the gyrator's input and output nodes around $V_{DD}/2$.

The transconductance of the parallel preselect filter is implemented using an inverter (see Fig. 3.3 (d)). The inverter is sliced into three parts for measurement purposes and can be controlled through a serial peripheral interface (SPI). As illustrated in Fig. 3.3 (b), a bias resistor (R_{Bias}) is placed in the transconductance feedback to bias the inverter around $V_{DD}/2$.

3.2.3 Design Guide for the Parallel Preselect Filter

This section develops a general design guide for determining the values of different components (i.e., $G_{M,P}$, R_{ON}, C_H, and L_H) of the proposed preselect filter based on high-level system specifications, such as the required 3-dB bandwidth (ω_{3dB}) and B1dB, and some circuit-level constraints like the main RX input 1-dB compression voltage for out-of-band blockers ($V_{IN,B}$) and the transconductance output 1-dB compression voltage ($V_{O,B}$). In this analysis, we assume that the main RX provides the input matching; the notch filter does not load the transconductance around ω_{LO}; and the effect of C_P and C_B on ω_{3dB} is negligible.

The design guide starts with $G_{M,P}$ estimation. At far-out frequencies, the preselect filter's input impedance is approximately $1/G_{M,P}$, and consequently, the transconductance's input voltage can be calculated by

$$V_{IN} = \frac{V_{s,B}}{1 + G_{M,P}R_s}, \tag{3.4}$$

where $V_{s,B}$ is the co-location blocker voltage, estimated by

$$V_{s,B} = \sqrt{8R_s \times 10^{\frac{B1dB}{10}}}. \tag{3.5}$$

In order to tolerate the co-location blocker, we need to satisfy $V_{IN} \leq V_{IN,B}$, hence,

$$G_{M,P} \geq \frac{1}{R_s}\left(\frac{\sqrt{8R_s \times 10^{\frac{B1dB}{10}}}}{V_{IN,B}} - 1\right). \tag{3.6}$$

Considering B1dB $= +8$ dBm and $V_{IN,B} = 0.26$ V (see Fig. 3.4 (a)), the required $G_{M,P}$ to satisfy this blocker is $\sim$105 mS.

At high offset frequencies from ω_{LO}, C_H and L_H exhibit very low and high impedance, respectively. Thus, the voltage gain of the transconductance can be estimated by $2R_{ON}G_{M,P} - 1$. In order to tolerate the co-location blocker voltage

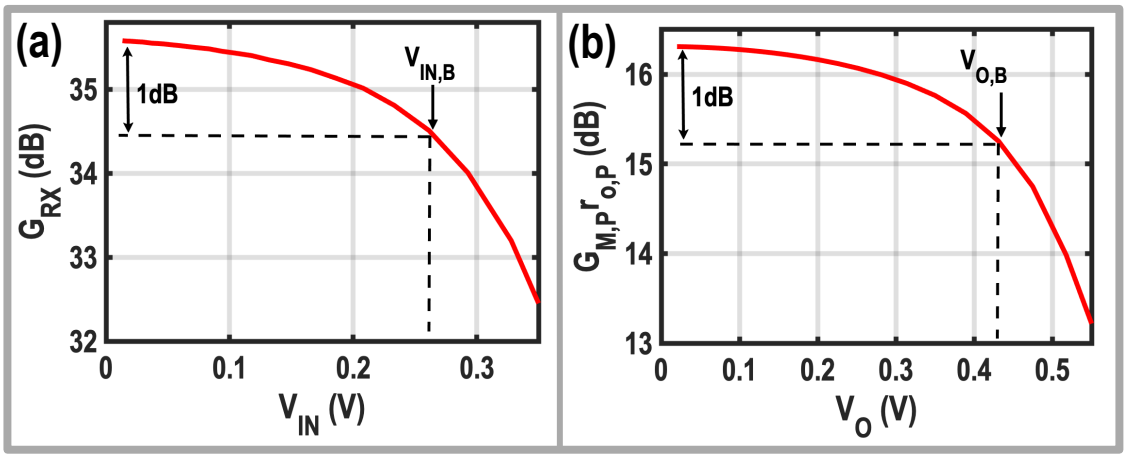

Figure 3.4: (a) Simulated main RX gain versus the input voltage created by an out-of-band blocker; (b) simulated transconductance gain versus its output voltage swing.

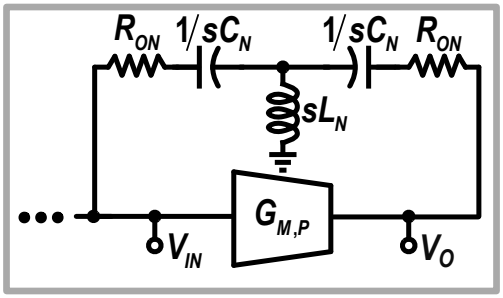

Figure 3.5: Simplified model of the parallel preselect filter.

at the output of the preselect filter, the following condition must be satisfied:

$$R_{ON} \leq \frac{1}{2G_{M,P}} \times \left(\frac{V_{O,B}(1 + G_{M,P}R_S)}{\sqrt{8R_S \times 10^{\frac{B1dB}{10}}}} + 1 \right) \tag{3.7}$$

Considering $V_{O,B} = 0.43\,\mathrm{V}$ (see the simulation result in Fig. 3.4 (b)), the maximum value of R_{ON} should be $12.5\,\Omega$ to satisfy the required B1dB of the 3GPP applications.

Since the passive mixers up-convert BB impedances to the RF frequencies, the parallel preselect filter in Fig. 3.3 (a) can be modeled with the circuit depicted in Fig. 3.5. Using the same method presented in [13], the third-order high-pass filters are replaced with $1/sC_N$ and sL_N, where $s = j(\omega - \omega_{LO})$ and C_N and L_N can be calculated by

$$C_N \approx \frac{M.C_H}{sinc^2\left(\frac{\pi}{M}\right)}, \tag{3.8}$$

$$L_N \approx sinc^2\left(\frac{\pi}{M}\right)\frac{L_H}{M}. \tag{3.9}$$

The next step is calculating C_H and L_H based on the ω_{3dB} requirement of the 5G applications. In this regard, the input transfer function at the RX input is derived as

$$G_{IN} = \frac{1}{2}\frac{2\frac{s^2}{\omega_N^2}+1}{\frac{s^3}{\omega_N^2\omega_P}+2\frac{s^2}{\omega_N^2}+\frac{s}{(1+G_{M,P}r_{O,P})\omega_P}+1}, \tag{3.10}$$

where ω_N and ω_P are $1/\sqrt{L_N C_N}$ and $2/(R_S C_N(1+G_{M,P}r_{o,P}))$, respectively. Note that the effect of passive mixers' R_{ON} is neglected in this calculation.

As can be inferred from (3.10), G_{IN} has two zeros at $\pm\omega_N/\sqrt{2}$ and two complex conjugate poles and one real pole created by the miller effect of C_N and $R_s/2$. Mathematical derivations lead to the following estimate for the 3-dB bandwidth

$$\omega_{3dB} = \omega_P\left|\frac{1-\frac{2}{\gamma^2}}{\frac{1}{\gamma^2}-\frac{1}{1+G_{M,P}r_{o,P}}}\right| \approx \omega_P\left(\gamma^2-2\right), \tag{3.11}$$

where $\gamma = \omega_N/\omega_{3dB}$. Since the frequency of the zeros should lie outside the ω_{3dB}, the minimum value of γ is $\sqrt{2}$. As can be gathered from (3.10), if a much larger value for γ is chosen, ω_{3dB} will mainly be defined by $(1+G_{M,P}r_{o,P})\,\omega_P$. This means that L_N shorts the middle point of the notch filter to the ground even after ω_{3dB}, and the transfer function relies on the real pole created by C_N and $R_s/2$. Hence, the filtering slope at the RX input becomes first-order, and the benefit of the proposed structure diminishes. On the contrary, choosing a value close to $\sqrt{2}$ for the γ pushes the zeros towards ω_{3dB}, creating stability issues.

By substituting ω_P in (3.11), the values C_N and L_N may be calculated by

$$C_N = \frac{2\left(\gamma^2-2\right)}{\omega_{3dB}\left(1+G_{M,P}r_{o,P}\right)R_s}, \tag{3.12}$$

$$L_N = \frac{1}{\gamma^2\omega_{3dB}^2 C_N}. \tag{3.13}$$

Finally, one can determine the values of the C_H and L_H from (3.8) and (3.9). As a design example, by choosing $\gamma = 1.8$, $\omega_{3dB} = 200\,\text{MHz}$, $\text{M} = 8$, and an intrinsic gain of 6.5 for the transconductance, the calculated values of the C_H and L_H are 2.2 pF and 350 nH, respectively. Similar values for C_H and L_H are used in the final implementation of the parallel preselect filter.

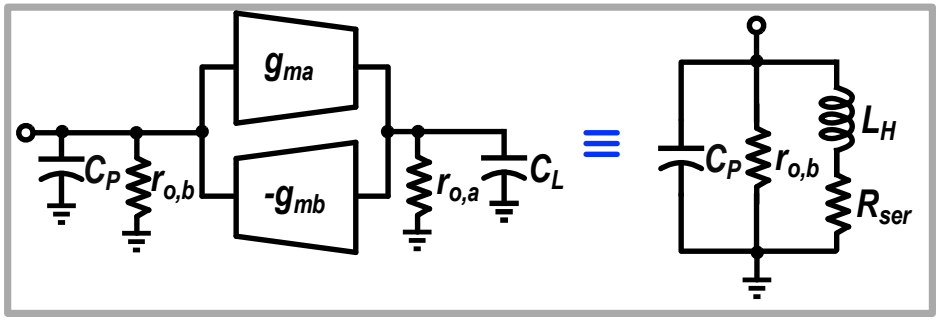

Figure 3.6: Gyrator schematic with its equivalent lumped-element model.

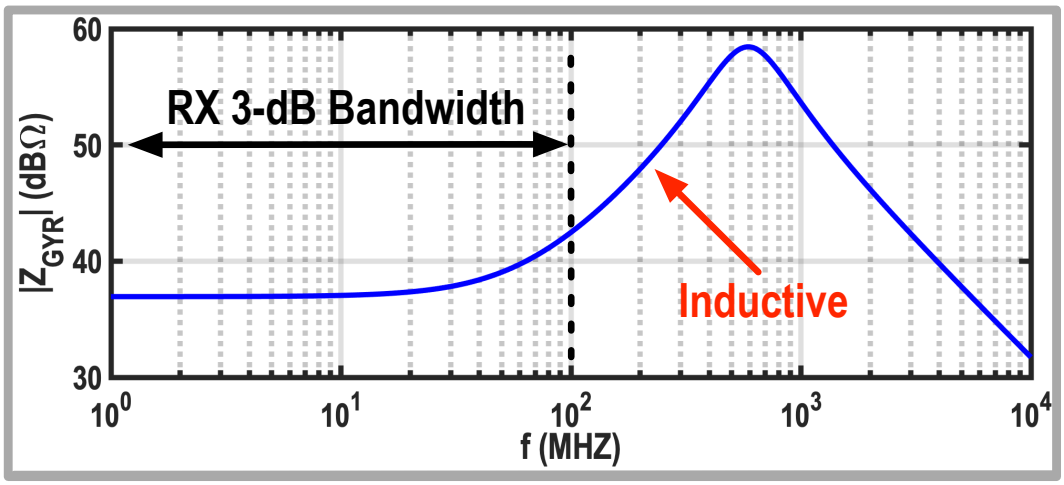

Figure 3.7: Simulated input impedance of the implemented gyrator.

After determining L_H, the design guide concludes by investigating the trade-offs in the L_H implementation using a gyrator with a load capacitor of $C_L/2$ (see Fig. 3.3 (c)). Fig. 3.6 shows the single-ended gyrator schematic with its equivalent lumped-element model. The gyrator is realized by a feedforward ($g_{m,a}$) and a return ($g_{m,b}$) transconductance with an output resistance of $r_{o,a}$ and $r_{o,b}$, respectively. In this model, C_P is the total parasitic capacitor at the gyrator input, dominated by $g_{m,a}$ input capacitor. As can be gathered from the lumped-element model and the simulation result in Fig. 3.7, the gyrator's input impedance at low frequencies is limited by an undesired series resistance, estimated by

$$R_{ser} = \frac{1}{g_{m,a} r_{o,a} g_{m,b}} \tag{3.14}$$

In order to minimize R_{ser}, the intrinsic gain of the $g_{m,a}$ and the value of $g_{m,b}$ should be maximized. Hence, employing long-channel devices for $g_{m,a}$ implementation and the minimum channel length transistors for $g_{m,b}$ realization is beneficial.

Beyond a cut-off frequency of $\omega_{ser} = R_{ser}/L_H$, the gyrator's input impedance becomes inductive with a value of

$$L_H = \frac{C_L}{g_{m,a}g_{m,b}}. \tag{3.15}$$

Since the effect of gyrator noise on the RX NF is negligible, (3.15) suggests choosing smaller values for C_L, and $g_{m,a}$ to optimize the chip area and power consumption. Note that ω_{ser} should be safely smaller than ω_{3dB} to ensure sharp filtering order at the RX input, resulting in a required minimum output resistance for the feedforward transconductance,

$$r_{o,a} = \frac{1}{C_L\omega_{3dB}}. \tag{3.16}$$

L_H eventually resonates with C_P at a self-resonance frequency of

$$\omega_{SRF} = \frac{1}{\sqrt{C_P L_H}}, \tag{3.17}$$

Beyond ω_{SRF}, the gyrator's input impedance becomes capacitive, and the filtering slope drops dramatically, as will be demonstrated in the measurement results. This means to maintain the filtering order over a wider frequency range, C_P must be minimized by realizing $g_{m,a}$ with the minimum channel length transistors. However, according to (3.14), this will increase R_{ser}, affecting the filtering shape at the passband edges. Consequently, there is a trade-off between R_{ser} and gyrator bandwidth.

3.3 Translational Feedback Network

3.3.1 Input Matching in Current-Mode RXs

In voltage-mode RXs, a resistor with a value of $R_s \times G_{LNA}$ (G_{LNA}: LNA's voltage gain) is usually placed in the LNA feedback to provide the input matching [64]. However, since the LNTA gain is small in current-mode RXs, and the feedback resistor must be significantly reduced, thus degrading the RX's NF. To decouple input matching from the LNTA's gain, as highlighted in purple shown in Fig. 3.8 (a), a translational feedback network [65–67] is adopted here by up-converting BB signals at TIAs' outputs and feeding them back to the RX input through a matching resistor (R_m) and an ac coupling capacitor (C_m). Due to the effective use of the RX voltage gain (A_0), the R_m value increases to $R_s \times A_0$, thus contributing negligibly to the RX's NF. Note that A_0 has a

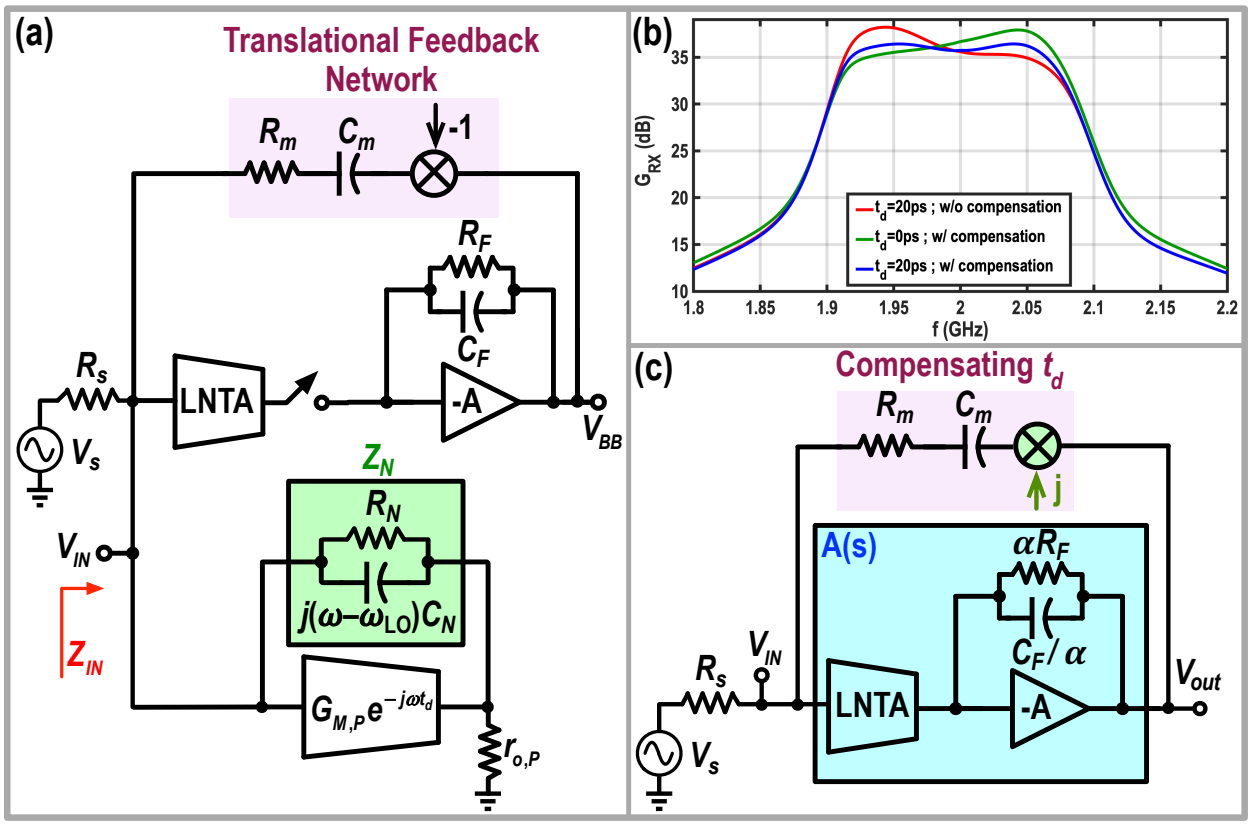

Figure 3.8: (a) Simplified block diagram of the proposed RX with a conventional translation loop for providing the input matching (for the sake of simplicity, Z_N is replaced by a first-order notch filter); (b) simulated G_{RX} in different scenarios; (c) Simplified block diagram of the main RX path with the proposed translational feedback network for compensating the side effects of parallel preselect filter delay.

positive sign; thus, a -1 multiplication is required in the translational feedback network to avoid positive feedback.

3.3.2 Delay of the Transconductance

In the preselect filter, the transconductance stage has a delay, which introduces an undesired phase shift in the current passing through the notch filter, thus changing the input impedance at the passband edges in opposite directions and creating a negative center frequency shift and a gain peaking at the lower edge of the passband, as shown in Fig. 3.8 (b). To analyze this phenomenon without any loss of generality, we assume that the notch filter is a simple first-order notch filter composed of an up-converted capacitor and a parallel resistor (i.e., $j(\omega - \omega_{LO})C_N$ and R_N in Fig. 3.8 (a)). In this simplified

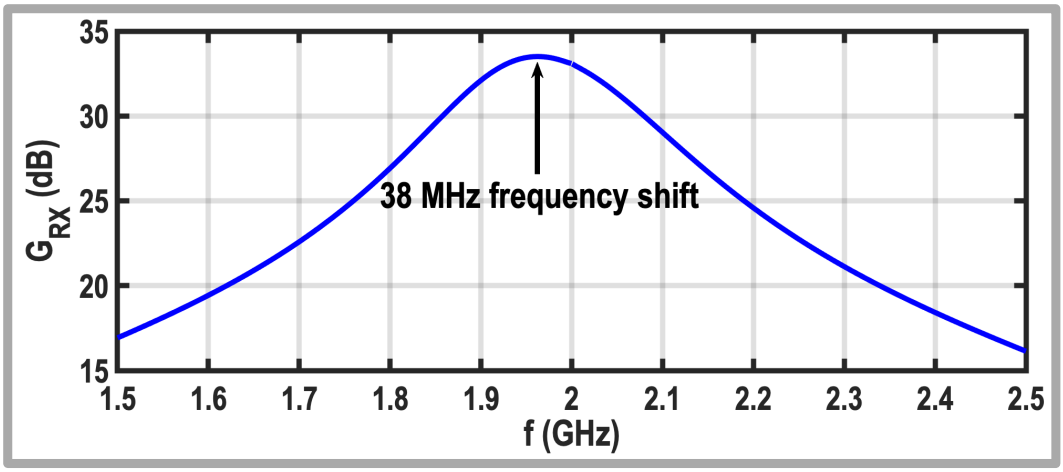

Figure 3.9: Simulated gain of Fig 3.8 (a) receiver with $G_{M,P}r_{o,P}=6$, $R_S = 50\,\Omega$, $C_N = 8\,\text{pF}$, $t_d = 20\,\text{ps}$, and $f_{LO} = 2\,\text{GHz}$.

case, the transfer function at the RX input is $G_{IN} = Z_{IN}/(Z_{IN} + R_S)$, in which

$$Z_{IN} \approx R_s \parallel \frac{Z_N}{G_{M,P}r_{o,P}} \times e^{j\omega t_d}, \tag{3.18}$$

and t_d is the delay of the transconductance. In the derivation of (3.18), it is assumed that the input impedance of the parallel preselect filter is the Miller effect of Z_N, and the voltage gain of the parallel preselect filter, $G_{M,P}r_{o,P}$, is much higher than one. By setting $d|G_{IN}|^2/d\omega = 0$, the shifted center frequency can be derived by

$$\omega_{peak,n} \approx \omega_{LO}\left(1 - \frac{2t_d}{G_{m,P}r_{o,P}R_sC_N}\right) \approx \omega_{LO}\left(1 - \frac{\omega_{3dB}t_d}{2}\right). \tag{3.19}$$

As indicated in (3.19), the amount of the frequency shift is much more severe in high bandwidth applications, such as 5G. For example, with $G_{M,P}r_{o,P} = 6$, $R_S = 50\,\Omega$, $C_N = 8\,\text{pF}$, $t_d = 20\,\text{ps}$, and $f_{LO} = 2\,\text{GHz}$, (3.19) estimates that the center frequency shifts to 1.967 GHz, while the simulation result in Fig. 3.9 shows that the center frequency lies at 1.962 GHz. Consequently, the simulation result is in good agreement with the presented calculations. To solve this issue, a polyphase notch filter has been proposed [70, 78], which requires M extra amplifiers to share the I and Q signals to compensate for the LNTA delay. However, these extra amplifiers should handle the large blockers in co-location applications, demanding substantial power consumption.

3.3.3 Proposed Translational Feedback Network

In order to compensate for the negative center frequency shift caused by the trans-conductance delay, we propose to intentionally realize a positive center frequency shift in the main RX path. Consequently, as shown in Fig. 3.8 (c), the "-1" multiplication is replaced with "j" multiplication in the translational loop to accomplish this goal. To calculate the induced frequency shift and for the sake of simplicity, the main RX path is modeled with a band-pass amplifier,

$$A\left(s\right)=\frac{A_0}{1+\frac{s}{\omega_{P1}}}\mid_{s=j(\omega-\omega_{LO})}, \tag{3.20}$$

where ω_{P1} is the dominant pole of the amplifier and equals to $1/(R_F C_F)$. Moreover, A_0 can be approximated by $\alpha G_M R_F$, in which α is $sinc^2\left(\pi/M\right)/M$ [102]. The amplifier has its maximum gain at ω_{LO}, and the gain drops with a first-order slope at out-of-band frequencies. The transfer function of the RX from the source (V_s) to the TIAs' outputs (V_{out}) can be derived as follows:

$$\frac{V_{out}}{V_s}=\frac{A_0}{1+\frac{\omega R_m C_m}{1+(\omega R_m C_m)^2}+j\left(\frac{\omega-\omega_{LO}}{\omega_{P1}}-\frac{(\omega R_m C_m)^2}{1+(\omega R_m C_m)^2}\right)}. \tag{3.21}$$

In the derivation of (3.21), R_m is assumed to be $(1+A_0)\times R_s$ to satisfy the input matching requirements. By setting $d|V_{out}/V_s|^2/d\omega=0$, the center frequency of the main RX path can be estimated by

$$\omega_{peak,p}\approx\omega_{LO}+\omega_{P1}\times\frac{\omega_{LO}^2 R_m^2 C_m^2}{1+\omega_{LO}^2 R_m^2 C_m^2}. \tag{3.22}$$

Consequently, the proposed technique shifts the passband center towards higher frequencies, and the amount of the frequency shift can be controlled by adjusting C_m without affecting other RX's characteristics. In the above analysis, it is assumed that the signal in the main RX path does not experience any delay for the sake of simplicity. As displayed in the green curve in Fig. 3.8 (b), when the preselect filter transconductance is replaced with an ideal component with no delay, the proposed translational loop changes the simulated RX transfer function by realizing a positive center frequency shift and a gain peaking at the upper edge of the passband. When the transconductance is implemented using real devices, the peak created by the translational feedback network cancels out the peak on the lower side, and a flat gain response can be achieved, as shown in the blue curve in Fig. 3.8 (b).

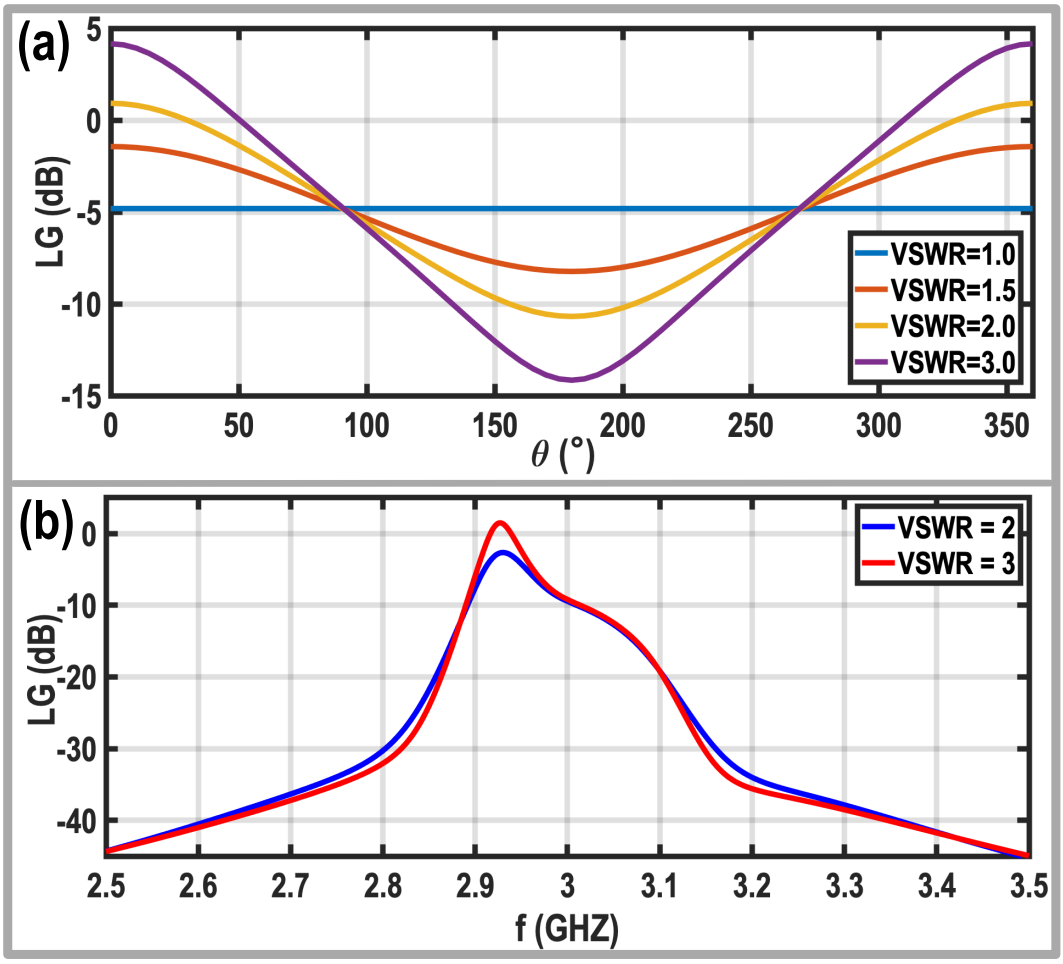

Figure 3.10: (a) Simulated loop gain versus the angle of the reflection coefficient for different VSWR values, using (3.23) and considering $f_{LO} = 3\,\text{GHz}$ and $C_m = 300\,\text{fF}$; (b) simulated loop gain of the implemented RX for VSWR = 2 ($Z_s = 100\,\Omega$) and 3 ($Z_s = 150\,\Omega$).

To ensure that the proposed translational loop does not sacrifice the receiver stability, the RX loop gain, LG, in the simplified model is calculated,

$$LG = \frac{jA_0 Z_s}{R_m + Z_s + \frac{1}{j\omega C_m}}, \tag{3.23}$$

where Z_s is the antenna source impedance. To satisfy the input matching, R_m should equal $(1 + A_0) \times 50\Omega$. Therefore, (3.23) can be simplified to

$$LG = \frac{jA_0 Z_s}{Z_s + 50 \times (1 + A_0) + \frac{1}{j\omega C_m}}. \tag{3.24}$$

When $Z_s = 50\,\Omega$, even in the worst-case scenario, in which the C_m impedance

becomes much smaller than R_m, the loop gain reaches $\frac{A_0}{2+A_0} < 1$, proving that the proposed translational network will not cause any stability issues. However, in practice, the antenna's impedance varies from its ideal value. Fig. 3.10 (a) shows the loop gain versus the angle of the reflection coefficient (θ) for different voltage standing wave ratios (VSWR), using (3.23) and considering $f_{LO} = 3\,\text{GHz}$ and $C_m = 300\,\text{fF}$. Based on (3.23) estimation, the loop gain exceeds one for $\text{VSWR} \geq 2$ at $\theta \approx 0$, where the antenna impedance is almost purely resistive and considerably larger than $50\,\Omega$. To verify the presented analysis, the loop gain of the entire RX chain is also simulated in Cadence using 'PSS' and 'PSTB', and the results are shown in Fig. 3.10 (b) for $\text{VSWR} = 2$ and 3. The loop gain of the RX chain is slightly lower than 0 dB, proving that the translational feedback network is stable for $\text{VSWR} \leq 2$.

3.3.4 Effect of RX Delay

This subsection recalculates the center frequency shift due to the proposed translational feedback loop by considering the delay of the main RX path, $t_{d,RX}$. The source of this delay mostly comes from the LNTA and the TIA's amplifier. Moreover, depending on the sign of the phase misalignment between the LOs of the main RX path and the translational feedback network, $t_{d,RX}$ slightly increases or decreases (for example, positive $t_{d,LO}$ increases $t_{d,RX}$ in Fig. 3.11 (a)). Taking the $t_{d,RX}$ into account, the main RX path can be modeled by a band-pass amplifier with a transfer function of

$$A(s) = \frac{A_0}{1 + \frac{s.e^{-j\omega t_{d,RX}}}{\omega_{P1}}} \Big|_{s=j(\omega-\omega_{LO})} . \tag{3.25}$$

The transfer function from the source to the output of the TIA can be derived using (3.25),

$$\frac{V_{out}}{V_s} = \frac{A_0}{D(\omega)}, \tag{3.26}$$

where $D(\omega)$ is given by

$$\begin{aligned} D(\omega) = 1 + \frac{\omega R_m C_m}{1 + (\omega R_m C_m)^2} + \sin(\omega t_{d,RX}) \times \frac{\omega - \omega_{LO}}{\omega_{P1}} \\ + j\left(\cos(\omega t_{d,RX}) \times \frac{\omega - \omega_{LO}}{\omega_{P1}} - \frac{(\omega R_m C_m)^2}{1 + (\omega R_m C_m)^2}\right). \end{aligned} \tag{3.27}$$

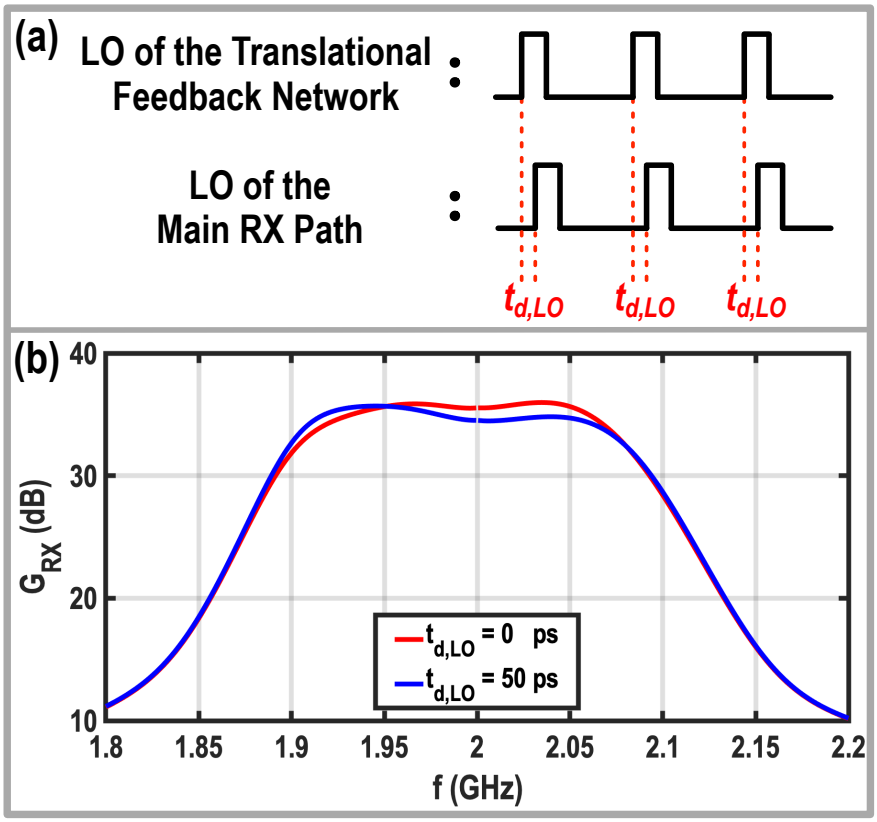

Figure 3.11: (a) Illustration of the phase misalignment between the LOs of the main RX path and the translational feedback network; (b) Simulated RX gain for different time shifts between the LOs of the main RX path and the translational feedback network.

By setting $d|V_{out}/V_s|^2/d\omega = 0$, the center frequency of the main RX path can be estimated by

$$\omega_{peak,p} = \frac{\omega_{LO} + \omega_{P1} \times \frac{(\omega R_m C_m)^2}{1+(\omega R_m C_m)^2}}{1 + t_{d,RX}\omega_{P1} \times \left(1 + \frac{\omega R_m C_m}{1+(\omega R_m C_m)^2}\right)}. \tag{3.28}$$

As can be gathered from (3.28), due to $t_{d,RX}$, the center frequency is shifted to lower frequencies than predicted by (3.22). This issue is also observed in the simulation results in Fig. 3.11 (b), in which adding a delay between the LOs of the main mixers and the translational feedback network creates a negative center frequency shift and a gain peaking at the lower edge of the passband. Hence, the value of C_m must be increased further to also compensate for the delay of the RX main path and the LO misalignment.

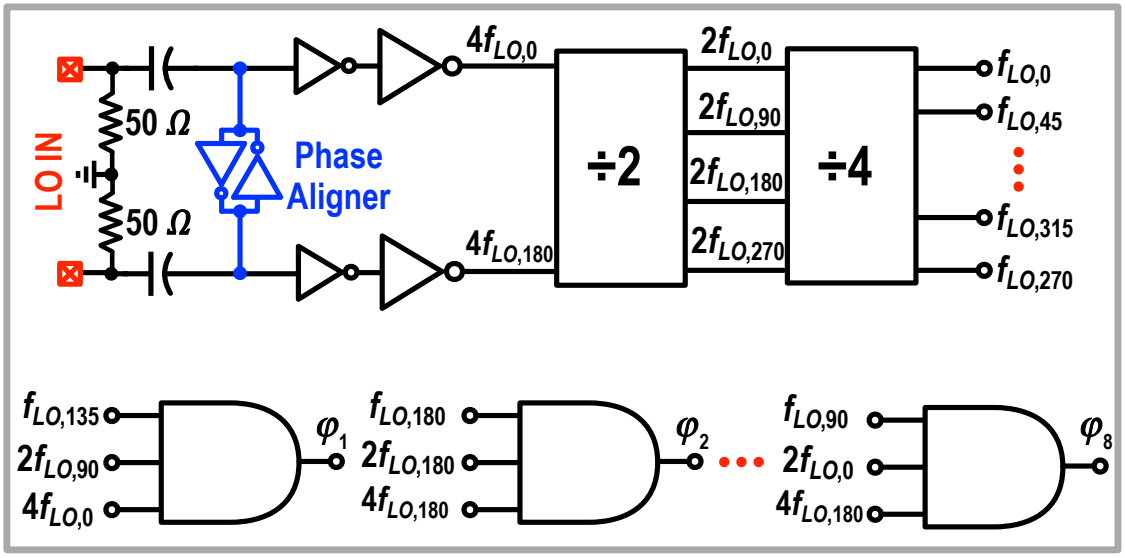

Figure 3.12: Block diagram of the LO generation circuit [70].

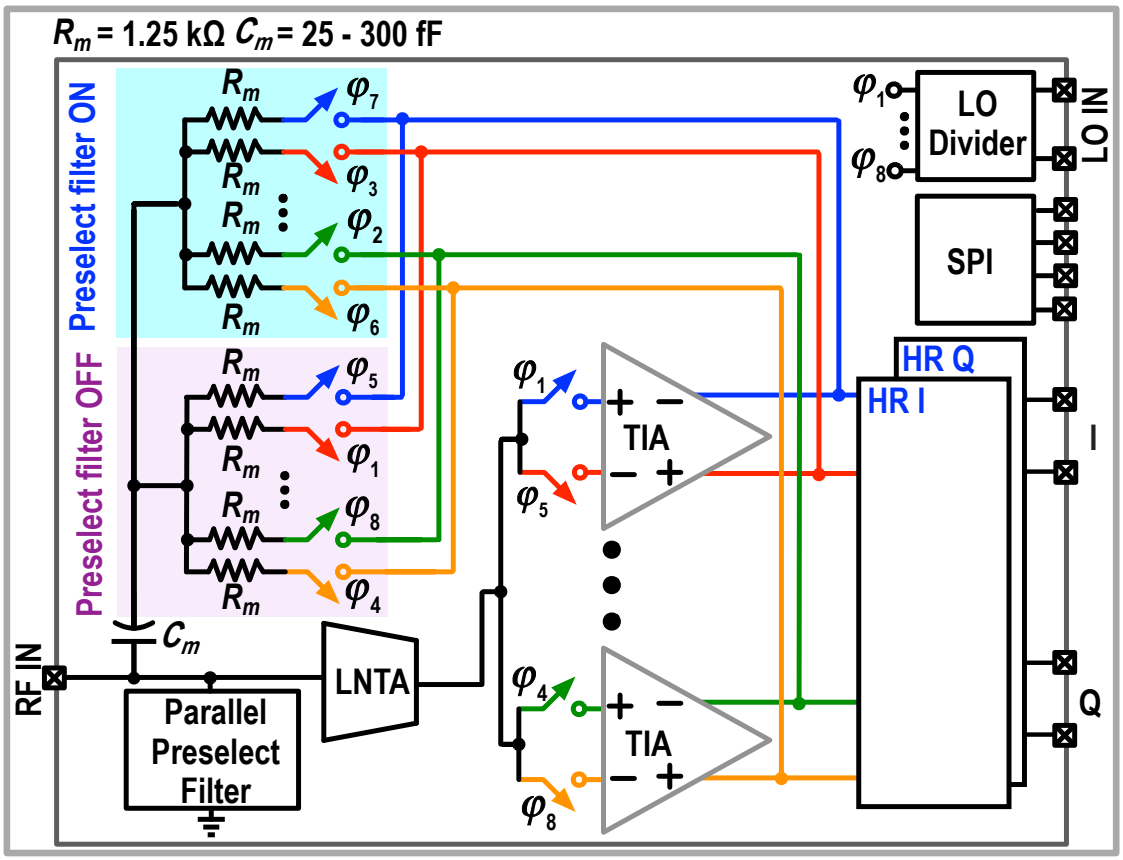

Figure 3.13: Complete block diagram of the proposed RX.

3.4 Circuit Implementation

Fig. 3.12 shows the complete block diagram of the LO generation unit. After the on-chip 50 Ω termination resistors, a phase aligner is employed at the input

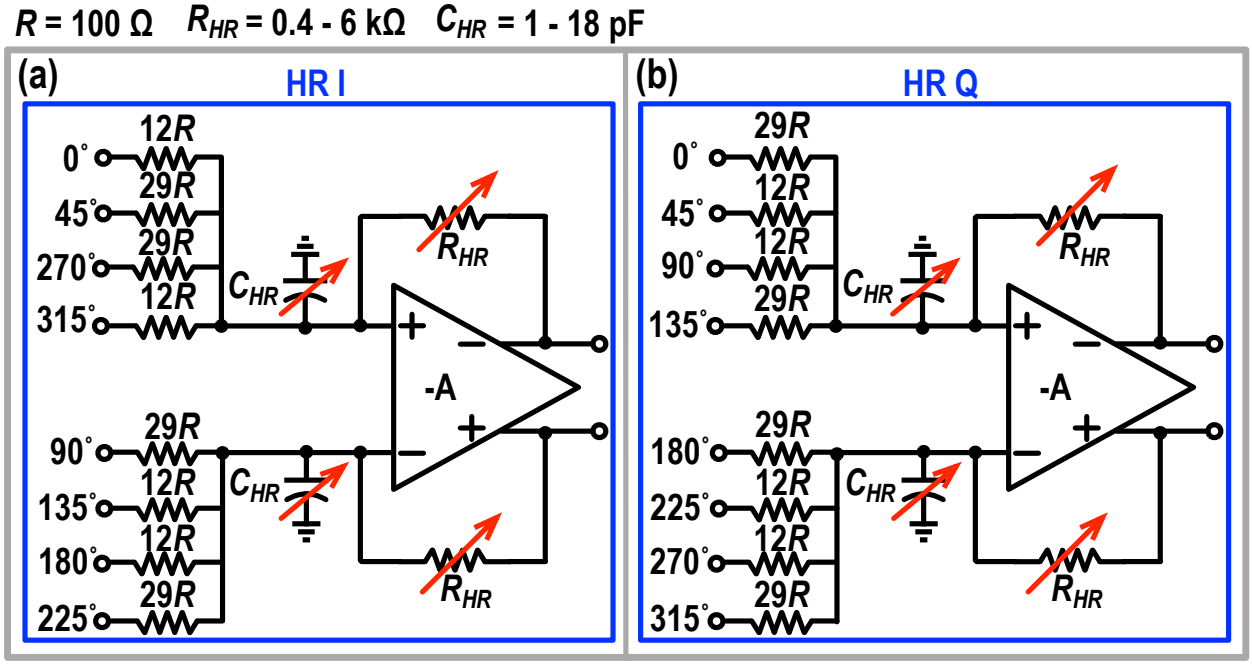

Figure 3.14: Schematic of implemented harmonic rejection circuit: (a) I path and (b) Q path.

of the LO generation to compensate for any phase and amplitude imbalance of the incoming differential off-chip clock. Then, off-chip LO is buffered and applied to a divide-by-two followed by a divide-by-four stage. Finally, the divide-by-four outputs are resampled with the outputs of the input buffer and the divide-by-two to generate non-overlapping LOs with minimum phase noise penalty, as described in [70].

Fig. 3.13 shows the complete block diagram of the proposed RX. SPI has been used to configure the chip in the linear and low-noise mode and to control all tunable components. The RF input signal is converted to an RF current by the LNTA, and then the RF current is down-converted to a BB current using passive mixers. The TIA converts the BB input current to a BB output voltage. Harmonic rejection (HR) [103] combines the output voltages of the TIAs to generate the BB I and Q signals. As illustrated in Fig. 3.14 (a) and (b), like in [78], the ratio of resistors is used to implement the $1 + \sqrt{2}$ scaling factor needed for the HR. An input capacitor (C_{HR}) is placed at the HR amplifier to absorb the out-of-band blocker current, thus relaxing the requirements of the HR amplifier. Since the voltage gain of the TIA is used to provide input matching, the RX voltage gain is only controlled by the tunable feedback resistor of the HR amplifier (i.e., R_{HR}).

In the low-noise mode, the parallel preselect filter is off; thus, -1 multipli-

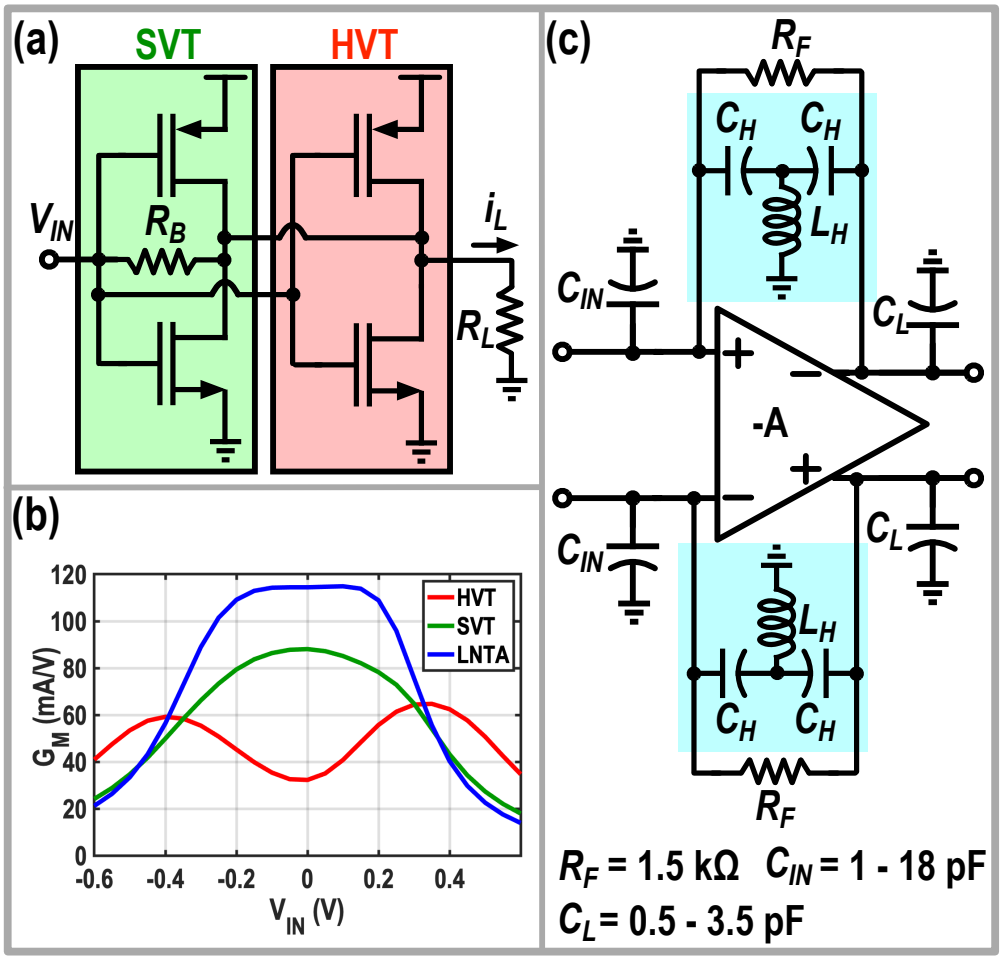

Figure 3.15: (a) Schematic of the implemented LNTA; (b) simulated G_m of the LNTA and its HVT-based and SVT-based transconductances versus the voltage swing around the input bias voltage of the LNTA; (c) schematic of the proposed third-order TIA.

cation is required in the translational feedback network. On the other hand, in the linear mode, the parallel select filter is on, and a j multiplication is required to compensate for the delay of the transconductance. As shown in Fig. 3.13, different phases of the LO are used to implement the required -1 and j multiplications. For example, in the low-noise mode, by following the output of the TIA connected to φ_1, one can observe that it is up-converted to RF using φ_5 (-1 multiplication). However, in the linear mode, the output of the TIA connected to φ_1 is up-converted to RF using φ_7 (j multiplication). To satisfy the input matching, the value of R_m is 1.25 kΩ. Moreover, the value of C_m can be tuned using SPI between 25 - 300 fF.

The RX out-of-band linearity performance is mainly determined by the LNTA. Hence, the LNTA should be able to handle the voltage swing created by large out-of-band blockers and stay linear. Fig. 3.15 (a) depicts the schematic of

the implemented LNTA. Like [104–106], the LNTA is composed of two inverters in parallel; One is implemented using the standard threshold voltage (SVT) devices, and the other is realized utilizing the high voltage threshold (HVT) devices. A feedback resistor, R_B, is also added to provide the bias voltage of the LNTA. As can be seen in Fig. 3.15 (b), when the two devices are in parallel, the LNTA provides constant G_M over a wider input voltage range, improving the out-of-band linearity performance of the proposed RX. Based on simulation results, the out-of-band IIP3 of the proposed LNTA is 5 dB higher, compared to the case in which the LNTA is implemented only by SVT devices.

Since the TIA converts the BB current to a BB voltage, a voltage swing will appear at its output. The close-in blockers of the base station applications create a large voltage swing at the output of the TIA, saturating its amplifier. Hence, it is desirable also to have sharp filtering at the output of the TIA. As shown in Fig. 3.15 (c), a third-order high pass impedance is also placed in the TIA's feedback to provide sharp filtering at the output of the TIA. Like the parallel preselect filter, BB inductors of the TIA are also implemented using a gyrator. The values of C_H and L_H here are similar to those used in the parallel preselect filter. Finally, a common-mode feedback similar to [21] is used to keep the dc bias of the TIA output around $V_{DD}/2$.

3.5 Noise Analysis

This section calculates the noise figure of the proposed RX in Fig. 3.1 (b) in the low-noise and linear modes. In the low-noise mode, the parallel preselect filter is off, and as explained in [21], the noise contribution of TIAs and the on-resistance of the mixer switches to the RX noise figure can be neglected due to the LNTA's high output impedance. Consequently, the noise figure in the low-noise mode can be estimated by

$$F_1 = \left(1 + \frac{1}{G_{M2}R_s} + \frac{R_s}{R_B}\right) \times \frac{1}{sinc^2\left(\frac{\pi}{M}\right)}, \tag{3.29}$$

where R_B is the bias resistor of the LNTA (see Fig. 3.15 (a)). Typically, R_B is chosen large, and the NF is related only to $G_M R_s$. Considering $G_{M2} = 100\,\text{mS}$, $M = 8$, and $R_B = 300\Omega$, (3.29) estimates an optimistic RX noise figure of 1.55 dB in the low-noise mode.

The next step is calculating the noise penalty due to the parallel preselect filter. Fig. 3.16 shows the equivalent model of the parallel preselect filter with the input-referred noise of the gyrator and the output current noise of the parallel

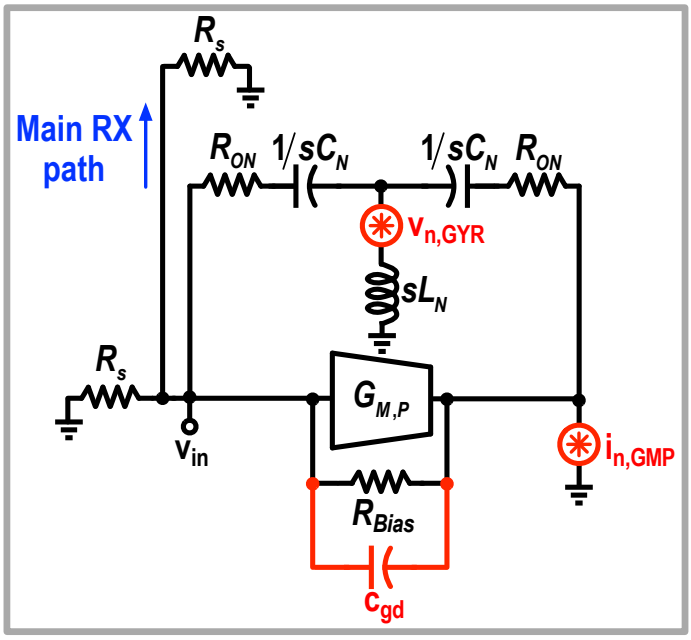

Figure 3.16: Simplified model of the proposed parallel preselect filter with the input-referred noise of the active blocks.

preselect filter transconductance. Since sL_N is short to ground at the in-band frequencies, the total input-referred noise penalty due to the parallel preselect filter can be derived as follows

$$v_{n,in}^2 = \left(\frac{r_{o,P}R_s}{2Z_F}\right)^2 i_{n,GMP}^2 + |\frac{j\,(\omega-\omega_{LO})\,C_N R_s}{2+j\,(\omega-\omega_{LO})\,C_N R_s}|^2 v_{n,GYR}^2, \tag{3.30}$$

where $Z_F = R_{Bias}||Z_N$, and R_{Bias} is the bias resistor of the transconductance of the parallel preselect filter. As can be deduced from (3.29), the noise of the gyrator is high-pass filtered by the notch filter capacitors and has a negligible effect on the noise penalty of the parallel preselect filter. Then, the NF of the proposed RX in the linear mode can be calculated by

$$F_2 = \left(1 + \frac{1}{G_{M2}R_s} + \frac{R_s}{R_B} + \frac{1}{G_{M,P}R_s}\left(\frac{A_P R_s}{2Z_F}\right)^2\right) \times \frac{1}{sinc^2\left(\frac{\pi}{M}\right)}, \tag{3.31}$$

where $A_P = G_{M,P} \times r_{o,P}$. Consequently, by choosing $Z_F \gg A_P \times R_s$, the noise penalty due to the activation of the parallel preselect filter can be minimized. In practice, as will be shown in Fig. 3.20 (a), the measured NF at the lowest operating frequency degrades only by 0.6 dB when changing the RX configuration from the low-noise mode to the linear mode. However, it is worth mentioning that the parallel preselect filter adds an extra parasitic capacitor to the RX input

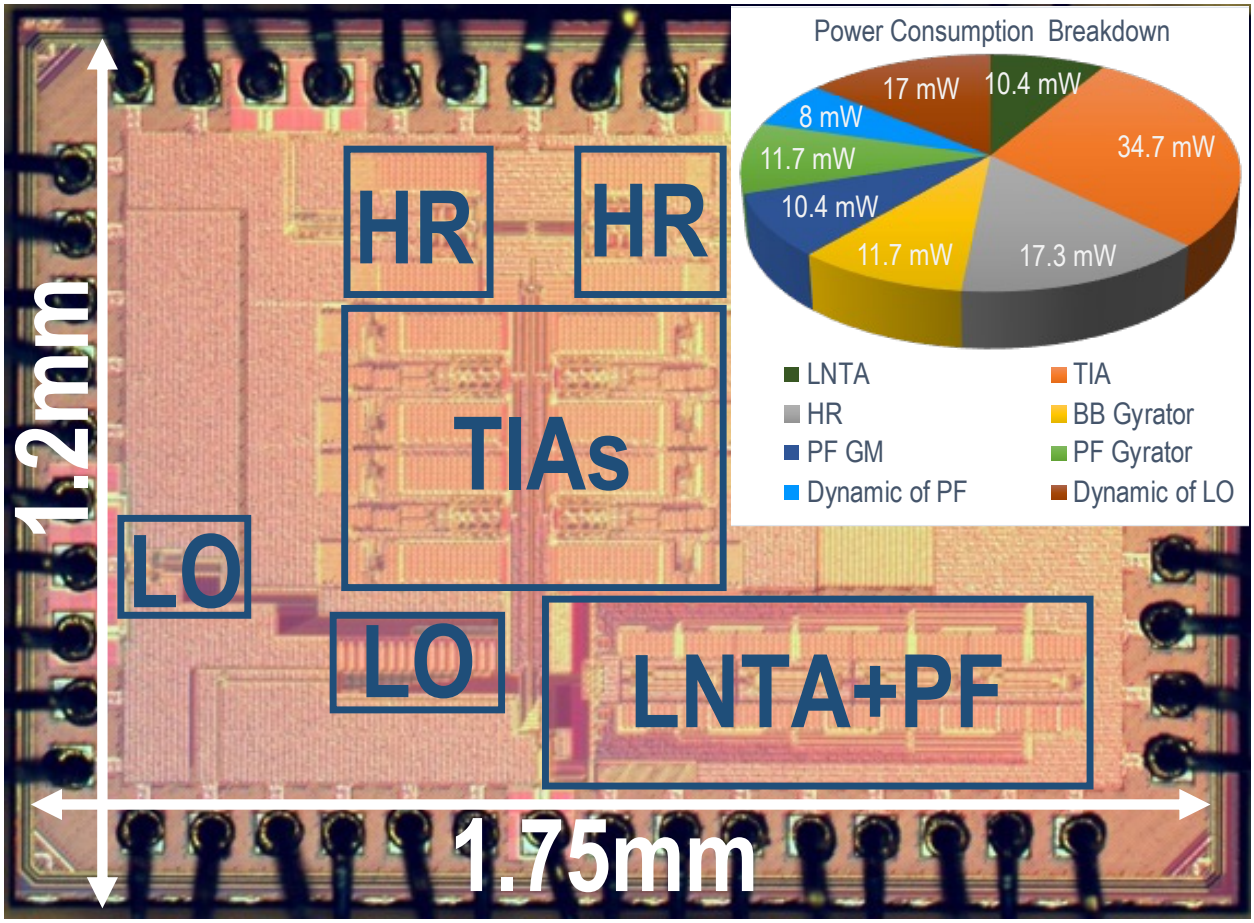

Figure 3.17: The die micrograph and the power consumption breakdown of the proposed RX at 1.5 GHz LO frequency.

(especially the Miller effect of c_{gd} in Fig. 3.16). This extra parasitic capacitor degrades the NF of the proposed RX as the LO frequency increases.

3.6 Measurement Results

The proposed RX was fabricated in TSMC 40-nm technology. As shown in Fig. 3.17, the fabricated prototype occupies $1.2 \times 1.75\,\text{mm}^2$, while the core area of the chip is $0.8\,\text{mm}^2$. The power consumption of the different blocks is summarized in Fig. 3.17 when the LO frequency is 1 GHz. The proposed RX was directly bond-wired on a four-layer FR4 printed circuit board (PCB). Fig. 3.18 shows the measurement setup. Keysight noise figure analyzer (N8973A) and network analyzer (P9375A) were used to respectively measure the NF and the input matching of the proposed RX. Keysight Infiniium (MSOS804A) with embedded 10-b ENOB analog to digital converters (ADCs) was employed

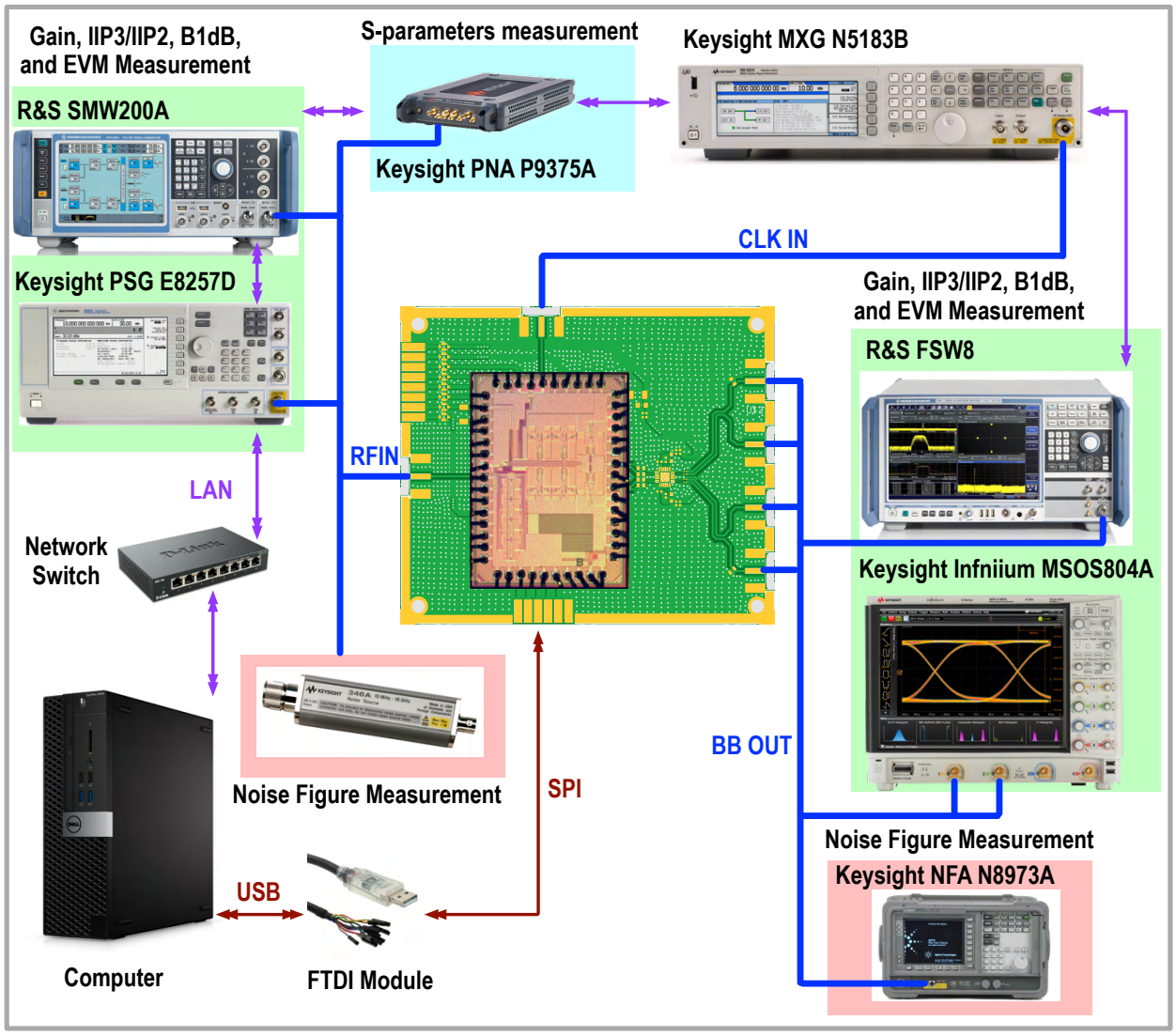

Figure 3.18: Measurement setup.

to capture the BB output of the chips for the error vector magnitude (EVM) measurements and 3GPP requirements. For the linearity and gain measurements, an R&S signal analyzer (FSW8) was used.

3.6.1 Wideband Operation

As shown in Fig. 3.19 (a), the proposed RX is functional from 0.5–3 GHz. The RX gain is 34.5 dB at 0.5 GHz LO frequency, and it reduces to 33.5 dB at 3 GHz due to the parasitic input capacitance of the RX. Moreover, the measured 3-dB bandwidth of the proposed RX is about 150 MHz. Fig. 3.19 (b) shows the measured S_{11} over the operating frequency range. The bandwidth in which S_{11} remains below -10 dB is ∼40% lower than the RX 3-dB bandwidth. As

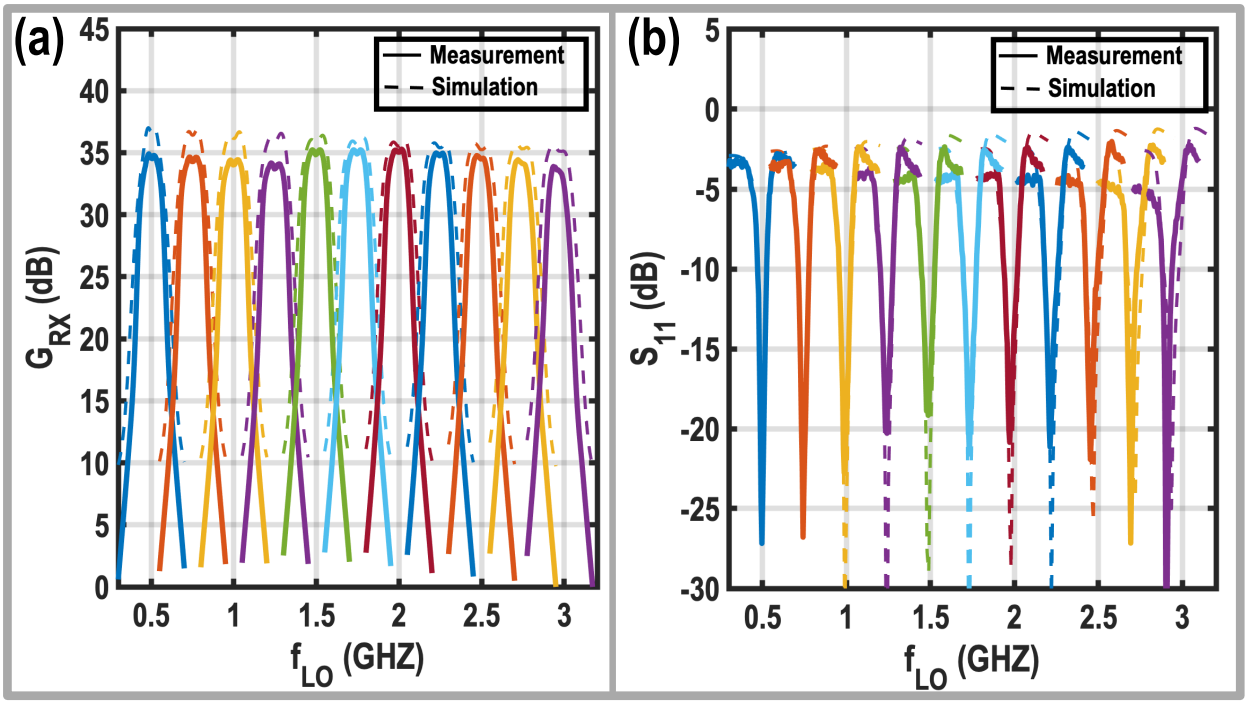

Figure 3.19: Measured (a) RX gain and (b) S_{11} over operating frequency.

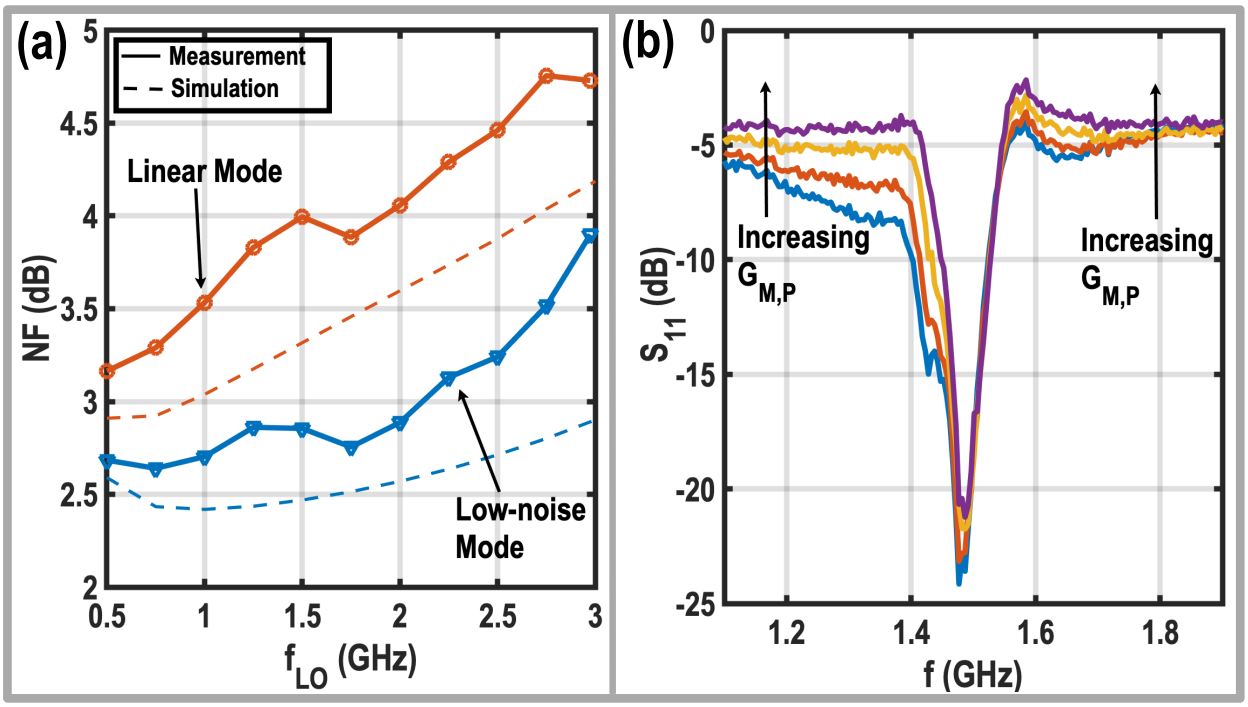

Figure 3.20: Measured (a) NF versus the LO frequency and (b) S_{11} for different $G_{M,P}$ values at 1.5 GHz LO frequency.

mentioned earlier, the input matching is provided by the Miller effect of R_m. Due to the RX channel selectivity, the RX's voltage gain reduces near the passband edges, increasing the RX input impedance and degrading S_{11}, as also

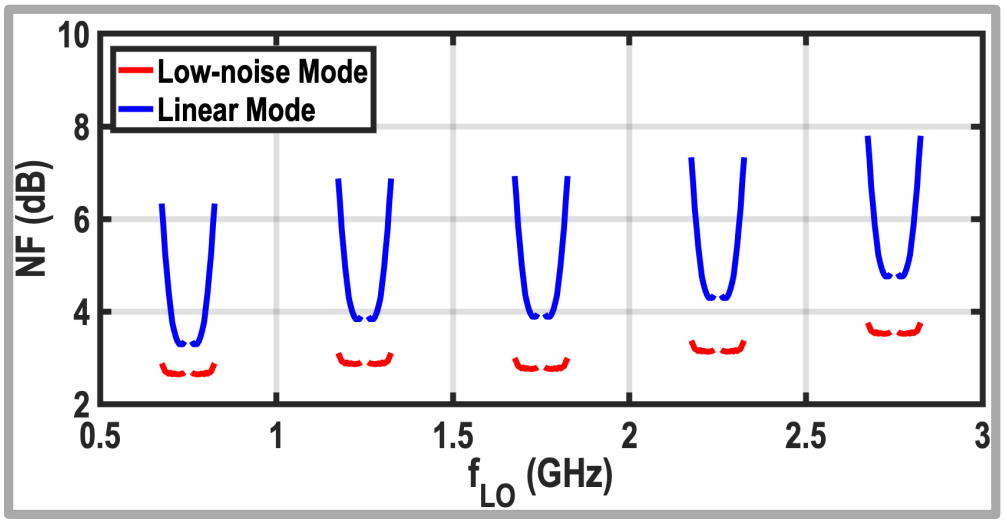

Figure 3.21: Measured NF versus the BB frequency for different LO frequencies.

discussed in [80].

The measured NF is depicted in Fig. 3.20 (a) versus the LO frequency. In the low-noise mode, the NF is 2.6 dB at 0.5 GHz LO frequency, and increases to 3.9 dB at the maximum LO frequency. In the worst case, the parallel preselect filter degrades the NF by 1.2 dB compared with the low-noise mode. As predicted by (3.3) and illustrated in Fig. 3.20 (b), increasing $G_{M,P}$ reduces the input impedance of the RX at the out-of-band frequencies, and therefore, the S_{11} reaches -4 dB for the maximum $G_{M,P}$, thus reflecting blocker signals at those frequencies. Fig. 3.21 shows the measured in-band NF versus the baseband frequency for different LO frequencies. The NF is measured for the baseband frequencies above 10 MHz due to the limitation of our instrument, Keysight N8974A. In the linear mode, the NF degrades near the passband edges for two reasons. First, as explained in the previous paragraph, the RX input impedance increases in those regions. Second, as shown in Section 3.5, the noise penalty of the parallel preselect filter is proportional to $(R_S/(R_{Bias}||Z_N))^2$. At low baseband frequencies, by choosing R_{Bias} big enough, this noise penalty can be ignored. However, as the baseband frequency increases, Z_N drops below R_{Bias}, thus making the noise penalty of the parallel preselect filter visible around the bandwidth edges.

Fig. 3.22 (a) shows the RX transfer function and filtering order in three different scenarios. In case-1, the parallel preselect filter and the BB inductors in the TIAs are disabled. Hence, the system just relies on the single real pole of the TIAs, showing only ∼-20 dB/dec roll-off. The BB inductors are turned on in case-2 while the parallel preselect filter is still off. In this case, the third-order

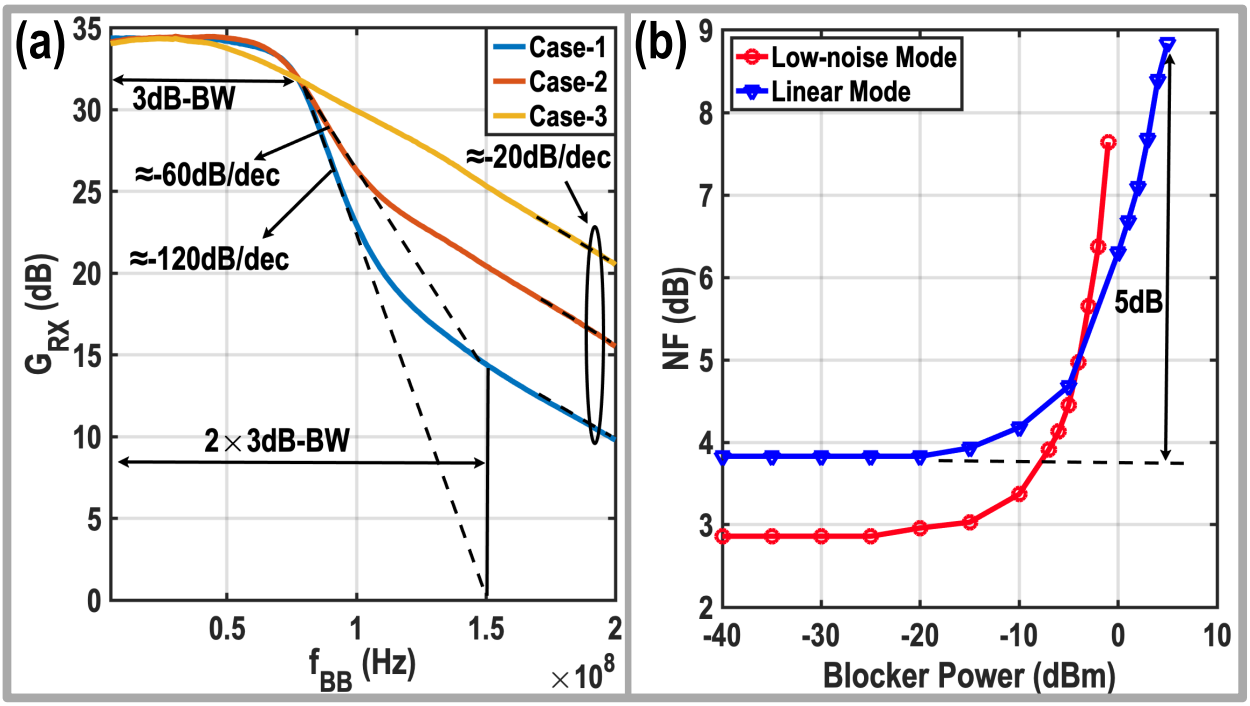

Figure 3.22: (a) The channel selectivity of the proposed RX; (b) blocker NF.

high pass filter creates complex conjugate poles, thus achieving a flat gain response and ∼-60 dB/dec roll-off. Finally, activating the parallel preselect filter realizes another third-order filtering and increases the transition roll-off to ∼-120 dB/dec for close-in blockers. Due to the limited bandwidth of the BB inductors in the TIAs and parallel preselect filter, the slope of the transition band returns to ∼-20dB/dec when the frequency exceeds the gyrators' bandwidth. The bandwidth of the BB inductors can be increased to preserve sixth-order filtering for a wider frequency range at the cost of power consumption.

The NF is also measured versus the power of the out-of-band blocker. The ratio of the blocker offset frequency to the BW_{RF} is 3.3. As depicted in Fig. 3.22 (b), in the presence of a +5 dBm out-of-band blocker, the NF degrades only by 5 dB.

Fig. 3.23 shows the RX in-band gain response in different cases. When the translational feedback network is off, there is a gain peaking at the lower side of the RX operating frequency due to the delay of the preselect filter transconductance (see blue curve in Fig. 3.23 (a)). Then, the translational feedback network is turned on, and the parallel preselect filter is disabled. As depicted in Fig. 3.23 (a), the translational feedback network creates another peak at the upper side of the transfer function (red curve). Finally, when both the translational feedback network and the parallel preselect filter are on, the

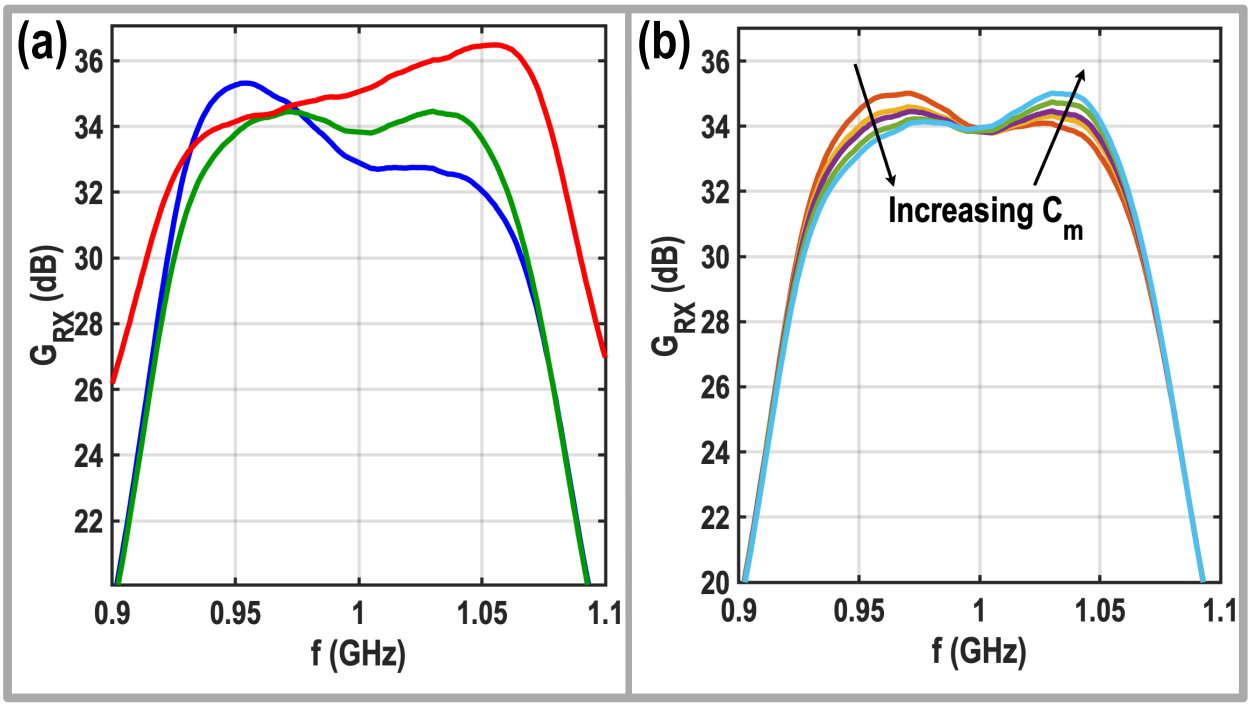

Figure 3.23: (a) The in-band gain response of the proposed RX in different scenarios; (b) the effect of C_m on the RX transfer function.

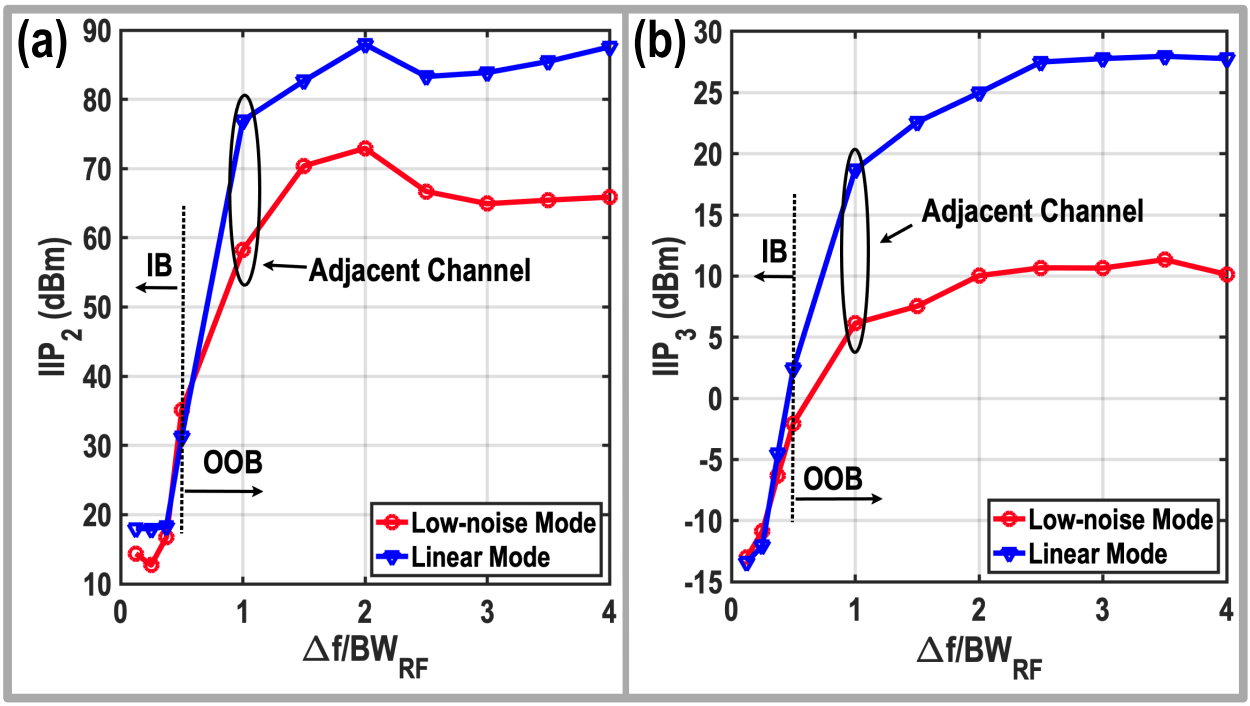

Figure 3.24: Measured IIP2 (a) and IIP3 (b) versus the offset frequency normalized to the RF bandwidth.

peaks at the lower and upper sides cancel out each other. Hence, a flat gain response can be achieved, and the in-band gain ripple is below 0.5 dB (green

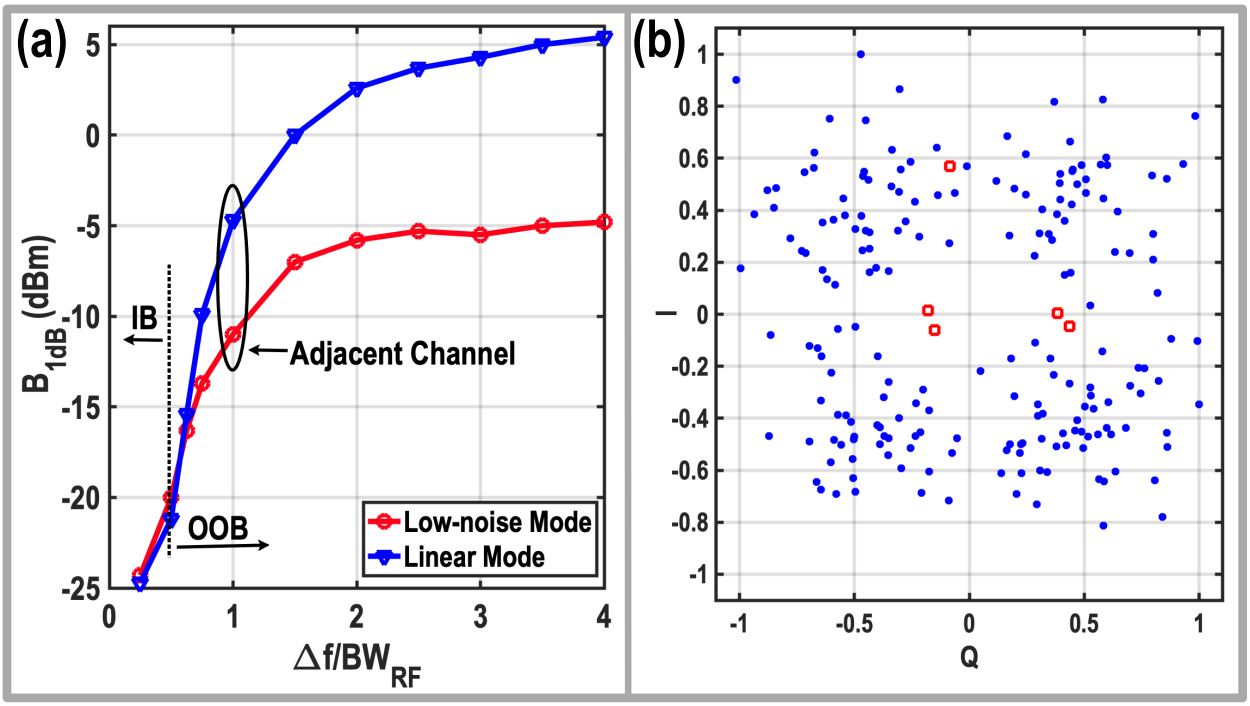

Figure 3.25: (a) Measured B1dB versus the normalized offset frequency; (b) measured constellation at the reference sensitivity for 100 MS/s signal (red squares represent the missed symbols).

curve in Fig. 3.23 (a)). As predicted by (3.22) and measured in Fig. 3.23 (b), increasing the value of C_m shifts the peak frequency towards the upper side of the operating frequency.

3.6.2 Linearity Measurements

The in-band and out-of-band IIP3 and IIP2 measurements are exhibited in Fig. 3.24 (a) and (b), respectively. The in-band IIP2 (IIP3) in the linear mode is +18 dBm (-13 dBm). Since the last gain stage of the RX limits the in-band linearity, in-band IIP2 (IIP3) for the low-noise mode is also +18 dBm (-13 dBm). For linear mode, the out-of-band IIP2 of the proposed RX is +65 dBm. Enabling the parallel preselect filter improves the out-of-band IIP2 to +85 dBm.

The out-of-band IIP3 for the low-noise mode is +11 dBm. Moreover, in the linear mode, the out-of-band IIP3 is +28 dBm which shows a 17 dB improvement compared to the low-noise mode. The large-signal operation of the proposed RX is depicted in Fig. 3.25 (a). An in-band blocker with -24 dBm power drops the gain of the proposed RX by 1 dB. Thanks to the sharp filtering of the proposed RX, the B1dB improves from -24 dBm to -5 dBm for the adjacent channel. For the low-noise mode, the out-of-band B1dB of the proposed RX is -5 dBm, and enabling the preselect filter improves it to +5 dBm. The measured B1dB is

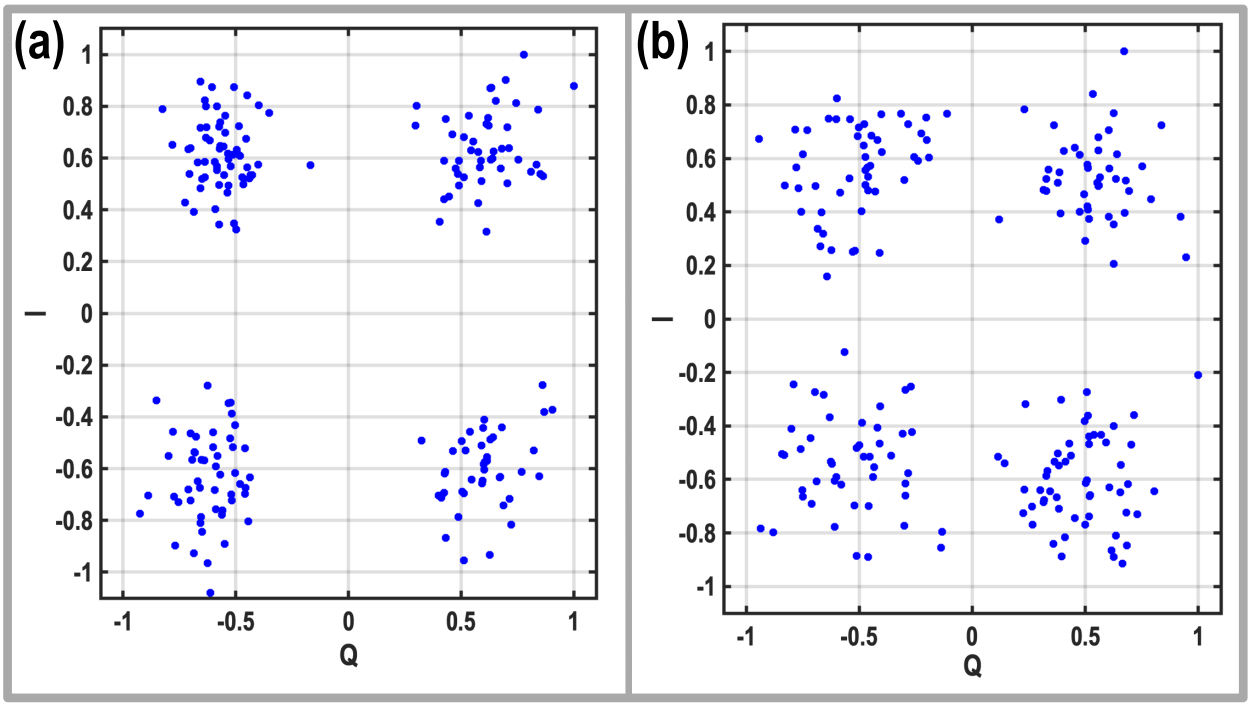

Figure 3.26: Measured constellation for 100 MS/s signal: (a) in the presence of a -38 dBm in-band blocker and (b) when a -15 dBm out-of-band blocker at 20 MHz offset frequency is applied to the RX.

-15.4 dBm for a close-in blocker located at 20 MHz offset frequency. While this B1dB is 0.4 dB lower than the required value of the 3GPP standard, it is still good enough to satisfy the close-in blocking test of the 3GPP.

3.6.3 3GPP Requirements

The performance of the proposed RX is also measured based on the 3GPP requirements for the microcell base station applications [1]. In order to do so, a 100 MS/s QPSK signal is applied to the input of the RX. The RX in-phase (I) and quadrature (Q) BB signals are then converted to digital by the ADC of the high-speed oscilloscope. The voltage gain of the RX assures that the quantization noise of the ADC does not degrade the SNR of the received signal. Finally, the captured BB data of the oscilloscope is post-processed in MATLAB.

First, the reference sensitivity requirement of the 5G microcell base station is investigated. Since the power of the desired signal is low, the proposed RX is configured in low-noise mode to ensure sub-3dB NF. The power of the desired signal is -83.7 dBm, hence, SNR of the signal at the RX output is 7.5 dB (note that the NF is 2.8 dB). As shown in Fig. 3.25 (b), the RX throughput is 97.5% for the reference sensitivity, thus satisfying the 3GPP requirement by a 2.5%

margin.

Second, the RX performance is measured in the presence of an in-band blocker. In this test, the RX throughput should be better than 95%, while the power of the desired signal is 6 dB higher than the reference sensitivity and an in-band modulated blocker with 20 MHz bandwidth and -38 dBm power is present. As depicted in Fig. 3.26 (a), since the EVM of the received signal is low enough (i.e., -11.7 dB), all the symbols are detected correctly, thus comfortably meeting the 3GPP requirement.

Third, the out-of-band blocking of the 5G microcell base station applications is investigated. A -15 dBm out-of-band blocker can be located at a 20 MHz offset frequency from the passband edge. In the presence of this blocker, sharp filtering is required to avoid gain saturation at the BB outputs of the RX. Hence, the proposed RX is configured in the linear mode. Similar to the in-band blocking scenario, the power of the desired signal is 6 dB higher than the reference sensitivity, representing 12.3 dB SNR (note that NF is 4 dB in the linear mode). As shown in Fig. 3.26 (b), the measured EVM is -9.7 dB in this case, and the throughput is 100%.

3.6.4 High-order QAM

In the next test, a 100 MS/s QAM-64 OFDM signal is applied to the input of the RX. As depicted in Fig. 3.27 (a), when the power of the input signal is -60 dBm, the measured EVM is -26.3 dB (note that the RX is configured in the linear mode). Then, the EVM is plotted versus the power of the input signal, P_S, in Fig. 3.27 (b). This curve can be divided into three regions. In region 1, the EVM is limited by the thermal noise, and increasing the signal power improves the EVM. Then, the EVM is limited by the I/Q imbalance and the phase noise of the LO in region 2. Finally, in region 3, the EVM is restricted by the distortion at the output of the RX due to limited in-band linearity. It is worth mentioning that the input signal has around a 10 dB peak-to-average ratio (PAPR). Hence, the high PAPR of the input signal degrades the performance of the RX for high input power signals.

In Fig. 3.28, the performance of the proposed RX is investigated in the presence of a 0 dBm continuous wave (CW) blocker located at a 500 MHz offset frequency from the desired -60 dBm 100MS/s QAM-64 OFDM signal. In the low-noise mode, the out-of-band blocker saturates the LNTA, and the desired signal cannot be appropriately received (see Fig. 3.28 (a)). Then, the proposed RX is configured in the linear mode. As illustrated in Fig. 3.28 (b), the measured

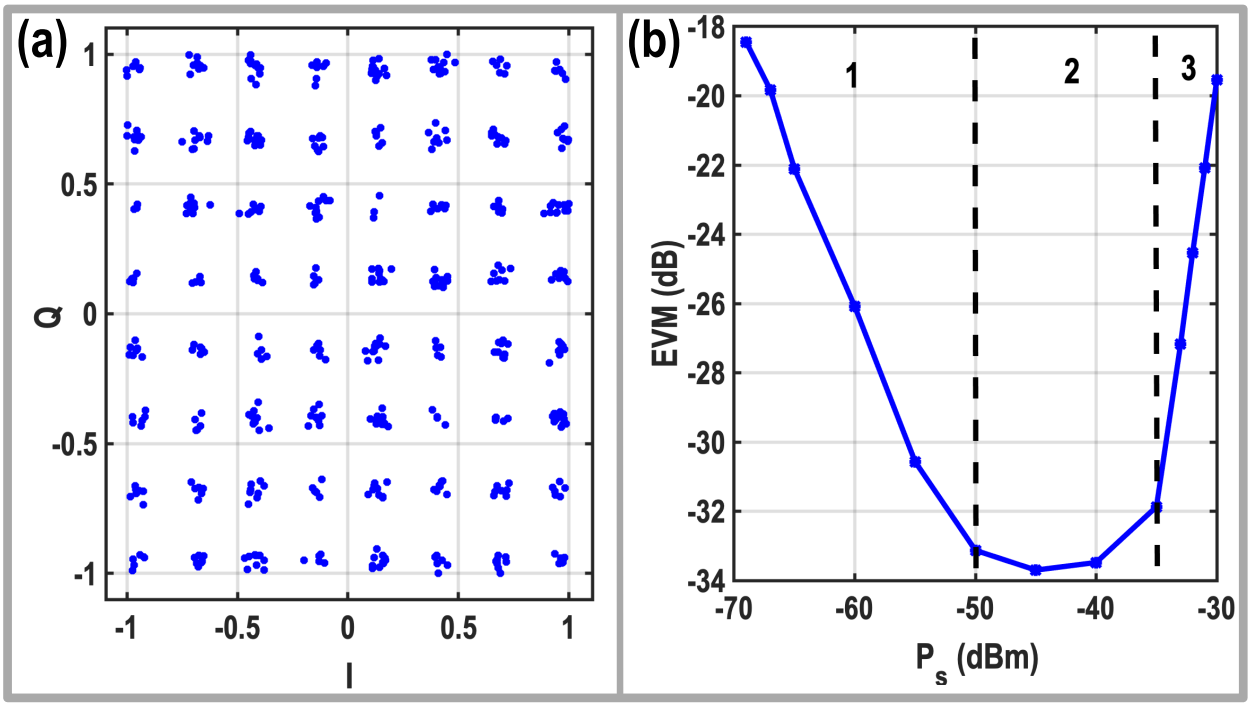

Figure 3.27: (a) Measured constellation for a 100 MS/s QAM-64 -60 dBm signal; (b) Measured EVM versus the input power of the desired signal.

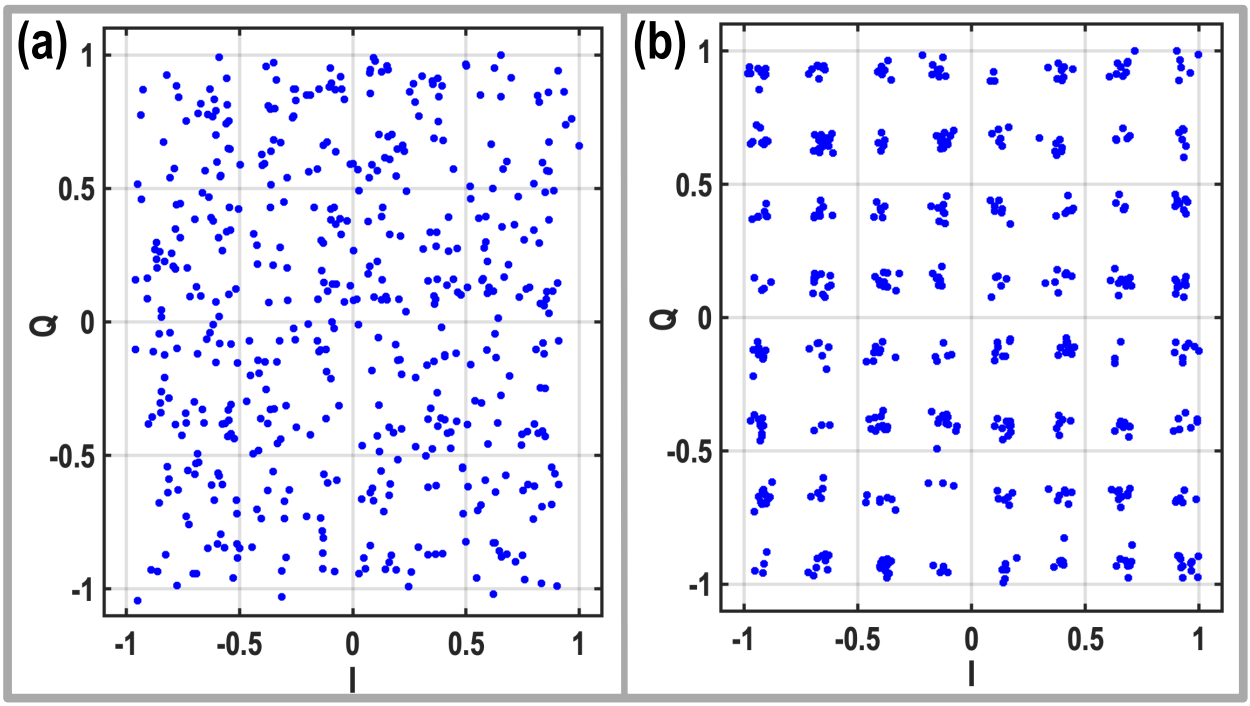

Figure 3.28: Measured constellation for a 100 MS/s QAM-64 -60 dBm signal in the presence of a 0 dBm out-of-band blocker: (a) low-noise mode (b) linear mode.

EVM is -24.3 dB in this case, which shows only 2 dB degradation compared to the EVM of 3.27 (a). This 2 dB degradation can also be inferred from Fig. 3.22 (b),

where the NF degrades by 2 dB in the presence of a 0 dBm blocker.

3.6.5 Performance Summary and Comparison

The performance of the proposed RX is summarized in Table 3.1 and compared to the state-of-the-art RXs. In the low-noise mode, the proposed RX can achieve sub-3dB NF while showing similar linearity performance compared to the other LNTA-based RXs. In the linear mode, however, it outperforms LNTA-based RXs [78, 81, 88, 98]. The LNA-Based RX in [87] offers better out-of-band IIP3, at the cost of using multiple supplies and a complex calibration scheme. Moreover, it only achieves 0.5 dBm B1dB and 80 MHz RF bandwidth compared to 5 dBm and 150 MHz of the proposed RX. Compared to the mixer-first RXs [58,60,61], the proposed RX achieves comparable out-of-band IIP2 and IIP3 while demonstrating better NF and filtering order. Filtering by aliasing RX [107] reports a better out-of-band IIP3 but with much higher NF, lower bandwidth, and operating frequency while its passband is not flat. Moreover, the proposed RX is the only RX that reports EVM in the presence of a 0 dBm blocker.

3.7 Conclusion

This Chapter presents a wideband RX in 40-nm CMOS technology for 5G microcell base station applications. Thanks to the proposed parallel preselect filter, a +5 dBm out-of-band B1dB is achieved, making the proposed RX a good candidate for microcell co-location applications. Third-order RF and BB filters are utilized to achieve -120 dB/dec channel selectivity to satisfy the close-in blocking scenario of the base station applications. A translational feedback network is placed in the feedback of the RX to reduce the in-band gain ripple to below 0.5 dB. The proposed RX is reconfigurable, and in the low-noise mode, it can achieve sub 3-dB NF while achieving +28 dBm out-of-band IIP3 in the linear mode. With a -60 dBm 100 MSym/s (0.6Gb/s) 64-QAM OFDM input signal, the RX EVM only degrades from -26.3 dB to -24.3 dB when facing a 0 dBm out-of-band blocker. Moreover, thanks to its current-mode operation and sharp filtering, the proposed RX meets all in-band and out-of-band 3GPP blocking requirements.

Table 3.1: Performance Summary And Comparison With State-Of-The-Art RXs.

	This Work		Wang JSSC 2021[79]	Razavi JSSC 2022[81]	Montazerolghaem ISSCC2021[88]	Musayev JSSC2019[98]	Kim OJSSC2022[87]	Krishnamurthy JSSC2019[60]	Pini JSSC2020[58]	Krishnamurthy SSCL2021[61]	Bu JSSC2022[107]
	Low Noise	Linear									
Architecture	LNTA Based		LNTA Based	LNTA Based	LNTA Based	LNTA Based	LNA Based	Mixer First	Mixer First	Mixer First	Slice-Based
Technique	Preselect filter and third-order TIA		Gm boosting N-path filter	Harmonic rejecting	Programmable zeros and second-order TIA	Quantized RX	Calibrated Quantized RX	Second-order TIA	Third-order current-mode filtering	High order impedance + N-path	Filtering by aliasing
Technology	40 nm CMOS		45 nm FDSOI	28 nm	40nm CMOS	65nm CMOS	65nm CMOS	28 nm CMOS	28nm CMOS	28nm CMOS	28 nm
f_{RF} (GHz)	0.5 - 3		0.2 - 2	0.4 - 6	0.4 - 3.2	0.7 – 1.4	1.7 – 2.2	0.2 - 2	0.5 - 2	0.2 - 3.5	0.1 - 1
Gain (dB)	25-45		40	54	36	36.8	23.2	13	32.4	16.3	10
Single Ended Input	Yes		Yes	Yes	Yes	Yes	Yes	Yes	No	Yes	Yes
Supply (V)	1.3		1.2/1.6	1	1.3/1.2	0.8/1/1.2	0.4/1.2/2.5	1.2	1.8/1.2	1.4/1.2	0.9
Active Area (mm^2)	0.8		1.05	1.9	0.6	0.25	0.33	0.48	0.16	1.5	1.3
NF (dB)	2.6 - 3.9	3.1 - 4.7	2.1-2.5	2.1†/4.42§	2.7 - 3.6	1.9	2.5	4.3 - 7.6	5.5£	6.5 - 12	10.8
0dBm BNF (dB)	N/A	6.5 $\Delta f/BW_{RF}$ = 3.3	6.7 $\Delta f/BW_{RF}$ = 4	5.2†/7.4§	8.4 $\Delta f/BW_{RF}$ = 3.1	6.6	5.9	6.4 $\Delta f/BW_{RF}$ = 5	10 $\Delta f/BW_{RF}$ = 4	9 $\Delta f/BW_{RF}$ = 3.1	14 $\Delta f/BW_{RF}$ = 6
In-band flatness	Yes	Yes	No	No	Yes	No	No	Yes	Yes	Yes	No
BW_{RF} (MHz)	180	150	20	0.2 - 160	160	30	80	18	260	30	5 - 20
Filtering-order (dB/dec)	-60	-120	-40	-60	-60	-20	-20	-40	-60	-80	-60¥
RF Selectivity (dB/dec)	N/A	-60	-20	-20	-20	N/A	N/A	-40	-20	-80	N/A
OOB IIP_3 (dBm)	7.5 $\Delta f/BW_{RF}$ = 1.5	22.6 $\Delta f/BW_{RF}$ = 1.5	5 $\Delta f/BW_{RF}$ = 1.5	9.8 $\Delta f/BW_{RF}$ = 25	10 $\Delta f/BW_{RF}$ = 1.5	1	26.1 $\Delta f/BW_{RF}$ = 1.5	19 $\Delta f/BW_{RF}$ = 1.6	21 $\Delta f/BW_{RF}$ = 1.5	23 $\Delta f/BW_{RF}$ = 1.5	30 $\Delta f/BW_{RF}$ = 1.5
OOB IIP_2 (dBm)	70.4 $\Delta f/BW_{RF}$ = 1.5	82.7 $\Delta f/BW_{RF}$ = 1.5	48 $\Delta f/BW_{RF}$ = 1.5	30 $\Delta f/BW_{RF}$ = 25	50 $\Delta f/BW_{RF}$ = 1.5	35	71 $\Delta f/BW_{RF}$ = 2.5	N/A	70 $\Delta f/BW_{RF}$ = 1.5	N/A	82 $\Delta f/BW_{RF}$ = 8
B_{-vga}(dBm)	-5 $\Delta f/BW_{RF}$ = 3.5	5 $\Delta f/BW_{RF}$ = 3.5	N/A	N/A	-5 $\Delta f/BW_{RF}$ = 2.5	-8.5	0.5	7 $\Delta f/BW_{RF}$ = 1.6	3 $\Delta f/BW_{RF}$ = 3	10 $\Delta f/BW_{RF}$ = 2	12.1 $\Delta f/BW_{RF}$ = 4
LO Leakage (dBm) at 1GHz	-90	-76	-85	N/A	-77	N/A	N/A	N/A	N/A	N/A	-85
EVM (dB)	-27.6‡	-26.3‡	N/A	-25.3¥	-26.4§	N/A	N/A	N/A	N/A	N/A	N/A
0dBm Blocker EVM (dB)	N/A	-24.3‡ $\Delta f/BW_{RF}$ = 3.3	N/A	N/A	N/A	N/A	N/A	N/A	N/A	N/A	N/A
Power (mW)	74 +17mW/GHz	96 +25mW/GHz	68-95	23 - 49	58.5 +17.6 mW/GHz	14 +37.2/GHz	6.5 18.5/GHz	143 18mW/GHz	21.6 + 7.8 mW/GHz	100 mW at 1GHz	21 – 31 /Channel

†Low noise mode, § Harmonic reject mode, £ loss of input balun excluded, ¥ Estimated from figure, ‡ -60dBm 100MS/s 64QAM OFDM, ŝ -60dBm 140MS/s 64QAM OFDM, ¢ -57dBm 80MS/s 256QAM.

3

Chapter

4

A Sub-7GHz Linear Receiver for 5G Local Area Base Station Applications

4.1 Introduction

New radios at low-band and mid-band frequencies are expected to remain the backbone of the 5G mobile communication due to their low path loss, which results in greater network coverage. As a result, the sub-6 GHz band of 5G new radio has recently been extended to 7.125GHz [1]. Generally, the operating frequency of wideband RXs is limited by the parasitic capacitors at the RF nodes. In the proposed LNTA-based RXs, to achieve decent out-of-band linearity performance, two different techniques are utilized. For user equipment RX, an N-path notch filter is utilized in the LNTA feedback, and for base station RX, a parallel preselect filter is placed at the RX input. However, as illustrated in Fig. 4.1 (a) and (b), utilizing these techniques introduces parasitic capacitors at the LNTA input and output, limiting the operating frequency.

In local area base station applications, the in-band blocking scenario is more

This chapter is written based on an ISSCC 2023 contribution [108], and an extended version based on this chapter has been accepted for publication at IEEE Journal of Solid-State Circuits [109].

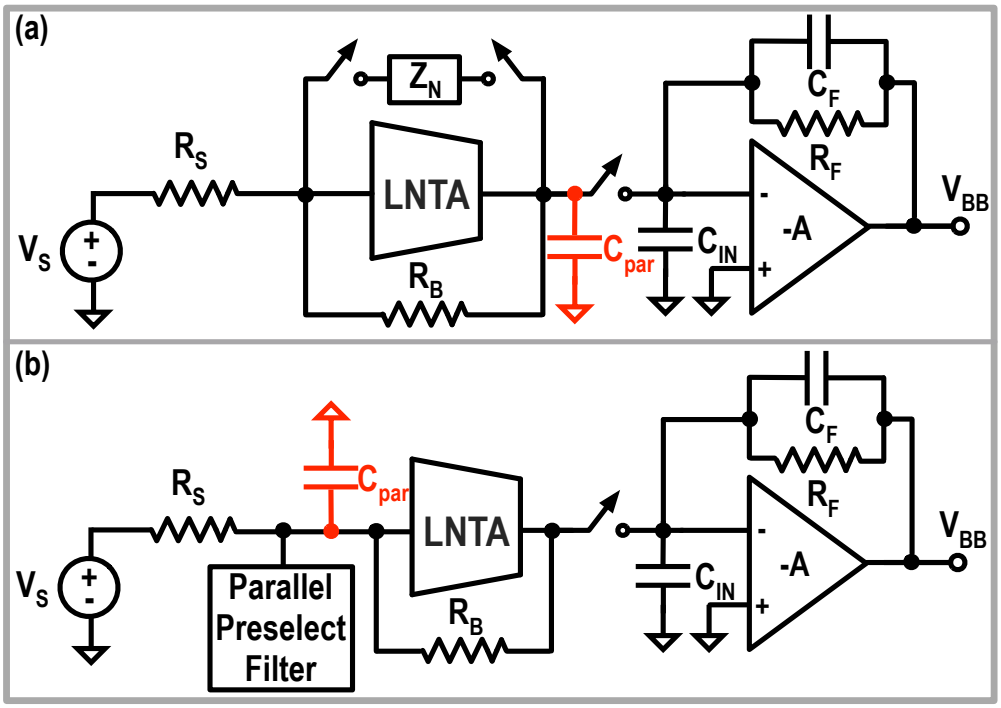

Figure 4.1: Proposed LNTA-based RXs with (a) N-path notch filter in the feedback of LNTA and (b) parallel preselect filter at the RX input.

stringent than the microcell base station applications, in which the power of the in-band blocker can be as high as -35 dBm. Moreover, the RF bandwidth of base-station RXs has been increased to 400 MHz for new radio bands above 3 GHz to meet the growing customer demand for higher data rates. Consequently, achieving in-band linearity becomes a significant challenge for baseband amplifiers in such high-bandwidth applications. Furthermore, despite the increase in RF bandwidth for 5G applications, the offset frequency of close-in blockers remains constant. For instance, in mid-band radios operating above 3 GHz, the offset frequency of close-in blockers is only 60 MHz [1]. To handle a -15 dBm close-in blocker at such a low offset frequency, the TIA must possess two critical features. First, the TIA's filtering should sufficiently suppress the close-in blockers to prevent voltage clipping at its output. Second, the loop gain of the TIA amplifier should be high not only within the 3-dB bandwidth to handle the in-band blocker but also at the bandwidth edge to suppress intermodulation between the in-band and close-in blockers.

Finally, in local area co-location applications, the RX should handle a -4 dBm blocker from other standards such as GSM. Since the frequency of the co-location far-out blocker is constant, the out-of-band rejection at the blocker offset frequency is limited at the RX input due to the enhanced RF bandwidth of

5G applications. Therefore, a new RF front-end scheme is needed to enhance the 3-dB bandwidth without compromising the out-of-band rejection and operating frequency.

In this Chapter, an LNTA-based RX is proposed to tackle the above-mentioned issues. Firstly, it employs a Rauch TIA to achieve a second-order response and higher loop gain around the bandwidth edge, two crucial features for high-bandwidth applications. A third-order impedance is also utilized in the TIA feedback to further enhance the RX's selectivity and suppress close-in blockers. Moreover, one set of N-path notch filter switches is merged with the down-converting switches to reduce the parasitic capacitance at the LNTA output and enhance the RX operating frequency. Finally, by utilizing the input impedance peaking of the TIA, we implemented a positive feedback technique to elegantly enhance BW_{RF} while achieving decent out-of-band linearity performance. This Chapter is organized as follows: Section 4.2 calculates the in-band linearity requirements of local area base station RX. Section 4.3 extensively analyzes the Rauch TIA and compares it with the first-order TIA to demonstrate its suitability for 5G applications. Sections 4.4 and 4.5 present the RF front-end architecture and analyze the RX in-band linearity. Section 4.6 discusses the circuit implementation of the proposed RX. The experimental results are shown in Section 4.7, and Section 4.8 concludes the Chapter.

4.2 In-Band Linearity Requirement

According to 3GPP standard, the RX throughput must exceed 95% when the input signal is a 50 MS/s QPSK signal with a power of -81.7 dBm, and a -35 dBm 20 MS/s modulated in-band blocker is present at the passband edge [1]. To calculate the required in-band third-order intercept point (IIP3), the in-band blocker is modeled with two -38 dBm tones ($P_{in,B}$), and the power of the third-order intermodulation tones P_{IM3} is considered 10 dB below the desired signal power to ensure 95% throughput with sufficient margin. The required IIP3 can be derived as follows:

$$IIP3 \geq 1.5P_{in,B} - 0.5P_{IM3} \rightarrow IIP3 \geq -11.15\,dBm. \tag{4.1}$$

Next, we estimate the minimum RX gain ($G_{RX,min}$) required to ensure that the quantization noise of the analog-to-digital converter (ADC) is 10 dB below the IM3 tones at the ADC input, preventing it from limiting the RX throughput.

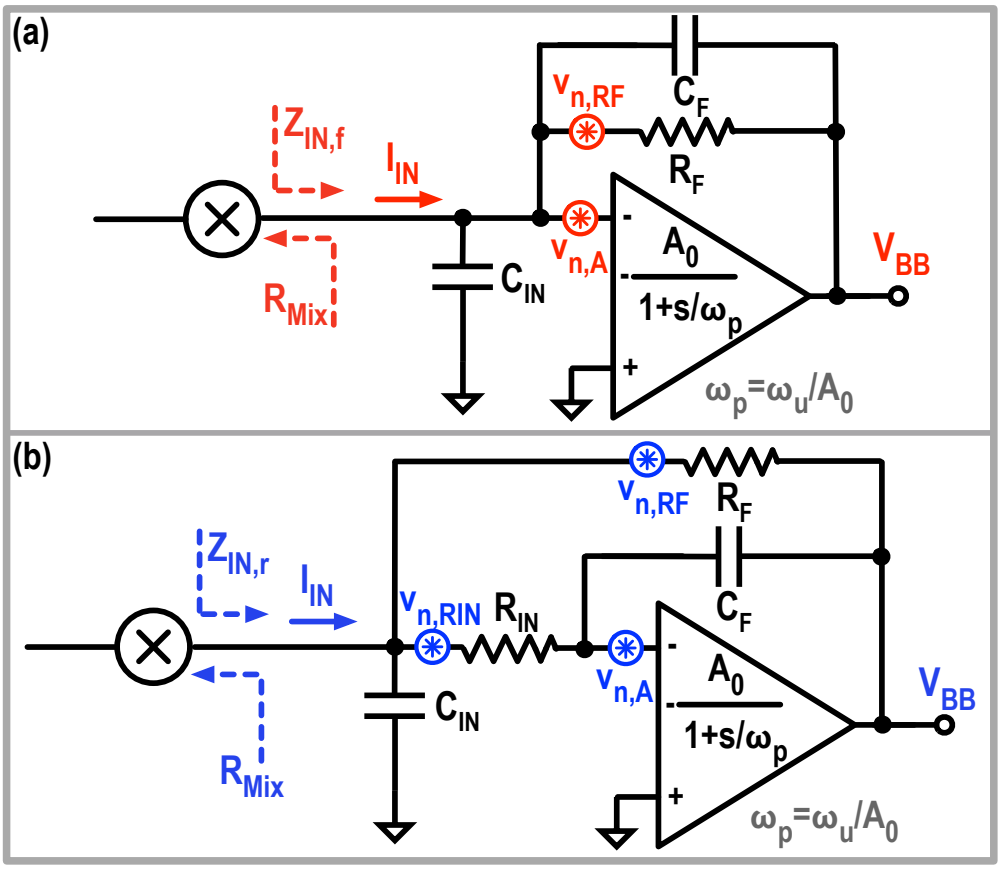

Figure 4.2: Block diagram of the (a) first-order TIA and (b) Rauch TIA.

Therefore,

$$P_{IM3} + G_{RX,min} - 10\,dB \geq FS - 6n - 1.76, \tag{4.2}$$

Where FS is the full-scale input power of the ADC and n is the number of bits. Assuming the use of a 12-bit ADC with $FS = +6$ dBm as in [50], $G_{RX,min} \geq 33.7$ dB is required. Thus, the required in-band OIP3 can be estimated as

$$OIP3 = IIP3 + G_{RX,min} \rightarrow OIP3 \geq 22.55\,dBm. \tag{4.3}$$

4.3 Transimpedance Amplifier

As mentioned earlier, the TIA limits the in-band linearity performance of current-mode RXs. Therefore, we compare two well-known TIA structures in this section to identify the better candidate for 5G applications. Fig. 4.2 shows the block diagrams of the first-order and Rauch TIAs [110]. Both TIAs use feedback impedance, comprising R_F and C_F, to convert the input current to a

baseband voltage, with C_{IN} placed at the TIA input to absorb the out-of-band blocker current. Unlike the first-order TIA, the Rauch TIA includes an extra series resistor, R_{IN}, between the TIA input and its amplifier input. The values of R_F and C_{IN} are chosen based on the gain and out-of-band blocker current requirements and are kept the same for both structures to ensure similar area, gain, and power consumption. We then compare the two structures in terms of transfer function, input impedance, linearity, performance under PVT variations, noise, and DC offset with C_F adjusted to achieve the same 3-dB bandwidth (ω_{3dB}) for both structures.

4.3.1 Transfer Function

Firstly, the transfer functions of both TIAs are calculated and compared. The frequency response of the first-order TIA can be calculated as follows:

$$Z_{21,f} = \frac{V_{BB}}{I_{IN}} = -\frac{R_F}{sR_F\left(C_F + \frac{C_F}{A(s)} + \frac{C_{IN}}{A(s)}\right) + 1}, \tag{4.4}$$

where V_{BB} and I_{IN} are the TIA's output voltage and input current, respectively. Furthermore, $A(s)$ is the gain of the TIA amplifier and is given by:

$$A(s) = \frac{A_0}{1 + \frac{s}{\omega_p}}, \tag{4.5}$$

where ω_p is the dominant pole of the TIA amplifier. Assuming that $A(s)$ is large enough across the 3-dB bandwidth, the transfer function is a first-order response, and $R_F C_F$ sets the 3-dB bandwidth. On the other hand, the transfer function of the Rauch TIA can be calculated as follows:

$$Z_{21,r} = -\frac{R_F}{s^2 R_{IN} C_{IN} R_F C_F + s\left(R_{IN} + R_F\right) C_F + 1}, \tag{4.6}$$

which shows a second-order low-pass response. Assuming $R_F \gg R_{IN}$, the natural frequency (ω_n) and damping ratio (ζ) can be calculated as:

$$\zeta = \frac{1}{2}\sqrt{\frac{R_F C_F}{R_{IN} C_{IN}}}, \tag{4.7}$$

$$\omega_n = \sqrt{\frac{1}{R_{IN} C_{IN} R_F C_F}}. \tag{4.8}$$

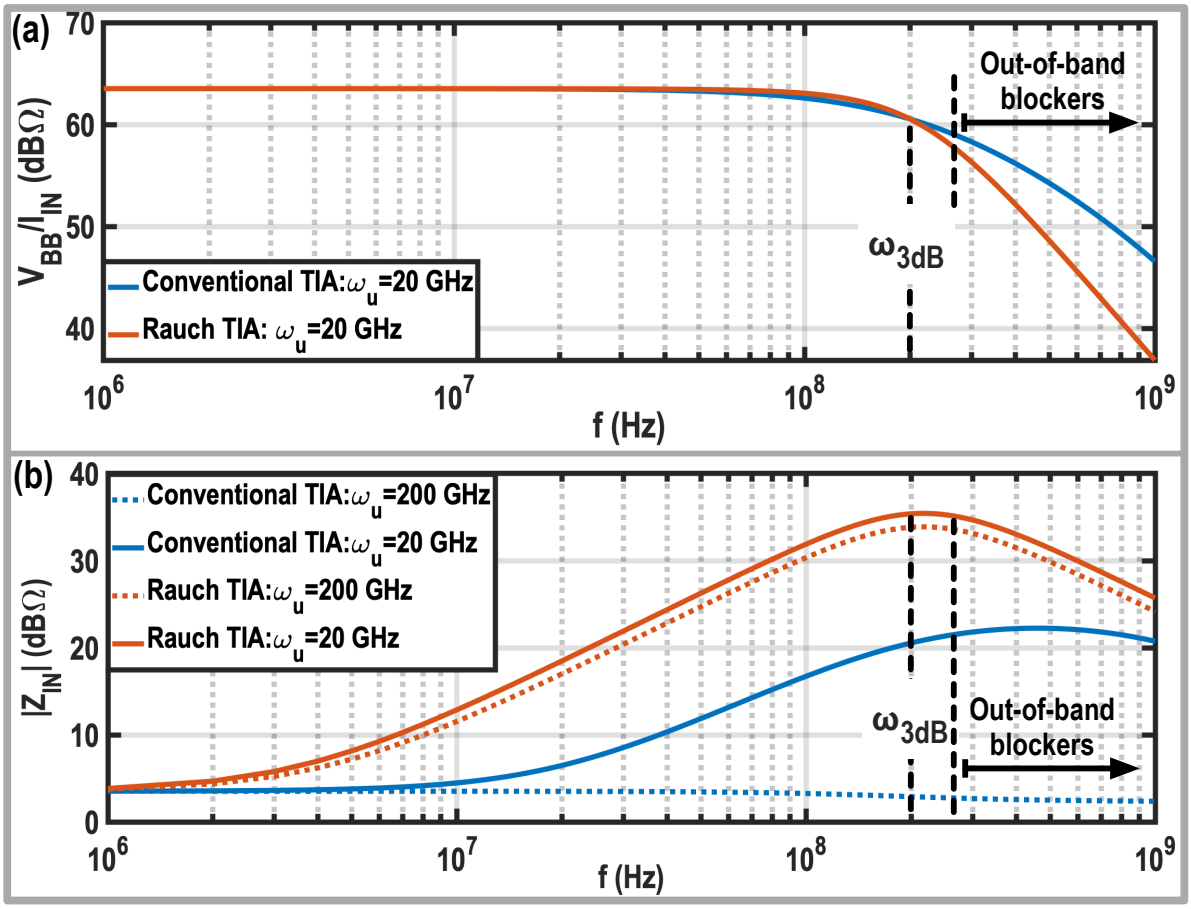

Figure 4.3: The simulated (a) transfer function and (b) input impedance of the first-order TIA and Rauch TIA in MATLAB (first-order TIA: $C_{IN} = 10\,\text{pF}$, $R_F = 1.5\,\text{k}\Omega$, $C_F = 605\,\text{fF}$, and A_0=60 dB; Rauch TIA: $C_{IN} = 10\,\text{pF}$, $R_{IN} = 50\,\Omega$, $R_F = 1.5\,\text{k}\Omega$, $C_F = 720\,\text{fF}$, and A_0=60 dB) for different unity gain bandwidths.

Moreover, the 3-dB bandwidth of the Rauch TIA is given by:

$$\omega_{3dB} = \omega_n \sqrt{1 - 2\zeta^2 + \sqrt{(2\zeta^2 - 1)^2 + 1}}. \tag{4.9}$$

Fig. 4.3 (a) compares the transfer function of the first-order and Rauch TIAs with nearly identical components, except for R_{IN} to achieve the same gain and 3-dB baseband bandwidth. Thanks to the complex conjugate poles of the Rauch TIA, it exhibits a flat in-band gain and a second-order low-pass response, which is desirable for 5G applications.

4.3.2 Input Impedance

Secondly, the input impedance (Z_{IN}) of both structures is compared. Considering $A(s) \gg 1$, the input impedance of the first-order TIA is derived as

follows:

$$Z_{IN,f} = \frac{R_F}{A(s)} \cdot \frac{1}{sR_F\left(C_F + \frac{C_{IN}}{A(s)}\right) + 1} \tag{4.10}$$

$$\xrightarrow{C_F \gg \frac{C_{IN}}{A(s)}} Z_{IN,f} \approx \frac{R_F}{A_0} \cdot \frac{1 + \frac{s}{\omega_p}}{1 + sR_FC_F}. \tag{4.11}$$

Hence, the input impedance of the first-order TIA consists of one zero, determined by the TIA amplifier's dominant pole, and one pole at $1/R_FC_F$. Typically, $1/R_FC_F$ also defines the TIA's 3-dB bandwidth, ω_{3dB}. Consequently, as can be gathered from (4.11), setting $\omega_p \geq \omega_{3dB}$ ensures that the TIA input impedance remains approximately constant across the in-band frequencies.

As shown in Fig. 4.3 (b), in a desired scenario ($\omega_p \geq \omega_{3dB}$), $Z_{IN,f}$ remains low and constant (i.e., R_F/A_0) across the 3-dB bandwidth. However, as discussed earlier, to meet this condition with $A_0 \geq 60\,\text{dB}$, the unity gain bandwidth of the TIA amplifier must exceed 200 GHz ($\omega_u = A_0 \cdot \omega_p$), which, if not impossible, is a highly challenging and power-hungry requirement. A more realistic value for ω_u is around 20 GHz, resulting in ($\omega_p \ll \omega_{3dB}$). Hence, $Z_{IN,f}$ remains R_F/A_0 near DC but begins to increase at ω_p, reaching its maximum at the bandwidth edge. Beyond ω_{3dB}, the input impedance becomes nearly constant due to the pole created by R_F and C_F. At higher baseband frequencies, C_{IN} dominates, reducing $Z_{IN,f}$. Therefore, the input impedance of the first-order TIA is highly sensitive to the TIA amplifier's gain bandwidth and PVT variations.

The input impedance of Rauch TIA can be calculated by:

$$Z_{IN,r} = \frac{R_F}{A(s)} \cdot \frac{sA(s)C_FR_{IN} + 1}{s^2R_{IN}C_{IN}R_FC_F + s\left(R_{IN} + R_F\right)C_F + 1}. \tag{4.12}$$

Due to its low-frequency zero at $1/(A_0C_FR_{IN})$, even when ($\omega_p \geq \omega_{3dB}$), $Z_{IN,r}$ increases from R_F/A_0 near DC to $R_{IN} \parallel R_F \approx R_{IN}$ at the bandwidth edge. It then drops by -20 dB/dec slope due to the complex poles at ω_{3dB}. This bandpass behavior will later be leveraged to improve the selectivity and bandwidth of the RF front end. Interestingly, as can be gathered from Fig. 4.3 (b), $Z_{IN,r}$ is primarily determined by the passive components and is largely insensitive to the amplifier gain and ω_u. However, since $Z_{IN,r}$ at the bandwidth edge approaches R_{IN}, the input impedance of the Rauch TIA can exceed that of the first-order TIA. Consequently, in LNTA-based RXs, designers must consider potential in-band linearity degradation due to the increased load on the LNTA. The impact of Rauch TIA impedance peaking on RX in-band linearity will be

discussed later in this paper.

4.3.3 Linearity

Next, the linearity of both TIA structures is evaluated by comparing their input/output voltage swing and the loop gain. As shown in Fig. 4.3 (a), the in-band transfer functions of both TIAs are nearly identical. The output voltage swing of the TIA amplifier is $-R_F I_{IN}$ for both, resulting in a corresponding input voltage of $R_F I_{IN}/A(s)$. Therefore, the input and output voltage swings of the TIA amplifiers are the same for in-band input signals.

Another key factor influencing the TIA's in-band linearity is loop gain. The loop gain of the first-order TIA is calculated as follows:

$$LG = \frac{-R_{Mix}}{R_{Mix}+R_F} \cdot \frac{A_0}{1+\frac{s}{\omega_p}} \cdot \frac{sR_F C_F + 1}{sR_F \parallel R_{Mix} C_{IN} + 1}, \tag{4.13}$$

where R_{Mix} is the impedance seen from the baseband port of passive mixers towards the RF front end. The loop gain has two poles (ω_p and $1/(R_F \parallel R_{Mix}C_{IN})$) and one zero ($1/(R_F C_F)$). As discussed earlier, in most practical cases, ω_p lies within the 3-dB bandwidth, acting as the dominant pole and decreasing the loop gain with a -20 dB/dec slope. Unfortunately, the second pole, $1/(R_F \parallel R_{Mix}C_{IN})$, typically lies below ω_{3dB}, since C_{IN} is much larger than C_F to absorb far-out out-of-band blocker current. Consequently, the loop gain experiences -40 dB/dec roll-off at the passband edge due to the second pole. Eventually, the zero at the bandwidth edge increases the slope back to -20 dB/dec, improving TIA's stability [90]. As can be gathered from Fig. 4.4, TIA in-band linearity is expected to worsen at the passband edges due to the significant drop in loop gain. Reducing C_{IN} shifts the second pole to higher frequencies, thus increasing the loop gain at the passband edges. However, C_{IN} also absorbs the out-of-band blocker currents. Hence, reducing C_{IN} increases the blocker swing at the baseband port of passive mixers, which degrades the out-of-band linearity performance of LNTA and passive mixers. This issue creates a trade-off between in-band and out-of-band linearity.

The loop gain of the Rauch TIA is derived as:

$$LG \approx \frac{-R_{Mix}}{R_{Mix}+R_F} \cdot \frac{A_0}{1+\frac{s}{\omega_p}} \cdot \frac{s^2 R_{IN} C_{IN} R_F C_F + s\left(R_{IN}+R_F\right) C_F + 1}{\left(sR_F \parallel R_{Mix} C_{IN} + 1\right)\left(sR_{IN} C_F + 1\right)}. \tag{4.14}$$

The loop gain of Rauch TIA has three poles and two zeros. The first two poles ω_p and $1/(R_F \parallel R_{Mix}C_{IN})$ are the same as those in the first-order TIA, while the

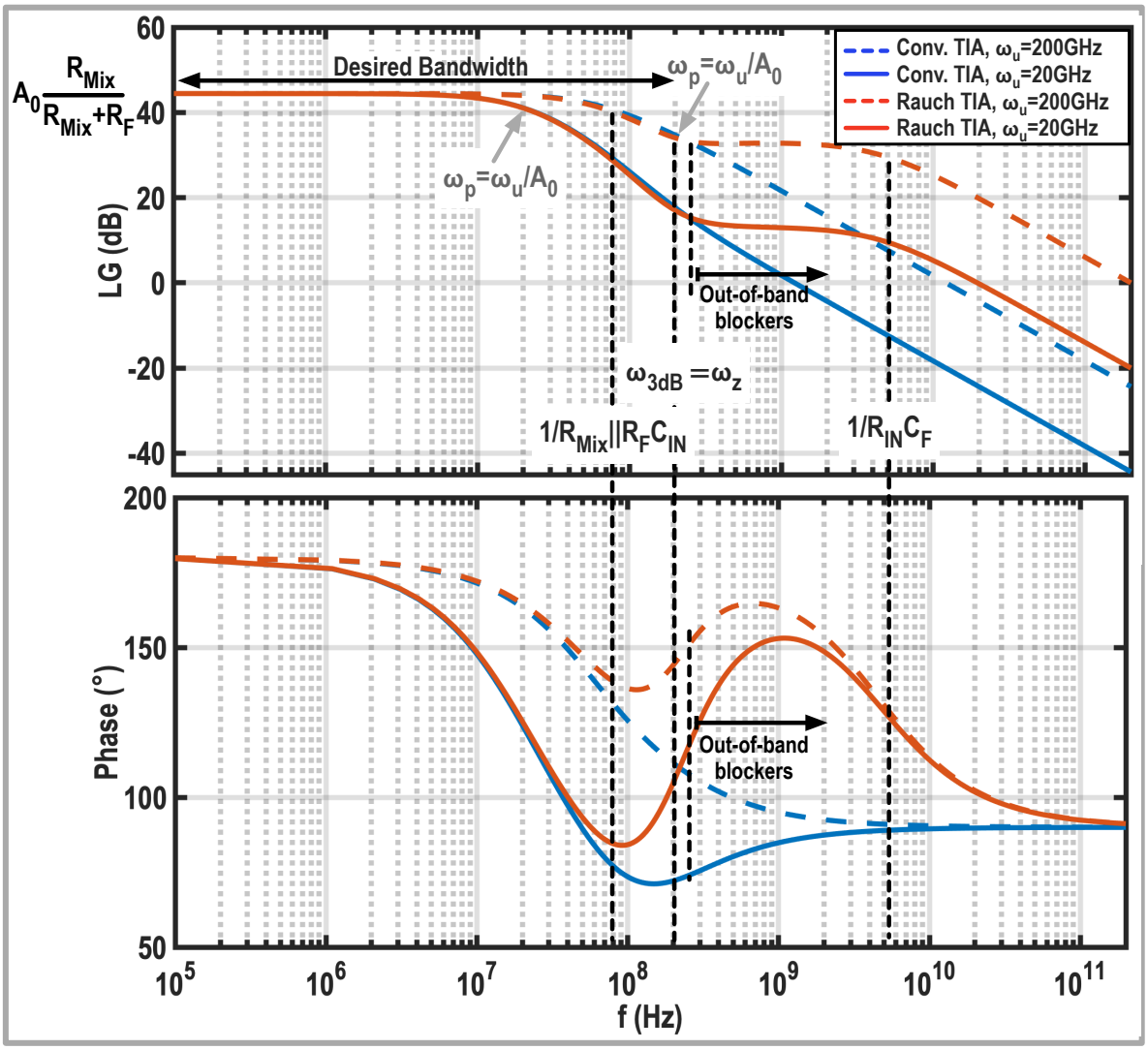

Figure 4.4: Bode plot of simulated loop gain for the first-order and Rauch TIAs.

third pole, $1/(R_{IN}C_F)$, is located far from the bandwidth edge. Consequently, the in-band response of the Rauch TIA's loop gain is similar to that of the first-order TIA. However, as illustrated in Fig. 4.4, the Rauch TIA loop gain also has two zeros at the bandwidth edge, which flatten the loop gain at the close-in out-of-band frequencies. This higher loop gain at out-of-band frequencies helps suppress intermodulation between in-band and close-in blockers, which can fall within the 3-dB bandwidth and degrade RX performance. Consequently, the Rauch structure exhibits better linearity performance in the presence of blockers compared with the first-order TIA.

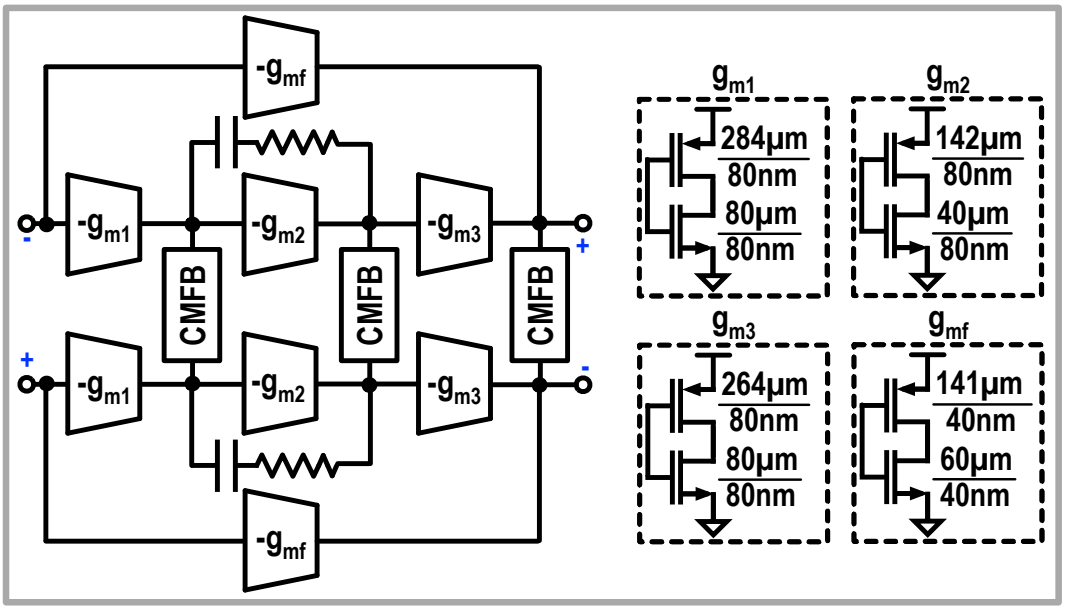

Figure 4.5: Schematic of the three-stage OTA.

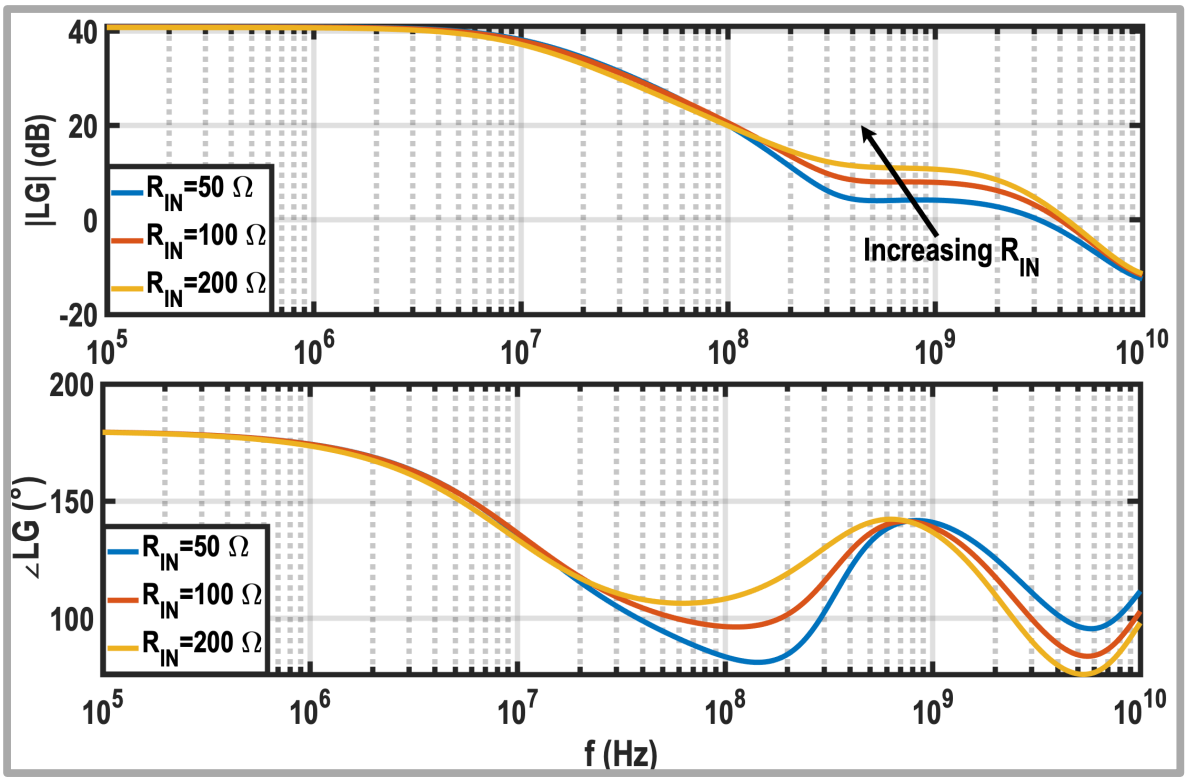

Figure 4.6: Simulated loop gain of the TIA.

The loop gain in the flat region can be estimated by:

$$|LG_{flat}| = A_0 \cdot \frac{\omega_p}{\omega_n} \cdot \sqrt{\frac{R_{IN}C_F}{R_F C_{IN}}} = \frac{\omega_u}{\omega_n} \cdot \sqrt{\frac{R_{IN}C_F}{R_F C_{IN}}}. \tag{4.15}$$

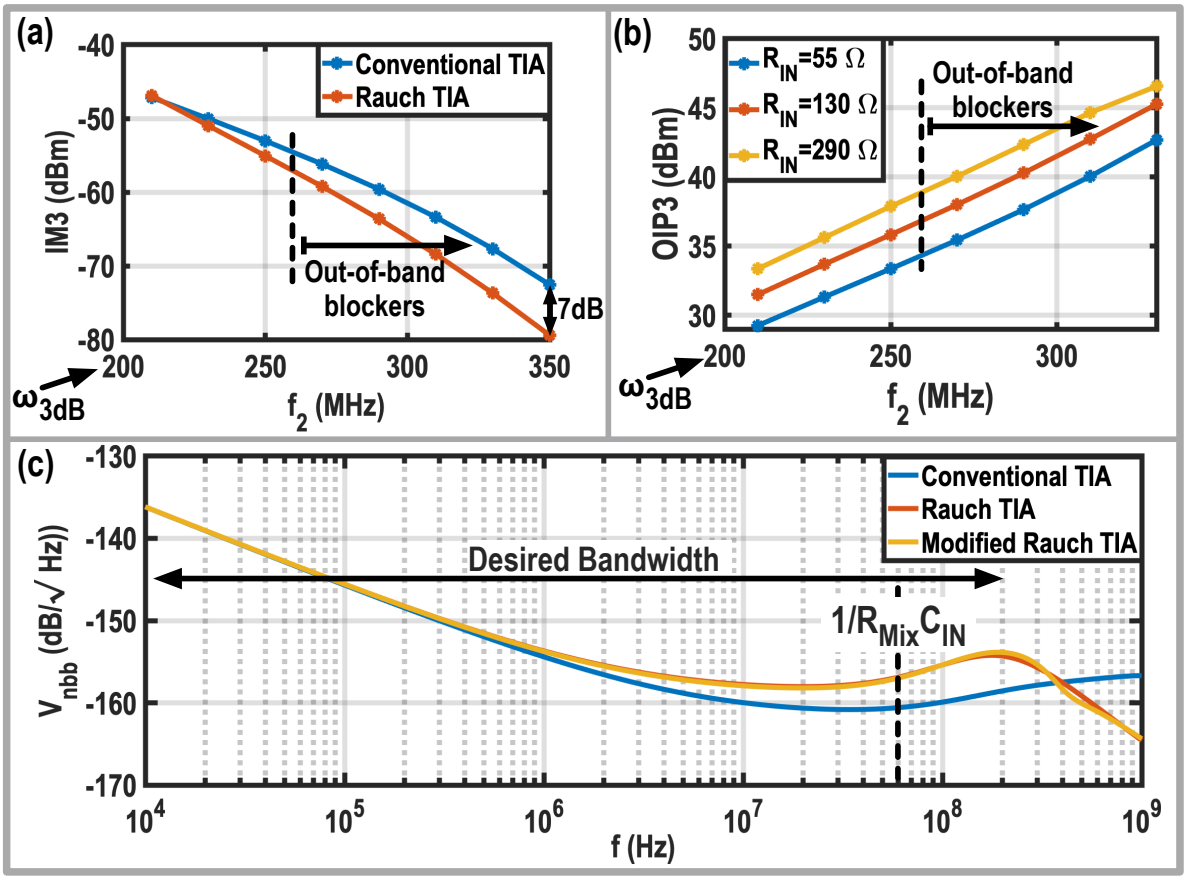

Figure 4.7: (a) Comparison between linearity performance of the first-order TIA and Rauch TIA; (b) Effect of increasing R_{IN} and reducing C_{IN} on the linearity performance of the Rauch TIA; (c) Comparison between the output noise of the first-order TIA, conventional Rauch TIA, and the modified Rauch TIA with an active third-order high-pass filter in its feedback.

At first glance, the simplest way to increase the loop gain in the flat region is by raising ω_u and lowering ω_n. However, enhancing ω_u increases the power consumption, and technology limitations will eventually impose a cap. Additionally, reducing ω_n necessitates a smaller ζ to maintain the same 3-dB bandwidth (see (4.9)), which can cause stability issues. Therefore, adjusting R and C is a more effective way to increase loop gain in the flat region. To maintain ζ and ω_n, the feedback and input RC constants ($R_F C_F$ and $R_{IN} C_{IN}$) must remain constant. Since R_F is set by the gain requirement of the RX chain, the only remaining adjustable parameters are R_{IN} and C_{IN}. Thus, to increase loop gain in the flat region while keeping the TIA transfer function constant, R_{IN} must be proportionally increased and C_{IN} reduced. Note that increasing R_{IN} raises the input impedance of the Rauch TIA, which degrades the linearity performance of LNTA. The effect of increasing R_{IN} on the LNTA and RX linearity will be discussed later in this paper.

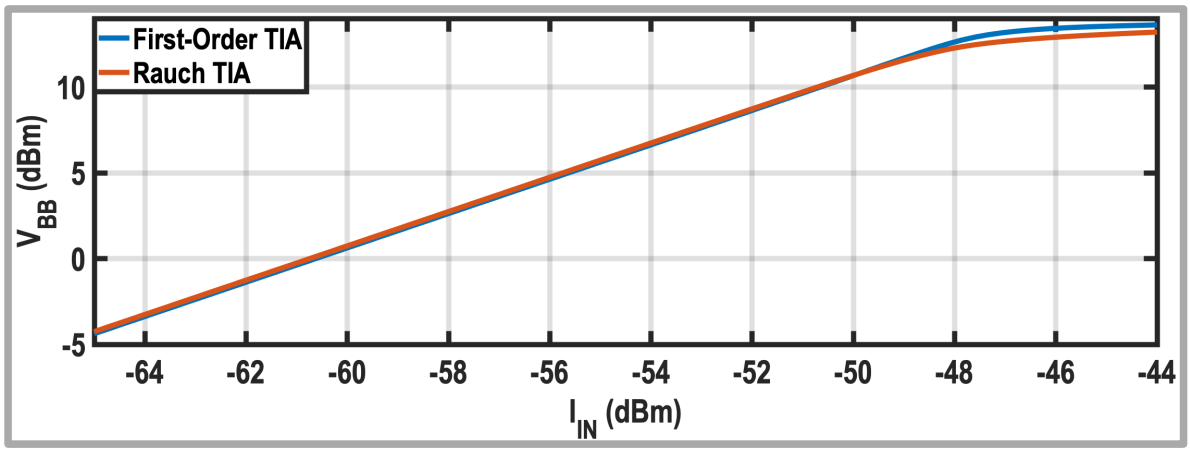

Figure 4.8: Simulated OP1dB of the first-order TIA and Rauch TIA at the passband edge.

Finally, the first-order TIA and Rauch TIA are simulated in Cadence using the same components used in the simulations presented in Fig. 4.3. As shown in Fig. 4.5, a three-stage operational transconductance amplifier (OTA) is designed as the TIA amplifier to achieve the desired loop gain and meet the in-band linearity requirements. Following the approach in [52], each stage of the OTA is constructed using inverters, with the detailed sizing of these inverters provided in Fig. 4.5. Common-mode feedback (CMFB) circuits [21] are placed at the output of each stage to ensure that each inverter is biased near the supply rail midpoint, $\sim V_{DD}/2$. To ensure OTA stability, two compensation techniques are employed: Miller compensation, which sets the dominant pole, and feedforward compensation, which introduces a high-frequency zero to counterbalance the second pole and maintain a sufficient phase margin. The simulated loop gain of the TIA is depicted in Fig. 4.6, where the worst phase margin is 73°, and increasing R_{IN} enhances the loop gain at the bandwidth edge.

Then, two tones (f_1 and f_2) are applied at the input, with the third-order intermodulation term (IM3) falling within the desired band. The first tone (f_1) is placed at the bandwidth edge (i.e. 200 MHz), while the second tone (f_2 is swept across the close-in blocker range. As shown in Fig. 4.7 (a), the Rauch TIA offers 7 dB better linearity performance than the first-order TIA, thanks to its selectivity and higher loop gain. Moreover, Fig.4.7 (b) shows the effect of increasing R_{IN} on the linearity performance of the Rauch TIA, resulting in a 5 dB improvement in linearity performance. However, as shown in Fig. 4.8, the simulated output 1-dB compression point (OP1dB) at the bandwidth edge of the Rauch TIA is slightly lower than first-order TIA (12.6 dBm compared to 13.3 dBm).

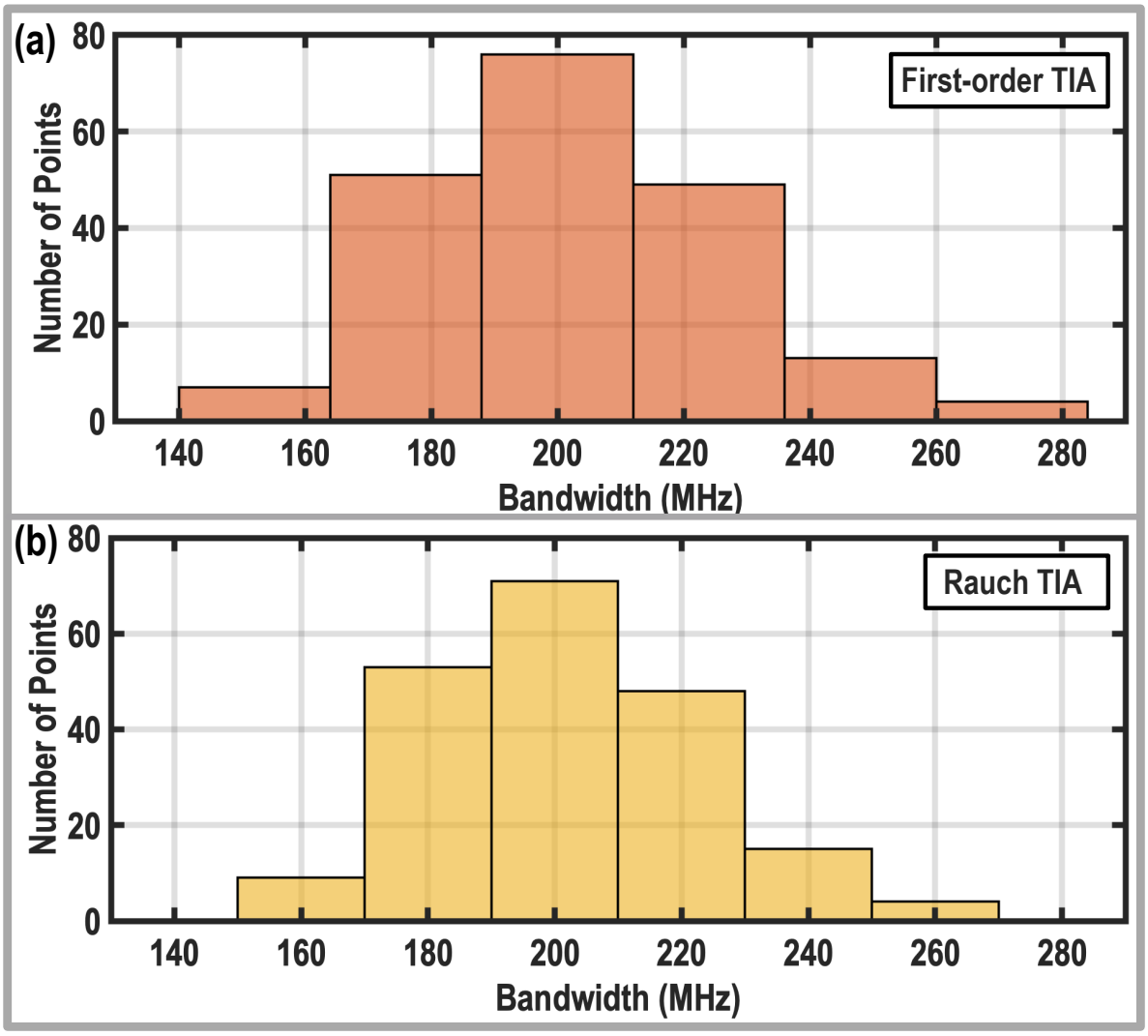

Figure 4.9: Monte Carlo simulation results showing the statistical variations in the 3-dB bandwidth of (a) First-order TIA, and (b) Rauch TIA.

4.3.4 Performance over PVT Variations

To evaluate the impact of process, voltage, and temperature (PVT) variations on the performance of the first-order and Rauch TIAs, a Monte Carlo simulation was conducted with global variations across 200 sample points. Since both TIA structures use identical feedback resistors, their transimpedance gains exhibit the same statistical distribution, with a standard deviation of 0.7 dB.

As can be gathered from (4.4) and (2.27), and illustrated in the simulation results in Fig. 4.9 (a) and (b), the 3-dB bandwidth of both TIA structures is sensitive to PVT variations. The first-order TIA demonstrates a slightly higher standard deviation in bandwidth (23.9 MHz) compared to the Rauch TIA

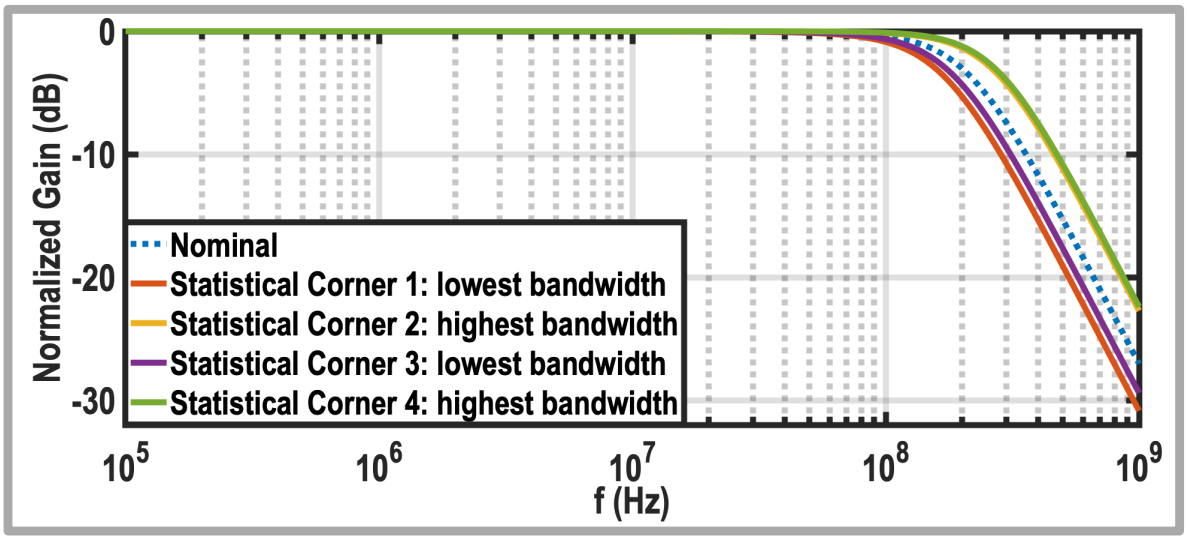

Figure 4.10: Normalized transfer function of Rauch TIA under extreme statistical corners.

(21.1 MHz), although both have an average 3-dB bandwidth of approximately 200 MHz. Consequently, calibration is required for both TIAs to maintain the desired 3-dB bandwidth.

To further assess the filtering behavior of Rauch TIA under extreme PVT conditions, four statistical corners were defined based on the highest and lowest bandwidth values observed in the Monte Carlo simulation. Fig. 4.10 shows the *normalized* transimpedance gain of Rauch TIA to compensate for gain variations across these corners to enhance visualization. As indicated by (2.26) and confirmed in Fig. 4.10, the filtering shape and slope of Rauch TIA remain largely unaffected by PVT variations, since the damping ratio depends on the resistors and capacitors ratios.

4.3.5 Noise

In the next step, the output noise of the first-order and Rauch TIAs is estimated and compared. As shown in Fig. 4.2, the TIA amplifier, R_F, and R_{IN} noise are modeled with $v_{n,A}$, $v_{n,RF}$, and $v_{n,RIN}$, respectively. The output noise of first-order TIA can be calculated as follows:

$$v_{nbb}^2 = v_{n,A}^2 \cdot \left(1 + \frac{R_F}{R_{Mix}} \cdot \frac{sR_{Mix}C_{IN} + 1}{sC_F R_F + 1}\right)^2 + v_{n,RF}^2 \cdot \left(\frac{1}{1 + sC_F R_F}\right)^2. \quad (4.16)$$

The R_F noise is low-pass filtered and directly appears at the TIA output. The noise transfer function of the TIA amplifier has one zero and one pole. Since the zero created by C_{IN} and R_{Mix} is within the 3-dB bandwidth, the noise of

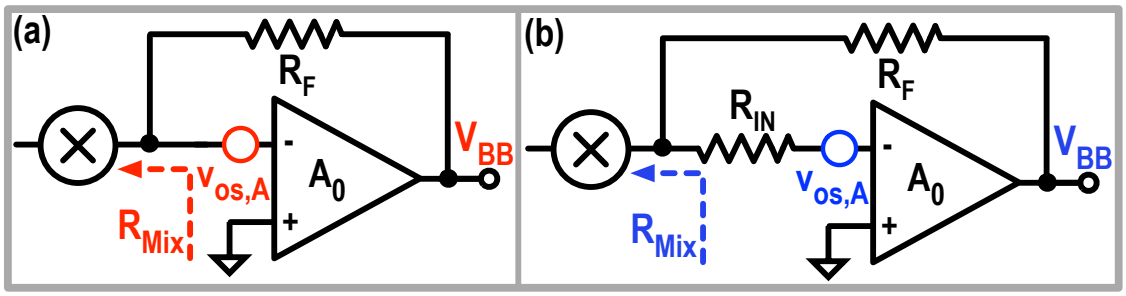

Figure 4.11: Simplified model for DC offset analysis of (a) the first-order TIA and (b) the Rauch TIA.

the TIA amplifier increases after the zero frequency. Then, the TIA output noise becomes constant at the bandwidth edge due to the pole formed by R_F and C_F (see simulation results in Fig. 4.7 (c)). Additionally, the overall TIA output noise improves with a larger R_{Mix}.

The output noise of the Rauch TIA is derived as follows:

$$v_{nbb}^2 = v_{n,A}^2 \cdot \left(1 + \frac{R_F}{R_{Mix}} \cdot \frac{sR_{Mix}C_{IN}+1}{s^2R_{IN}C_{IN}C_FR_F + sC_FR_F\left(1+\frac{R_{IN}}{R_F||R_{Mix}}\right)+1}\right)^2$$
$$+ v_{n,RF}^2 \cdot \left(\frac{1}{s^2R_{IN}C_{IN}C_FR_F + sC_FR_F\left(1+\frac{R_{IN}}{R_F||R_{Mix}}\right)+1}\right)^2$$
$$+ v_{n,RIN}^2 \cdot \left(\frac{R_F}{R_{Mix}} \cdot \frac{sR_{Mix}C_{IN}+1}{s^2R_{IN}C_{IN}C_FR_F + sC_FR_F\left(1+\frac{R_{IN}}{R_F||R_{Mix}}\right)+1}\right)^2. \quad (4.17)$$

Similar to the first-order TIA, the zero formed by C_{IN} and R_{Mix} increases the in-band noise of Rauch TIA. Beyond the bandwidth edge, the noise contributions from all components decrease due to the presence of two complex conjugate poles in their respective noise transfer functions. However, as can be observed in Fig. 4.7 (c), compared to the first-order TIA, the Rauch TIA includes an additional noise source, R_{IN}, which degrades its overall noise performance. Consequently, there is another trade-off between noise and linearity of the Rauch TIA: increasing R_{IN} improves its loop gain and in-band linearity but degrades its output noise.

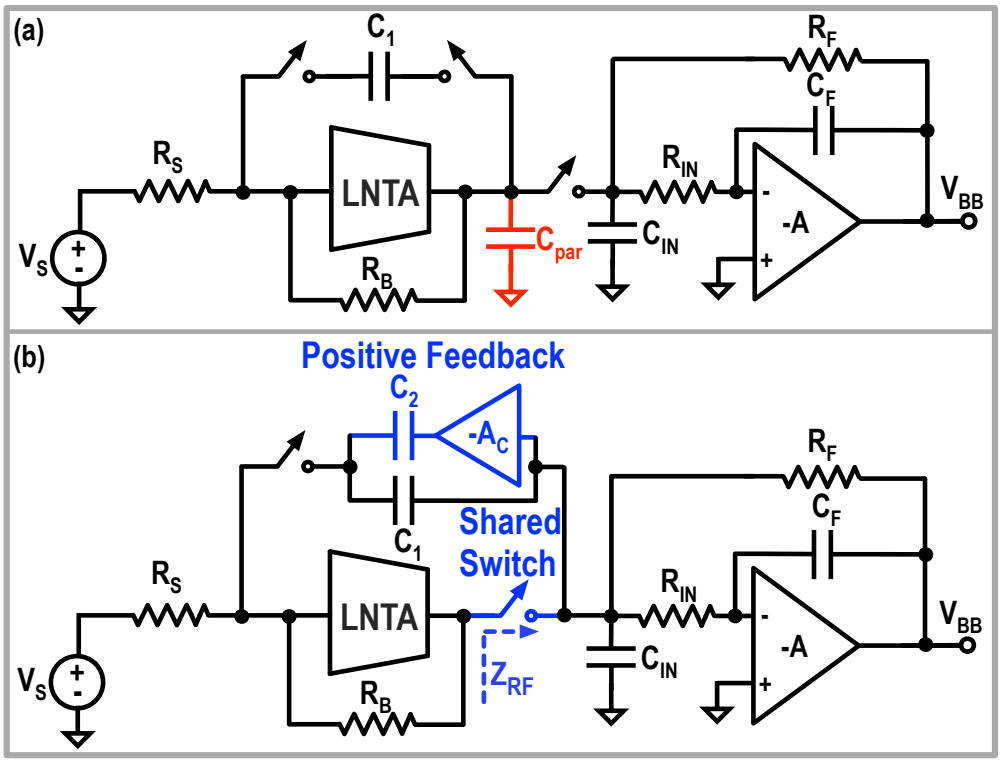

Figure 4.12: Current-mode RX utilizes the Rauch TIA with (a) conventional RF front-end and (b) proposed RF front-end.

4.3.6 DC Offset

In current-mode RXs, the TIA is the primary contributor to overall DC offset performance, making it crucial to analyze the DC offset transfer function for both first-order and Rauch TIA configurations. Fig. 4.11 shows the simplified model for DC offset calculations, where the TIA amplifier's DC offset is modeled as a voltage source, $v_{os,A}$, and all capacitors are removed, as they act as open circuits at DC. Notably, the DC offset transfer function for both TIAs is the same and can be calculated by

$$DC_{offset} = v_{os,A}\left(1 + \frac{R_F}{R_{Mix}}\right). \tag{4.18}$$

Therefore, increasing R_{Mix} helps reduce the gain of the TIA amplifier DC offset.

4.3.7 Discussion

While the in-band noise of the Rauch TIA is higher than that of the first-order TIA, this issue can be mitigated by utilizing an LNTA to relax the TIA's noise requirements. The Rauch TIA also has a higher input impedance, which

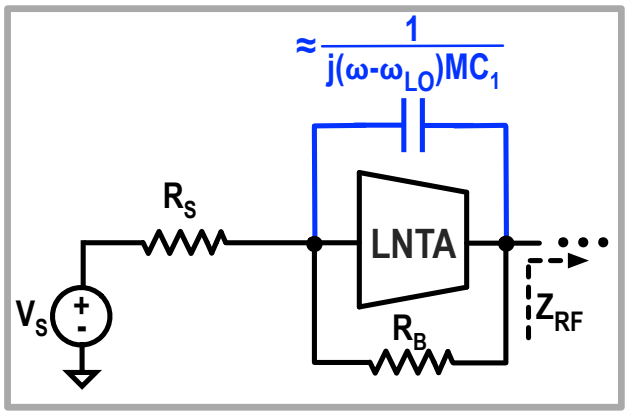

Figure 4.13: The equivalent model of the RF front end of the preliminary RX structure in Fig. 4.12 (a).

could raise concerns about the potential degradation of in-band linearity in LNTA-based RXs. However, as will be demonstrated later in this paper, this is not the case. Notably, the Rauch TIA provides better selectivity and higher loop gain at the bandwidth edge, which are key advantages for handling close-in blockers in 5G applications. Therefore, this work employs Rauch TIA to leverage its superior selectivity and loop gain characteristics.

4.4 Proposed RF Front-End

As can be gathered from (4.13) and (4.14), the TIA loop gain is limited by the impedance observed from the baseband port of passive mixers towards the RF front end, denoted R_{Mix}. In mixer-first RXs, R_{Mix} is constrained by both the antenna impedance ($50\,\Omega$) and the large parasitic capacitors of passive mixers. To address this, we incorporate an LNTA that offers a higher output impedance than the antenna and alleviates parasitic capacitance at the LNTA output by allowing for reduced sizes of the down-converting passive mixers.

4.4.1 Expanding RX Operating Frequency

Fig. 4.12 (a) presents a preliminary block diagram of the proposed RX consisting of an LNTA and the Rauch TIA. An N-path notch filter is placed in the LNTA feedback to achieve RF selectivity at the RX input [45, 69–75, 78, 79, 81, 85, 88, 99, 100]. However, two switch sets at the LNTA output —one for the N-path notch filter and another for the down-converting passive mixers— increase the total parasitic capacitance at the LNTA output (denoted as C_{par}). This parasitic capacitance, in combination with the LNTA output resistance, creates a pole that limits the operating frequency of prior-art LNTA-based RXs

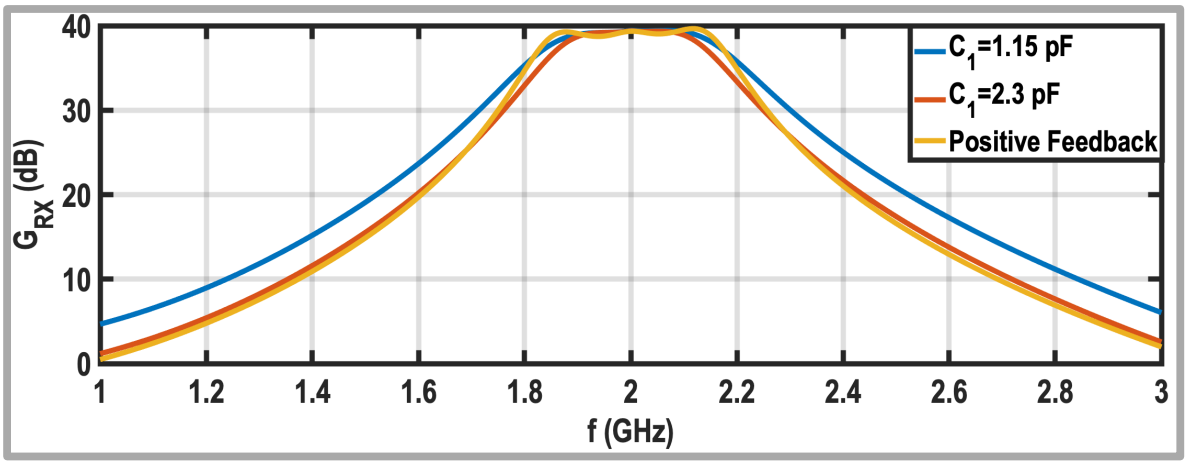

Figure 4.14: Comparing the RX far-out front-end rejection. Blue and red curves are simulated using the conventional structure with an N-path notch filter in the LNTA feedback, and the orange one employs the proposed structure.

to below 6 GHz [45,69–75,78,79,81,85,88,99,100]. To enhance the RX operating frequency, Fig. 4.12 (b) combines the two switch sets into one [97,111], reducing C_{par} and allowing the pole to shift beyond 8 GHz.

4

4.4.2 3-dB Bandwidth Expansion

The 3-dB bandwidth of the preliminary RX structure in Fig. 4.12 (a) is limited at its input node. Due to the transparency of passive mixers, the capacitors in the N-path notch filter are upconverted to the RF domain. As a result, the N-path notch filter can be modeled as a bandpass-shaped impedance in the RF domain, as illustrated in Fig. 4.13 and discussed in [70]. Therefore, the RX input bandwidth is governed by the Miller effect of N-path notch filter (C_{Miller}) and the antenna resistance (R_S) , which can be estimated as follows:

$$BW_{RF} = \frac{2}{R_S C_{Miller}} \approx \frac{2}{R_S A_{v,LNTA} M C_1}, \tag{4.19}$$

where C_1 and M represent the unit capacitor of the N-path notch filter and the number of the local oscillator (LO) phases, respectively. $A_{v,LNTA}$ is the LNTA voltage gain and can be approximated by $G_m Z_{RF}(f)$, where G_m is the LNTA's transconductance and $Z_{RF}(f)$ is its load. For 5G new radios, the RF bandwidth reach up to 400 MHz for operating frequencies above 3 GHz, necessitating a reduction in C_1 to increase the bandwidth. However, simulation results in Fig. 4.14 show that reducing C_1 from 2.3 pF to 1.15 pF to boost the RF bandwidth from 200 MHz to 400 MHz leads to a 4 dB degradation in out-of-band rejection

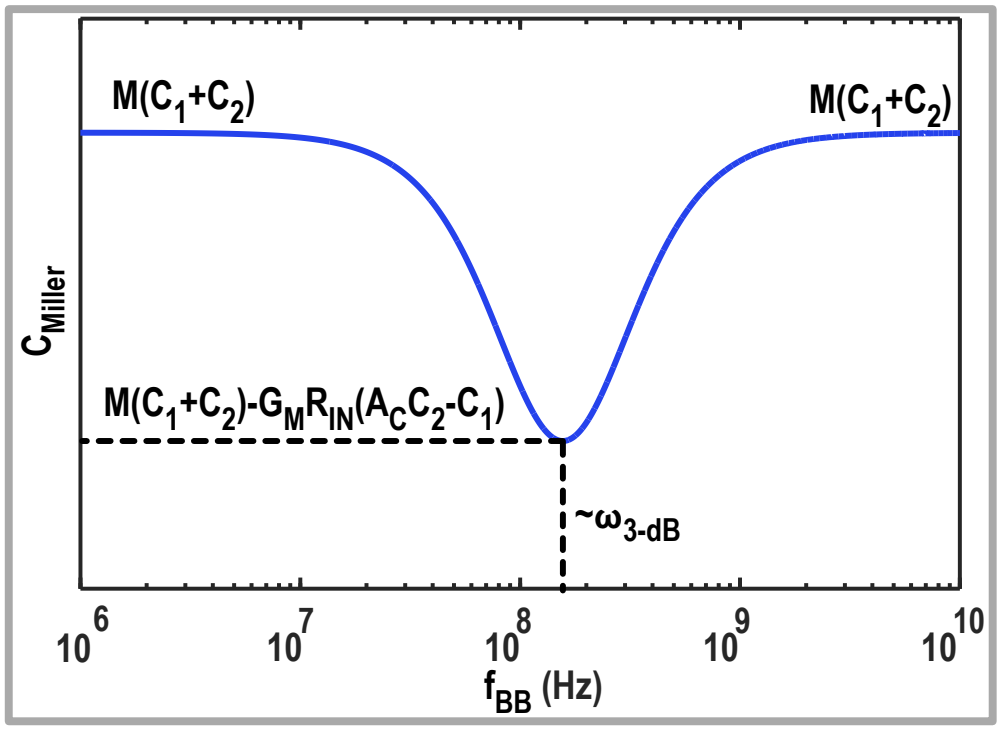

Figure 4.15: Effective Miller capacitor versus the baseband frequency.

at a specific far-out offset frequency from the LO frequency. This degradation may impact RX performance in base station co-location applications where a -4 dBm blocker is present.

This work leverages the bandpass-shaped input impedance of the Rauch TIA to enhance the RF bandwidth without compromising the out-of-band rejection and linearity. To achieve this, a positive feedback branch, consisting of an amplifier (A_c) and a series capacitor (C_2), is introduced in parallel with C_1, as depicted in Fig. 4.12 (b). This technique modifies the Miller capacitor at the RX input to:

$$C_{Miller} = M \cdot (\,(1 + G_m Z_{RF}\,(f))\,C_1 + (1 - G_m Z_{RF}\,(f)\,A_C)\,C_2). \tag{4.20}$$

At low baseband frequencies, the input impedance of Rauch TIA is R_F/A_0, which effectively reduces Z_{RF} and undermines the impact of positive feedback. Hence, as shown in Fig. 4.15, the equivalent Miller capacitor is at its maximum, $M\,(C_1 + C_2)$. As the frequency increases, the input impedance of the Rauch TIA starts to rise towards R_{IN}, enhancing the effect of the positive feedback path. At the passband edges, Z_{RF} can be approximated by R_{IN}/M, leading to

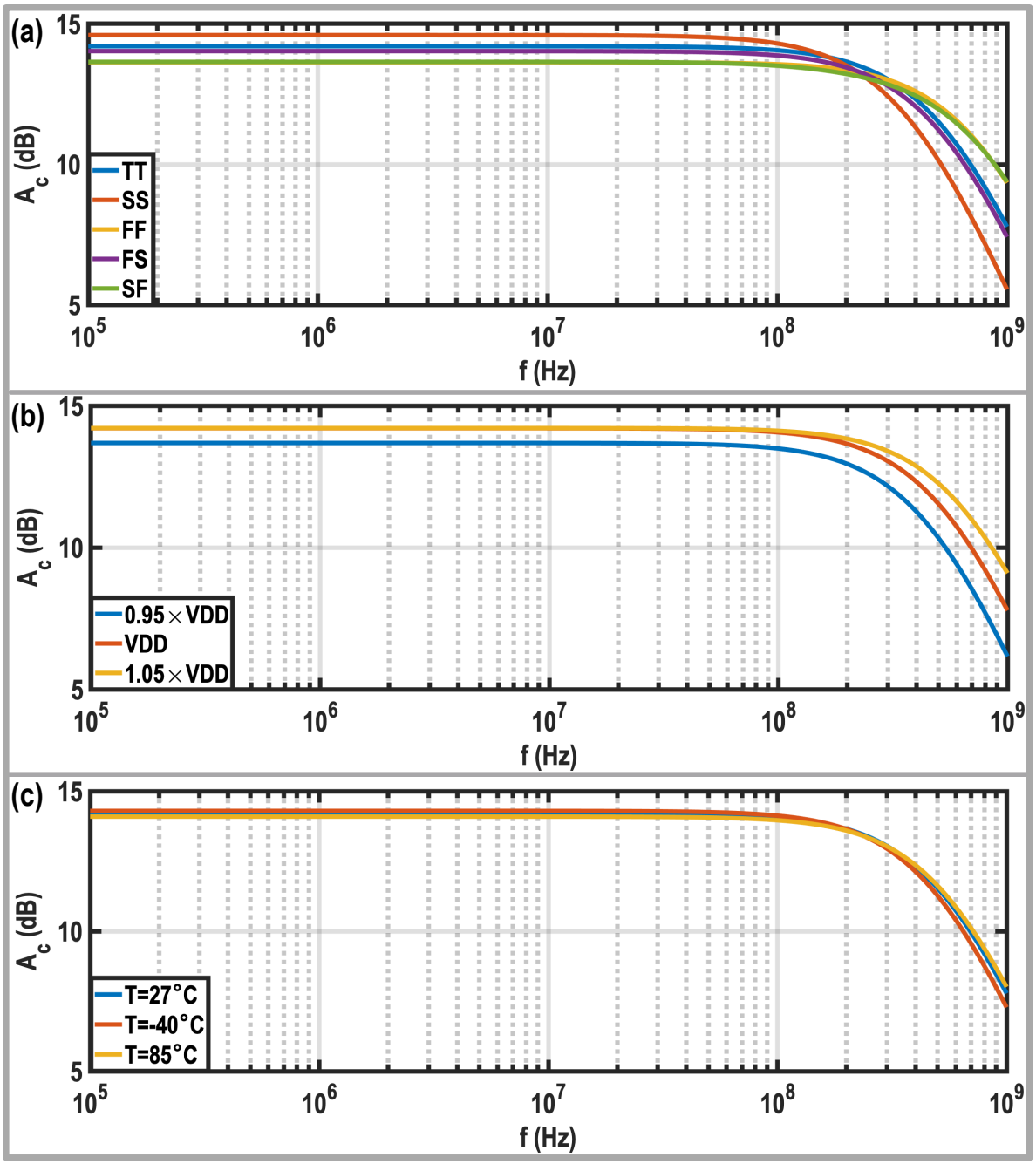

Figure 4.16: Gain of positive feedback amplifier across (a) process, (b) supply, and (c) temperature variations.

the following approximation for the Miller capacitor:

$$C_{Miller} = M \times (C_1 + C_2) - G_m R_{IN} \left(A_c C_2 - C_1\right). \tag{4.21}$$

Therefore, as shown in Fig. 4.15, the proposed positive feedback structure reduces the Miller capacitance at the bandwidth edge, thus flattening the RX in-

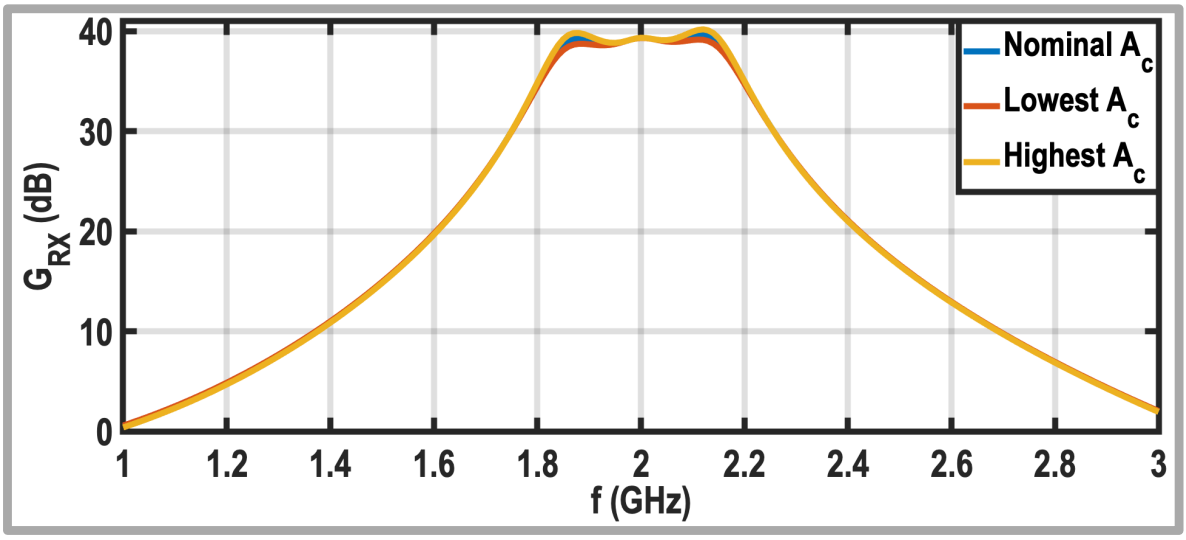

Figure 4.17: Simulated RX gain for the worst-case scenarios of A_c.

band response and expanding the RX bandwidth. At out-of-band frequencies, as can be inferred from (4.12), the input impedance of the Rauch TIA decreases due to the presence of its poles, which diminishes the effect of the proposed positive feedback. As a result, the Miller capacitance increases at far-out frequencies, returning to $M(C_1 + C_2)$. This behavior enhances the out-of-band rejection and improves the filtering roll-off of the proposed RX. Fig. 4.14 demonstrates that, compared to the conventional structure, the proposed positive feedback effectively boosts the 3-dB bandwidth, flattens the in-band response, increases roll-off, and maintains out-of-band rejection. Additionally, the noise and linearity requirements for the added amplifiers are relaxed, as their inputs are connected to the TIA virtual ground, and their noise experiences bandstop filtering when appearing at the RX output.

4.4.3 Impact of PVT-induced Variations of Positive Feedback Amplifier

As can be gathered from (4.21), an increase in the gain of the positive feedback amplifier, A_c, due to PVT variations can cause the Miller capacitance to become negative at the bandwidth edges, potentially leading to stability issues. To evaluate this, the amplifier gain, implemented with a self-biased inverter, was simulated under various PVT conditions, as shown in Fig. 4.16. For the nominal corner, the simulated gain is 14.2 dB, with a 3-dB bandwidth exceeding 500 MHz. The PVT-induced gain variation is limited to ± 0.6 dB, as PVT variations affect both transconductance and output resistance in opposing directions, keeping the overall gain stable.

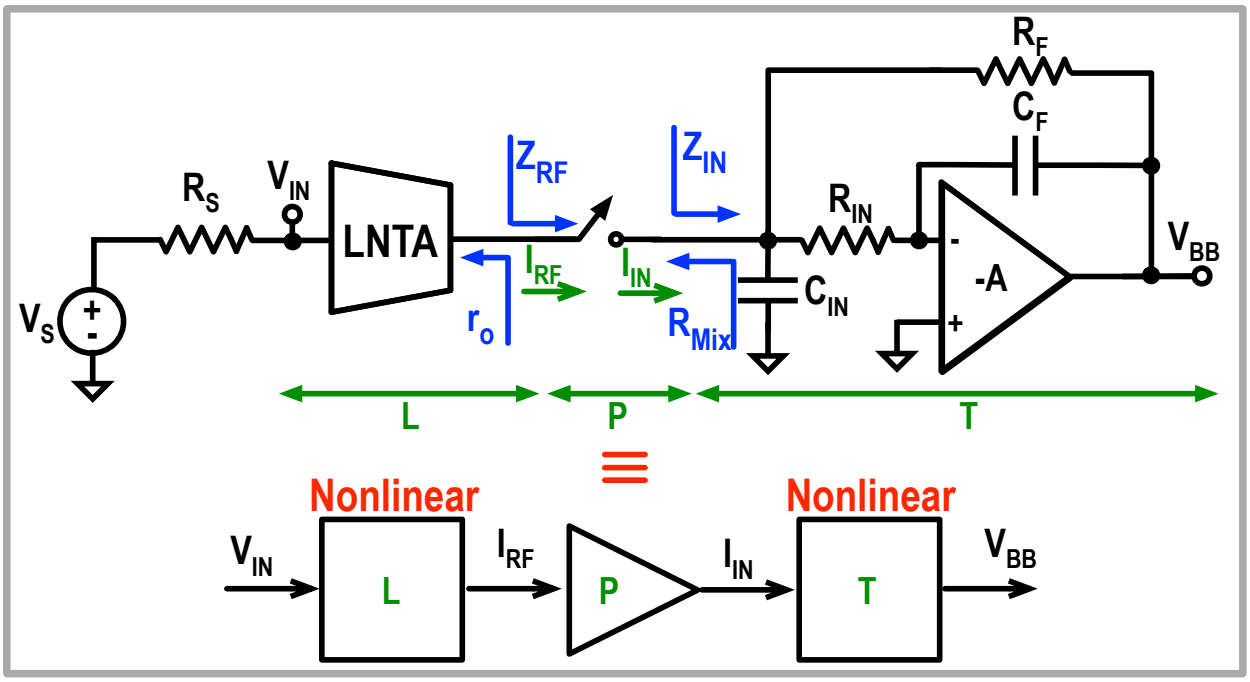

Figure 4.18: A simplified model of the proposed RX for in-band linearity analysis.

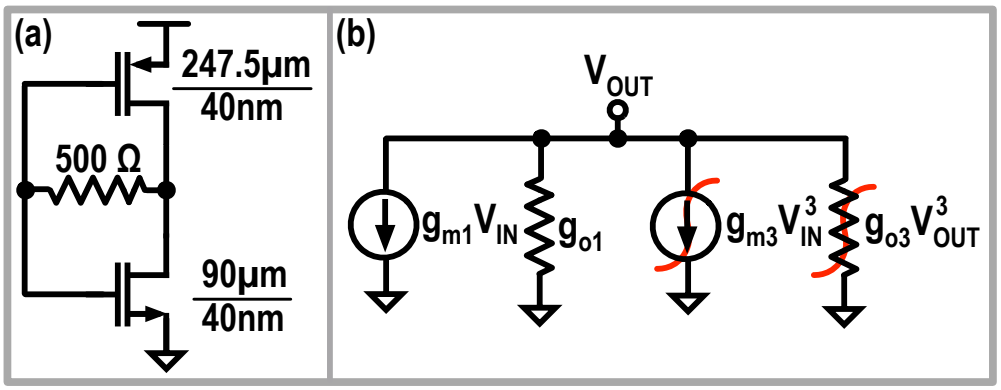

Figure 4.19: (a) Transistor-level implementation of the LNTA; (b) Small signal model of the LNTA.

To evaluate worst-case scenarios, A_c was intentionally varied by $\pm 1.8\,\text{dB}$ in the RX chain gain simulations. As shown in Fig. 4.17, these variations result in only $\pm 0.6\,\text{dB}$ change in RX gain peaking. Thus, PVT-induced variations in A_c do not cause stability issues. Moreover, the resulting RX gain peaking can easily be compensated by adjusting C_2.

4.5 RX In-Band Linearity

In this section, we analyze the in-band linearity of the proposed receiver. Fig. 4.18 presents a simplified RX model, which consists of three cascaded blocks:

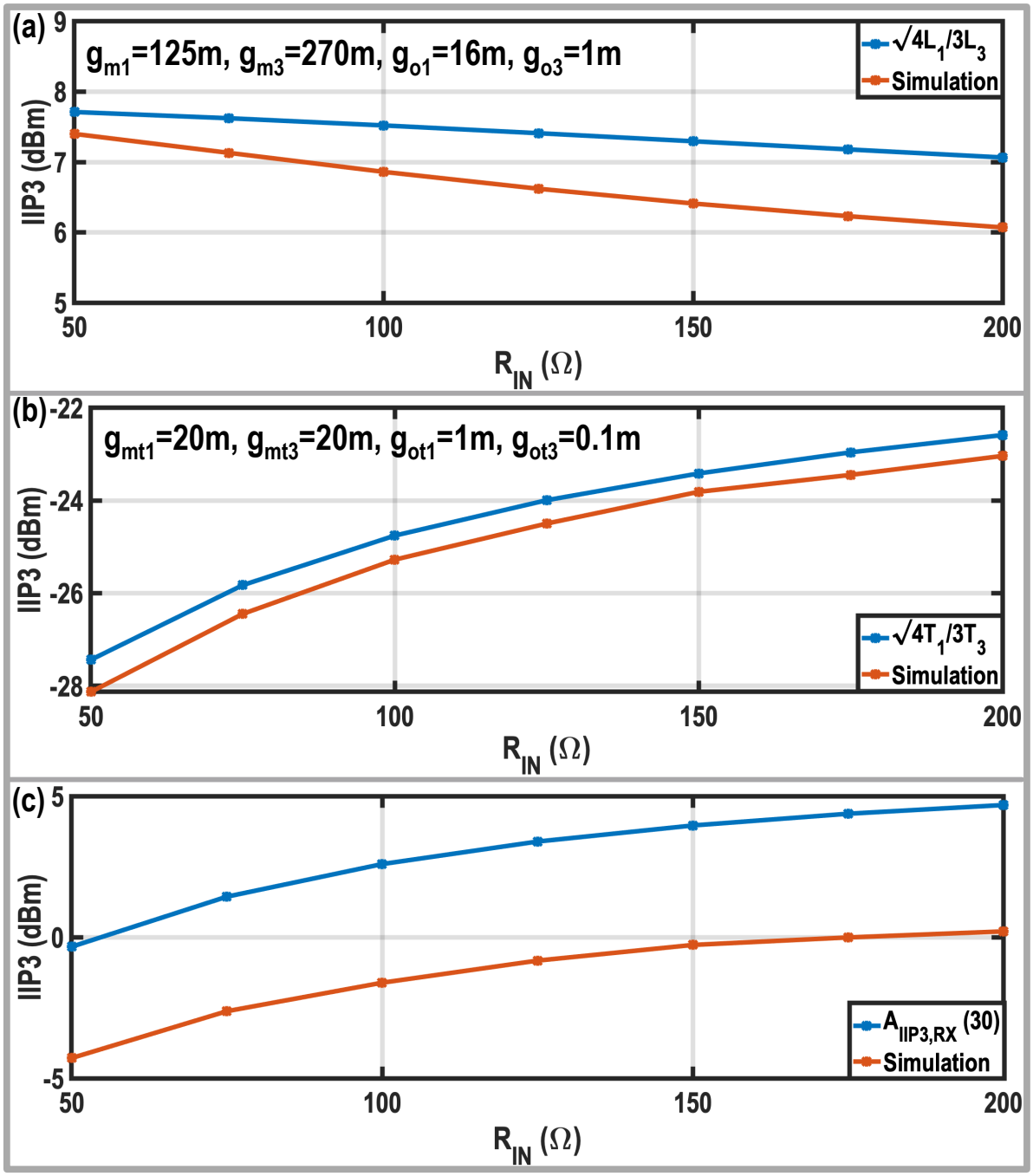

Figure 4.20: Simulated and calculated in-band linearity of the (a) LNTA, (b) TIA, and (c) proposed RX.

the LNTA (L), the passive mixers (P), and the TIAs (T). Note that the on-resistance and nonlinearity of the passive mixers are neglected in this analysis, as the LNTA and TIAs are considered the primary sources of nonlinearity. Moreover, since the in-band linearity is analyzed in this section, the nonlinearity of LNTA and TIAs is assumed to be frequency-independent across the desired

bandwidth. We will first analyze the nonlinearity of the LNTA and TIAs individually, following the methodology established in [112]. Subsequently, we will calculate the overall nonlinearity of the RX chain.

4.5.1 LNTA

The LNTA has two main nonlinearity sources: the nonlinearity of its transconductance and its output resistance. Assuming a cubic relationship between the LNTA output voltage and the input voltage (V_{IN}), the LNTA output current (I_{RF}) can be derived by applying Kirchhoff's Current Law (KCL) at the LNTA output. By neglecting higher-order harmonics, we obtain

$$I_{RF} = -\frac{r_o}{Z_{RF}+r_o}\cdot g_{m1}V_{IN} - \frac{r_o}{Z_{RF}+r_o}\left(g_{m3}+g_{o3}\left(g_{m1}Z_L\right)^3\right)V_{IN}^3, \tag{4.22}$$

where g_{m1} and r_o are the equivalent LNTA's transconductance and output resistance, respectively, while $Z_L{=}r_o \parallel Z_{RF}$ is the LNTA's load. Moreover, as illustrated in Fig. 4.19 (b), g_{m3} and g_{o3} correspond to the third-order nonlinearity of the LNTA's transconductance and output conductance.

As inferred from (4.22) and discussed in [113], the nonlinearity of Z_{RF} may induce nonlinear RF-domain current at the LNTA output. At low offset frequencies, Z_{RF} is significantly smaller than r_o, making the nonlinear current contribution of Z_{RF} negligible. As the offset frequency increases, the input impedance of the Rauch TIA approaches R_{IN}, which is linear and almost independent of the TIA amplifier's nonlinearity. Consequently, the input impedance of the Rauch TIA does not induce nonlinear RF current, leaving the nonlinearity of the LNTA as the dominant source of nonlinear RF current.

The first-order and third-order Volterra kernel transforms can then be derived as:

$$L_1\left(j\omega_1\right) = -\frac{r_o}{Z_{RF}(j\omega_1)+r_o}\cdot g_{m1}, \tag{4.23}$$

$$L_3\left(j\omega_1, j\omega_2, j\omega_3\right) = -\frac{r_o}{Z_{RF}(j\omega_1+j\omega_2+j\omega_3)+r_o}\cdot\Big(g_{m3} + g_{o3}\cdot\left(g_{m1}Z_L\left(j\omega_1\right)\right)\cdot\left(g_{m1}Z_L\left(j\omega_2\right)\right)\cdot\left(g_{m1}Z_L\left(j\omega_3\right)\right)\Big), \tag{4.24}$$

where L_1 and L_3 represent the linear and third-order nonlinear terms, respectively. When two in-band tones with amplitudes of A and frequencies of ω_1 and ω_2 are applied to the RX input, the third-order inter-modulation (IM3) tones

Table 4.1: The summary of extracted linearity parameters of LNTA and TIA amplifier last stage.

LNTA	g_{m1}	g_{m3}	g_{o1}	g_{o3}
	125 m	270 m	16 m	1 m
TIA Amplifier Last Stage	g_{mt1}	g_{mt3}	g_{ot1}	g_{ot3}
	20 m	20 m	1 m	0.1 m

in the LNTA output current occur at $2\omega_1 - \omega_2$ and $2\omega_2 - \omega_1$. Using (4.24), the amplitude of IM3 tones can be calculated as $3/4A^3|L_3(j\omega_1, j\omega_1, -j\omega_2)|$ and $3/4A^3|L_3(j\omega_2, j\omega_2, -j\omega_1)|$. The IIP3 of the LNTA is then estimated by $\sqrt{4L_1/3L_3}$.

As shown in Fig. 4.19 (a), the LNTA is implemented using a self-biased inverter with low-voltage threshold (LVT) devices of minimum channel length to minimize parasitic capacitance at the RX input. A 500 Ω shunt resistive is also used to bias the transistors in saturation. By sweeping the input and output voltages, the output current variation is simulated to estimate the transconductance and output conductance nonlinearity. The resulting linearity parameters are summarized in Table 4.1. The values of g_{m3} and $g_{o,3}$ are then used to calculate the LNTA's IIP3. Fig. 4.20 (a) shows the simulated and estimated IIP3 of LNTA at the bandwidth edge versus R_{IN}, in which increasing R_{IN} from 50 Ω to 200 Ω results in only a ≈1.3 dB IIP3 degradation.

4.5.2 TIA

Next, the nonlinearity of the Rauch TIA is analyzed by decomposing the TIA (T) into two main components: the feedforward path (H) and the feedback path (F), as outlined in [112]. As shown in Fig. 4.21 (a), to calculate H, F, and T, the amplifier and feedback impedance are modeled as follows: The feedback current is represented with two current sources at the TIA input, while R_F and C_F are placed at the TIA input and output to account for their loading effects. Additionally, the TIA amplifier is also modeled with two cascade stages: A_{v1} and G. A simplified system model of the Rauch TIA is then developed, as illustrated in Fig. 4.21 (b). Using this model, we first calculate the Volterra kernel transforms of the feedforward and feedback paths, and finally, derive the Volterra kernel transforms of the overall TIA.

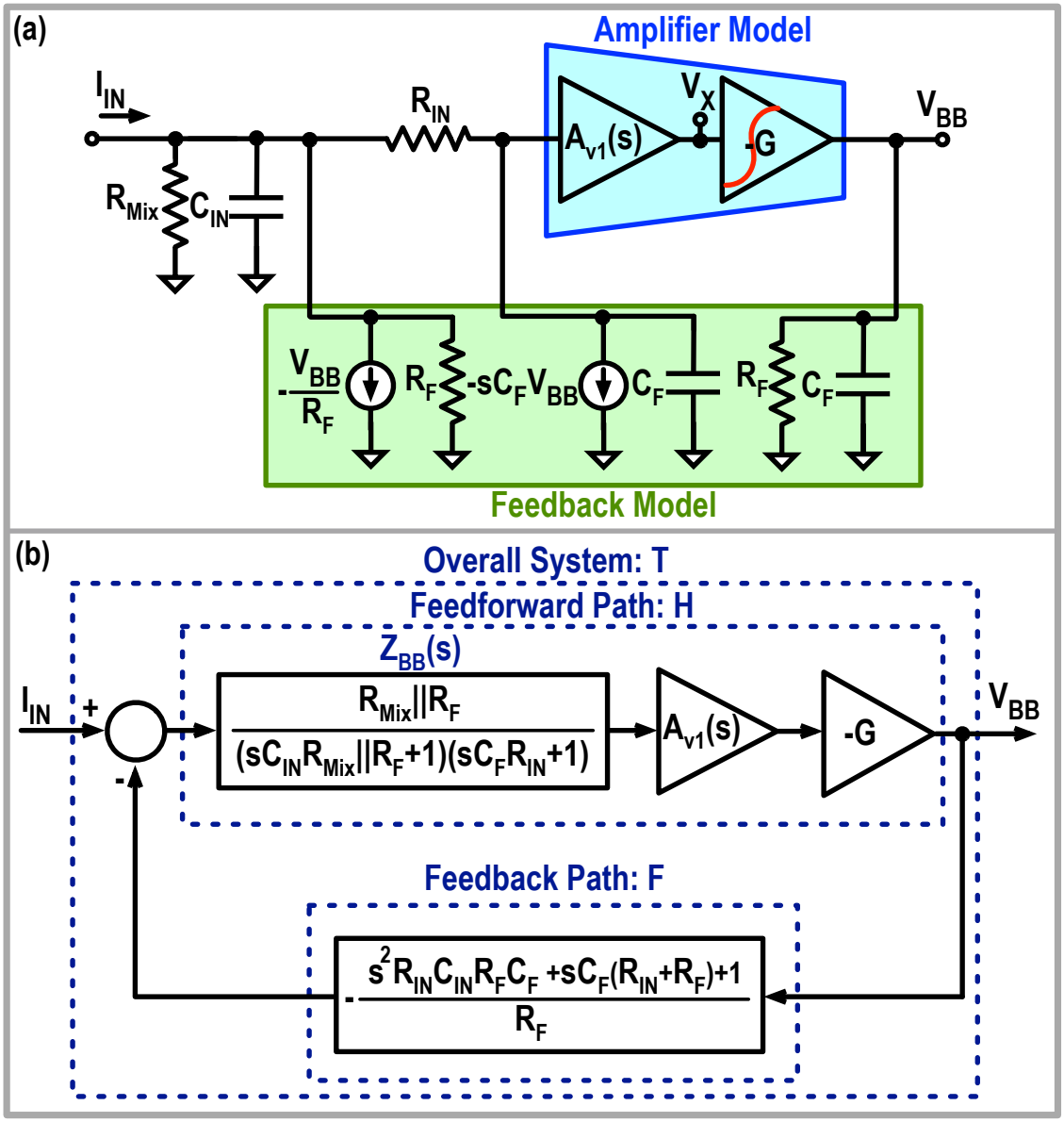

Figure 4.21: (a) Simplified schematic of the Rauch TIA to account for R_F and C_F loading effects; (b) Equivalent approximated model of the Rauch TIA.

4.5.2.1 Feedforward Path

Miller compensation is usually used within A_{v1} for stability purposes, setting the dominant pole of the TIA amplifier, ω_p. A_{v1} is frequency-dependent for in-band signals since $\omega_p < \omega_{3dB}$, as discussed earlier. However, due to the low voltage swing at the TIA input, A_{v1} remains linear and does not contribute to TIA nonlinearity. Furthermore, R_F and C_F have negligible loading effects on G, making G frequency independent for the in-band signals. Because of the large voltage swing at the TIA output, G is the primary source of nonlinearity in

the TIA, with two main nonlinearities stemming from its transconductance and output resistance. The Volterra kernel transforms of G can be calculated using the same procedure used for the LNTA:

$$G_1 = -g_{mt1} r_{ot1}, \tag{4.25}$$

$$G_3 = -\left(\left(g_{mt1} r_{ot1} \right)^3 g_{ot3} + g_{mt3} \right) r_{ot1}, \tag{4.26}$$

where g_{mt1} (g_{mt3}) and g_{ot1} (g_{ot3}) represent the linear (third-order nonlinearity) components of the transconductance and output conductance of the amplifier's final stage, considering a small-signal nonlinearity model similar to that shown in Fig. 4.19 (b). Considering the model in Fig. 4.21 (b), the Volterra kernel transforms of the feedforward path are calculated using (4.25) and (4.26),

$$H_1(j\omega) = -G_1 A_{v1}(j\omega) Z_{BB}(j\omega), \tag{4.27}$$

$$\begin{aligned} &H_3(j\omega_1, j\omega_2, j\omega_3) = -G_3(j\omega_1, j\omega_2, j\omega_3) \cdot \\ &A_{v1}(j\omega_1) Z_{BB}(j\omega_1) A_{v1}(j\omega_2) Z_{BB}(j\omega_2) A_{v1}(j\omega_3) Z_{BB}(j\omega_3), \end{aligned} \tag{4.28}$$

where $Z_{BB}(s)$ is defined by

$$Z_{BB}(j\omega) = \frac{R_F || R_{Mix}}{\left(j\omega R_F \parallel R_{Mix} C_{IN} + 1 \right) \left(j\omega R_{IN} C_F + 1 \right)}. \tag{4.29}$$

4.5.2.2 Feedback Path

Since the feedback path only consists of passive elements, it is linear and does not contribute to the TIA's nonlinearity. Therefore, the third-order Volterra kernel transform of the feedback path is 0, and its first-order Volterra kernel transform is

$$F_1(j\omega) = -\frac{-\omega^2 R_{IN} C_{IN} R_F C_F + j\omega \left(R_{IN} + R_F \right) C_F + 1}{R_F}. \tag{4.30}$$

4.5.2.3 Overall TIA

To calculate the Volterra kernel transforms of the TIA, the gain reduction factor of the TIA loop must first be derived:

$$R(j\omega) = -\frac{1}{1 + H_1(j\omega) F_1(j\omega)} = -\frac{1}{1 + LG(j\omega)}, \tag{4.31}$$

where LG is given by (4.14). The first-order Volterra kernel transform of the Rauch TIA is

$$T_1(j\omega) = H_1(j\omega)R(j\omega) = \frac{H_1(j\omega)}{1 + H_1(j\omega)F_1(j\omega)}. \tag{4.32}$$

Assuming the TIA amplifier has a high voltage gain, (4.32) simplifies to $1/F_1(j\omega)$, as given in (4.6). Finally, the third-order Volterra kernel transform of the Rauch TIA can be derived as follows:

$$\begin{aligned} T_3(j\omega_1, j\omega_2, j\omega_3) =& R(j\omega_1)R(j\omega_2)R(j\omega_3) \cdot H_3(j\omega_1, j\omega_2, j\omega_3) \\ & \cdot R(j\omega_1 + j\omega_2 + j\omega_3). \end{aligned} \tag{4.33}$$

When two input currents at ω_1 and ω_2 are applied to the TIA input, two IM3 tones are generated at $2\omega_1 - \omega_2$ and $2\omega_2 - \omega_1$. Assuming the input current amplitude is I, the IM3 tones have amplitudes of $3/4I^3|T_3(j\omega_1, j\omega_1, -j\omega_2)|$ and $3/4I^3|T_3(j\omega_2, j\omega_2, -j\omega_1)|$. After replacing (4.31) into (4.33), the third-order Voltera kernel transform for the in-band IM3 tone $(2\omega_1 - \omega_2)$ can be recalculated:

$$\begin{aligned} T_3(j\omega_1, j\omega_2, j\omega_3) =& \frac{1}{1 + LG(j\omega_1)} \cdot \frac{1}{1 + LG(j\omega_1)} \cdot \frac{1}{1 + LG(-j\omega_2)} \cdot \\ & H_3(j\omega_1, j\omega_2, j\omega_3) \cdot \frac{1}{1 + LG(j\omega_1 + j\omega_1 - j\omega_2)}. \end{aligned} \tag{4.34}$$

Thus, enhancing the loop gain at the frequencies of the blockers and IM3 tones improves the in-band linearity performance of the TIA.

Similar to the LNTA, the values of g_{mt3} and g_{ot3} for the TIA are estimated by monitoring the output current of the last stage of the Rauch TIA while sweeping its input and output voltages. The simulated results are summarized in Table 4.1. These values are used to calculate the TIA's IIP3. Fig. 4.20 (b) shows the simulated and estimated IIP3 of TIA at the bandwidth edge versus R_{IN}, where increasing R_{IN} from 50 Ω to 200 Ω improves IIP3 by 5 dB, aligning well with IIP3 calculations ($\sqrt{4T_1/3T_3}$). Note that the values of R_F, C_{IN}, C_F, and R_{IN} are similar to those used in Fig. 4.3 with C_F slightly adjusted for 3-dB bandwidth tuning.

4.5.3 RX Chain

As mentioned earlier, the entire RX chain can be viewed as a cascade of the LNTA, passive mixers, and TIAs (see L, P, and T in Fig. 4.18). P is a linear gain block, and the differential gain of the passive mixers is $2/M\text{sinc}(1/M)$.

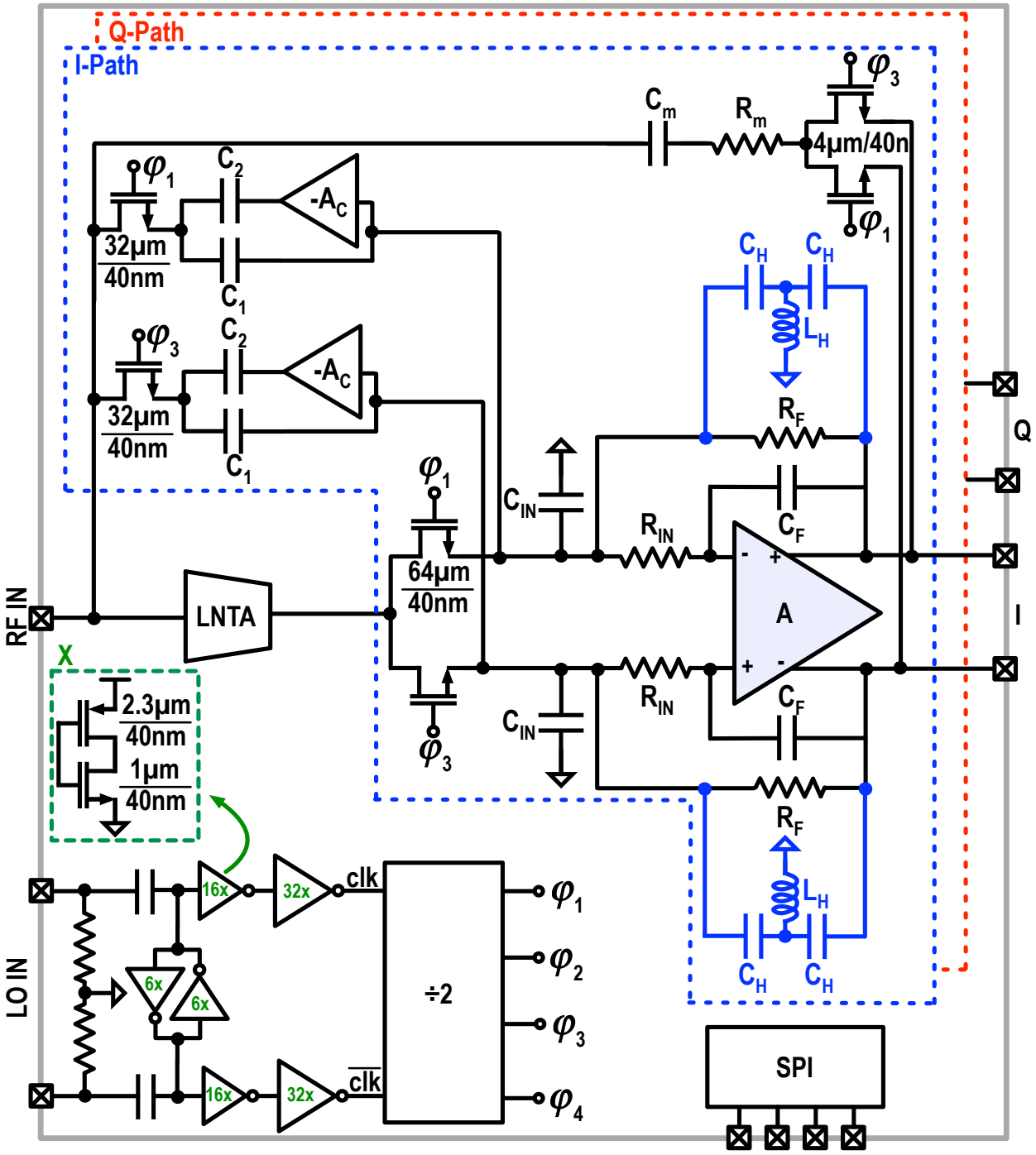

Figure 4.22: The proposed RX block diagram.

Thus, I_{IN} in Fig. 4.21 (a) equals to $2/M\text{sinc}(1/M)I_{RF}$. Considering this point, the IIP3 of the RX chain ($A_{IIP3,RX}$) can be calculated as follows [114]:

$$\frac{1}{A^2_{IIP3,RX}} = \frac{1}{A^2_{IIP3,LNTA}} + \frac{\left(\frac{2}{M}\text{sinc}(\frac{1}{M})L_1\right)^2}{A^2_{IIP3,TIA}}, \tag{4.35}$$

where $A_{IIP3,LNTA}$ and $A_{IIP3,TIA}$ are the IIP3 of the LNTA and TIA, respectively. Fig. 4.20 (c) shows the simulated IIP3 of the RX chain where increasing R_{IN} enhances the IIP3 by 4 dB, which closely matches the 5 dB improvement predicted by (4.35). However, a 3.8 dB discrepancy exists between the simulated and calculated RX IIP3 values. To simplify our analysis, we neglected the second-order nonlinearity of the TIA and LNTA. This decision is based on the fact that the TIA functions as a pseudo-differential circuit, while the LNTA is implemented using a single inverter-based amplifier, where the second-order nonlinearity can be minimized through careful sizing of the NMOS and PMOS devices [115]. However, it is important to note that the second-order nonlinearity is not completely eliminated. As discussed in [112], the interaction between the second-order nonlinearities of two cascaded blocks contributes to third-order nonlinearities, leading to a mismatch between the calculated and simulated IIP3 values. One approach to mitigate the second-order distortion is to add an AC coupling capacitor between the LNTA and the passive mixers. This capacitor would allow the signals at the operating frequency to pass through while blocking the second-order intermodulation tones at lower frequencies. Simulation results show that adding this capacitor improves the in-band linearity of the RX by approximately 2 dB, bringing the simulation results closer to the calculated values. However, to pass the desired signals at the lowest operational frequency of 0.4 GHz, the AC coupling capacitor would need to be relatively large. This would introduce significant parasitic capacitance at the LNTA output, which could degrade the RX's operating frequency and noise performance. Consequently, despite the resulting degradation in linearity, we chose not to include this capacitor in the design in order to preserve the operating frequency.

4.5.4 Discussion

In this section, we analyzed the impact of increasing R_{IN} and reducing C_{IN} on the linearity performance of the RX. An increase in R_{IN} degrades the in-band linearity of the LNTA but improves the in-band linearity of the Rauch TIA. Since the RX's overall in-band linearity is mainly limited by the Rauch TIA, increasing R_{IN} enhances the RX's overall linearity. However, it is important to note that in advanced CMOS technologies with supply voltages below 1 V, the nonlinearity degradation of the LNTA could dominate, potentially outweighing the improvement achieved in the Rauch TIA.

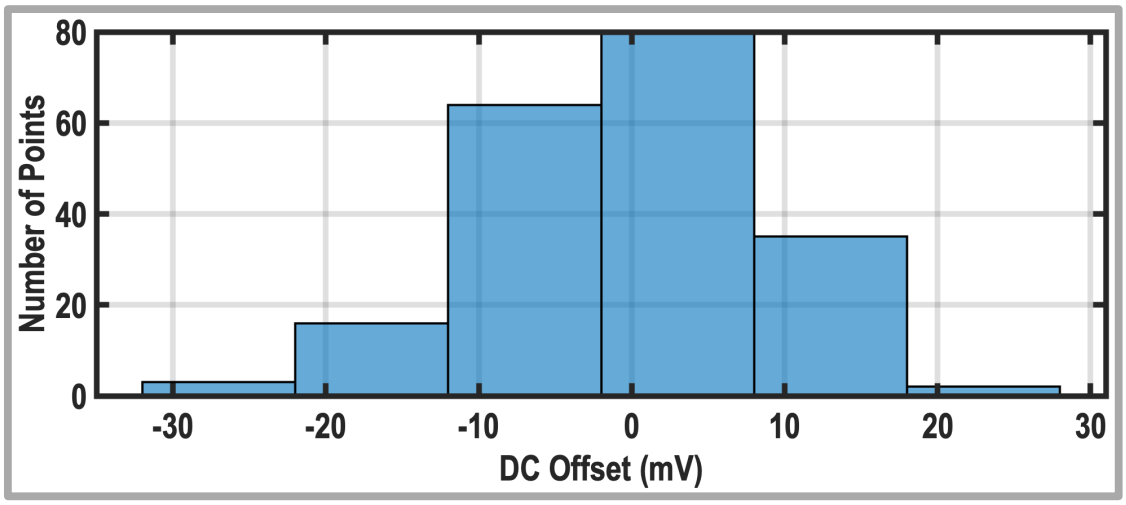

Figure 4.23: Monte Carlo simulation results of DC offset at the RX output.

Table 4.2: The tunable range of the utilized key components of the proposed RX.

C_1	C_2	C_{IN}	R_{IN}	C_F	R_F
2.3-9.2 pF	0.19-1.5 pF	2.3-34.4 pF	50-200 Ω	0.24-1.44 pF	0.4-1.6 kΩ

4.6 Circuit Implementation

Fig. 2.17 shows the complete block diagram of the proposed RX. All key parameters of the proposed RX (C_1, C_2, C_{IN}, R_{IN}, C_F, and R_F) are tunable and can be controlled via the Serial Peripheral Interface (SPI). The tunable ranges for these parameters are summarized in Table 4.2.

The input signal is converted into an RF current by the LNTA, which is then down-converted by 4-phase passive mixers, and the TIAs eventually convert it to baseband voltages to generate in-phase (I) and quadrature (Q) signals. To achieve input matching, the output voltages from the TIAs are upconverted to the RF domain, combined, and then applied to the RF input of the RX via the matching resistor and capacitor (R_m and C_m). A -1 multiplication in the translational feedback network ensures the stability of the input matching loop [65]. The passive mixers are implemented using NMOS transistors, with their dimensions shown in Fig. 2.17. Additionally, similar to the LNTA in Fig. 4.19 (a), the positive feedback amplifier is realized with a compact self-biased inverter. However, smaller devices are employed in the positive feedback amplifier (PMOS:9.4 μm/40 nm, NMOS:4 μm/40 nm) to reduce power consumption. A 10 kΩ feedback resistor is used to bias the amplifier and slightly attenuate its gain, preventing stability issues. At the in-band frequencies, the series capacitor (C_2

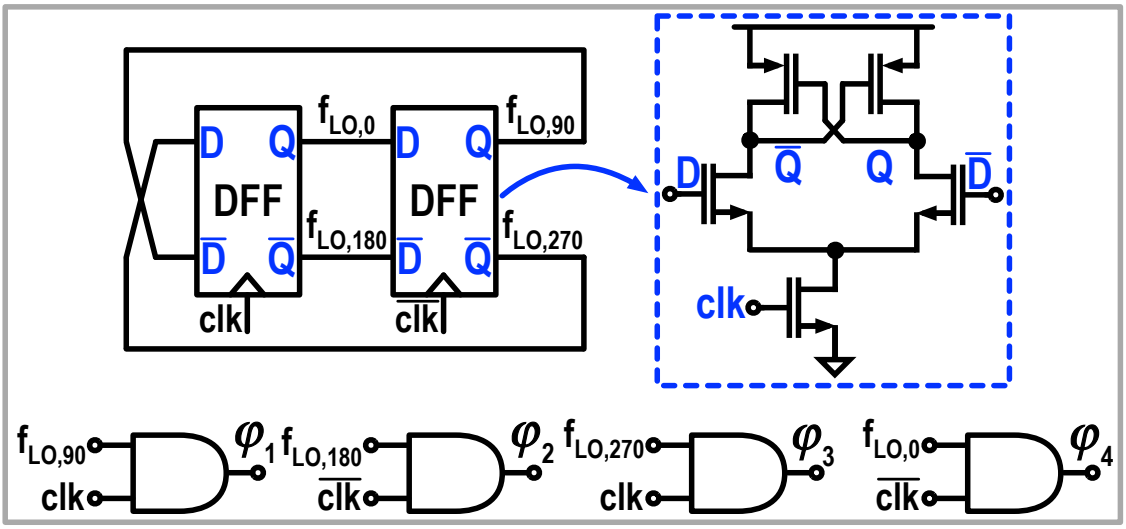

Figure 4.24: Schematic of LO generation block.

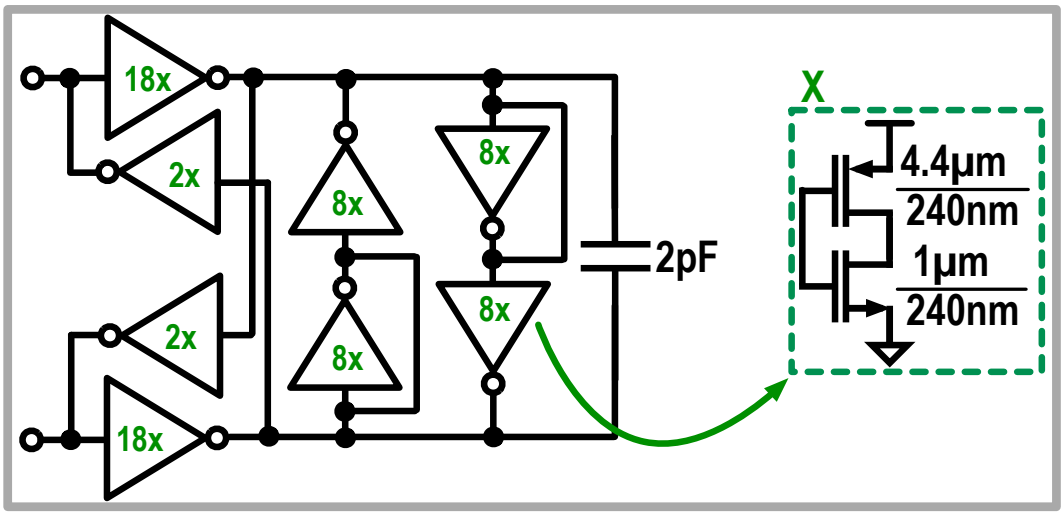

Figure 4.25: Active implementation of the differential inductor.

in Fig. 2.17) presents high impedance, ensuring that the noise and nonlinearity of the positive feedback amplifier do not degrade the RX performance.

Fig. 4.23 shows the simulated DC offset of the proposed RX using PSS analysis in cadence. The simulated standard deviation of DC offset is 9.2 mV at the RX output. Due to the relatively low DC offset, analog domain cancellation is unnecessary. While it may slightly reduce the dynamic range of the off-chip ADC, DC offset cancellation can be efficiently handled in the digital domain.

In the proposed RX, a differential off-chip LO signal is first buffered and then passed through a divide-by-two stage to generate the 4-phase non-overlapping LOs. The detailed schematic of LO generation block is shown in Fig. 4.24.

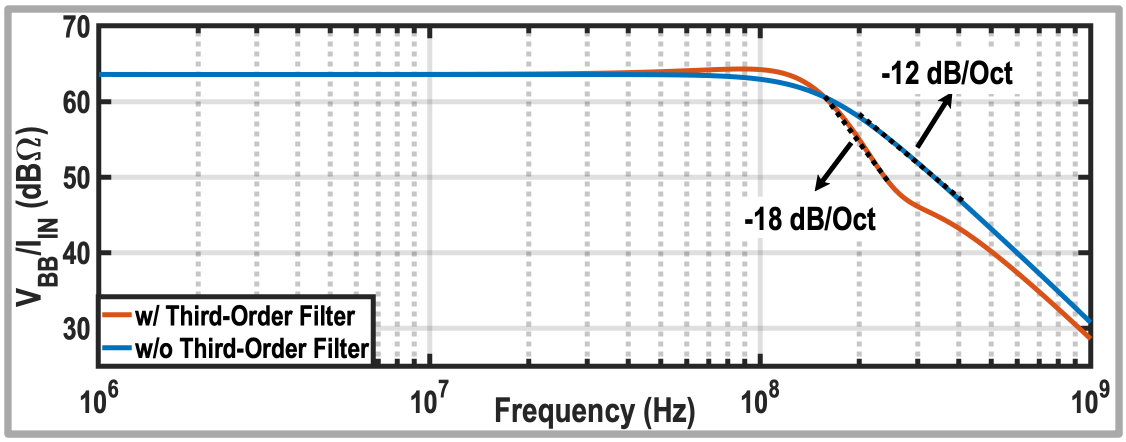

Figure 4.26: Filtering response of Rauch TIA before and after adding the third-order impedance.

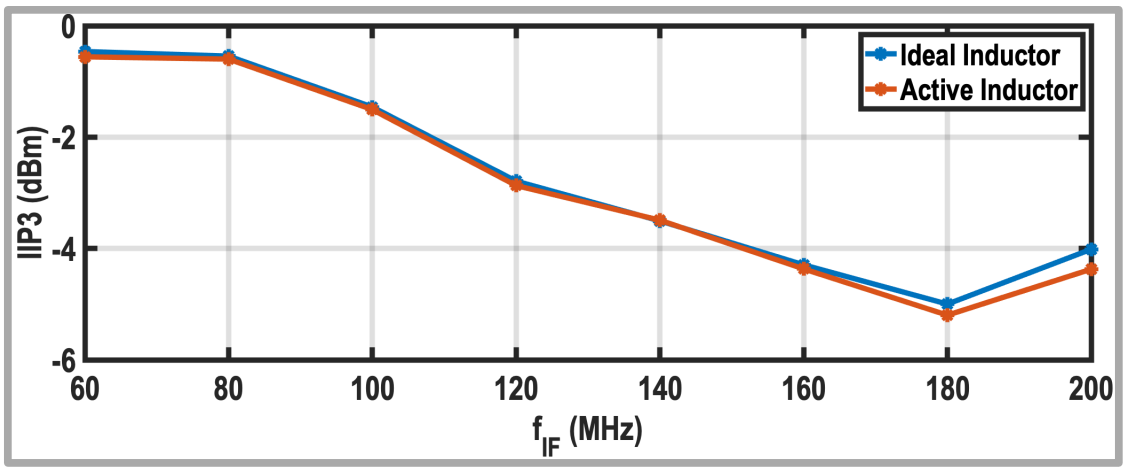

Figure 4.27: Effect of the active inductor on the simulated RX in-band IIP3.

Two cascaded flip-flops [70] are utilized to generate four 50% duty cycle clocks. These clocks are then resampled with the buffered input clocks to produce 25% non-overlapping LOs, which drive the passive mixers.

As mentioned earlier, one of the main challenges in 5G applications is the presence of close-in blockers, which necessitate sharp filtering. In this work, a third-order high-pass filter is placed in parallel with the R_F to further increase the selectivity of the Rauch TIA (highlighted in blue in Fig. 2.17). To implement the baseband inductors for the high pass filter, the ground ports of the inductors, driven by complementary LOs, are connected and replaced with a single inductor. The resulting inductor is realized using a gyrator with a capacitor load, as shown in Fig. 4.25. The inverters in the active inductor are implemented using large-channel devices to minimize the undesired series resistance of the active inductor [100]. Like Nauta's cell [101], four extra inverters

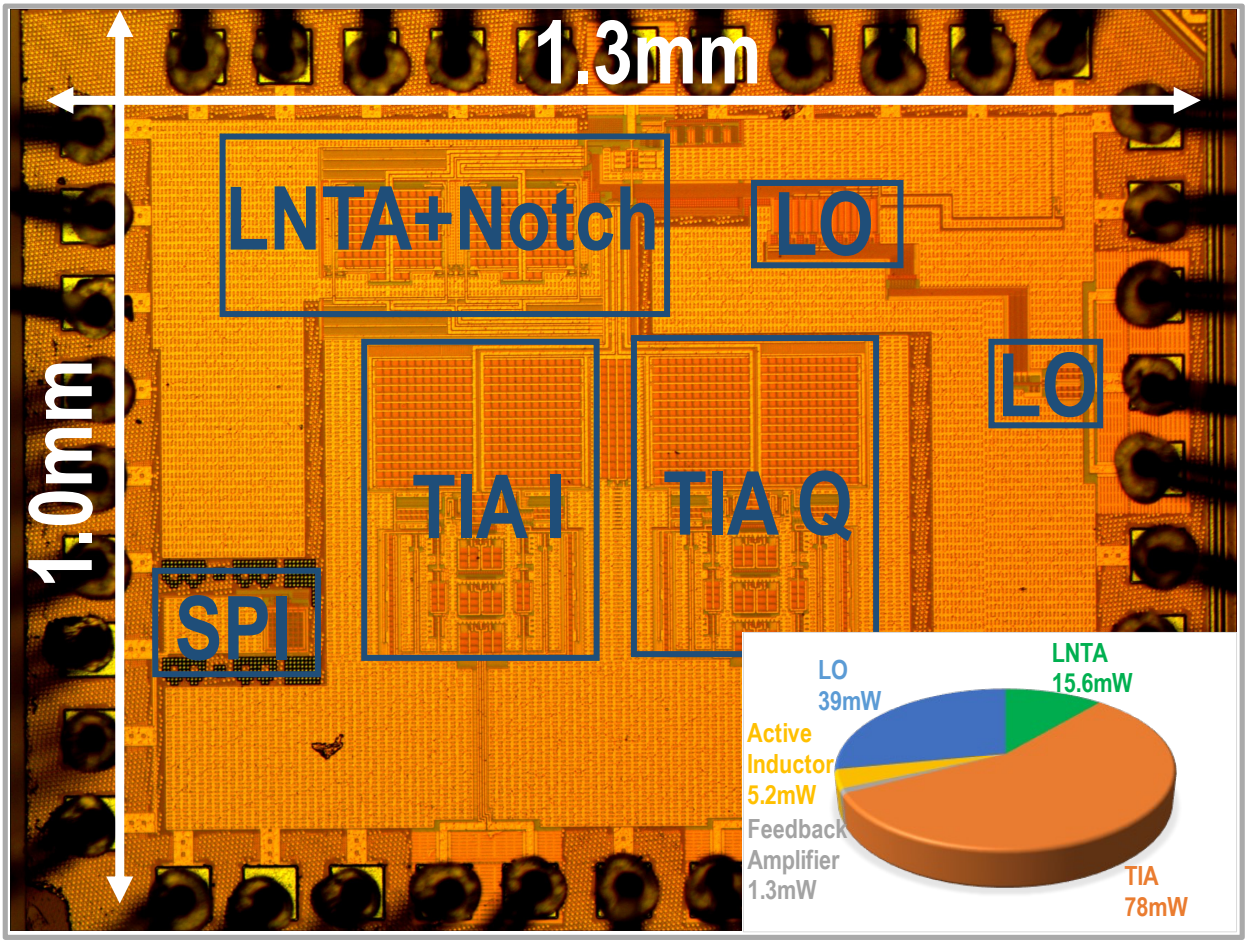

Figure 4.28: Die micrograph and power consumption breakdown at $f_{LO} = 3\,\text{GHz}$.

are used at the gyrator output to ensure the transistors remain in saturation. Fig. 4.26 shows that the TIA's transition slope increases to -18 dB/oct with the third-order high pass filter. However, due to the limited bandwidth of the gyrator, the filtering order reduces to second-order at far-out offset frequencies. Note that the nonlinearity and noise generated by the active inductor appear at the TIA output after undergoing high-pass filtering, which helps relax its noise and linearity requirements. To assess this effect, two RX schematics were simulated in Cadence: one with the active inductor and the other with an ideal inductor. Two in-band tones were applied to the RX ($f_1 = f_{LO} + f_{IF}$ and $f_2 = f_{LO} + f_{IF} - 10\,MHz$), with f_{IF} swept across the 3-dB bandwidth. As shown in Fig. 4.27, the degradation in in-band linearity is minimal throughout most of the bandwidth, with only a 0.2 dB reduction at the bandwidth edge. Additionally, as illustrated in Fig. 4.7 (c), the active inductor causes a 0.5 dB increase in the output noise of the Rauch TIA.

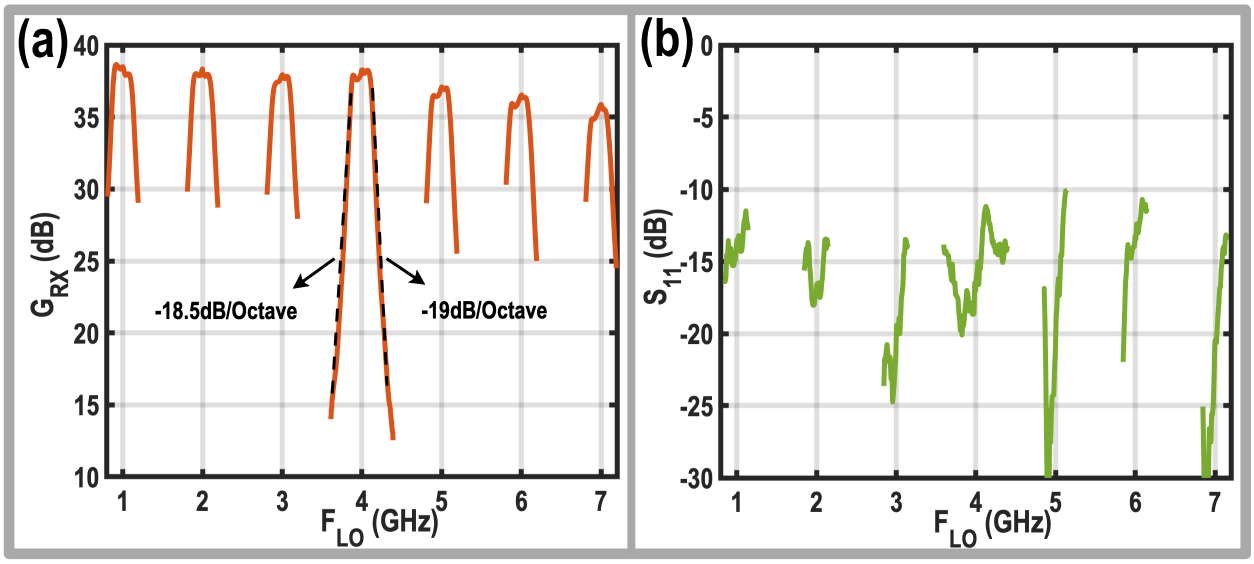

Figure 4.29: Measured (a) gain and (b) in-band S_{11} over the operating frequency.

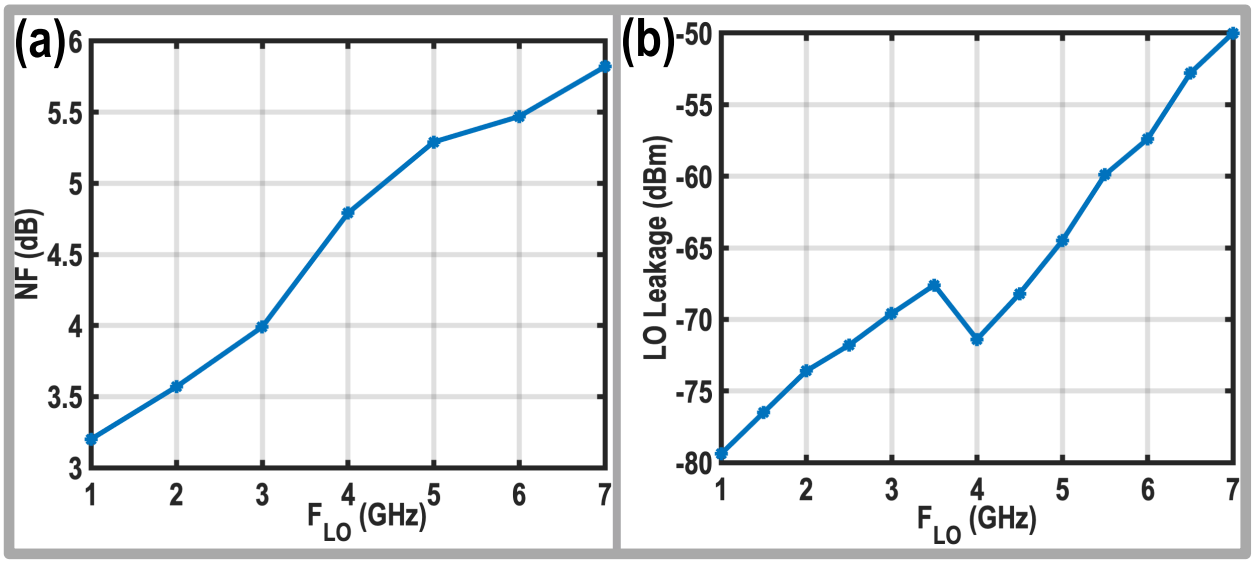

Figure 4.30: Measured (a) NF and (b) LO leakage across the operating frequency.

4.7 Measurement Results

The proposed RX is implemented in TSMC 40-nm Bulk CMOS technology. Fig. 4.28 shows the die micrograph of the proposed RX, with the chip's core area and active area measuring 1.3 mm^2 and 0.4 mm^2, respectively. The RX consumes between 105.2 and 194.9 mW from a 1.3-V supply while operating over a frequency range of 0.4 to 7.3 GHz. The power consumption breakdown at 3 GHz LO frequency (f_{LO}) is depicted in Fig. 4.28.

Fig. 4.29 (a) shows the measured gain versus the operating frequency, with

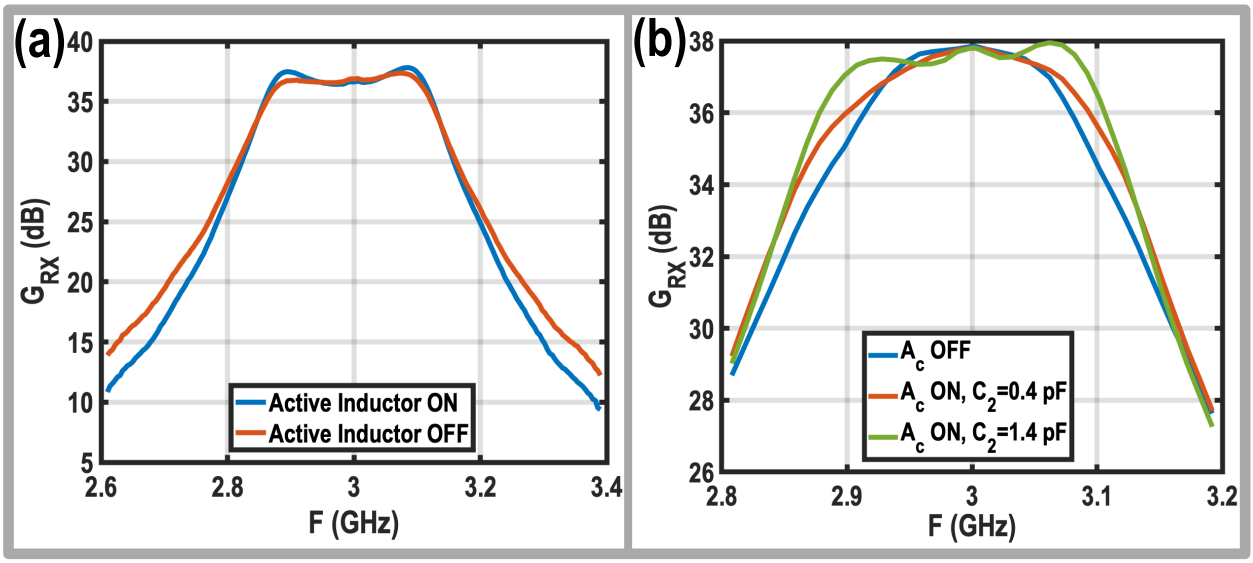

Figure 4.31: (a) Effect of the third-order impedance on the selectivity of the proposed RX; (b) Extending the measured 3-dB bandwidth with the proposed positive feedback.

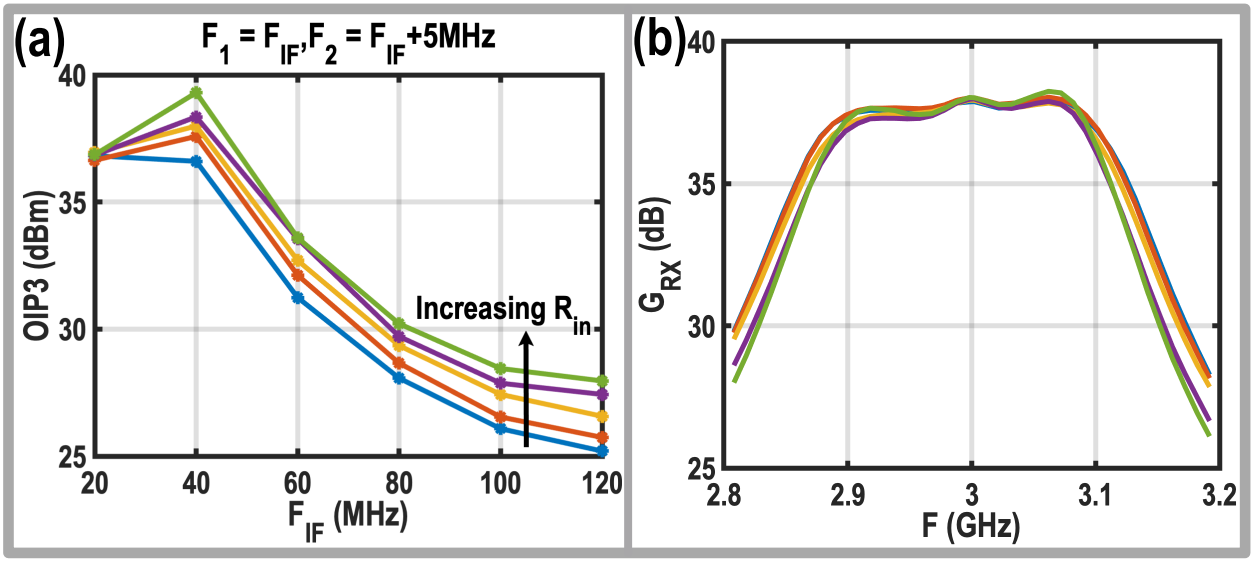

Figure 4.32: (a) Improving the measured in-band OIP3 by increasing R_{IN} and reducing C_{IN}; (b) Impact of increasing R_{IN} and reducing C_{IN} on the RX in-band gain transfer function.

a gain of 38.5 dB at low LO frequencies, and 35.8 dB at high LO frequencies. Due to the parasitic capacitors, the measured RF bandwidth is about 300 MHz, compared to the desired 400 MHz. The filtering order of the proposed RX is better than -60 dB/dec. Fig. 4.29 (b) shows the measured in-band S_{11}, which remains below -10 dB across the 3-dB bandwidth and operating frequency. The measured NF, shown in Fig. 4.30 (a), is 3.2 dB at $f_{LO} = 1$ GHz and increases to 5.8 dB at $f_{LO} = 7$ GHz. The measured LO leakage is -80 dBm at the lowest LO

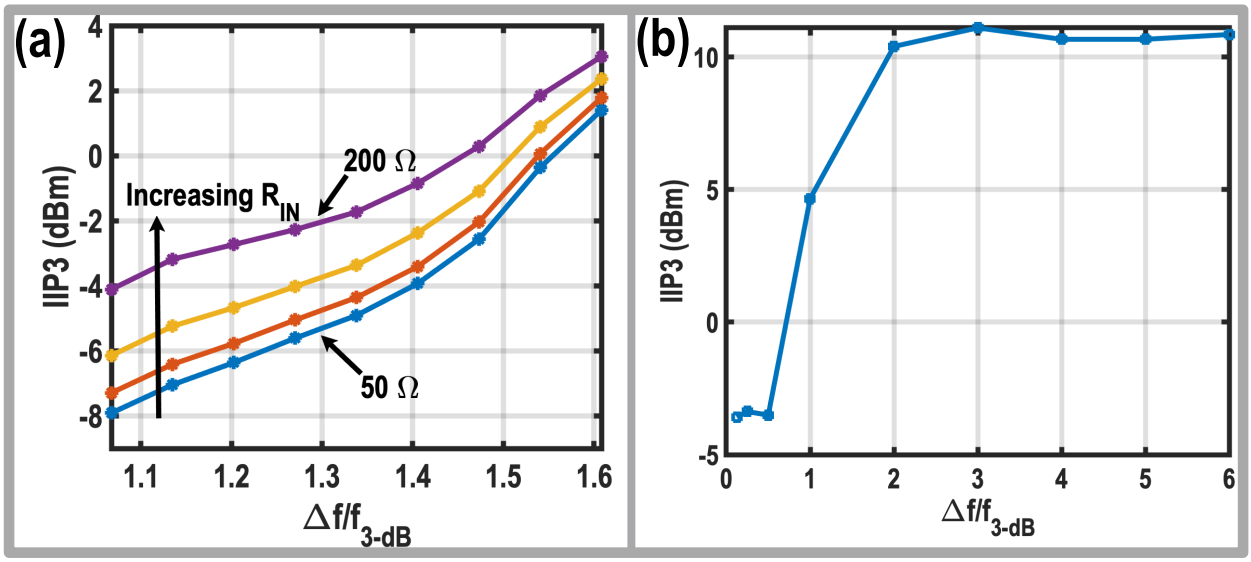

Figure 4.33: (a) Reduction of IM3 generated by in-band and close-in blockers through increasing R_{IN} and reducing C_{IN}; (b) Measured IIP3 versus the offset frequency.

frequency, and increases to -50 dBm at the highest LO frequency, as shown in Fig. 4.30 (b).

Fig. 4.31 (a) highlights the impact of the third-order high pass filter on the selectivity of the proposed RX, where enabling the active inductor improves the RX selectivity by -10 dB/dec. As demonstrated in the measured results shown in Fig. 4.31 (b), activating the positive feedback amplifier (A_c) and adjusting the value of C_2 increases the RX bandwidth without sacrificing the far-out out-of-band rejection.

Fig. 4.32 (a) presents the measured in-band linearity. Two tones at $f_1 = f_{IF}$ and $f_2 = f_{IF} + 5$ MHz are applied to the RX input, with f_{IF} swept across the 3-dB bandwidth. The measured in-band OIP3 is approximately 38 dBm when f_{IF} is below 40 MHz. Due to the limited bandwidth of the loop gain, the in-band linearity starts to degrade at $f_{IF} = 40$ MHz, reaching 27 dBm near the 3-dB bandwidth. Furthermore, as predicted by (4.15) and confirmed by the measurement results in Fig. 4.32 (b), simultaneously increasing R_{IN} and reducing C_{IN} enhances the loop gain at the passband edges. Moreover, fig. 4.32 (b) further demonstrates that increasing R_{IN} and reducing C_{IN} has a negligible impact on the RX filtering shape and order.

Fig. 4.33 (a) illustrates the measured RX linearity in the presence of in-band and close-in blockers. Two tones, $f_1 = f_{LO} + f_{3dB}$ and $f_2 = f_{LO} + \Delta f$, are applied to the RX such that their intermodulation product falls within the desired band. Then, Δf is swept across the close-in blocker range. As shown

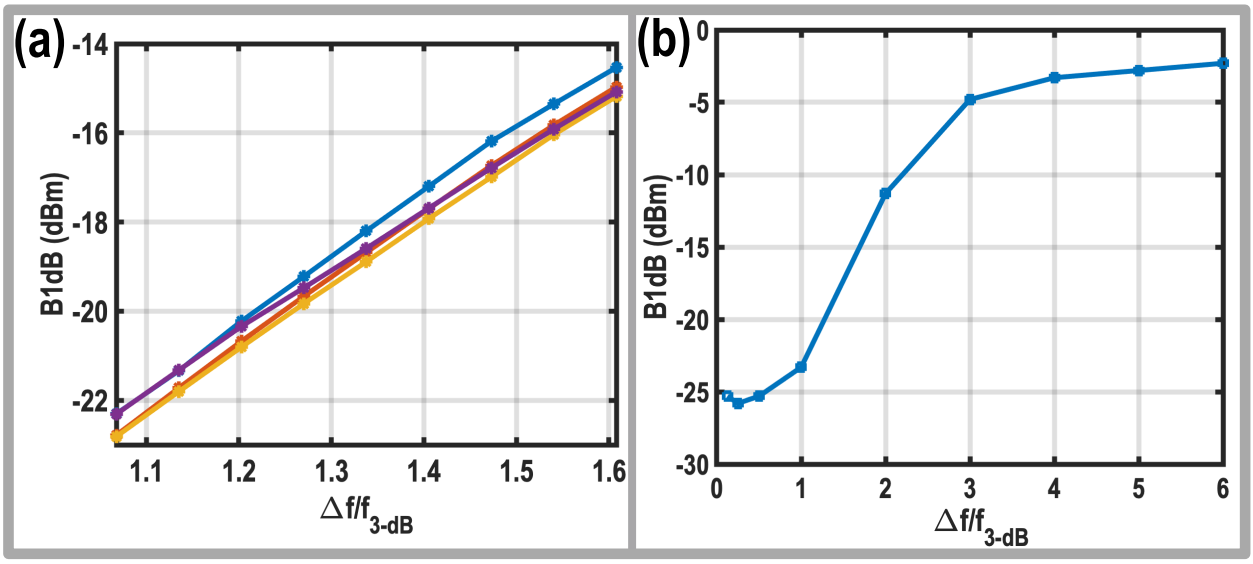

Figure 4.34: (a) Effect of increasing R_{IN} and reducing C_{IN} on the measured B1dB across the close-in blocker range; (b) Measured B1dB versus the offset frequency.

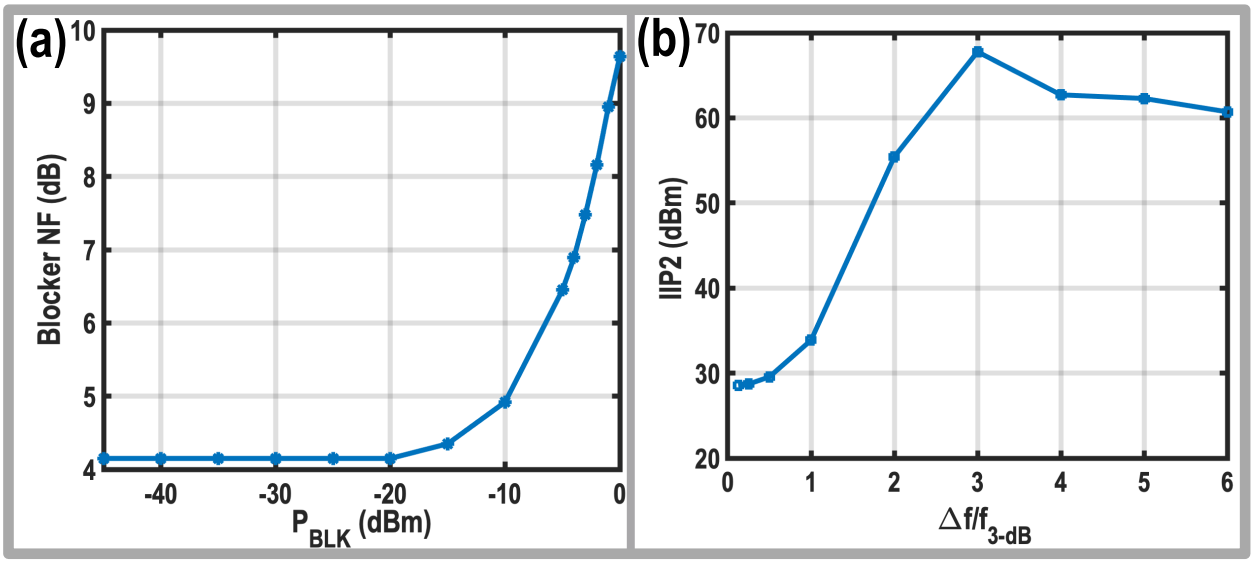

Figure 4.35: (a) Measured blocker NF versus the blocker power; (b) Measured IIP2 versus the offset frequency.

in Fig. 4.33 (a), simultaneously increasing R_{IN} and reducing C_{IN} improves the IIP3 by approximately 3.8 dB. However, a trade-off between in-band and out-of-band linearity can be observed. As Δf increases, the IIP3 improvement diminishes due to the lower C_{IN} value. For the IIP3 measurements, two tones at $f_1 = f_{LO} + \Delta f$ and $f_2 = f_{LO} + 2\Delta f - 5\,\text{MHz}$ are applied to the RX input, where Δf is the offset frequency from the LO frequency. Δf is then swept to measure the RX IIP3 versus the offset frequency, as shown in Fig. 4.33 (b). The

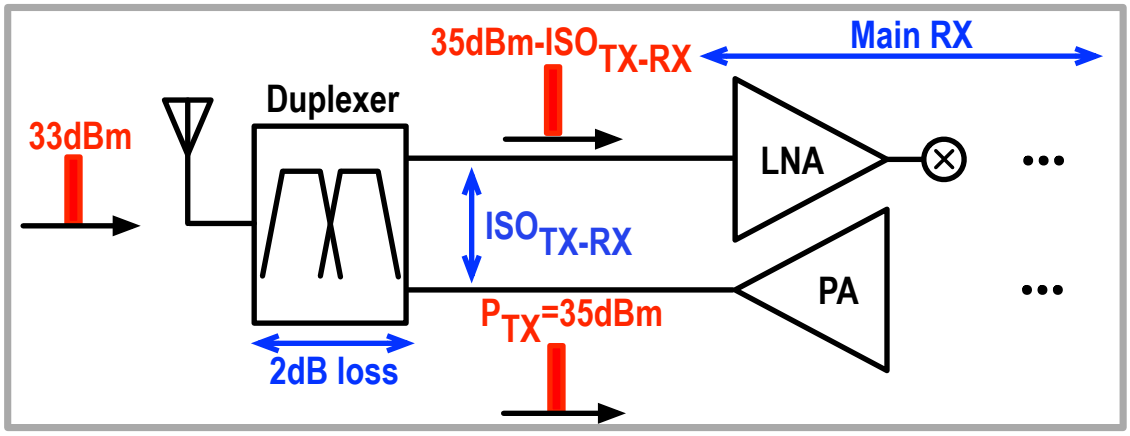

Figure 4.36: Front-end block diagram of an FDD transceiver.

measured in-band IIP3 is -3.4 dBm and reaches 10.4 dBm at $\Delta f/f_{3dB} = 2$.

To investigate the effect of increasing R_{IN} and reducing C_{IN} on the blocker 1-dB compression point (B1dB) performance, a desired signal at $f_{sig} = f_{LO}$+5 MHz and a blocker at $f_{blk} = f_{LO} + \Delta f$ are applied to the RX input. Then, Δf is swept across the close-in blocker range. As illustrated in Fig. 4.34 (a), unlike IIP3, the B1dB of the proposed RX does not improve with increased R_{IN} and reduced C_{IN} across the close-in blocker range, as the large-signal operation of the RX is constrained by the supply voltage. Moreover, Fig. 4.34 (a) shows the measured B1dB versus the blocker offset frequency. The in-band B1dB is -25.8 dBm, and increases to -2.3 dBm at far-out offset frequencies.

The RX NF is also measured in the presence of a blocker located at $\Delta f/f_{3dB} = 5$. As depicted in Fig. 4.35 (a), a 0 dBm blocker degrades the RX NF by 5.5 dB. In the second-order input intercept point (IIP2) measurement shown in Fig. 4.35 (b), two tones are applied at frequencies $f_1 = f_{LO} + \Delta f$ and $f_2 = f_{LO} + \Delta f - 5$ MHz, while Δf is swept. The measured in-band IIP2 is 28.6 dBm, and increases to 55.4 dBm at $\Delta f/f_{3dB} = 2$. To meet the performance requirements for 5G frequency division duplex (FDD) applications, the proposed RX requires a duplexer. This duplexer should provide certain isolation between the TX and RX ports, which be calculated in the following.

In FDD systems, as shown in Fig. 4.36, TX power (P_{TX}) leaks into the RX input due to the limited isolation between the transmitter and receiver ports of the duplexer (denoted as ISO_{TX-RX}). This leakage generates second-order intermodulation (IM2) in the RX path due to the limited IIP2 of the proposed RX. To prevent degradation of the signal-to-noise ratio (SNR), the IM2 power (P_{IM2}) caused by the TX leakage must be at least 10 dB lower than the RX reference sensitivity (P_{ref}). Consequently, the required duplexer isolation for a

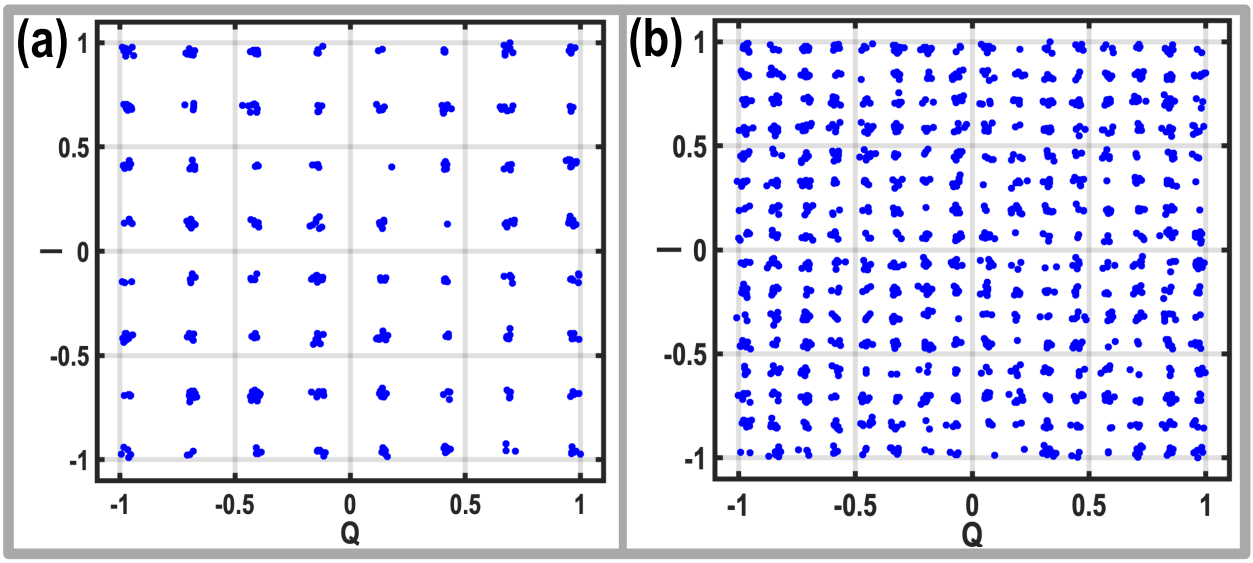

Figure 4.37: Measured constellation of the proposed RX for -55 dBm 100 MS/s (a) 64-QAM and (b) 256-QAM input signals.

given RX IIP2 performance can be calculated using the following equation:

$$ISO_{TX-RX} = (P_{TX} - 3) - \frac{IIP2 + P_{IM2}}{2}$$
$$\rightarrow ISO_{TX-RX} = (P_{TX} - 3) - \frac{IIP2 + P_{ref} - 10}{2}, \tag{4.36}$$

where the -3 dB term accounts for the modulated TX signal. This equation clearly shows the trade-off between the RX IIP2 and the duplexer ISO_{TX-RX} requirements. According to 3GPP standards for local area base station applications, the reference sensitivity should be better than -87.7 dBm for channel bandwidths greater than 50 MHz, with the transmitter's radiated power at the antenna being 33 dBm. Taking into account a 2 dB loss in the duplexer between the TX and antenna ports, P_{TX} must be approximately 35 dBm. Additionally, considering an RX RF bandwidth of 75 MHz and a frequency spacing of 20 MHz between the RX and TX bandwidth edges, we obtain a ratio of $\Delta f / f_{3-dB} = 1.53$. The measured IIP2 of the proposed RX at this offset frequency is +46 dBm. Therefore, to meet the FDD transceiver performance requirements, the proposed RX requires a duplexer with $ISO_{TX-RX} \geq 58$ dB between its TX and RX ports—an ambitious goal to achieve. Therefore, the IIP2 performance of the proposed RX should be enhanced in future implementations, either by adopting a fully differential LNTA and TIA or by employing calibration techniques similar to those discussed in [69].

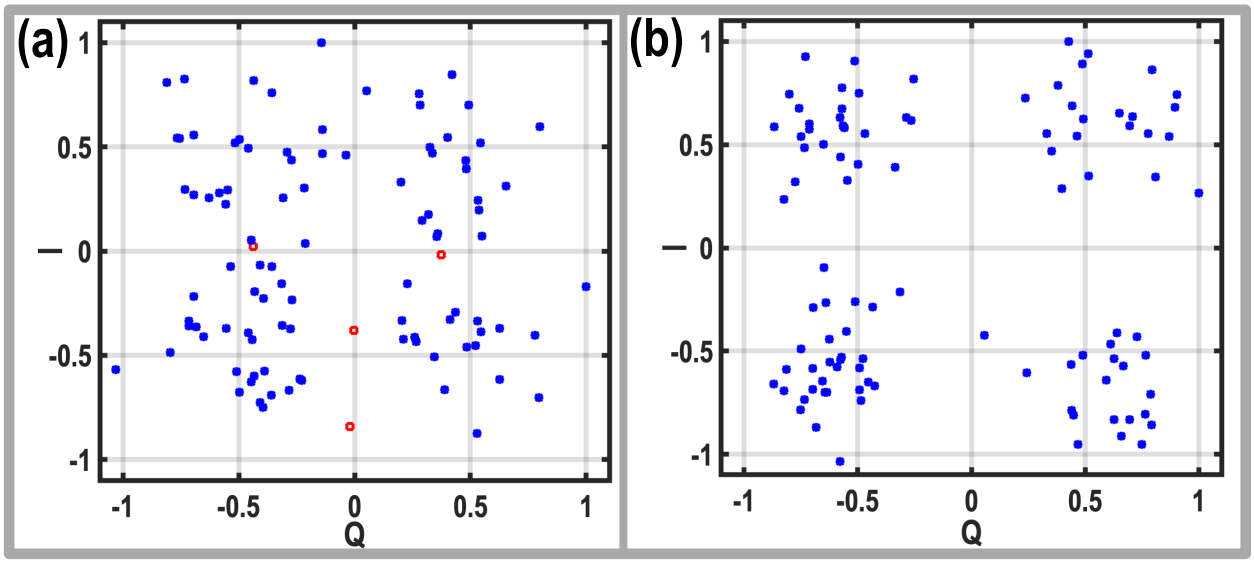

Figure 4.38: (a) Measured constellation at the reference sensitivity; (b) Measured constellation in the presence of a -35 dBm in-band blocker.

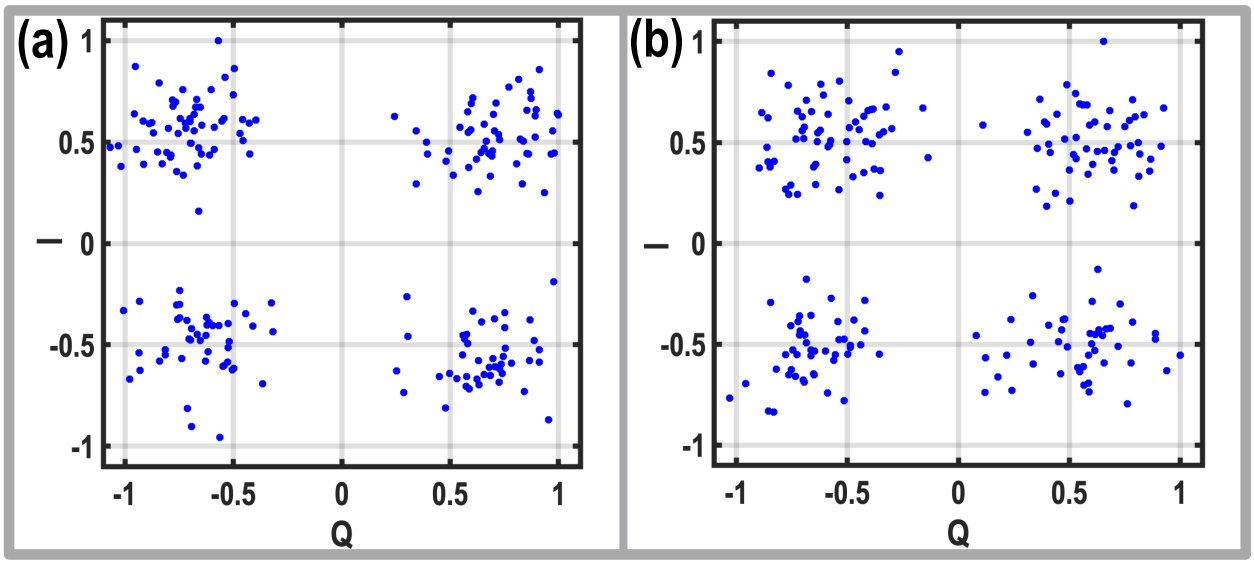

Figure 4.39: Measured constellation in the presence of (a) a -15 dBm close-in blocker and (b) a -4 dBm far-out blocker.

Next, the RX performance is evaluated using high-order quadrature amplitude modulation (QAM) schemes, as illustrated in Fig. 4.37. Applying a -55 dBm 100 MS/s QAM-64 signal to the RX input results in a measured error vector magnitude (EVM) of -31 dB. The EVM slightly degrades to -30.2 dB with a QAM-256 signal, while maintaining the same sampling rate and input power.

Following the 3GPP standard, the RX is further evaluated. The first test measures reference sensitivity, where the throughput must exceed 95% for a 50 MS/s QPSK signal with an input power of -87.7 dBm. To measure reference

Table 4.3: Performance Summary And Comparison With Prior Art.

	Lien JSSC 2018 [54]	Bhat JSSC 2022 [52]	Montazerolghaem ISSCC 2021 [88]	Razavi JSSC 2022[81]	This Work
Architecture	Mixer first	Mixer first	LNTA based	LNTA based	LNTA based
Technology	45 nm SOI	22 nm SOI	40 nm	28 nm	40 nm
f_{RF} (GHz)	0.2 - 8	1 - 6	0.4 - 3.2	0.4 - 6	0.4 – 7.3
Gain (dB)	21	22.4	36	54	38
Flat BW	Yes	No	Yes	No	Yes
Single Ended Input	No	No	Yes	Yes	Yes
BW (MHz)	20	350	160	0.2 - 160	300
NF (dB)	2.3 - 7	2.5 - 5	2.7 – 3.6	2.1†/4.42§	3.2 - 5.8
0dBm Blocker NF (dB)	4.7	N/A	8.4	5.2†/7.4§	9.65
Filtering roll-off (dB/dec)	-40	-20	-55	-60	-60
IB OIP3 (dBm)	21	28.5-34.4	17	19$	27-38
OOB IIP_3 (dBm)	39 $\Delta f/\omega_{3\text{-dB}} = 8$	18 $\Delta f/\omega_{3\text{-dB}} = 5.7$	10 $\Delta f/\omega_{3\text{-dB}} = 3$	3$ $\Delta f/\omega_{3\text{-dB}} = 12.5$	11 $\Delta f/\omega_{3\text{-dB}} = 3$
OOB IIP_2 (dBm)	88 $\Delta f/\omega_{3\text{-dB}} = 8$	N/A	50 $\Delta f/\omega_{3\text{-dB}} = 3$	20$ $\Delta f/\omega_{3\text{-dB}} = 12.5$	67.7 $\Delta f/\omega_{3\text{-dB}} = 3$
B1dB(dBm)	12 $\Delta f/\omega_{3\text{-dB}} = 4$	3 $\Delta f/\omega_{3\text{-dB}} = 5.7$	-5 $\Delta f/\omega_{3\text{-dB}} = 5$	N/A	-4.8 $\Delta f/\omega_{3\text{-dB}} = 3$
EVM (dB)	N/A	N/A	-26.4¥	-25.3¢	-31œ
Supply (V)	1.2	0.83	1.3/1.2	1	1.3
Active Area (mm^2)	0.8	0.48	0.6	1.9	0.42
Power (mW)	50mW+ 30mW/GHz	172	58.5+ 17.6mW/GHz	23 - 49	100+ 13mW/GHz

†Low noise mode, § Harmonic reject mode, $ Maximum bandwidth, ¢ -57dBm 80MS/s 64-QAM, , ¥ -60dBm 140MS/s 64-QAM, œ -55dBm 100MS/s 64-QAM.

sensitivity, we apply 100 symbols to the input of our RX. As shown in Fig. 4.38 (a), the RX achieves a throughput of 96% for the reference sensitivity, satisfying the 3GPP requirement (96 symbols out of 100 symbols are received correctly). Note that the red dots represent the missing symbols. For blocking tests, the throughput must exceed 95% when the input signal power is 6 dB higher than the reference sensitivity level. In the in-band blocking test, a -35 dBm 20 MS/s modulated in-band blocker at the passband edge is combined with the desired signal and applied to the RX input. Thanks to the RX's excellent in-band linearity, 100% of the symbols are received correctly, as shown in Fig. 4.38 (b). In the 5G close-in blocking scenario, a -15 dBm close-in blocker at 60 MHz offset frequency from the bandwidth edge is applied to the RX. As

illustrated in Fig. 4.39 (a), all the symbols are received correctly, demonstrating the RX's high selectivity. For the co-location blocking test, While receiving the desired signal at 3 GHz, a -4 dBm far-out blocker located at 900 MHz is applied to the RX. The proposed RX receives all the symbols correctly in this scenario as well (Fig. 4.39 (b)). The measured EVM is -9.9 dB for the far-out blocking test, corresponding to a 1.4 dB signal-to-noise ratio (SNR) degradation caused by reciprocal mixing and the nonlinearity of the proposed RX.

The performance of the proposed RX is summarized in Table 4.3 and compared with the state-of-the-art RXs [52, 54, 81, 88] having similar bandwidth and operating frequency. This work demonstrates superior in-band linearity and selectivity. It is also the only RX that has been tested for reference sensitivity and various blocking scenarios specific to local area base station applications, successfully passing all tests.

4.8 Conclusion

This Chapter presented a wideband LNTA-based receiver for 5G local area base station applications, covering both the low-band and mid-band frequencies. To identify the optimal TIA architecture, the first-order and Rauch TIAs are extensively analyzed and compared in terms of the transfer function, input impedance, loop gain, and noise. Based on the analysis, the Rauch TIA was chosen for its superior selectivity and higher loop gain. A third-order high-pass filter was also added in parallel with its feedback resistor to further enhance the selectivity of the Rauch TIA. The RX integrates the Rauch TIAs with passive mixers and an LNTA featuring an N-path notch filter in its feedback. To extend the RX operating frequency, two switch sets at the LNTA output —one for the N-path notch filter and another for the down-converting mixers— were merged. Moreover, the band-pass characteristic of the TIA input impedance is used to introduce positive feedback in the LNTA, enhancing the 3-dB bandwidth without sacrificing the RX's out-of-band rejection. Fabricated in 40 nm bulk CMOS technology, The proposed RX meets the 3GPP requirements for reference sensitivity, in-band blocking, close-in blocking, and out-of-band blocking, making it well-suited for 5G local area base station applications.

4

Chapter

5

Conclusion

5.1 Thesis Outcomes

The introduction of fifth-generation (5G) mobile communication has addressed the growing demand for higher data rates by expanding the available bandwidth for sub-6 GHz radios. Despite the increased bandwidth, the required blocker offset frequency in 5G applications has remained unchanged due to the congested sub-6 GHz spectrum, compared to the earlier communication standards, such as LTE. Hence, the main focus of this thesis was on proposing wideband RXs that are resilient to the stringent blocking scenarios of the 5G user equipment (UE) and base station (BS) applications.

Wideband RXs for 5G must handle close-in blockers while providing high bandwidth. Therefore, 5G RXs require sufficient selectivity in both the RF and baseband domains to suppress close-in blockers and prevent voltage clipping in the baseband amplifiers. Additionally, in co-location scenarios, large blockers from other standards, such as GSM, should also be handled. This requires the RXs to handle significant currents induced by far-out blockers. Furthermore, although termed sub-6-GHz, the 5G spectrum now extends up to 7 GHz to benefit from both lower path loss and broader bandwidth availability in the low- and mid-band frequencies. Thus, the proposed RXs must operate up to 7 GHz and support very high bandwidths to meet evolving 5G requirements.

In this context, the thesis presents three distinct wideband RX architectures, each designed for a different node within the 5G mobile communication — user equipment, microcell base stations, and local area base stations. The proposed RXs are fabricated in 40-nm CMOS technology and address key challenges in in-band linearity, out-of-band linearity, sensitivity, selectivity, and operating frequency.

In Chapter 2, a highly selective RX was proposed for 5G UE applications. To meet the challenging blocker requirement of 5G UE applications, the following are proposed:

- Two zeros around the LNTA transfer function to enhance the selectivity of an RF front-end and suppress close-in blockers
- A current-sinking path to reduce the RX input impedance at far-out offset frequencies, thereby improving its out-of-band linearity
- Replaced the feedback capacitor of TIA with a load capacitor to enhance RX selectivity and filter close-in blockers

This RX satisfies both reference sensitivity and out-of-band blocking specifications for 5G TDD UE, making it suitable for high-performance mobile applications.

In Chapter 3, to address co-location blocking conditions and close-in blockers in microcell base stations, a highly linear and reconfigurable RX was proposed with the following features:

- A parallel preselect filter with third-order filtering to improve the RX selectivity and B1dB of the RF front-end
- Utilized a third-order impedance in the baseband domain to increase the RX selectivity and suppress the close-in blockers
- A translational feedback network in the RX feedback to simultaneously achieve input matching and a flat in-band gain response

The RX operates in both low-noise and linear modes, achieving sub-3 dB NF and +28 dBm IIP3, and meets 3GPP blocking requirements even under high out-of-band blockers of co-location applications.

In Chapter 4, a wideband LNTA-based RX was developed for local area base station applications, covering both low-band and mid-band frequencies up to 7 GHz. To meet the stringent linearity requirement, high bandwidth, and wideband operation, the following contributions are introduced:

- Identified the Rauch TIA as a suitable candidate for 5G applications to achieve highly linear and selective RX
- Sharing the switches of down-converting mixers and the N-path notch filter at the LNTA output to reduce the parasitic capacitor at the LNTA output and enhance the RX operating frequency
- A positive feedback technique to enhance the RX bandwidth without sacrificing out-ot-band rejection of RF front-end by utilizing the band-pass shaped input impedance of a TIA

This RX meets 3GPP requirements for sensitivity, in-band blocking, and out-of-band blocking, making it a strong candidate for local area 5G infrastructure.

5.2 Recommendations for Future Developments

Although the proposed receivers are functional and can satisfy the reference sensitivity and blocking requirements for 5G user equipment, microcell base station, and local area base station applications, there is still room for performance improvements.

One challenge that N-path filters encounter is charge injection. Charge injection can lead to signal sharing between the I and Q paths, which degrades the symmetry of the RX transfer function at the lower and upper sides of the operating frequency. As shown in Fig. 5.1, CMOS switches can be used to minimize charge injection by generating a reverse charge from the PMOS transistor. However, this technique requires both LO and $\overline{\text{LO}}$, which results in higher power consumption and reduced operating frequency.

One of the challenges of N-path filters is operating at high LO frequencies due to technology limitations. For instance, the operating frequency of N-path filters is limited to below 3 GHz when the number of phases is set to 8, primarily due to the difficulty of generating 12.5% non-overlapping LO phases. However, as shown in Fig. 5.2, generating LO signals with a 25% pulse width and 45o phase shift is still possible for operating frequencies above 3 GHz [118]. In this case, the overlap between LO phases can degrade the image rejection and noise performance of the RX. To address this, as shown in Fig. 5.3, previous works [116, 118] suggest placing two inductors between overlapping LO paths to improve the RX's degraded noise performance. This technique can also be utilized to mitigate the charge injection issue in N-path notch filters.

As discussed in Chapter 2, two zeros are introduced to suppress close-in blockers in user equipment applications. To implement these zeros, a series

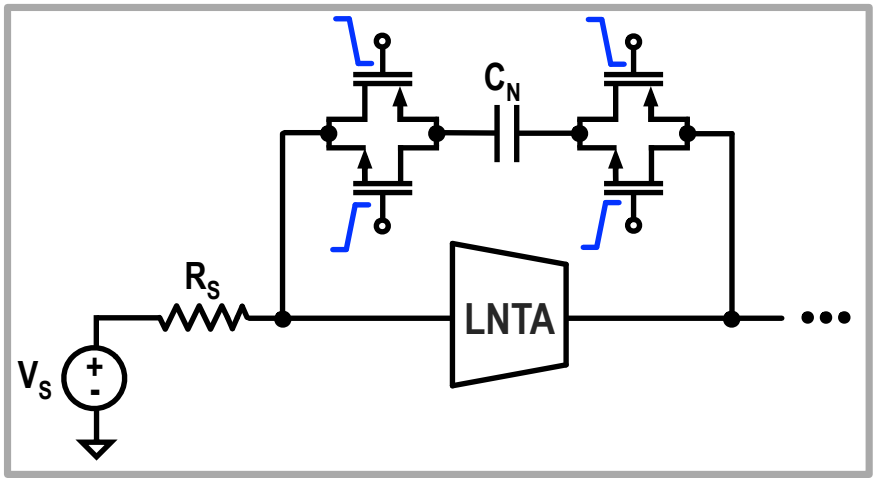

Figure 5.1: Utilizing CMOS switches to minimize the effect of charge injection in N-path notch filters.

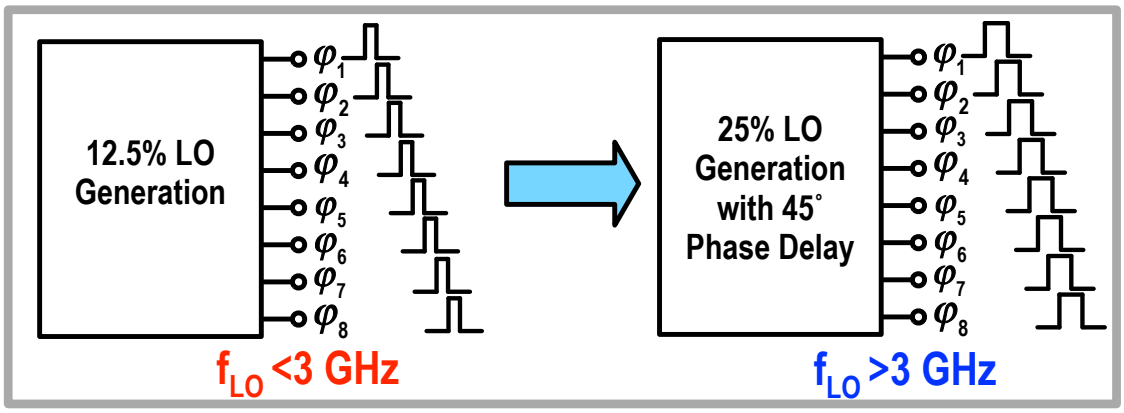

Figure 5.2: Increasing the operating frequency of the N-path filters by utilizing 25% LO signals with 45◦ phase delay.

impedance is added before the N-path notch filter. As depicted in Fig. 5.4, the components of this series impedance can be utilized to isolate the LO phases, thereby enhancing the symmetry of the RX transfer function around the operating frequency, which was compromised by charge injection. However, this structure requires four inductors, significantly increasing the chip area and high-frequency routing complexity. As shown in Fig. 5.5, the design can be further optimized by reducing the number of inductors to two by sharing the input and output inductors. Finally, by using 25% LO phases with a 45◦ shift, as in [116, 118], the RX operating frequency can exceed 3 GHz and reach up to 7 GHz, aligning with current 5G standard trends.

In Chapter 4, a three-stage Operational Transconductance Amplifier (OTA) is employed to increase loop gain and achieve adequate in-band linearity. To ensure

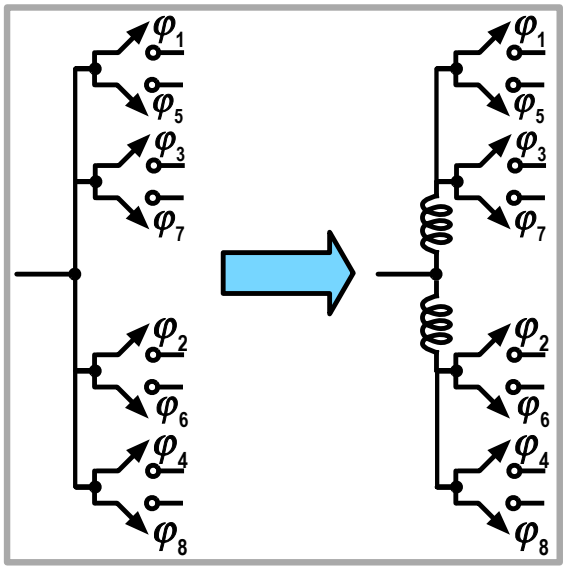

Figure 5.3: Improving the RX noise and image rejection performance by adding two isolation inductors [116].

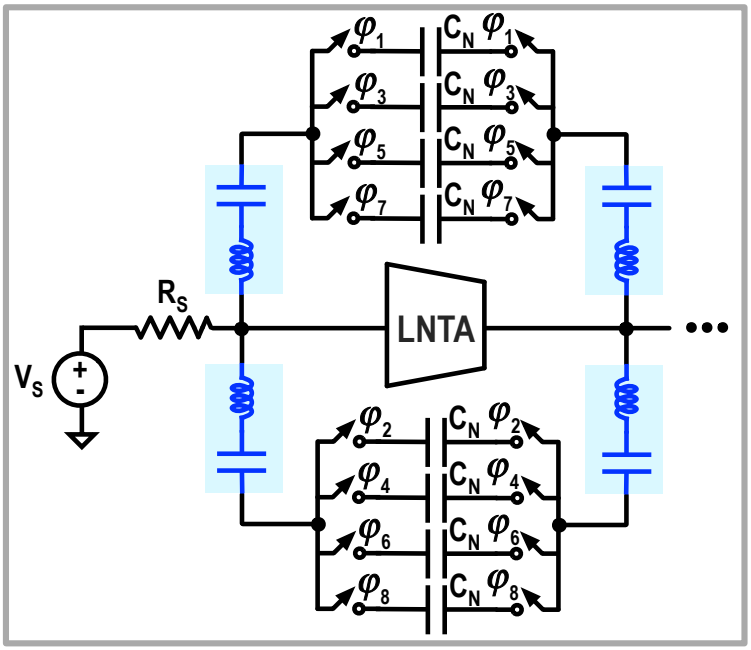

Figure 5.4: Improving the symmetry of RX transfer function around the operating frequency.

stability in this OTA design, two stabilization techniques are implemented. First, Miller compensation is applied in the second stage to establish the dominant pole and shift the second pole at the second stage output to higher frequencies. Second, a feedforward path is introduced between the input and output of the OTA to create a high-frequency zero and sustain gain at high frequencies. However, since the feedforward path operates at high frequencies, smaller channel

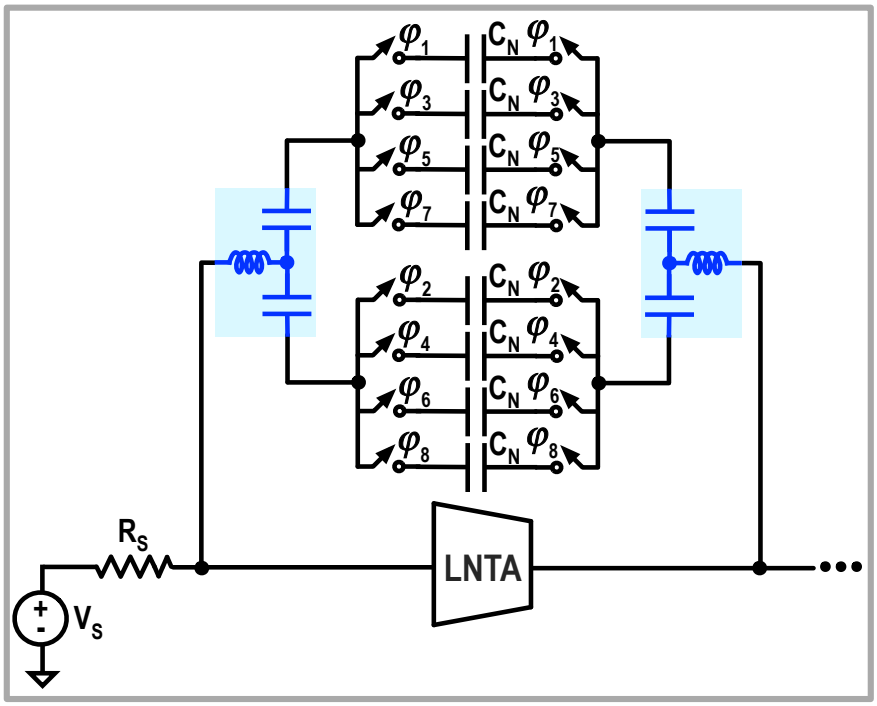

Figure 5.5: The modified impedance to reduce the number of the inductors.

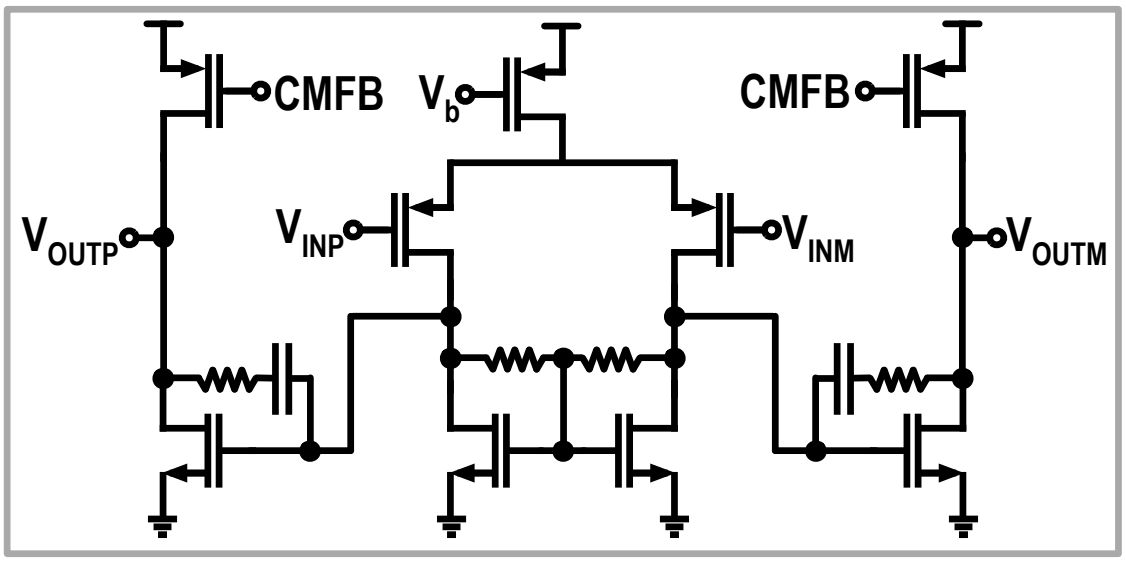

Figure 5.6: A two-stage OTA with Miller compensation [117].

devices are used for its implementation. These smaller channel devices have low output resistance, which loads the OTA's output stage. Consequently, the feedforward path reduces both the overall OTA gain and the TIA loop gain, limiting the RX's achievable in-band linearity performance.

Alternatively, a two-stage OTA can serve as the TIA amplifier, as shown

in Fig. 5.6 [117]. Miller compensation is used here to stabilize the OTA by creating a dominant pole below the 3-dB bandwidth and pushing the output pole of the OTA to higher frequencies. However, this dominant pole reduces loop gain across the 3-dB bandwidth, which degrades RX in-band linearity at the bandwidth edge. As discussed in Chapter 4, the Rauch TIA introduces two zeros that help flatten the loop gain at the passband edge, enhancing OTA stability. Consequently, Miller compensation may not be necessary for stability. Instead, the second dominant pole of the OTA should first be identified, followed by the implementation of a novel compensation technique to shift this pole to higher frequencies. This approach minimizes RX in-band linearity degradation across the 3-dB bandwidth, allowing for a higher 3-dB bandwidth target. Such a structure can be beneficial in applications like digital pre-distortion (DPD) loops, where a wider bandwidth than the 3GPP standard is required to estimate power amplifier (PA) nonlinearity [119].

In this thesis, three different LNTA-based RXs were proposed for 5G cellular applications. These designs reveal a fundamental trade-off between out-of-band linearity, in-band linearity, and operating frequency. Improving out-of-band linearity, for instance, requires increasing the input capacitance of the TIA and the size of the passive mixers. However, a larger TIA input capacitor reduces the loop gain, thereby degrading in-band linearity. Similarly, reducing the on-resistance of passive mixers adds parasitic capacitance to RF nodes, which not only limits the RX's operating frequency but also reduces the LNTA's output resistance at high frequencies, further degrading loop gain and RX in-band linearity performance. While LNTA linearization techniques can enhance out-of-band linearity, they often introduce additional input parasitics, again limiting the RX's frequency range. These trade-offs highlight the complexity of designing wideband receivers with simultaneously high in-band and out-of-band linearity, making it a compelling and ongoing area for future research.

Bibliography

[1] E. U. T. R. Access, "Base Station (BS) Radio Transmission and Reception (Release 17) document TS 38.104," *V17.6.0*, June 2022.

[2] ——, "User Equipment (UE) Radio Transmission and Reception document TS 38.101-1," *V16.8.0*, June 2021.

[3] M. Darvishi, "Active N-path filters:Theory and design," Ph.D. dissertation, UTwente, Sep. 2013.

[4] B. Razavi, "The Active Inductor [A Circuit for All Seasons]," *IEEE Solid-State Circuits Magazine*, vol. 12, no. 2, pp. 7–11, 2020.

[5] H. Busignies and M. Dishal, "Some Relations between Speed of Indication, Bandwidth, and Signal-to-Random-Noise Ratio in Radio Navigation and Direction Finding," *Proceedings of the IRE*, vol. 37, no. 5, pp. 478–488, 1949.

[6] W. R. Lepage, C. R. Cahn, and J. S. Brown, "Analysis of a comb filter using synchronously commutated capacitors," *Transactions of the American Institute of Electrical Engineers, Part I: Communication and Electronics*, vol. 72, no. 1, pp. 63–68, 1953.

[7] B. D. Smith, "Analysis of Commutated Networks," *Transactions of the IRE Professional Group on Aeronautical and Navigational Electronics*, vol. PGAE-10, pp. 21–26, 1953.

[8] A. Ghaffari, E. A. M. Klumperink, M. C. M. Soer, and B. Nauta, "Tunable High-Q N-Path Band-Pass Filters: Modeling and Verification," *IEEE Journal of Solid-State Circuits*, vol. 46, no. 5, pp. 998–1010, 2011.

[9] A. Ghaffari, E. A. M. Klumperink, and B. Nauta, "Tunable N-Path Notch Filters for Blocker Suppression: Modeling and Verification," *IEEE Journal of Solid-State Circuits*, vol. 48, no. 6, pp. 1370–1382, 2013.

[10] A. Ghaffari, E. A. Klumperink, and B. Nauta, "A differential 4-path highly linear widely tunable on-chip band-pass filter," in *2010 IEEE Radio Frequency Integrated Circuits Symposium*, 2010, pp. 299–302.

[11] A. Ghaffari, E. Klumperink, and B. Nauta, "8-Path tunable RF notch filters for blocker suppression," in *2012 IEEE International Solid-State Circuits Conference*, 2012, pp. 76–78.

[12] A. Mirzaei, H. Darabi, J. C. Leete, and Y. Chang, "Analysis and Optimization of Direct-Conversion Receivers With 25% Duty-Cycle Current-Driven Passive Mixers," *IEEE Transactions on Circuits and Systems I: Regular Papers*, vol. 57, no. 9, pp. 2353–2366, 2010.

[13] A. Mirzaei, H. Darabi, and D. Murphy, "Architectural Evolution of Integrated M-Phase High-Q Bandpass Filters," *IEEE Transactions on Circuits and Systems I: Regular Papers*, vol. 59, no. 1, pp. 52–65, 2012.

[14] E. A. Klumperink, H. J. Westerveld, and B. Nauta, "N-path filters and mixer-first receivers: A review," in *2017 IEEE Custom Integrated Circuits Conference (CICC)*, 2017, pp. 1–8.

[15] S. Hari, C. J. Ellington, and B. A. Floyd, "A Reflection-Mode N-Path Filter Tunable From 6 to 31 GHz," *IEEE Journal of Solid-State Circuits*, vol. 58, no. 7, pp. 1973–1986, 2023.

[16] C. J. Ellington, S. Hari, and B. A. Floyd, "Analysis and Design of Baseband Circuits for Higher-Order Reflection-Mode N-Path Filters," *IEEE Transactions on Circuits and Systems I: Regular Papers*, vol. 70, no. 12, pp. 5152–5165, 2023.

[17] E. Zijlma, S. van Zanten, R. Plompen, E. A. M. Klumperink, R. A. R. v. d. Zee, and B. Nauta, "Analysis and Design of a Low-Loss 1–10 GHz Capacitive Stacking N-Path Filter/Mixer," *IEEE Journal of Solid-State Circuits*, pp. 1–15, 2024.

[18] S. Garimella, S. Garikapati, A. Nagulu, and H. Krishnaswamy, "Passive Frequency Shifting of N-Path Filters Through Rotary Clocking: Analysis and Design," *IEEE Transactions on Circuits and Systems I: Regular Papers*, vol. 71, no. 1, pp. 73–84, 2024.

[19] C. Andrews and A. C. Molnar, "A Passive Mixer-First Receiver With Digitally Controlled and Widely Tunable RF Interface," *IEEE Journal of Solid-State Circuits*, vol. 45, no. 12, pp. 2696–2708, 2010.

[20] J. Gong, B. Patra, L. Enthoven, J. van Staveren, F. Sebastiano, and M. Babaie, "A 0.049mm2 7.1-to-16.8GHz Dual-Core Triple-Mode VCO Achieving 200dB $\mathbf{FoM_A}$ in 22nm FinFET," in *2022 IEEE International Solid-State Circuits Conference (ISSCC)*, vol. 65, 2022, pp. 1–3.

[21] D. Murphy, H. Darabi, A. Abidi, A. A. Hafez, A. Mirzaei, M. Mikhemar, and M.-C. F. Chang, "A Blocker-Tolerant, Noise-Cancelling Receiver Suitable for Wideband Wireless Applications," *IEEE Journal of Solid-State Circuits*, vol. 47, no. 12, pp. 2943–2963, 2012.

[22] P. Song and H. Hashemi, "RF Filter Synthesis Based on Passively Coupled N-Path Resonators," *IEEE Journal of Solid-State Circuits*, vol. 54, no. 9, pp. 2475–2486, 2019.

[23] M. Darvishi, R. van der Zee, and B. Nauta, "Design of Active N-Path Filters," *IEEE Journal of Solid-State Circuits*, vol. 48, no. 12, pp. 2962–2976, 2013.

[24] M. Darvishi, R. van der Zee, E. A. M. Klumperink, and B. Nauta, "Widely Tunable 4th Order Switched G $_m$-C Band-Pass Filter Based on N-Path Filters," *IEEE Journal of Solid-State Circuits*, vol. 47, no. 12, pp. 3105–3119, 2012.

[25] A. Nagulu, M. Yi, Y. Zhuang, S. Garikapati, and H. Krishnaswamy, "A 1-to-5GHz All-Passive Frequency-Translational 4th-Order N-path Filter with Low-Power Clock Boosting for High Linearity and Relaxed P_{dc}-Frequency Trade-Off," in *2023 IEEE International Solid-State Circuits Conference (ISSCC)*, 2023, pp. 378–380.

[26] A. Nagulu, Y. Zhuang, M. Yuan, S. Garikapati, and H. Krishnaswamy, "A Third-Order Quasi-Elliptic N-Path Filter With Enhanced Linearity Through Clock Boosting," *IEEE Journal of Solid-State Circuits*, vol. 58, no. 12, pp. 3351–3363, 2023.

[27] G. Qi, H. Guo, Y. Li, and P.-I. Mak, "A BW-Extended Fourth-Order Gain-Boosted N-Path Filter Employing a Switched gm–C Network," *IEEE Journal of Solid-State Circuits*, vol. 59, no. 10, pp. 3183–3191, 2024.

[28] Andrews, Caroline and Molnar, Alyosha C., "Implications of Passive Mixer Transparency for Impedance Matching and Noise Figure in Passive Mixer-First Receivers," *IEEE Transactions on Circuits and Systems I: Regular Papers*, vol. 57, no. 12, pp. 3092–3103, 2010.

[29] C. Andrews, L. Diamente, D. Yang, B. Johnson, and A. Molnar, "A Wideband Receiver With Resonant Multi-Phase LO and Current Reuse Harmonic Rejection Baseband," *IEEE Journal of Solid-State Circuits*, vol. 48, no. 5, pp. 1188–1198, 2013.

[30] D. H. Mahrof, E. A. M. Klumperink, Z. Ru, M. S. Oude Alink, and B. Nauta, "Cancellation of OpAmp Virtual Ground Imperfections by a Negative Conductance Applied to Improve RF Receiver Linearity," *IEEE Journal of Solid-State Circuits*, vol. 49, no. 5, pp. 1112–1124, 2014.

[31] A. Nejdel, M. Abdulaziz, M. Törmänen, and H. Sjöland, "A positive feedback passive mixer-first receiver front-end," in *2015 IEEE Radio Frequency Integrated Circuits Symposium (RFIC)*, 2015, pp. 79–82.

[32] H. Westerveld, E. Klumperink, and B. Nauta, "A cross-coupled switch-RC mixer-first technique achieving +41dBm out-of-band IIP3," in *2016 IEEE Radio Frequency Integrated Circuits Symposium (RFIC)*, 2016, pp. 246–249.

[33] Y.-C. Lien, E. A. M. Klumperink, B. Tenbroek, J. Strange, and B. Nauta, "High-Linearity Bottom-Plate Mixing Technique With Switch Sharing for N -path Filters/Mixers," *IEEE Journal of Solid-State Circuits*, vol. 54, no. 2, pp. 323–335, 2019.

[34] V. K. Purushothaman, E. Klumperink, B. T. Clavera, and B. Nauta, "A Sub-mW All-Passive RF Front End with Implicit Capacitive Stacking Achieving 13 dB Gain, 5 dB NF and +25 dBm OOB-IIP3," in *2019 IEEE Radio Frequency Integrated Circuits Symposium (RFIC)*, 2019, pp. 91–94.

[35] V. K. Purushothaman, E. A. M. Klumperink, B. T. Clavera, and B. Nauta, "A Fully Passive RF Front End With 13-dB Gain Exploiting Implicit Capacitive Stacking in a Bottom-Plate N-Path Filter/Mixer," *IEEE Journal of Solid-State Circuits*, vol. 55, no. 5, pp. 1139–1150, 2020.

[36] P. K. Sharma and N. Nallam, "Breaking the Performance Tradeoffs in N-Path Mixer-First Receivers Using a Second-Order Baseband Noise-

Canceling TIA," *IEEE Journal of Solid-State Circuits*, vol. 55, no. 11, pp. 3009–3023, 2020.

[37] E. Zolkov and E. Cohen, "A Mixer-First Receiver With Enhanced Matching Bandwidth by Using Baseband Reactance-Canceling LNA," *IEEE Solid-State Circuits Letters*, vol. 4, pp. 109–112, 2021.

[38] B. Guo, H. Wang, Y. Wang, K. Li, L. Li, and W. Zhou, "A Mixer-First Receiver Frontend with Resistive-Feedback Baseband Achieving 200 MHz IF Bandwidth in 65 nm CMOS," in *2022 IEEE Radio Frequency Integrated Circuits Symposium (RFIC)*, 2022, pp. 31–34.

[39] S. Araei, S. Mohin, and N. Reiskarimian, "19.2 An Interferer-Tolerant Harmonic-Resilient Receiver with >+10dBm 3rd-Harmonic Blocker P1dB for 5G NR Applications," in *2023 IEEE International Solid-State Circuits Conference (ISSCC)*, 2023, pp. 18–20.

[40] K. Shi, A. A. Abidi, and H. Darabi, "Second-Order Transimpedance Amplifiers in Mixer-First Receivers: Design for Optimum Blocker Tolerance," *IEEE Transactions on Circuits and Systems I: Regular Papers*, vol. 70, no. 5, pp. 1821–1834, May 2023.

[41] H. Seo and J. Zhou, "A Passive-Mixer-First Acoustic-Filtering Superheterodyne RF Front-End," *IEEE Journal of Solid-State Circuits*, vol. 56, no. 5, pp. 1438–1453, 2021.

[42] H. Seo, M. Sha, and J. Zhou, "A Passive-Mixer-First Acoustic-Filtering Chipset Using Mixed-Domain Recombination," *IEEE Transactions on Microwave Theory and Techniques*, vol. 70, no. 7, pp. 3346–3360, 2022.

[43] H. Seo and J. Zhou, "A 2.5-to-4.5-GHz Switched-LC-Mixer-First Acoustic-Filtering RF Front-End Achieving <6dB NF, +30dBm IIP3 at 1×Bandwidth Offset," in *2020 IEEE Radio Frequency Integrated Circuits Symposium (RFIC)*, 2020, pp. 283–286.

[44] A. Kumari and D. Bhatt, "A 0.5–2.5 GHz Mixer First Receiver With 200 MHz RF Bandwidth and +18.5 dBm OB-IIP3 in 180 nm CMOS for 5G NR Band," *IEEE Transactions on Circuits and Systems I: Regular Papers*, vol. 71, no. 6, pp. 2576–2589, 2024.

[45] B. Guo, H. Wang, L. Li, and W. Zhou, "A 65 nm CMOS Current-Mode Receiver Frontend with Frequency-translational Noise Cancelation and 425

MHz IF Bandwidth," in *2023 IEEE Radio Frequency Integrated Circuits Symposium (RFIC)*, 2023, pp. 21–24.

[46] S. Weinreich and B. Murmann, "A 0.6–1.8-mW 3.4-dB NF Mixer-First Receiver With an N-Path Harmonic-Rejection Transformer-Mixer," *IEEE Journal of Solid-State Circuits*, vol. 58, no. 6, pp. 1508–1518, 2023.

[47] S. Araei, S. Mohin, and N. Reiskarimian, "Harmonic-Resilient Fully Passive Mixer-First Receiver for Software-Defined Radios," *IEEE Journal of Solid-State Circuits*, vol. 58, no. 12, pp. 3396–3407, 2023.

[48] ——, "5.2 0.25-to-4GHz Harmonic-Resilient Receiver with Built-In HR at Antenna and BB Achieving +14/+16.5dBm 3rd/5th IB Harmonic B1dB," in *2024 IEEE International Solid-State Circuits Conference (ISSCC)*, 2024.

[49] S. Araei and N. Reiskarimian, "Implementation and Application of Harmonic Reset Switching in Passive Mixers," *IEEE Journal of Solid-State Circuits*, pp. 1–13, 2024.

[50] D. J. McLaurin, K. G. Gard, R. P. Schubert, M. J. Manglani, H. Zhu, D. Alldred, Z. Li, S. R. Bal, J. Fan, O. E. Gysel, C. M. Mayer, and T. Montalvo, "A highly reconfigurable 65nm CMOS RF-to-bits transceiver for full-band multicarrier TDD/FDD 2G/3G/4G/5G macro basestations," in *2018 IEEE International Solid-State Circuits Conference - (ISSCC)*, 2018, pp. 162–164.

[51] A. N. Bhat, R. van der Zee, S. Finocchiaro, F. Dantoni, and B. Nauta, "A Baseband-Matching-Resistor Noise-Canceling Receiver Architecture to Increase In-Band Linearity Achieving 175MHz TIA Bandwidth with a 3-Stage Inverter-Only OpAmp," in *2019 IEEE Radio Frequency Integrated Circuits Symposium (RFIC)*, 2019, pp. 155–158.

[52] A. N. Bhat, R. A. R. van der Zee, and B. Nauta, "A Baseband-Matching-Resistor Noise-Canceling Receiver With a Three-Stage Inverter-Only OpAmp for High In-Band IIP3 and Wide IF Applications," *IEEE Journal of Solid-State Circuits*, vol. 56, no. 7, pp. 1994–2006, 2021.

[53] Y. Lien, E. Klumperink, B. Tenbroek, J. Strange, and B. Nauta, "24.3 A high-linearity CMOS receiver achieving +44dBm IIP3 and +13dBm B1dB for SAW-less LTE radio," in *2017 IEEE International Solid-State Circuits Conference (ISSCC)*, 2017, pp. 412–413.

[54] Y.-C. Lien, E. A. M. Klumperink, B. Tenbroek, J. Strange, and B. Nauta, "Enhanced-Selectivity High-Linearity Low-Noise Mixer-First Receiver With Complex Pole Pair Due to Capacitive Positive Feedback," *IEEE Journal of Solid-State Circuits*, vol. 53, no. 5, pp. 1348–1360, 2018.

[55] Y. Lien, E. Klumperink, B. Tenbroek, J. Strange, and B. Nauta, "A mixer-first receiver with enhanced selectivity by capacitive positive feedback achieving +39dBm IIP3 and <3dB noise figure for SAW-less LTE Radio," in *2017 IEEE Radio Frequency Integrated Circuits Symposium (RFIC)*, 2017, pp. 280–283.

[56] E. C. Szoka and A. Molnar, "Circuit Techniques for Enhanced Channel Selectivity in Passive Mixer-First Receivers," in *2018 IEEE Radio Frequency Integrated Circuits Symposium (RFIC)*, 2018, pp. 292–295.

[57] G. Pini, D. Manstretta, and R. Castello, "Analysis and Design of a 20-MHz Bandwidth, 50.5-dBm OOB-IIP3, and 5.4-mW TIA for SAW-Less Receivers," *IEEE Journal of Solid-State Circuits*, vol. 53, no. 5, pp. 1468–1480, 2018.

[58] ——, "Analysis and Design of a 260-MHz RF Bandwidth +22-dBm OOB-IIP3 Mixer-First Receiver With Third-Order Current-Mode Filtering TIA," *IEEE Journal of Solid-State Circuits*, vol. 55, no. 7, pp. 1819–1829, 2020.

[59] S. Krishnamurthy and A. M. Niknejad, "Design and Analysis of Enhanced Mixer-First Receivers Achieving 40-dB/decade RF Selectivity," *IEEE Journal of Solid-State Circuits*, vol. 55, no. 5, pp. 1165–1176, 2020.

[60] ——, "Synthesis and Design of Enhanced N-Path Filters With 60-dB/decade RF Selectivity," *IEEE Solid-State Circuits Letters*, vol. 3, pp. 522–525, 2020.

[61] ——, "An Enhanced Mixer-First Receiver With Distortion Cancellation, Achieving 80-dB/decade RF Selectivity and +8-dBm B1dB for Adjacent Channel Blockers," *IEEE Solid-State Circuits Letters*, vol. 4, pp. 64–67, 2021.

[62] ——, "Enhanced Passive Mixer-first Receiver Driving an Impedance with 40dB/decade Roll-off, Achieving +12dBm Blocker-P1dB, +33dBm IIP3 and sub-2dB NF Degradation for a 0dBm Blocker," in *2019 IEEE Radio Frequency Integrated Circuits Symposium (RFIC)*, 2019, pp. 139–142.

[63] S. van Zanten, R. van der Zee, and B. Nauta, "5.5 A Stacking Mixer-First Receiver Achieving >20dBm Adjacent-Channel IIP3 Consuming less than 25mW," in *2024 IEEE International Solid-State Circuits Conference (ISSCC)*, vol. 67, 2024, pp. 96–98.

[64] J. W. Park and B. Razavi, "A Harmonic-Rejecting CMOS LNA for Broadband Radios," *IEEE Journal of Solid-State Circuits*, vol. 48, no. 4, pp. 1072–1084, 2013.

[65] X. He and H. Kundur, "A compact SAW-less multiband WCDMA/GPS receiver front-end with translational loop for input matching," in *2011 IEEE International Solid-State Circuits Conference*, 2011, pp. 372–374.

[66] R. Chen and H. Hashemi, "A 0.5-to-3 GHz Software-Defined Radio Receiver Using Discrete-Time RF Signal Processing," *IEEE Journal of Solid-State Circuits*, vol. 49, no. 5, pp. 1097–1111, 2014.

[67] ——, "Reconfigurable Receiver With Radio-Frequency Current-Mode Complex Signal Processing Supporting Carrier Aggregation," *IEEE Journal of Solid-State Circuits*, vol. 50, no. 12, pp. 3032–3046, 2015.

[68] A. Mirzaei, H. Darabi, A. Yazdi, Z. Zhou, E. Chang, and P. Suri, "A 65 nm CMOS Quad-Band SAW-Less Receiver SoC for GSM/GPRS/EDGE," *IEEE Journal of Solid-State Circuits*, vol. 46, no. 4, pp. 950–964, 2011.

[69] J. Borremans, G. Mandal, V. Giannini, B. Debaillie, M. Ingels, T. Sano, B. Verbruggen, and J. Craninckx, "A 40 nm CMOS 0.4–6 GHz Receiver Resilient to Out-of-Band Blockers," *IEEE Journal of Solid-State Circuits*, vol. 46, no. 7, pp. 1659–1671, 2011.

[70] J. W. Park and B. Razavi, "Channel Selection at RF Using Miller Bandpass Filters," *IEEE Journal of Solid-State Circuits*, vol. 49, no. 12, pp. 3063–3078, 2014.

[71] F. Lin, P.-I. Mak, and R. P. Martins, "An RF-to-BB-Current-Reuse Wideband Receiver With Parallel N-Path Active/Passive Mixers and a Single-MOS Pole-Zero LPF," *IEEE Journal of Solid-State Circuits*, vol. 49, no. 11, pp. 2547–2559, 2014.

[72] C.-k. Luo, P. S. Gudem, and J. F. Buckwalter, "A 0.4–6-GHz 17-dBm B1dB 36-dBm IIP3 Channel-Selecting Low-Noise Amplifier for SAW-Less 3G/4G FDD Diversity Receivers," *IEEE Transactions on Microwave Theory and Techniques*, vol. 64, no. 4, pp. 1110–1121, 2016.

[73] L. Zhang, A. Natarajan, and H. Krishnaswamy, "Scalable Spatial Notch Suppression in Spatio-Spectral-Filtering MIMO Receiver Arrays for Digital Beamforming," *IEEE Journal of Solid-State Circuits*, vol. 51, no. 12, pp. 3152–3166, 2016.

[74] G. Qi, P.-I. Mak, and R. P. Martins, "A 0.038-mm2 SAW-Less Multiband Transceiver Using an N-Path SC Gain Loop," *IEEE Journal of Solid-State Circuits*, vol. 52, no. 8, pp. 2055–2070, 2017.

[75] G. Qi, B. van Liempd, P.-I. Mak, R. P. Martins, and J. Craninckx, "A SAW-Less Tunable RF Front End for FDD and IBFD Combining an Electrical-Balance Duplexer and a Switched-LC N-Path LNA," *IEEE Journal of Solid-State Circuits*, vol. 53, no. 5, pp. 1431–1442, 2018.

[76] A. Rasekh and M. S. Bakhtiar, "Wide-Band RF Front End for SAW-Less Receivers Employing Active Feedback and Far Out-of-Band Blocker Rejection Circuit," *IEEE Journal of Solid-State Circuits*, vol. 54, no. 6, pp. 1528–1540, 2019.

[77] S. Lecchi, D. Manstretta, and R. Castello, "An Interferer-Tolerant RX with Translational Positive Feedback for 5G NR Applications Achieving 3.4 dB NF and 18 dBm OOB IIP3," in *ESSCIRC 2023- IEEE 49th European Solid State Circuits Conference (ESSCIRC)*, 2023, pp. 57–60.

[78] H. Wang, Z. Wang, and P. Heydari, "28.7 A Wideband Blocker-Tolerant Receiver with High-Q RF-Input Selectivity and <-80dBm LO Leakage," in *2019 IEEE International Solid-State Circuits Conference - (ISSCC)*, 2019, pp. 450–452.

[79] ——, "An LO Leakage Suppression Technique for Blocker-Tolerant Wideband Receivers With High-Q Selectivity at RF Input," *IEEE Journal of Solid-State Circuits*, vol. 56, no. 6, pp. 1682–1696, 2021.

[80] H. Razavi and B. Razavi, "A 0.4-6 GHz Receiver for LTE and WiFi," in *2021 Symposium on VLSI Circuits*, 2021, pp. 1–2.

[81] ——, "A 0.4–6 GHz Receiver for Cellular and WiFi Applications," *IEEE Journal of Solid-State Circuits*, vol. 57, no. 9, pp. 2640–2657, 2022.

[82] S. Yun, C. Cho, S. Jo, and K. Kwon, "A 2.7-dB NF 55-dBm IIP2 Blocker-Tolerant Receiver Front End Employing Dual RF and BB N -Path Filters for 5G New Radio Cellular Applications," *IEEE Transactions on Microwave Theory and Techniques*, pp. 1–15, 2024.

[83] S. Jo, H. Kim, and K. Kwon, "IIP2-Calibration-Free 5G NR Cellular Receiver Front-End With Mixer-Sharing Global N -Path Notch Filter Feedback Achieving + 72 dBm IIP2," *IEEE Transactions on Circuits and Systems I: Regular Papers*, pp. 1–13, 2024.

[84] C. Tao, L. Lei, C. Zheng, Y. Huang, Z. Hong, and X. Zeng, "A Low-Power, Compact, 0.1–5.5-GHz, 40-dBm IB OIP3 LNTA-First Receiver for SDR," *IEEE Journal of Solid-State Circuits*, vol. 59, no. 9, pp. 2761–2773, 2024.

[85] Z. Lin, P.-I. Mak, and R. P. Martins, "Analysis and Modeling of a Gain-Boosted N-Path Switched-Capacitor Bandpass Filter," *IEEE Transactions on Circuits and Systems I: Regular Papers*, vol. 61, no. 9, pp. 2560–2568, 2014.

[86] J. Y. Kim and A. Liscidini, "A 2GHz voltage mode power scalable RF-Front-End with 2.5dB-NF and 0.5dBm-1dBCP," in *2022 IEEE Custom Integrated Circuits Conference (CICC)*, 2022, pp. 1–2.

[87] ——, "A Reconfigurable Power-Efficient Quantized Analog RF Front-End With Smart Calibration," *IEEE Open Journal of the Solid-State Circuits Society*, vol. 2, pp. 165–174, 2022.

[88] M. A. Montazerolghaem, S. Pires, L. C. de Vreede, and M. Babaie, "6.5 A 3dB-NF 160MHz-RF-BW Blocker-Tolerant Receiver with Third-Order Filtering for 5G NR Applications," in *2021 IEEE International Solid-State Circuits Conference (ISSCC)*, vol. 64, 2021, pp. 98–100.

[89] M. A. Montazerolghaem, L. C. N. de Vreede, and M. Babaie, "A Highly Selective Receiver With Programmable Zeros and Second-Order TIA," *IEEE Journal of Solid-State Circuits*, vol. 59, no. 6, pp. 1668–1683, 2024.

[90] B. Razavi, "The Transimpedance Amplifier [A Circuit for All Seasons]," *IEEE Solid-State Circuits Magazine*, vol. 11, no. 1, pp. 10–97, 2019.

[91] ——, *Design of Analog CMOS Integrated Circuits*. McGraw-Hill Higher Education, 2016. [Online]. Available: https://books.google.nl/books?id=hFzmCwAAQBAJ

[92] C.-M. Hung, R. Staszewski, N. Barton, M.-C. Lee, and D. Leipold, "A digitally controlled oscillator system for SAW-less transmitters in cellular handsets," *IEEE Journal of Solid-State Circuits*, vol. 41, no. 5, pp. 1160–1170, 2006.

[93] M. Babaie and R. B. Staszewski, "An Ultra-Low Phase Noise Class-F 2 CMOS Oscillator With 191 dBc/Hz FoM and Long-Term Reliability," *IEEE Journal of Solid-State Circuits*, vol. 50, no. 3, pp. 679–692, 2015.

[94] ——, "A study of RF oscillator reliability in nanoscale CMOS," in *2013 European Conference on Circuit Theory and Design (ECCTD)*, 2013, pp. 1–4.

[95] D. P. Murphy, *Noise in large-signal, time-varying RF CMOS circuits: Theory and design*. University of California, Los Angeles, 2012.

[96] S. Pavan and E. Klumperink, "Analysis of the Effect of Source Capacitance and Inductance on N -Path Mixers and Filters," *IEEE Transactions on Circuits and Systems I: Regular Papers*, vol. 65, no. 5, pp. 1469–1480, 2018.

[97] H. Hedayati, W.-F. A. Lau, N. Kim, V. Aparin, and K. Entesari, "A 1.8 dB NF Blocker-Filtering Noise-Canceling Wideband Receiver With Shared TIA in 40 nm CMOS," *IEEE Journal of Solid-State Circuits*, vol. 50, no. 5, pp. 1148–1164, 2015.

[98] J. Musayev and A. Liscidini, "A quantized analog rf front end," *IEEE Journal of Solid-State Circuits*, vol. 54, no. 7, pp. 1929–1940, 2019.

[99] M. A. Montazerolghaem, L. C. N. de Vreede, and M. Babaie, "A 0.5-3GHz Receiver with a Parallel Preselect Filter Achieving 120dB/dec Channel Selectivity and +28dBm Out-of-Band IIP3," in *2022 IEEE Custom Integrated Circuits Conference (CICC)*, 2022, pp. 11–12.

[100] ——, "A Highly Linear Receiver Using Parallel Preselect Filter for 5G Microcell Base Station Applications," *IEEE Journal of Solid-State Circuits*, vol. 58, no. 8, pp. 2157–2172, 2023.

[101] B. Nauta, "A CMOS transconductance-C filter technique for very high frequencies," *IEEE Journal of Solid-State Circuits*, vol. 27, no. 2, pp. 142–153, 1992.

[102] S. Krishnamurthy, F. Maksimovic, L. Iotti, and A. M. Niknejad, "Analysis and Design of Submilliwatt Interference-Tolerant Receivers Leveraging N-Path Filter-Based Translational Positive Feedback," *IEEE Transactions on Microwave Theory and Techniques*, vol. 69, no. 7, pp. 3496–3509, 2021.

[103] J. Weldon, R. Narayanaswami, J. Rudell, L. Lin, M. Otsuka, S. Dedieu, L. Tee, K.-C. Tsai, C.-W. Lee, and P. Gray, "A 1.75-GHz highly integrated narrow-band CMOS transmitter with harmonic-rejection mixers," *IEEE Journal of Solid-State Circuits*, vol. 36, no. 12, pp. 2003–2015, 2001.

[104] R. Chen and H. Hashemi, "Reconfigurable blocker-resilient receiver with concurrent dual-band carrier aggregation," in *Proceedings of the IEEE 2014 Custom Integrated Circuits Conference*, 2014, pp. 1–4.

[105] B.-K. Kim, D. Im, J. Choi, and K. Lee, "A Highly Linear 1 GHz 1.3 dB NF CMOS Low-Noise Amplifier With Complementary Transconductance Linearization," *IEEE Journal of Solid-State Circuits*, vol. 49, no. 6, pp. 1286–1302, 2014.

[106] C. Tao, J. Huang, L. Lei, Y. Huang, Z. Hong, and X. Zeng, "A Compact 0.1–1.95 GHz, 1.5 dB NF LNTA Based on Cascode Inverters," *IEEE Transactions on Circuits and Systems II: Express Briefs*, vol. 71, no. 2, pp. 597–601, 2024.

[107] S. Bu and S. Pamarti, "A Dual-Channel High-Linearity Filtering-by-Aliasing Receiver Front-End Supporting Carrier Aggregation," *IEEE Journal of Solid-State Circuits*, vol. 57, no. 5, pp. 1457–1469, 2022.

[108] M. A. Montazerolghaem, L. C. N. de Vreede, and M. Babaie, "19.1 A 300MHz-BW, 27-to-38dBm In-Band OIP3 sub-7GHz Receiver for 5G Local Area Base Station Applications," in *2023 IEEE International Solid-State Circuits Conference (ISSCC)*, 2023, pp. 292–294.

[109] M. A. Montazerolghaem and M. Babaie, "A Sub-7-GHz Linear Receiver for 5G Local Area Base Station Applications," *IEEE Journal of Solid-State Circuits*, pp. 1–17, 2025.

[110] H. Jung, D. R. Utomo, S.-K. Han, J. Kim, and S.-G. Lee, "An 80 MHz Bandwidth and 26.8 dBm OOB IIP3 Transimpedance Amplifier With Improved Nested Feedforward Compensation and Multi-Order Filtering," *IEEE Transactions on Circuits and Systems I: Regular Papers*, vol. 67, no. 10, pp. 3410–3421, Oct. 2020.

[111] M. K. Lenka and G. Banerjee, "A Wideband Blocker-Tolerant Receiver With Frequency-Translational Resistive Feedback," *IEEE Transactions on Very Large Scale Integration (VLSI) Systems*, vol. 27, no. 5, pp. 993–1006, May 2019.

[112] P. Wambacq and W. M. Sansen, *Distortion analysis of analog integrated circuits*. Springer Science & Business Media, 2013, vol. 451.

[113] X. Li, F. Yin, and J. C. Rudell, "Effects of Receiver Input Impedance on Nonlinear Distortion in Full-Duplex Radios," in *2021 IEEE International Symposium on Circuits and Systems (ISCAS)*, 2021, pp. 1–5.

[114] B. Razavi, *RF Microelectronics*. Prentice hall New York, 2012, vol. 2.

[115] H. Zhang and E. Sánchez-Sinencio, "Linearization Techniques for CMOS Low Noise Amplifiers: A Tutorial," *IEEE Transactions on Circuits and Systems I: Regular Papers*, vol. 58, no. 1, pp. 22–36, 2011.

[116] C. Andrews, C. Lee, and A. Molnar, "Effects of LO harmonics and overlap shunting on N-phase passive mixer based receivers," in *2012 Proceedings of the ESSCIRC (ESSCIRC)*, 2012, pp. 117–120.

[117] J. Jiang, J. Kim, A. I. Karsilayan, and J. Silva-Martinez, "A 3–6-GHz Highly Linear I-Channel Receiver With Over +3.0-dBm In-Band P1dB and 200-MHz Baseband Bandwidth Suitable for 5G Wireless and Cognitive Radio Applications," *IEEE Transactions on Circuits and Systems I: Regular Papers*, vol. 66, no. 8, pp. 3134–3147, 2019.

[118] S. Huang and A. Molnar, "A 3.7-6.5GHz 8-Phase N-Path Mixer-First Receiver with LO Overlap Suppression Achieving <5dB NF and >5dBm OOB B1dB," in *2021 IEEE Radio Frequency Integrated Circuits Symposium (RFIC)*, 2021, pp. 87–90.

[119] T. Ibrahim, M. Beikmirza, M. Alavi, and L. de Vreede, "A Quadrature Harmonic Rejection Voltage-Domain Mixer with 20 dBm OIP3 and 800 MHz IF Bandwidth," in *2024 19th European Microwave Integrated Circuits Conference (EuMIC)*, 2024, pp. 443–446.

List of Figures

1.1 A simplified example of cellular network used for GSM. 2
1.2 Two well-known transceiver architectures used in wireless communications: (a) FDD and (b) TDD. 3
1.3 5G spectrum. 4
1.4 BER versus SNR for different modulation schemes. 5
1.5 Some examples of new radio operating bands. 5
1.6 Conventional RX architecture with band-select filters to choose different frequency bands. 6
1.7 A typical implementation of N-path filter. 8
1.8 Replacing Z_{BB} with baseband capacitors and its equivalent model. 8
1.9 NF degradation due to the mixing between the LO phase noise and out-of-band blocker. 9
1.10 SNR degradation due to the reciprocal mixing of LO phase noise and out-of-band blockers. 10
1.11 Conventional current-mode RX architecture. 12
1.12 (a) Conventional mixer-first RXs block diagram; (b) Adding a matching resistor to improve the in-band linearity performance of mixer-first RXs; Canceling the noise of matching resistor in (c) RF and (d) baseband domain. 13
1.13 (a) Conventional LNTA-based RX architecture; (b) Adding a translational feedback network to achieve input-matching in LNTA-based architectures; (c) An N-path filter is placed at the RX input to achieve RF filtering; (d) Utilizing N-path notch filter in the feedback of LNTA to achieve RF filtering. 14
1.14 The simulated input impedance (a) and LNTA gain (b) of the conventional LNTA-based RXs. 15

2.1 Conventional LNTA-based RX architecture with the equivalent model of the N-path notch filter in its feedback. Note that for simplicity, in these conceptual diagrams, an explicit shunt resistor, R_m, is used for the input matching. 20
2.2 Comparison between the simulated (a) G_{LNTA} and (b) G_{IN} of the conventional LNTA-based architecture and the proposed RX. Note that LNTA, mixers, and TIAs are implemented using ideal elements, and the notch filters are realized by RLC components with $R_{ON} = 7.7\,\Omega$. 21
2.3 The proposed impedance in the feedback of the LNTA. For simplicity, the same shunt resistor is used for the input matching. . 22
2.4 Evolution of implementing the proposed impedance using two N-path notch filters and a gyrator. 24
2.5 Preliminary block diagram of the proposed RX, where the proposed programmable filter is placed in the LNTA's feedback. . . 25
2.6 (a) Block diagram of the RX front-end. An auxiliary N-path filter is added to reduce the RX input impedance at far-out frequencies; (b) The equivalent model of the proposed RX architecture at far-out offset frequencies. 26
2.7 The circuit level simulation results of (a) G_{LNTA} and (b) G_{IN} for the proposed structure shown in Fig. 2.6, using the components' values calculated in the design guide. 28
2.8 The simplified model of the RX front-end for the stability analysis. 29
2.9 Simulated loop gain of the RX front-end for different VSWR values. 30
2.10 Schematics of (a) the second-order TIA, (b) its common-mode feedback circuit, and (c) the utilized TIA amplifier. 31
2.11 Simulated TIA transfer function with/without C_L. 33
2.12 The deviations of the frequency response of the second-order TIA against (a) ±20% variations of C_{IN} and C_L, (b) ±20% R_F variations, and (c) only g_{mt} and r_{ot} changes over PVT variations. 34
2.13 The fluctuation of (a) g_{mt}, (b) r_{ot}, and (c) $g_{mt} \times r_{ot}$ over PVT variations using Monte Carlo simulations. 35
2.14 (a) Feedback model with Y parameters for the second-order TIA; (b) Bode plot of the TIA amplifier loop gain. 37
2.15 Simulated magnitude and phase response of the TIA's loop gain. 38
2.16 (a) Simulated RX NF versus g_{mt}; (b) simulated flicker noise corner of the TIA amplifier versus the channel length of its input transistors. 39

2.17 The block diagram of the proposed RX. 41
2.18 Schematics of the implemented level shifter for biasing the LOs. 42
2.19 Schematics of the implemented (a) LNTA, (b) positive, and (c) negative transconductance of the gyrator. 43
2.20 Simplified model of the proposed RX for NF calculation. 43
2.21 The simulated noise factor of the proposed RX realized with real devices versus the LO frequency. 45
2.22 (a) Die micrograph of the proposed RX; (b) Power consumption breakdown at 1.5 GHz LO frequency. 46
2.23 Measured (a) G_{RX}, (b) in-band S_{11}, and (c) the Smith chart view of the measured S_{11} at $f_{LO} = 1.5\,\text{GHz}$. 47
2.24 Effect of the programmable zeros on (a) S_{11} and (b) G_{RX} at $f_{LO} = 1.5\,\text{GHz}$. 47
2.25 (a) Improving the RX selectivity by adjusting the value of C_L at $f_{LO} = 1.5\,\text{GHz}$; (b) enhancing the 3-dB bandwidth of the RX by increasing g_{mt} at $f_{LO} = 1.5\,\text{GHz}$ 48
2.26 Harmonic rejection performance of the proposed RX 48
2.27 (a) Measured NF versus the LO frequency; (b) Measured NF versus the baseband frequency at $f_{LO} = 1.5\,\text{GHz}$. 49
2.28 Measured (a) LO leakage for two samples and (b) frequency shift of the proposed RX normalized to BW_{RF} versus the LO frequency. 50
2.29 Measured (a) IIP3 and (b) IIP2 versus the offset frequency (Δf) normalized to BW_{RF} at $f_{LO} = 1.5\,\text{GHz}$. 50
2.30 Measured (a) B1dB versus the blocker offset frequency, and (b) blocker noise figure versus the blocker power at $f_{LO} = 1.5\,\text{GHz}$. . 51
2.31 (a) Measured constellation at reference sensitivity; Measured constellation in the presence of (b) -44 dBm blocker located at 15 MHz offset, (c) -30 dBm blocker at 60 MHz offset frequency, and (d) -15 dBm blocker at 85 MHz offset frequency while signal power is 16 dB higher than the reference sensitivity level. . . . 52
2.32 The measured constellation of 100 MS/s -60 dBm QAM-64 signal: (a) without blocker and (b) with -5 dBm blocker located at $\Delta f/\omega_{3dB} = 3.1$. 53

3.1 (a) Conventional LNTA-based structure to achieve RF selectivity [64,71,73–75,78–80,85]; (b) proposed RX with a parallel preselect filter. 58

3.2 Comparison between the analytical and simulation results of (a) $Z_{IN} \parallel R_m$ and (b) G_{IN} of the conventional and proposed RX when Z_N is an LC-based third-order notch filter. 60

3.3 (a) Initial schematic and (b) final implementation of the proposed parallel preselect filter using impedance up-conversion of a third-order high-pass filter; (c) implementation of the BB inductor using active gyrator; (d) schematic of the parallel preselect filter's transconductance. 63

3.4 (a) Simulated main RX gain versus the input voltage created by an out-of-band blocker; (b) simulated transconductance gain versus its output voltage swing. 65

3.5 Simplified model of the parallel preselect filter. 65

3.6 Gyrator schematic with its equivalent lumped-element model. . 67

3.7 Simulated input impedance of the implemented gyrator. 67

3.8 (a) Simplified block diagram of the proposed RX with a conventional translation loop for providing the input matching (for the sake of simplicity, Z_N is replaced by a first-order notch filter); (b) simulated G_{RX} in different scenarios; (c) Simplified block diagram of the main RX path with the proposed translational feedback network for compensating the side effects of parallel preselect filter delay. 69

3.9 Simulated gain of Fig 3.8 (a) receiver with $G_{M,P}r_{o,P} = 6$, $R_S = 50\,\Omega$, $C_N = 8\,\text{pF}$, $t_d = 20\,\text{ps}$, and $f_{LO} = 2\,\text{GHz}$. 70

3.10 (a) Simulated loop gain versus the angle of the reflection coefficient for different VSWR values, using (3.23) and considering $f_{LO} = 3\,\text{GHz}$ and $C_m = 300\,\text{fF}$; (b) simulated loop gain of the implemented RX for VSWR = 2 ($Z_s = 100\,\Omega$) and 3 ($Z_s = 150\,\Omega$). 72

3.11 (a) Illustration of the phase misalignment between the LOs of the main RX path and the translational feedback network; (b) Simulated RX gain for different time shifts between the LOs of the main RX path and the translational feedback network. . . . 74

3.12 Block diagram of the LO generation circuit [70]. 75

3.13 Complete block diagram of the proposed RX. 75

3.14 Schematic of implemented harmonic rejection circuit: (a) I path and (b) Q path. 76

3.15 (a) Schematic of the implemented LNTA; (b) simulated G_m of the LNTA and its HVT-based and SVT-based transconductances versus the voltage swing around the input bias voltage of the LNTA; (c) schematic of the proposed third-order TIA. 77
3.16 Simplified model of the proposed parallel preselect filter with the input-referred noise of the active blocks. 79
3.17 The die micrograph and the power consumption breakdown of the proposed RX at 1.5 GHz LO frequency. 80
3.18 Measurement setup. 81
3.19 Measured (a) RX gain and (b) S_{11} over operating frequency. . . 82
3.20 Measured (a) NF versus the LO frequency and (b) S_{11} for different $G_{M,P}$ values at 1.5 GHz LO frequency. 82
3.21 Measured NF versus the BB frequency for different LO frequencies. 83
3.22 (a) The channel selectivity of the proposed RX; (b) blocker NF. 84
3.23 (a) The in-band gain response of the proposed RX in different scenarios; (b) the effect of C_m on the RX transfer function. . . . 85
3.24 Measured IIP2 (a) and IIP3 (b) versus the offset frequency normalized to the RF bandwidth. 85
3.25 (a) Measured B1dB versus the normalized offset frequency; (b) measured constellation at the reference sensitivity for 100 MS/s signal (red squares represent the missed symbols). 86
3.26 Measured constellation for 100 MS/s signal: (a) in the presence of a -38 dBm in-band blocker and (b) when a -15 dBm out-of-band blocker at 20 MHz offset frequency is applied to the RX. 87
3.27 (a) Measured constellation for a 100 MS/s QAM-64 -60 dBm signal; (b) Measured EVM versus the input power of the desired signal. 89
3.28 Measured constellation for a 100 MS/s QAM-64 -60 dBm signal in the presence of a 0 dBm out-of-band blocker: (a) low-noise mode (b) linear mode. 89

4.1 Proposed LNTA-based RXs with (a) N-path notch filter in the feedback of LNTA and (b) parallel preselect filter at the RX input. 94
4.2 Block diagram of the (a) first-order TIA and (b) Rauch TIA. . . 96
4.3 The simulated (a) transfer function and (b) input impedance of the first-order TIA and Rauch TIA in MATLAB (first-order TIA: $C_{IN} = 10$ pF, $R_F = 1.5$ kΩ, $C_F = 605$ fF, and A_0=60 dB; Rauch TIA: $C_{IN} = 10$ pF, $R_{IN} = 50\,\Omega$, $R_F = 1.5$ kΩ, $C_F = 720$ fF, and A_0=60 dB) for different unity gain bandwidths. 98

4.4 Bode plot of simulated loop gain for the first-order and Rauch TIAs. 101
4.5 Schematic of the three-stage OTA. 102
4.6 Simulated loop gain of the TIA. 102
4.7 (a) Comparison between linearity performance of the first-order TIA and Rauch TIA; (b) Effect of increasing R_{IN} and reducing C_{IN} on the linearity performance of the Rauch TIA; (c) Comparison between the output noise of the first-order TIA, conventional Rauch TIA, and the modified Rauch TIA with an active third-order high-pass filter in its feedback. 103
4.8 Simulated OP1dB of the first-order TIA and Rauch TIA at the passband edge. 104
4.9 Monte Carlo simulation results showing the statistical variations in the 3-dB bandwidth of (a) First-order TIA, and (b) Rauch TIA. 105
4.10 Normalized transfer function of Rauch TIA under extreme statistical corners. 106
4.11 Simplified model for DC offset analysis of (a) the first-order TIA and (b) the Rauch TIA. 107
4.12 Current-mode RX utilizes the Rauch TIA with (a) conventional RF front-end and (b) proposed RF front-end. 108
4.13 The equivalent model of the RF front end of the preliminary RX structure in Fig. 4.12 (a). 109
4.14 Comparing the RX far-out front-end rejection. Blue and red curves are simulated using the conventional structure with an N-path notch filter in the LNTA feedback, and the orange one employs the proposed structure. 110
4.15 Effective Miller capacitor versus the baseband frequency. 111
4.16 Gain of positive feedback amplifier across (a) process, (b) supply, and (c) temperature variations. 112
4.17 Simulated RX gain for the worst-case scenarios of A_c. 113
4.18 A simplified model of the proposed RX for in-band linearity analysis. 114
4.19 (a) Transistor-level implementation of the LNTA; (b) Small signal model of the LNTA. 114
4.20 Simulated and calculated in-band linearity of the (a) LNTA, (b) TIA, and (c) proposed RX. 115
4.21 (a) Simplified schematic of the Rauch TIA to account for R_F and C_F loading effects; (b) Equivalent approximated model of the Rauch TIA. 118

4.22 The proposed RX block diagram. 121
4.23 Monte Carlo simulation results of DC offset at the RX output. 123
4.24 Schematic of LO generation block. 124
4.25 Active implementation of the differential inductor. 124
4.26 Filtering response of Rauch TIA before and after adding the third-order impedance. 125
4.27 Effect of the active inductor on the simulated RX in-band IIP3. 125
4.28 Die micrograph and power consumption breakdown at $f_{LO} = 3$ GHz. 126
4.29 Measured (a) gain and (b) in-band S_{11} over the operating frequency. 127
4.30 Measured (a) NF and (b) LO leakage across the operating frequency. 127
4.31 (a) Effect of the third-order impedance on the selectivity of the proposed RX; (b) Extending the measured 3-dB bandwidth with the proposed positive feedback. 128
4.32 (a) Improving the measured in-band OIP3 by increasing R_{IN} and reducing C_{IN}; (b) Impact of increasing R_{IN} and reducing C_{IN} on the RX in-band gain transfer function. 128
4.33 (a) Reduction of IM3 generated by in-band and close-in blockers through increasing R_{IN} and reducing C_{IN}; (b) Measured IIP3 versus the offset frequency. 129
4.34 (a) Effect of increasing R_{IN} and reducing C_{IN} on the measured B1dB across the close-in blocker range; (b) Measured B1dB versus the offset frequency. 130
4.35 (a) Measured blocker NF versus the blocker power; (b) Measured IIP2 versus the offset frequency. 130
4.36 Front-end block diagram of an FDD transceiver. 131
4.37 Measured constellation of the proposed RX for -55 dBm 100 MS/s (a) 64-QAM and (b) 256-QAM input signals. 132
4.38 (a) Measured constellation at the reference sensitivity; (b) Measured constellation in the presence of a -35 dBm in-band blocker. 133
4.39 Measured constellation in the presence of (a) a -15 dBm close-in blocker and (b) a -4 dBm far-out blocker. 133

5.1 Utilizing CMOS switches to minimize the effect of charge injection in N-path notch filters. 140
5.2 Increasing the operating frequency of the N-path filters by utilizing 25% LO signals with 45◦ phase delay. 140
5.3 Improving the RX noise and image rejection performance by adding two isolation inductors [116]. 141

5.4 Improving the symmetry of RX transfer function around the operating frequency. 141
5.5 The modified impedance to reduce the number of the inductors. 142
5.6 A two-stage OTA with Miller compensation [117]. 142

List of Tables

2.1 Performance Summary And Comparison With State-Of-The-Art RXs. 55

3.1 Performance Summary And Comparison With State-Of-The-Art RXs. 91

4.1 The summary of extracted linearity parameters of LNTA and TIA amplifier last stage. 117
4.2 The tunable range of the utilized key components of the proposed RX. 123
4.3 Performance Summary And Comparison With Prior Art. 134

Summary

To meet the growing demand for higher data rates, the fifth generation (5G) of mobile communication has been introduced for low-band, mid-band, and high-band frequencies. In 5G applications, higher bandwidth and complex modulation schemes are employed for this purpose.

To mitigate the high path loss associated with mm-wave frequencies, greater focus has been placed on low-band and mid-band radios. Even the operating frequency of sub-6 GHz radios has been extended to sub-7 GHz. However, the congested sub-7 GHz spectrum has kept the offset frequency of close-in blockers constant compared to the previous standards, such as 4G. This imposes stringent requirements on receiver (RX) selectivity and linearity.

This thesis presents reconfigurable wideband low noise transconductance amplifier (LNTA)-based RXs for sub-7 GHz radios. The proposed RXs have high bandwidth and decent noise figure (NF) performance to employ high-order modulation schemes and achieve a high data rate. This thesis introduces techniques to enhance the RX selectivity for suppressing the close-in blockers of 5G user equipment, microcell base station, and local area base station applications. Moreover, this thesis proposes RXs with decent far-out out-of-band linearity for base station co-location applications where strong blockers are present from other standards.

Chapter 1 outlines the evolution of wireless communication leading to 5G applications. It introduces the 5G standard and highlights its stringent requirements on RX operating frequency, bandwidth, noise figure, and linearity. Following a brief discussion on N-path filters and their role in enabling wideband RXs, Chapter 1 reviews state-of-the-art RX designs and identifies their limitations for 5G applications. Finally, it defines the objectives and scope of this thesis.

Chapter 2 targets 5G user equipment applications and introduces a wideband

blocker tolerant receiver fabricated in 40-nm bulk CMOS technology. By incorporating programmable zeros and a second-order transimpedance amplifier (TIA), the RX achieves enhanced selectivity and fulfills the stringent linearity requirements of 5G for close-in blockers. An auxiliary path is employed to reduce the RX input impedance at far-out offset frequencies, creating a current-sinking path for far-out blockers. In this way, the proposed RX achieves decent out-of-band linearity performance. To determine the component values for both the RF front-end and the second-order TIA, two design guides are developed based on the 5G standard. The proposed RX successfully meets 5G requirements for reference sensitivity and out-of-band blocking tests.

Chapter 3 presents a wideband RX for 5G microcell base station applications. This Chapter targets microcell co-location scenarios. Hence, it adopts a parallel preselect filter to achieve decent far-out out-of-band B1dB. Third-order RF and baseband filters deliver sixth-order channel selectivity to handle close-in blockers of base station applications, where the ratio of blocker offset frequency to RX bandwidth is 1/10. Additionally, a translational feedback network provides input matching and minimizes in-band gain ripple to below 0.5 dB. The RX's reconfigurable architecture supports a low-noise mode and linear mode. Leveraging its current-mode operation and sharp filtering, the implemented RX in 40-nm CMOS technology complies with all 3GPP requirements for reference sensitivity, in-band blocking, and out-of-band blocking.

Chapter 4 introduces a wideband LNTA-based RX for 5G local area base station applications. The proposed RX covers both low- and mid-band frequencies. Firstly, this Chapter determines the optimal TIA architecture for 5G applications. To do so, the first-order and Rauch TIAs were thoroughly analyzed and compared in terms of transfer function, input impedance, loop gain, and noise performance. The Rauch TIA was selected for its superior selectivity and higher loop gain for out-of-band signals, with additional selectivity enhancement by adopting a third-order high-pass filter integrated in parallel with the TIA feedback resistor. The RX incorporates the Rauch TIAs with passive mixers and an LNTA featuring an N-path notch filter in its feedback. To enhance the RX's operating frequency range, two switch sets at the LNTA output (one for the N-path notch filter and another for the down-converting mixers) were merged. Furthermore, the band-pass characteristic of the TIA input impedance is leveraged to introduce positive feedback in the LNTA, increasing the 3-dB bandwidth without compromising out-of-band rejection. The resulting design is fabricated using 40 nm bulk CMOS technology, and the proposed RX satisfies 3GPP requirements for reference sensitivity, in-band blocking, close-in blocking,

and out-of-band blocking, making it a strong candidate for 5G local area base station applications.

Chapter 5 provides a brief discussion of the proposed ideas presented in this thesis and offers suggestions for future research directions.

Samenvatting

Om aan de groeiende vraag naar hogere datasnelheden te voldoen, is de vijfde generatie (5G) mobiele communicatie geïntroduceerd voor de lage, midden en hoge frequentiebanden. In 5G-toepassingen worden hogere bandbreedtes en complexe modulatieschema's gebruikt om dit doel te bereiken. Om het hoge signaalverlies dat gepaard gaat met mm-wave frequenties te beperken, ligt er meer nadruk op radio's voor de lage en midden-frequentiebanden. Zelfs nu de werkfrequentie van sub-6 GHz radio's is uitgebreid naar sub-7 GHz. Echter, het overvolle sub-7 GHz spectrum heeft ervoor gezorgd dat de frequentieverschillen van nabijgelegen stoorzenders constant is gebleven ten opzichte van eerdere standaarden, zoals 4G. Dit stelt strenge eisen aan de selectiviteit en lineariteit van de ontvanger (RX). Dit proefschrift presenteert breedband ontvangers die gebaseerd zijn op ruisarme transconductantie versterkers (LNTA) voor sub-7 GHz radio's. De voorgestelde RX's hebben een hoge bandbreedte en een goed ruisgetal (NF) nodig om hogere-orde modulatieschema's te ondersteunen en een hoge datasnelheid te behalen. Dit proefschrift introduceert technieken om de selectiviteit van de RX te verbeteren voor het onderdrukken van nabijgelegen stoorzenders bij 5G-gebruikersapparatuur, microcel-basisstations en lokale basisstations. Bovendien stelt deze thesis RX's voor met een goede lineariteit buiten de ontvangstband voor de co-locatiescenario's van basisstations, waar sterke stoorzenders veroorzaakt door andere draadloze systemen aanwezig zijn.

Hoofdstuk 1 schetst de evolutie van draadloze communicatie die heeft geleid tot 5G-toepassingen. Het introduceert de 5G-standaard en benadrukt de strenge eisen aan de werkfrequentie, bandbreedte, ruisgetal en lineariteit van de RX. Na een korte bespreking van N-path-filters en hun rol bij het mogelijk maken van breedband RX's, biedt dit hoofdstuk een overzicht van de huidige RX-ontwerpen

This summary is translated to Dutch by Jan Prummel. Leo de Vreede and his wife edited the Dutch summary.

en identificeert het hun beperkingen voor 5G-toepassingen. Tot slot worden de doelstellingen en reikwijdte van deze thesis gedefinieerd.

Hoofdstuk 2 richt zich op 5G-gebruikersapparatuur en introduceert een breedband RX die bestand is tegen stoorzenders, welke vervaardigd is in 40-nm bulk CMOS-technologie. Door programmeerbare nulpunten en een transimpedantieversterker (TIA) met een tweede orde overdrachtsfunctie te integreren, biedt de RX verbeterde selectiviteit en voldoet hij aan de strenge lineariteitseisen van 5G voor nabijgelegen stoorzenders. Een extra signaal pad wordt gebruikt om de ingangsimpedantie van de RX te verminderen bij grote frequentieverschillen, hierdoor ontstaat een lage impedantie voor stoorzenders buiten de ontvangstband. Om de componentwaarden te bepalen voor zowel het RF-front-end als de tweede-orde TIA, zijn ontwerprichtlijnen ontwikkeld op basis van de 5G-standaard. De voorgestelde RX voldoet aan de 5G-eisen voor gevoeligheid en buiten-de-band-blokker scenario's.

Hoofdstuk 3 presenteert een breedband RX voor 5G-microcelbasisstations. Dit hoofdstuk richt zich op co-locatiescenario's van microcelbasisstations en maakt gebruik van een parallel geschakeld voorselectie-filter om een goede lineariteit buiten de band (B1dB) te bereiken. De derde-orde RF- en basisbandfilters leveren een zesde-orde kanaalselectiviteit om nabijgelegen stoorzenders in basisstations te onderdrukken, waarbij de verhouding van het frequentieverschil van de stoorzender tot de bandbreedte van de RX 1/10 is. Daarnaast biedt een translationeel feedbacknetwerk ingangsimpedantie aanpassing en minimaliseert het de rimpel in de versterking tot minder dan 0,5 dB binnen de ontvanger bandbreedte. De herconfigureerbare architectuur van de RX ondersteunt zowel een lage-ruismodus als een lineaire modus. Dankzij zijn stroom-georiënteerde en scherpe filtering voldoet de geïmplementeerde RX in 40-nm CMOS-technologie aan alle 3GPP-eisen voor gevoeligheid en blokkers scenario's zowel binnen als buiten de ontvangstband.

Hoofdstuk 4 introduceert een breedband LNTA-gebaseerde RX voor 5G lokale basisstations. De voorgestelde RX dekt zowel de lage als middenfrequentiebanden. Dit hoofdstuk bepaalt eerst de optimale TIA-architectuur voor 5G-toepassingen. Hiervoor zijn eerste-orde en Rauch-TIA's geanalyseerd en vergeleken op overdrachtsfunctie, ingangsimpedantie, lusversterking en ruisprestaties. De Rauch-TIA is geselecteerd vanwege zijn superieure selectiviteit en hogere lusversterking, met aanvullende selectiviteitsverbetering door een derde-orde hoogdoorlaatfilter welke parallel is geïntegreerd aan de TIA-tegenkoppelweerstand. De RX combineert Rauch-TIA's met passieve mixers en een LNTA met een N-path-notch-filter in de tegenkoppeling. Om

het werkfrequentiebereik van de RX te verbeteren, zijn twee schakelingen bij de LNTA-uitgang samengevoegd: één voor het N-path-notch-filter en een andere voor de mixer. Bovendien wordt de banddoorlaatkarakteristiek van de TIA-ingangsimpedantie benut om positieve tegenkoppeling in de LNTA te introduceren, wat de 3-dB-bandbreedte vergroot zonder concessies te doen aan de onderdrukking van buiten-de-band blokkers. Gerealiseerd in 40-nm bulk CMOS-technologie voldoet de RX aan de 3GPP-eisen voor; gevoeligheid, binnen-de-band blokkers, dichtbij en buiten-de-band blokkers, waardoor het ontwerp een sterke kandidaat is voor ontvanger toepassingen in 5G basisstations.

Hoofdstuk 5 biedt een korte bespreking van de voorgestelde ideeën in dit proefschrift en geeft suggesties voor toekomstige onderzoeksrichtingen.

List of Publications

Journal Papers

- **M. A. Montazerolghaem**, L. C. N. de Vreede, and M. Babaie, "A Highly Linear Receiver Using Parallel Preselect Filter for 5G Microcell Base Station Applications," *IEEE Journal of Solid-State Circuits*, vol. 58, no. 8, pp. 2157-2172, Aug. 2023.
- **M. A. Montazerolghaem**, L. C. N. de Vreede, and M. Babaie, "A Highly Selective Receiver With Programmable Zeros and Second-Order TIA," *IEEE Journal of Solid-State Circuits*, vol. 59, no. 6, pp. 1668-1683, June 2024.
- **M. A. Montazerolghaem** and M. Babaie, "A Sub-7-GHz Linear Receiver for 5G Local Area Base Station Applications," in *IEEE Journal of Solid-State Circuits*.

Conference Papers

- **M. A. Montazerolghaem**, S. Pires, L. C. N. de Vreede, and M. Babaie, "6.5 A 3dB-NF 160MHz-RF-BW Blocker-Tolerant Receiver with Third-Order Filtering for 5G NR Applications," *2021 IEEE International Solid-State Circuits Conference (ISSCC)*, Feb. 2021, pp. 98-100.
- **M. A. Montazerolghaem**, L. C. N. de Vreede, and M. Babaie, "A 0.5-3GHz Receiver with a Parallel Preselect Filter Achieving 120dB/dec Channel Selectivity and +28dBm Out-of-Band IIP3," *2022 IEEE Custom Integrated Circuits Conference (CICC)*, Apr. 2022, pp. 11-12.
- **M. A. Montazerolghaem**, L. C. N. de Vreede, and M. Babaie, "19.1 A 300MHz-BW, 27-to-38dBm In-Band OIP3 sub-7GHz Receiver for 5G Local Area Base Station Applications," *2023 IEEE International Solid-State Circuits Conference (ISSCC)*, Feb. 2023, pp. 292-294.

- B. Prabowo, O. Pietx-Casas, **M. A. Montazerolghaem**, G. Scappucci, L. M. K. Vandersypen, F. Sebastiano, M. Babaie, "29.3 A Cryo-CMOS Receiver with 15K Noise Temperature Achieving 9.8dB SNR in 10μs Integration Time for Spin Qubit Readout," *2024 IEEE International Solid-State Circuits Conference (ISSCC)*, Feb. 2024, pp. 474-476.

Acknowledgement

Finally, my Ph.D. journey has come to an end. It has been a long and challenging path, filled with both highs and lows. Like other chapters of life, it brought moments of joy and moments of hardship. Yet, as I began writing this thesis, I was surprised to feel a tinge of sadness, perhaps because it marked the closing of my academic journey. Now, it is time to turn the page and look ahead to the future. Completing this Ph.D. would not have been possible without the unwavering support of my colleagues, friends, and family. It's time to express my deepest gratitude to all those who supported me throughout this journey.

First of all, I would like to express my heartfelt thanks to my daily supervisor, Dr. Masoud Babaie.

Initially, I had plans to pursue my Ph.D. in the United States, but due to President Trump's travel ban on Iranian students, I was unable to go (He signed the travel ban less than 48 hours before my flight to the United States). That moment left me deeply disappointed, and after a while, I found myself again searching for another opportunity in Europe or Canada. It was during this time that my friend at the University of Alberta, Ali Basaligheh, mentioned a young professor at TU Delft with whom I might be able to work. Encouraged by his suggestion, I decided to send you an email to explore the possibility of joining your research group.

I still remember our first technical interviews and how passionately and differently you approached RF circuits. That impression stayed with me and ultimately convinced me to join your research group, even though you only offered me a 9-month evaluation period, while I had already secured a full Ph.D. scholarship from another university.

Time passed, and now we are approaching the end of our journey, despite the bumpy road we traveled. I must confess that working with you wasn't easy in the beginning, but that challenge helped me grow and fundamentally changed

the way I approach technical issues. Together, we submitted three ISSCC papers, two of which were accepted. Throughout those intense submission periods, I witnessed dedication and the effort you put into supporting each of your students. I learned so much from you—not only about research, but also about how careful planning and strategic thinking can pave the way to success. I would also like to extend my sincere thanks to your respected wife, Mina, and your newborn son, Alborz, for all the extra hours you devoted to reviewing and improving my papers. Your family's patience and support did not go unnoticed.

Throughout my Ph.D., I always had your full support, and there is one moment I will never forget. My first chip had an issue, and we decided to do a re-tapeout. Unfortunately, the second revision had an issue, and the chip was not functional. It was the toughest moment of my Ph.D., and I don't think I could have made it through without your support. You encouraged me to do another tape-out to fix the issue. That meant everything to me.

Thank you, Masoud, for your unwavering support, help, and guidance throughout this journey.

Next, I would like to thank my Ph.D. promoter, Prof. Leo de Vreede. As the head of our research group, you always supported me with patience and listened to my concerns throughout my Ph.D. journey. I still remember the day I told you I couldn't obtain my U.S. visa, and you graciously agreed to present my paper at ISSCC 2023. You put in a tremendous amount of effort to deliver the presentation, and your presentation was very well-received at ISSCC, ultimately leading to an invitation for the IEEE SSCL Special Issue. Although we were not heavily involved in day-to-day research together, I learned much from you during my academic development. You always offered valuable guidance at critical moments in my Ph.D., often with memorable advice such as: "Don't shoot yourself in the foot!" and "Don't hit concrete with your head!"

As a final favor, you even took the time to edit the Dutch summary of my thesis, and surprisingly, you asked your wife to double-check it as well. I want to express my gratitude for all the support you provided during my Ph.D.

I would like to extend my sincere appreciation to my Ph.D. committee members: Prof. Wambacq, Dr. Craninckx, Dr. Manstretta, Dr. Reiskarimian, Prof. Makinwa, and Prof. Serdijn. Thank you for the time you dedicated to reviewing my Ph.D. thesis and for providing valuable and insightful comments.

I would also like to thank the other professors in the ELCA group: Prof. Vaucher, Dr. Spirito, Dr. Verhoeven, and Dr. Gao. My deepest gratitude goes to Dr. Morteza Alavi for all the political and technical discussions we had throughout my Ph.D. journey.

During my Ph.D., I received a great deal of help and support from the support staff of the ELCA research group and the Microelectronics Department. First of all, I would like to extend my appreciation to Atef Akhnoukh, who supported us during the tape-out phases. Atef, I wish you all the best and hope you enjoy your retirement. I am also grateful to Zu Yao Chang, who wire-bonded our chips to the PCBs. I was able to catch my last ISSCC deadline with your suggestion. Thank you for all your help and support, Zu Yao. I also extend my appreciation to Antoon Frehe for IT support, and to Dr. Juan Bueno Lopez for his invaluable assistance during chip measurements—your support is greatly appreciated. Finally, I would like to acknowledge the kind help of our secretaries, Marion de Vlieger and Alana Datema-Heijbers. Dear Marion, I hope you enjoy your well-deserved retirement with your grandchildren.

At this moment, I would like to express my appreciation to my former professors in Iran, Dr. Mehdi Habibi and Dr. Mohammad Yavari. I still remember your inspiring lectures on Fundamentals of Microelectronics and Analog IC Design—they sparked my interest in the field and ultimately led me to choose Microelectronics as my career path.

During my Ph.D., I had the privilege of supervising two MSc students, Madhumitha Jayavel and Simon Verkleij. Watching your growth and development was one of the most rewarding experiences of my Ph.D. I wish you both all the very best in your future careers.

My deepest gratitude goes to Mohsen Mortazavi, Nasim Bakhshaei, Masoud Pashaeifar, Mohammad Reza Beikmirza, Mohsen Hashemi, and Milad Mehrpou for all the fruitful discussions we had during our breaks. I would also like to thank all my friends in the ELCA group: Zhong Gao, Anil Kumar Kumaran, Gagan Singh, Amir Arsalan Kiavar, Jordi van der Meulen, Ehsan Shokrolahzadeh, Jun Feng, Nawaf Almotairi, Linghan Zhang, Rob Bootsman, Dieuwert Mul, Richard Coesoij, Ying Wu, Maneesh Verma, Satoushi Malotaux, Carmine De Martino, Luca Galatro, Yue Chen, Ronaldo Martins da Ponte, Rishabh Gurbaxani, and Arash Noroozi. I want to extend my gratitude to my friends at QuTech: Bagas Prabowo, Bishnu Parta, Jiang Gong, Niels Fakkel, Alireza Ghaffari, and Gerd Kiene. Lastly, I would like to thank Alessandro Urso and Yiyu Shen for all the coffee breaks we shared to ease the tension of the Ph.D. journey.

I was fortunate to find a close-knit group of Iranian friends in the Netherlands: Nasim and Mohsen, Mahsa and Masoud and their lovely daughter Lena, Maryam and Amin, Boshra and Mohammad Reza, Maryam and Milad, Samira and Amir Arsalan, and Negin and Mohsen. Thank you all for the memories we shared over the past few years. My appreciation also goes to my Iranian friends around

the world: Sajad, Mohsen, Reza, Alireza, and Meysam. Lastly, I would like to express my deepest gratitude to my best friend, Navid. Our friendship has lasted nearly 17 years. Thank you for all the wonderful memories—from endless card games to our political discussions.

I want to express my deepest love and gratitude to my incredible parents, Maman and Baba. Baba, from the very beginning, you guided me on this path with your wisdom and encouragement. I still remember when I started my bachelor's studies, you told me, "You're a good electrical engineer when you publish a paper in IEEE." That single sentence stayed with me and became a driving force during my Master's—and ultimately led me to complete my Ph.D. Maman, I witnessed the countless sacrifices you made for me. You even hid your illness so I could focus on completing my final tape-out. I am deeply sorry I wasn't by your side while you underwent chemotherapy.

I also send my love and heartfelt gratitude to my sister, Atefeh, my brother-in-law, Mohammad, and my lovely niece, Parimah. I wish you a lifetime filled with happiness and love. To my little sister, Narges—thank you for your endless love and support. I wish you all the best in your future career and endeavors.

I send my deepest gratitude and love to my wonderful parents-in-law. Since the day I became part of your family, I have felt your unwavering support and affection. I also want to acknowledge how difficult it must be to have Bahar far from you. I'm truly sorry for taking her so far away, and I deeply appreciate your understanding and love. My warmest thanks also go to my sister-in-law, Negar. You are an exceptionally talented student with the potential to shine in the years ahead. I sincerely hope that you and Bahar will be able to live close to each other again in the near future.

Bahar, the love of my life—I can hardly find the words to thank you. You are the reason I was able to carry this burden and reach the end of my Ph.D. journey. After every difficult moment, you were always there to lift my spirits and motivate me to keep going. I have always admired your patience and unwavering support, especially during the countless long nights—even those late hours in the lab, measuring chips past midnight. I know how emotional and difficult it was for you to leave your family and move to the Netherlands. I will forever be grateful for the sacrifices you made. This Ph.D. belongs to both of us—it would not have been possible without you. You are the pillar of my life, and your love gives me the strength to face any challenge that lies ahead.

Mohammad Ali Montazerolghaem
Delft, May 2025

Chip Micrograph Gallery

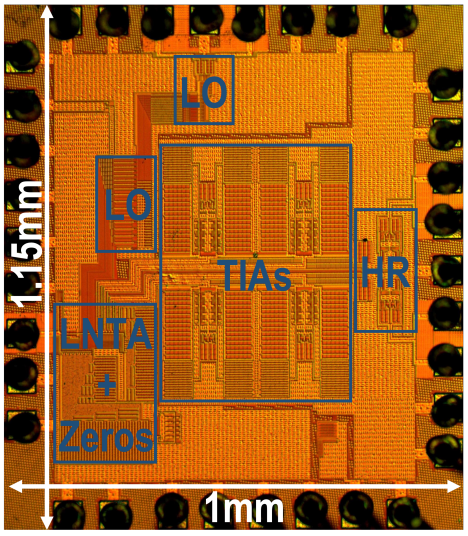

A wideband blocker tolerant receiver for 5G user equipment applications

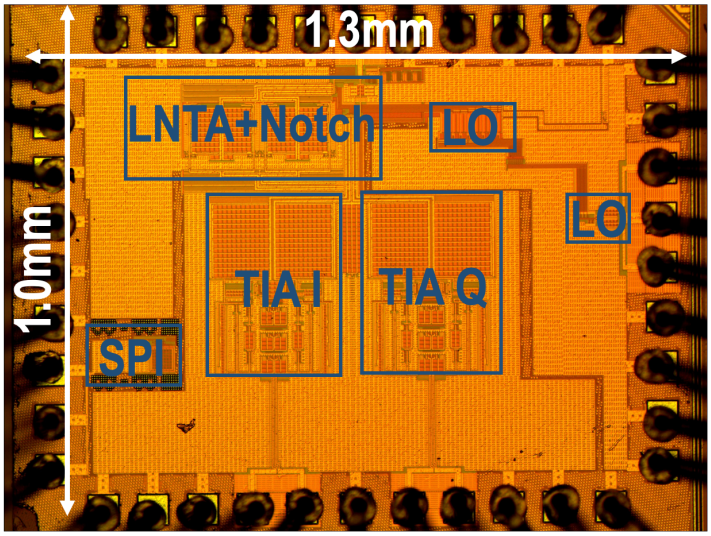

A sub-7GHz receiver for 5G local area base station applications

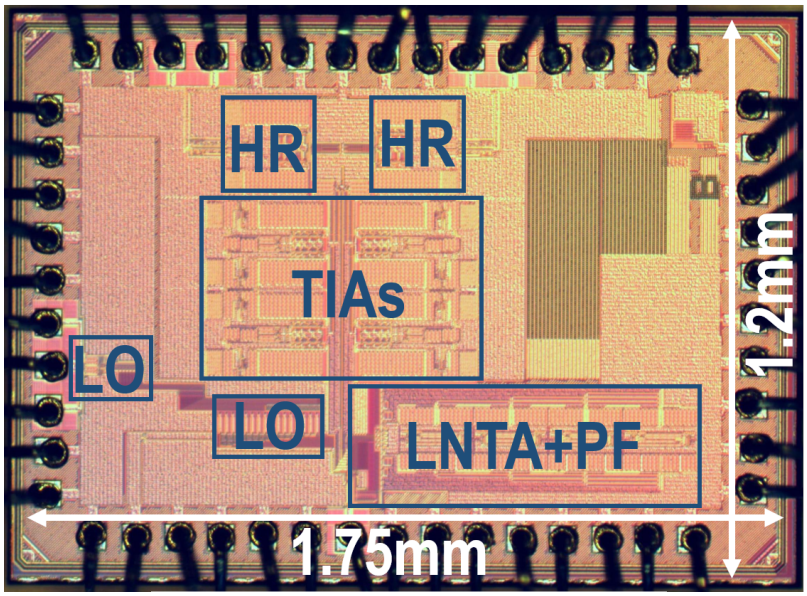

A highly linear receiver for 5G medium range base station applications

About the Author

Mohammad Ali Montazerolghaem received the B.Sc. and M.Sc. degrees in electrical engineering from the University of Isfahan, Isfahan, Iran, in 2012, and the Amirkabir University of Technology, Tehran, Iran, in 2014, respectively. He is currently pursuing the Ph.D. degree with the ELCA research group at Delft University of Technology, Delft, The Netherlands.

In December 2022, he joined Renesas Electronics, 's-Hertogenbosch, The Netherlands, where he is currently a Senior RFIC Designer. His research interests include high-performance receivers for 5G cellular and base station applications, as well as low-power transceivers for IoT applications.

Mr. Montazerolghaem serves as a reviewer for the IEEE Journal of Solid-State Circuits, IEEE Solid-State Circuits Letters, and IEEE Transactions on Circuits and Systems—I: Regular Papers.